



ScuDo
Scuola di Dottorato - Doctoral School
WHAT YOU ARE, TAKES YOU FAR



**UNIVERSITÀ
DI TORINO**

Research Programme
Doctoral Program in Urban and Regional Development (36th Cycle)

Cryosphere processes and hydrogeological systems: analysis and interactions

Michele Mondani

* * * * *

Tutor

Prof. Stefano Lo Russo

Co tutor

Prof. Monica Papini

Prof. Glenda Taddia

Doctoral Examination Committee:

Politecnico di Torino
March, 2024

Declaration

I hereby declare that the contents and organization of this dissertation constitute my own original work and do not compromise in any way the rights of third parties, including those relating to the security of personal data.

Michele Mondani

Turin, October 2023

* This dissertation is presented in partial fulfillment of the requirements for Ph.D. degree in the Graduate School of Politecnico di Torino (ScuDo).

Acknowledgment

ABSTRACT

Water drought problems concerning mountain aquifers are increasing. They are caused by evolution of climate conditions and pluviometric regimes that are favoring less winter snowpack, more intense and less frequent rainfall. Permanent cryosphere bodies melting are helping several mountain aquifers resources, although they are an unreliable source of water because once they are extinct they take thousands of years to reconstitute themselves.

The increasing drought problems concern more the territorial planning aimed to water resource management, since most of drinkable water comes directly from groundwater resources. Climate change has affected largely the cryosphere evolution: snow, ice, frost is subjected to a sharp cycle trends of temperature, causing their intense melting and being source of instabilities, water unbalance and solid transportation.

Increasing temperature cycles frequency have already caused several disasters driven by large cryosphere bodies melting and moving. Sometimes, lot of melted water infiltrates leading to slope saturation and possible collapse.

Here comes the intention to study cryosphere process as snow melting by cross-correlating spring and weather station information with the help of hydrogeochemical surveys and statistical analysis of time series, resulting in a whole comprehension of snow and ice behaviors.

Hydrogeologic equipment will be necessary to establish new relationship between cryosphere melting and the effective water release from this system.

The main goal of this research is to distinguish which aquifers do not perceive contributions from the permanent cryosphere and thus suffer from the new precipitation regimes, and instead the mountain aquifers whose water crisis is hidden by contributions from glacier and permafrost melt.

So initially a hydrogeological input output analysis will be carried out, among five monitored springs and their weather stations, to understand the compliance of the spring response to rain and snow amounts. After which, an attempt will be made to trace the spring anomalies with the extraordinary melting phenomena in the surrounding environment resulting from glacier and permafrost.

Moreover, in this thesis work, some laboratory experiment will be presented to understand the role of snow melting, which is becoming faster according to Climate Change effect, as a triggering factor for shallow landslides.

Keywords:

Cryosphere melting, Climate change, Precipitations evolution, Hydrogeology, Spring hydrograph analysis, Mountain aquifers, Water Resources, Slope instabilities.

Contents:

1 INTRODUCTION.....	17
1.1 Cryosphere.....	19
1.1.1 Snow.....	21
1.1.2 Glacier.....	24
1.2.3 Permafrost.....	25
1.2 Mountain aquifers and springs.....	27
1.3 New precipitation regimes.....	28
1.4 Shallow landslides	29
1.5 The 2030 Agenda.....	31
2 MATERIAL AND METHODS.....	33
2.1 Territorial frame.....	33
2.2 Case Studies.....	38
2.2.1 Alpe Perrot.....	38
2.2.2 Cheserod.....	41
2.2.3 Mascognaz.....	44
2.2.4 Promiod.....	48
2.2.5 Promise.....	51
2.3 Meteorological analysis.....	54
2.4 Spring analysis.....	59
2.4.1 Hydrograph analysis.....	60
2.4.2 System classification.....	65
2.4.3 Statistical characterization.....	67
2.4.4 Trend analysis.....	69
2.4.5 Hyrdogeochemical analysis.....	71
2.5 Annual Precipitation and discharge	72

2.6 Mascognaz weather station.....	74
2.7 Rutor Glacier mass balance.....	80
2.8 Shallow landslide experimental setup.....	84
3 RESULTS.....	86
3.1 Weather stations results.....	86
3.2 Spring analysis results.....	100
3.3 Precipitation and discharge correlation.....	131
3.4 Snowmelt statistical analysis.....	136
3.5 Rutor Glacier mass balance.....	140
3.6 Shallow landslide simulations.....	145
4 DISCUSSION.....	153
4.1 Mountain aquifer discussion.....	153
4.2 Shallow landslides discussion.....	161
5 CONCLUSION.....	164
5.1 Further and future research developments.....	168
6 REFERENCES.....	169

List of figures:

Figure 1. Water components percentage in the world.....	20
Figure 2. Rutor Glacier, photo taken during a field survey on October 21th, 2022.....	25
Figure 3. Thermodynamic scheme of permafrost according to Van Everdingen (1998).....	26
Figure 4. A: Photo of a Shallow Landslide; B: Scheme of a Shallow Landslide (Mezaal and Pradhan, 2018).....	30
Figure 5. Aosta Valle map by (Paschetta et al., 2016).....	34
Figure 6. Locations of monitored springs in Aosta Valley.....	35
Figure 7. Regional Geology of Aosta Valley.....	36
Figure 8. Analyzed springs with related weather stations in Aosta Valley.....	37
Figure 9. Territorial map with Alpe Perrot spring and Champorcher- PMB weather station; below it is represented a 3D Google Earth Pro image with the spring surrounding area.....	39
Figure 10. Alpe Perrot spring depicted in Geotectonic map of the Aosta Valley, scale 1:100000, (De Giusti, et al., 2003).....	40
Figure 11. Territorial map with Cheserod spring and Gressan – Pila Leissè weather station; below it is represented a 3D Google Earth Pro image with the spring surrounding area.....	43
Figure 12. Cheserod spring depicted in Geotectonic map of the Aosta Valley, scale 1:100000, (De Giusti, et al., 2003).....	44
Figure 13. Territorial map with Mascognaz spring and Ayas– Alpe Aventine weather station; below it is represented a 3D Google Earth Pro image with the spring surrounding area.....	45
Figure 14. Mascognaz spring depicted in Geotectonic map of the Aosta Valley, scale 1:100000, (De Giusti, et al., 2003).....	46
Figure 15. Territorial map with Promiod spring and Chamois – Lac de Lou weather station; below it is represented a 3D Google Earth Pro image with the spring surrounding area.....	49

Figure 16. Promiod spring depicted in Geotectonic map of the Aosta Valley, scale 1:100000, (De Giusti, et al., 2003).....	50
Figure 17. Territorial map with Promise spring and La Thuile - Villaret weather station; below it is represented a 3D Google Earth Pro image with the spring surrounding area.....	52
Figure 18. Promise spring depicted in Geotectonic map of the Aosta Valley, scale 1:100000, (De Giusti, et al., 2003).....	53
Figure 19. a: Bascule Rain Gauge conveying mouth; b: Bascule Rain Gauge heating system; c: Termo-igrometer measuring Temperature and Relative Humidity; d: Ultrasonic sensor for Snow depth recording.....	54
Figure 20. Ordinary Least Squares of y regression (Ludbrook, 2010).....	56
Figure 21. Rainfall time series characterization for two different weather station in Aosta Valley (Gizzi et al., 2022).....	58
Figure 22. Typical set-up of a monitored spring (Mondani, Gizzi and Taddia, 2022).....	60
Figure 23. Four Hydrogeological years represented for the Alpe Perrot spring.....	61
Figure 24. Formation and movement of a groundwater "wave" generated by a localized recharge event.....	61
Figure 25. Components of a discharge hydrograph.....	62
Figure 26. Monthly Discharge BoxPlot population example by (Leone et al., 2021).....	67
Figure 27. Standardized Discharge Index example as reported by (Leone et al., 2021).....	68
Figure 28. An example of Schoeller diagram by authors (Balestra, Fiorucci and Vigna, 2022).....	72
Figure 29. Mascognaz nivo-meteorological station geographic location and photos (Panzeri and Mondani, 2022).....	75
Figure 30. Nivo-Meteorological statio set-up. Tower1 is equipped with atmospheric sensors, Tower 2 with Snowpack sensors (Mondani, Gizzi and Taddia, 2022).....	77
Figure 31. Snow melt experiment on the Laboratory Landslide simulator. GoPro cameras attached on the frames above the snow.....	80

Figure 32. Rutor Glacier mass balance. Observation period (2005, 2022). (ARPA VDA, 2022).....	81
Figure 33. Location of Rutor Glacier, weather stations and Promise spring.....	82
Figure 34. A: Simulator geometry without soil and in horizontal position. B: Simulator inclined of 35° with a soil layer of 15 cm positioned on the slab; C: TDR probe; D: electrodes array of geo-resistivity survey; E: soil foot frontal view (Panzeri and Mondani, 2022).....	84
Figure 35. Left side: frontal view of snow melting simulation; right side: conceptual scheme of the simulation with geometries and sensors positions. (Panzeri and Mondani, 2022).....	85
Figure 36. A: Position of the bended hose on the simulator, it is within a portion of gravel and sand soil; B: Photo of the drilled hose.....	86
Figure 37. Time series of Precipitations, Snow Depth and Temperature of Champorcher-Petit Mont Blanc weather station.....	88
Figure 38. Time series of Monthly Precipitation, Precipitation Frequency and Precipitation Intensity of Champorcher-Petit Mont Blanc weather station.....	89
Figure 39. Time series of Precipitations, Snow Depth and Temperature of Gressan-Pila Leissè weather station.....	90
Figure 40. Time series of Monthly Precipitation, Precipitation Frequency and Precipitation Intensity of Gressan-Pila Leissè weather station.....	91
Figure 41. Time series of Precipitations, Snow Depth and Temperature of Ayas-Alpe Aventine weather station.....	92
Figure 42. Time series of Monthly Precipitation, Precipitation Frequency and Precipitation Intensity of Ayas-Alpe Aventine weather station.....	93
Figure 43. Time series of Precipitations, Snow Depth and Temperature of Chamois-Lac de Lou weather station.....	94
Figure 44. Time series of Monthly Precipitation, Precipitation Frequency and Precipitation Intensity of Chamois-Lac de Lou weather station.....	95
Figure 45. Time series of Precipitations, Snow Depth and Temperature of La Thuile-Villaret weather station.....	96
Figure 46. Time series of Monthly Precipitation, Precipitation Frequency and Precipitation Intensity of La Thuile-Villaret weather station.....	97
Figure 47. Hydrographs of the five springs analyzed.....	101

Figure 48. Alpe Perrot hydrogeological years duration series (grey dots and lines), discretized in recharge period (blue bars) and discharge period (orange bars).....	105
Figure 49. Cheserod hydrogeological years duration series (grey dots and lines), discretized in recharge period (blue bars) and discharge period (orange bars).....	106
Figure 50. Mascognaz hydrogeological years duration series (grey dots and lines), discretized in recharge period (blue bars) and discharge period (orange bars).....	106
Figure 51. Promiod hydrogeological years duration series (grey dots and lines), discretized in recharge period (blue bars) and discharge period (orange bars).....	107
Figure 52. Promise hydrogeological years duration series (grey dots and lines), discretized in recharge period (blue bars) and discharge period (orange bars).....	108
Figure 53. Alpe Perrot recession with Bussinesq and Maillet interpolation (SOURCE).....	109
Figure 54. Cheserod recession with Bussinesq and Maillet interpolation (SOURCE).....	110
Figure 55. Mascognaz recession with Bussinesq and Maillet interpolation (SOURCE).....	111
Figure 56. Promiod recession with Bussinesq and Maillet interpolation (SOURCE).....	112
Figure 57. Promise recession with Bussinesq and Maillet interpolation (SOURCE).....	107
Figure 58. Annual time series of Water stored at the end of recession (Wt) and Renewal time rate (Trin) of Promise spring.....	114
Figure 59. Hourly time series of Discharge and Electric Conductivity (EC) for each spring along an hydrogeological year.....	116
Figure 60. Standard Discharge Index of the 5 springs, using 1 month discharge resolution and gamma distribution.....	119
Figure 61. Standard Discharge Index of the 5 springs, using 3 months discharge resolution and gamma distribution.....	120

Figure 62. Box Plot representing the monthly population of discharge for every spring analyzed.....	121
Figure 63. Alpe Perrot spring Schoeller Diagram.....	126
Figure 64. Cheserod spring Schoeller Diagram.....	126
Figure 65. Mascongaz spring Schoeller Diagram.....	127
Figure 66. Promiod spring Schoeller Diagram.....	127
Figure 67. Promise spring Schoeller Diagram.....	128
Figure 68. Piper Diagram of the five monitored spring, each symbol refers to a different year of sampling.....	130
Figure 69. Code piece for Solid and Liquid precipitation separation.....	132
Figure 70. Left: Alpe Perrot annual discharge and annual total precipitation comparison. Right: Annual discharge and precipitation correlation, best correlation with black dots and total correlation with black and grey dots.....	132
Figure 71. Left: Cheserod annual discharge and annual total precipitation comparison. Right: Annual discharge and precipitation correlation, best correlation with black dots and total correlation with black and grey dots.....	133
Figure 72. Left: Mascognaz annual discharge and annual total precipitation comparison. Right: Annual discharge and precipitation correlation, best correlation with black dots and total correlation with black and grey dots.....	134
Figure 73. Left: Promiod annual discharge and annual total precipitation comparison. Right: Annual discharge and precipitation correlation, best correlation with black dots and total correlation with black and grey dots.....	135
Figure 74. Left: Promise annual discharge and annual total precipitation comparison. Right: Annual discharge and precipitation correlation, best correlation with black dots and total correlation with black and grey dots.....	135
Figure 75. Summary of MLR regression result in Python (Statsmodel). The model is described by coefficient column where x1 is Temperature independent variable and const is the constant of the model relation.....	137
Figure 76. Summary of MLR regression result in Python (Statsmodel). The model is described by coefficient column where x1 is Temperature, x2 is Snow Density, x3 is Absorbed Radiation and const is the constant of the model relation.....	138

Figure 77. Photogrammetric evolution of snow surface which loses thickness along time.....	139
Figure 78. Annual Ablation and Mass Balance of Rutor Glacier.....	140
Figure 79. Annual time series of Summer Mean Temperature and Glacier Total Ablation from 2005 to 2022.....	141
Figure 80. Correlation between Summer Mean Temperature and Glacier Total Ablation with coefficient of determination R^2	142
Figure 81. A: Graph representing normalized Residual (Q-Ptot) and Glacier Mass Balance (GMB) with Min Max method; B: Graph representing the same normalized variables with Mean,Std method.....	144
Figure 82. Top view photos from the GoPro cameras in different moments during the Experiment 1.....	146
Figure 83. A: snow depth evolution recorded by observation; B: cumulated runoff water gathered inside the bawl along the experiment; C: volumetric water content recorded during the experiment; D: temperature registered by the three sensors placed along the landslide simulator located at the maximum depth of soil layer (cit paper mondani panzeri).....	147
Figure 84. A,B,C,D,E: tomography results at different moment during the experiment.....	148
Figure 85. Top view photos from the GoPro cameras in different moments during the Experiment 2.....	149
Figure 86. A: Water content detected by TDR during the simulation. B, C, D, E, F: tomography results at different moment during the experiment.....	151
Figure 87. Alpine Permafrost Index Map (Boeckli et al., 2012) with springs location.....	154
Figure 88. Alpe Perrot territory with RAVdA, 2022 information about glaciers and rock glaciers.....	155
Figure 89. Cheserod territory with RAVdA, 2022 information about glaciers and rock glaciers.....	156
Figure 90. Mascognaz territory with RAVdA, 2022 information about glaciers and rock glaciers.....	157
Figure 91. Promiod territory with RAVdA, 2022 information about glaciers and rock glaciers.....	158

Figure 92. Promise territory with RAVdA, 2022 information about glaciers and rock glaciers.....	159
Figure 93. A, B, C: sketches representing the three phases of the Experiment 1. The size of arrows indicates qualitatively the amount of water in each of its component; Heat flux and temperature variation are represented with the temperature gradient symbol on the right side. D: Cumulative runoff graph obtained during the simulation divided in the three phases	162
Figure 94. A: six phases sketch representing the evolution of Experiment 2; B: six phases sketch representing the evolution of Experiment 3	163

List of tables:

Table 1. Type of snow according to the density.....	22
Table 2. SDI values.....	69
Table 3. Sensors used for the statistic tests.....	77
Table 4. Meteorological results summary, positive trend in green and negative trend in red.....	98
Table 5. Hydrogeological years of the analyzed springs. Charge and Discharge seasons are also presented.....	101
Table 6. Alpe Perrot recession parameters summarized for every hydrogeological year.....	109
Table 7. Cheserod recession parameters summarized for every hydrogeological year.....	110
Table 8. Mascognaz recession parameters summarized for every hydrogeological year.....	111
Table 9. Promiod recession parameters summarized for every hydrogeological year.....	112
Table 10. Promise recession parameters summarized for every hydrogeological year.....	113

Table 11. Table that summarize the Correlation Factor results from each spring.....	117
Table 12. Summary of statistic tests performed for each spring, in green are those results that confirm the increasing trend, in red for the decreasing trend.....	122
Table 13. List of chemical parameters gathered in different sampling campaigns for each analyzed spring.....	125
Table 14. Normalized time series of: Spring Discharge (Q), Total Precipitation (Ptot), Residual Discharge (Q-Ptot) and Glacier Mass Balance (GMB), using two different normalization methods.....	143
Table 15. Summary of spring hydrographic basin information.....	160

Chapter 1

INTRODUCTION

Over the past decade, the environmental system has received considerable anthropogenic pressure, from the standpoint of pollution and the release of huge amounts of greenhouse gases (Karimi *et al.*, 2021).

The environment has acted with a severe response, in many ways, from biodiversity decreasing to desertification and more impactful hydrometeorological conditions (Jentsch and Beierkuhnlein, 2008; Kappelle, Van Vuuren and Baas, 1999; Jehanzaib *et al.*, 2020). The climate system is the main subject that maintains the ecosystems, thus in the equilibrium of organic and inorganic substances such as water and nutrients. Having undergone a sudden change, it is generating a series of chain reactions on the surrounding environment (Weiskopf *et al.*, 2020; Chersich *et al.*, 2015).

Especially, the climate is altering the water cycle, which is responsible in generating the conditions of life leading to a domino effects on the ecosystem balance related to a particular environment.

Besides, being fundamental element for flora and fauna, fresh water is a necessary resource for human activities, both from the point of view of drinking water consumption and from the point of view of exploitation for industrial, livestock and agricultural purposes. The alteration of this resource, naturally can generate economic and agribusiness crises in a different human communities (Chenoweth, 2008; Oki and Quioco, 2020).

In addition, the relentless exploitation of this resource and its ever-increasing need raises several questions about its ability to be managed and the potential damage that fresh water resource may suffer.

Water consumption has increased about sixfold over 100 years, caused by economic development and exponential population growth (UNESCO, 2019). Of course, currently, considering population growth projections, unsustainable exploitation is taking place, which can lead to severe problems in the future (Senatore, G. ,2013).

The massive use of water use and the various sources of pollutants generated by anthropogenic activity are diminishing what are clean supplies of water bodies (Maeda *et al.*, 2011).

The cryosphere, understood as the sum of all water in the solid state, is one of the most threatened system according to the rising climate which consequently is altering its conditions by increase the intensity of the melting processes.

The cryosphere system, which is mainly dominated by temperatures conditions, plays a key role in terrestrial cooling, given its properties of reflecting most of the sun's radiation by means of Albedo effect (Hotaling *et al.*, 2021; Pistone, Eisenman and Ramanathan, 2014). Its disappearance, therefore, generates a further rise in temperatures.

It also contributes in the global water balance. The melting of the seasonal cryosphere, i.e., snow, is an important feeding factor for high mountain aquifers, which in turn go on to supply the alluvial aquifers.

The importance of groundwater, is mainly dictated by the protective conditions it possesses, especially against pollutants but also by the biochemical interaction processes with the surrounding environment (Foster *et al.*, 2013).

From this, the importance of groundwater resources is because they are protected by aquifer system in which they circulate. In fact, they often hold the overall characteristics to be conveyed into the aqueduct network without special treatment.

Therefore, it is also important to preserve these resources from an economic point of view, given the expensive cost in the purification processes of already polluted fresh water (Cazcarro, López-Morales and Duchin, 2016; Xie *et al.*, 2022).

Indeed, in this thesis paper, a spring analysis will be conducted to characterize the evolution in recent years of water resources in a particular area. Where, a series of climatic changes are taking place, resulting in changes in water supplies from rain, snow, ice.

The latter factors, naturally go to destabilize mountain aquifers, which are affected by abruptly changing the amounts of water storage and spring runoff.

Indeed, the effects of such mutations can be seen by observing the progressive depletion of some hydrogeological systems (Carvalho-Santos *et al.*, 2017; Amanambu *et al.*, 2020), rather than the recharge of others that are nourished by a conspicuous supply from the melting of the cryosphere.

Therefore, it is important to study the new meteorological and rainfall regimes to understand the evolution of water amounts from precipitation and to check for compatibility with spring behaviors verifying the compliance with them. Where discordant effects are noted, external causes that may lead to such imbalances should be understood, including modification of the hydrogeological system or new inputs from glacial melt and permafrost (Khamis *et al.*, 2016; Levy *et al.*, 2015).

In fact, in this research project, it will be brought to light the variation of some spring characteristics of five case studies in the Aosta Valley territory in relation to weather conditions, to understand how water resources in the territory are varying, why they vary, and qualitatively propose a future scenario depending on the results obtained.

These springs are equipped with sensors that are recording discharge, water temperature and electric conductivity parameters from 2011. Their information are

coupled to the ones are coming from closest weather station in order to study water input characteristics (rainfall, snow) and atmospheric characteristics such as air temperature.

Therefore, by means of pluriannual data series gathered by the aforementioned hydrometeorological sensors applied throughout the studied territory, it is possible to obtain a relevant statistical analysis on groundwater evolution in time according to which environmental drivers (temperature, snow, rainfall characteristics, glacier melting, permafrost melting).

The time series analysis performed will bring to light the current water balance transition in Aosta Valley, in particular, considering the importance of cryosphere evolution in the territory, which play the crucial role of leading the water resources system in the next future. The goal is to understand the evolution of groundwater bodies in mountain environments to improve management of water resources and play Governance actions to reduce economic and social consequences.

The decompensation of the cryosphere in favour of huge amounts of water released into the environment can also result in ground instability phenomena that undergo saturation. Therefore, a laboratory analysis will also be conducted to understand the criticality of this phenomenon as a triggering factor for surface landslides. In addition, statistical field analysis will be conducted to understand which atmospheric and ice/snowpack conditions are most influential in the cryosphere melting process. The goal is to improve spatial accuracy and predictability precision of triggering thresholds maps of shallow landslides induced by cryosphere melting process.

1.1 Cryosphere

The cryosphere collectively describes all forms of frozen water on the Earth's surface - sea ice, ice sheets, ice caps, glaciers, snow cover, river and lake ice, permafrost, seasonally frozen ground and solid precipitation. It is an important component in the context of climate change as it affects and is affected by changes in temperature. In particular, glaciers, the Greenland ice sheet, polar and mountain permafrost and Arctic sea-ice are expected to be dramatically altered by climate change.

Furthermore, the huge amount of water coming from sharp seasonal rising up temperature, which is becoming more intense and discontinuous, generate now hydrological dynamics necessary to be studied and evaluated.

So than, the importance of cryosphere behaviours as remarkable important water body must be put on foreground just considering that on the earth only 3 % of water is

owned by fresh water, in which 68,7 % is stock in ice and snow, 29,9 % is ground water and 0, 26 % is shallow water (lake and rivers) (White, 1993).

Where is Earth's Water?

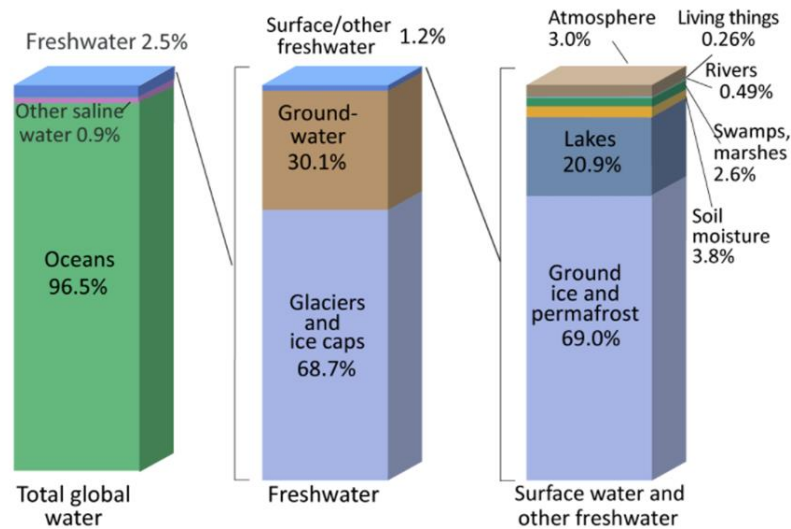


Figure 1. Water components percentage in the world

The cryosphere plays a fundamental role in recharging the aquifers, its slow but constant melting optimizes the infiltration process by minimizing water losses due to runoff (Jódar *et al.*, 2020).

Therefore, its preservation plays a key role in the water balance and in cooling the temperature of the planet.

Its disappearance together with increasing in rainfall intensity, which favor more runoff process rather than infiltration, could be a threaten factor for groundwater resources maintenance.

By the end of the century, the changing cryosphere will bring changes to landscapes, hydrogeological processes as well as the biology of mountain systems such as the Alps (Fountain *et al.*, 2012). Above all, the impact will not only be of the mountain areas but also downstream, as lowland areas are fed by conspicuous water inputs from the melting of the cryosphere (Beniston *et al.*, 2018).

To stop the trend of the cryosphere disappearing, according to the Paris Agreement, projections have been made that carbon dioxide emissions would need to be halved by 2030 in order to maintain the 1.5°C temperature increase limit. Otherwise, if not, the cryosphere system would reach an irreversible condition, and any remedy would be useless to avoid drastic effects on the ecosystem (Kloenne *et al.*, 2022).

On this purpose, some authors have studied that the possible loss of mass of the entire global glacier, excluded poles, can be estimated around 64 % by the end of the century if the global average warming is passing 2 °C during this century (Shannon *et al.*, 2019).

From this concern, this study aims to understand the effects of such developments from the hydrogeological point of view to show the possible future scenarios of high mountain aquifers, which are the effect of what is happening from the climate, rainfall and cryosphere point of view.

The cryosphere in mountain environment, is mainly divided into three components which are seasonal snow, glaciers and permafrost. They will be described in detail in the following sections.

1.1.1 Snow

Snow is one of the main hydrological inputs for high mountain aquifers, its constant and slow water release during melt cycles makes the infiltration process efficient. Many mountain springs, in fact, have a spring hydrograph that shows the annual recharge peak just after the time of almost complete snowpack melt during the spring season (Jódar *et al.*, 2020).

Examining a section made in a snowpack, it can be seen that it consists of a mass of layers of snow with different physical and mechanical characteristics. Each layer was formed in the course of a snowfall and in the meteorological conditions of the moment of the fall, as well as the subsequent ones gave it its characteristics. However, these layers will continue to evolve until the final dissolution.

In addition to the meteorological conditions, topographical exposure plays a very important role, since it can strongly influence the effect of meteorological events.

The snowpack is therefore a heterogeneous material. The physical and mechanical characteristics largely depend on the types of snow crystals that compose it. Observing the fresh snow that settles, it is noticeable that some transformations of the initial crystals are influenced by thermodynamic and mechanical effects. These transformations, that are called metamorphisms, will lead from fresh snow to melting, through continuous evolution.

The transition phases are characterized by combinations of crystals or snow grains at different stages of evolution. Snow is a porous material whose temperature is always lower or at most equal to 0 °C. Snow is said to be dry when it is made up of a mixture of air and ice at a negative temperature. The air contains water vapor so water is present in its two gas and solid phases.

When there is the presence of liquid water in the snow, the three phases of the water are in thermodynamic equilibrium and this results in a temperature of 0 ° C. When the snow is dry, the metamorphisms of the snow grains are formed with the vapor phase, while in the case of wet snow, they happen basically with the liquid phase, being the gaseous phase generally quite reduced.

This is the reason why two types of metamorphisms are distinguished: the dry snow metamorphism and the wet snow one. In addition to these thermodynamic transformations, the snow crystals can undergo transformations related to mechanical factors due to the wind, or to the weight of the upper snow layers, when they are buried. Therefore, there are numerous factors and engines of metamorphisms. Some are related only to dry snow, some related with the presence of liquid water inside the snow mantle and other that intervene in modifying the structure of the snow crystals such as wind, stress pattern and avalanches (Balzan, F., 2013).

Snow is considered, as well, a source that provides water to a terrain usually in the spring season. The mechanisms which involve snow are different with respect to the ones that involve the rainfall and are strongly related to the physical characteristics of the first. In fact, its amount, its density and other external parameters like temperature and humidity, influence the water receiving process of the soil that is obtained thanks to the melting of snow. The depth of the layer together with the density determine the amount of water that is present above the soil. Density, in particular, is an important factor that is used in order to classify the different type of snow (Peterson W.S.B, 2006).

Table 2. Type of snow according to the density

Type of snow	densities (kg/m ³)
New snow (immediately after falling in calm)	50-70
Damp new snow	100-200
Settled snow	200-300
Depth hoar	100-300
Wind packed snow	350-400
Firn	400-830
Very wet snow and firn	700-800
Glacier ice	830-917

Snow humidification, which is usually called wet snow metamorphosis, can take place in two ways: by melting the surface of the snowpack under the effect of the positive energy balance of snow / atmosphere exchanges (hot air, strong solar radiation, etc.) or with the direct contribution of liquid water such as rainfalls event.

The humidification of the snow layers essentially takes place on the surface of the snowpack, at the interface with the atmosphere where mass and energy flows are exchanged. Whether it is rain water or surface melt water, its deep penetration does not occur in a homogeneous way, but through preferential paths or percolation paths.

Variable LWC (Liquid Water Content) can therefore be found in a layer of wet snow, or even on the same horizontal level in wet and dry areas. However, for a layer of snow whose base does not lean on an impermeable surface, there is more often water drainage as soon as its capacity to retain water, given by capillarity, is exceeded.

The water retention value of snow depends mainly on its density rather than humidification. In fact, it varies between 12% by mass for densities of the order of 250 kg / m³ and 7% for densities of the order of 500 kg / m³. Under these conditions, metamorphism implies a fairly rapid rounding of the grains, and the appearance of rounded grains (symbol: O) can be observed.

The enlargement of grains depends on LWC: very slow for small LWCs and faster with LWCs close to the retention value. Experience shows that a recent snow subjected to a humidification for 16 days, turns into snow with rounded grains whose diameter reaches about 0.2 mm with a maximum LWC of the order of 2%, and 0.6 mm if the LWC is 10%.

More generally, the rounded grain sizes are typically between 0.2 and 2 mm. On the scale of the snow layer, there is a progressive increase in density (up to 500 kg / m³), and the cohesion decrease with LWC increase.

When a layer of humidifying snow leans on an impermeable surface, or on a layer of snow in which water cannot flow (larger grains or less dense snow), a saturated layer can form. Under these conditions, the metamorphism occurs under a very strong LWC regime. On the one hand, the enlargement of the grains is rapid and on the other hand, the ice bonds as well as the capillary ones between the grains disappear.

At the scale of the layer the density is significant and the cohesion becomes very weak. Therefore, phenomena such as the slipping of wet snow avalanches can occur. When the wet snows undergo a cooling, the liquid water present freezes progressively creating solid bonds between the rounded grains with the formation of agglomerates of numerous mm, and sometimes crusts of ice.

The snow then acquires an excellent cohesion called "freezing". This is what can be observed frequently in spring with alternating daytime heating followed by nighttime cooling.

All types of snow can be transformed with humidification into rounded grains, however it is the only transformation that grains such as ground hoar and "bullet" snow can undergo. In fact, the heart of winter, strong warming accompanied by rain can be healthy for the future of a snowpack made fragile by the presence of the aforementioned kind of snow layers (Balzan, F., 2013).

1.1.2 Glacier

Glaciers, generally, are those bodies of ice generated by the accumulation of snowfall, the accretion over the years of the same is caused by the incomplete melting of the seasonal snowpack, which goes on to accumulate on mantles from previous years.

Glaciers cover about 10 percent of the earth, although only one percent of this is not in areas remote from human activities. These are generally located at high altitudes, but at latitudes where human settlement development is permitted (Cuffey, K. M., & Paterson, W. S. B. ,2010).

Throughout history, especially in alpine areas, glaciers have been the major players in shaping morphology with their accretion and retreat. In historical phases such as glaciations, winter accumulations far outweigh summer ablation processes, while in historical phases such as the contemporary one, ablation processes outweigh accumulation processes.

Compared with snow, where the increase in density usually occurs through melting and freezing of the layers, in the case of glacier, density increases as a function of the pressure brought into play by the overlying mantle. Compaction in that case reduces the free energy given the decrease in the snow exchange surface area, so molecules are redistributed in the way that the total surface area of the crystal is reduced making it smoother (Maeno, N., & Ebinuma, T. ,1983).

In addition to the melting and accumulation processes of glaciers, it is also important to consider their dynamic behavior. Indeed, they, being often located on more or less steep slopes, are influenced by gravity, to which they respond according to some with viscous behavior in which the mass undergoes elongation in tensile conditions and shortening in compressive situations. Indeed, it is well known, in tensile zones, the presence of crevasses which are long, deep cracks that split the body of the glacier (van der Veen, 1999).

The fractures generated by the glacier's tensional state promote the circulation of water within the glacier. An actual drainage system is created within the glacier, which develops into fractures, channels and can even flow into lakes both created within the glacier and on the ground surface (Boon and Sharp, 2003; Nienow, Sharp and Willis, 1998).

In mountainous environments, glaciers usually develop on the northern slope, where there is less exposure to solar radiation and thus ablation processes are reduced. In fact, as we shall see, temperature is the main factor in the process of wet metamorphism, where the exchange of energy with the air, causes crystals to melt in the form of latent heat.

In addition, the likelihood of glaciers forming increases with elevation, since the thermal gradient means that as 100 meters of elevation increases, there is a 0.6 °C drop, which favors higher elevations to remain below thermal zero for a long time throughout the year.

Since they are extremely linked to climatic conditions, currently one must understand the threat of seeing them disappear in a few years.

In addition, there is a risk that much of the water that comes from glaciers may be contaminated with significant concentrations of metals-substances that have accumulated within ice layers due to anthropogenic pollution (Hodson, 2014; Gabrieli and Barbante, 2014).

The accumulation processes of a particular year lead to enrichment of glaciers with pollutants of the respective year. Such as lead enrichment during the Roman Empire and during the period of leaded gasoline.



Figure 2. Rutor Glacier, photo taken during a field survey on October 21th, 2022

1.1.3 Permafrost

The word permafrost defines a physical condition rather than a material condition. This condition is especially prevalent in high latitude or high elevation periglacial zones.

The definition of permafrost comes from the status of permanent ground frost "permanent frost." Given the current situation of rapidly changing climatic conditions

this definition has been changed to "perennially-frozen-permafrost" which better reflects the relationship between frozen ground and time, giving a better meaning according to its evolution in time (Dobinski, 2011).

Based only on physical properties, the status of permafrost depends only on temperature, in fact such is considered to be that portion of the lithosphere where temperature remains below zero degrees Celsius as depicted in **Fig 3**.

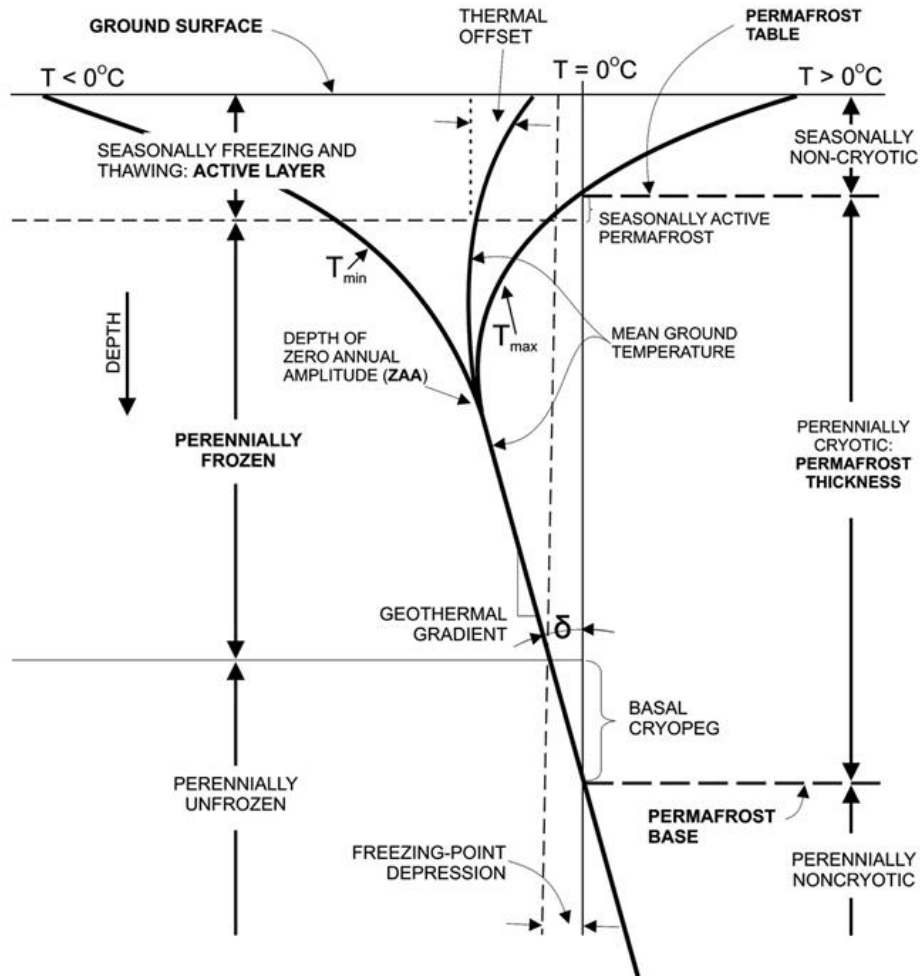


Figure 3. Thermodynamic scheme of permafrost according to Van Everdingen (1998).

As can be seen in the **Fig. 3**, the lower limit of permafrost layer fluctuates according to the temperature increase given by the Earth's thermal gradient, in fact below a certain depth the temperature returns above zero. Instead, the upper limit of permafrost is driven by the ground surface temperature influenced by atmospheric temperature. In fact, there is a portion of the ground above the permafrost called the "active" zone, which drops below zero in winter seasons and rises above zero in summer seasons.

Permafrost may or may not contain water in the liquid or solid state. According to Van Everdingen (1998) definition, permafrost without the presence of water is called dry permafrost.

In case there is presence of water, the medium looks like a three-phase, with the matrix of soil, ice, and even a small component of water in the liquid state (Anderson and Morgenstern, 1973).

In the alpine environment, permafrost is mostly seen in the form of rock glaciers in the periglacial environment, generally between altitudes of 2000 and 3000 meters. They usually derive from the debris fans or from terminal moraines of glaciers. In fact, the processes that generate these forms can be separated or combined into periglacial, glacial and paraglacial (landscape relaxation) (Knight, Harrison and Jones, 2019).

So in these cases, portions of porous matrix resulting from these debris accumulations are formed over the rock substrate.

Rock glaciers are also classified according to the presence of ice within them, they are said to be active if this condition is verified and also manifest movements, inactive if they do not move there is still the presence of ice, and fossil if they are characterized by neither movements nor ice.

As reported by the authors (Jones *et al.*, 2019), rock glaciers are very important from the hydrological point of view, they have greater resilience than glaciers climatically. They usually have less attention than the latter because more difficult to be studied since the ice volumes are usually hidden inside the deposits textures.

Rock glaciers many times contain significant volumes of ice, which becomes a water resource that is released in diurnal, seasonal, annual, and decadal cycles. Rising temperature trends are clearly accelerating the processes of water release from these forms, going to offset water scarcity in several alpine areas.

1.2 Mountain Aquifers and Springs

Mountain aquifers are the ones that then, through springs outflow and underground connections, go on to feed the large aquifer systems in the alluvial plains. They at this time, being small in size, are undergoing abrupt changes due to the evolution of weather regimes in the high mountains (Somers and McKenzie, 2020), leading to varying seasonal snowfall amounts, different rainfall characteristics, and very important melting process of glaciers and permafrost.

The importance of the water resource in the mountains is mainly due to its high quality (Tokatli, Köse and Çiçek, 2013), since as water intersects more anthropized areas, its vulnerability to pollutant increases. In fact, mountain communities, often use the high-

altitude water resource for drinking water purposes by adopting fast and low-cost purification processes. Therefore, policies are being adopted to manage and understand the evolution of mountain water resources as a function of climate change (Viviroli *et al.*, 2011).

The water that comes out of mountain springs often has oligomineral characteristics, having circulated in short circuits. This characteristic makes it usable in the market and for feeding into the aqueduct network.

The metals factor is the only one that needs to be checked before feeding into the artificial network, since the water may have been enriched in toxic metals such as Arsenic, Lead and Chromium by passing through rock formations rich of them (Welch *et al.*, 2000).

This recent period has brought high variability from the point of view of climatic conditions, this necessarily induces a change in the balance of these mountain water resources. Outcomes in this concern are often brought to light by several analysis about spring discharge, water temperature and water electrical conductivity parameters over time. (Ravbar, Engelhardt and Goldscheider, 2011; Szczucińska and Wasielewski, 2013).

The variation in these parameters over time can indicate the variation in water inputs in terms of quantity, quality and location according to the aquifer system type (Chiaudani *et al.*, 2019). That is, to understand the changes in hydrological input quantities and the variation in input types over time.

Thus, in several cases especially through the time series of flow rate over time it is possible to study the different recharge inputs to the aquifer and distinguish between snow melt, rainfall and melt of the permanent cryosphere. (Jeelani *et al.*, 2017).

These methodological approaches can be useful to better understand the evolution of mountain water resources and identify possible scenarios.

Currently, particularly on the Alpine altitudes, there is a decrease in rainfall amounts over years which will be better explained in the next chapter, this naturally leads to less water supply to aquifers unless they are fed by other inputs such as glacial and permafrost melt.

1.3 New Precipitation regimes

It is also important to determine the evolution of rainfall characteristics over time to understand the behaviors of water resources as a function of meteoric water availability. Above all, to understand what is the importance of the influence of the cryosphere net of rainfall inputs in areas surrounding mountain aquifers.

All over the world there have been changes in atmospheric and precipitation parameters in recent years, such as in Central Europe there is less summer rainfall and more spring rainfall with an increasing atmospheric temperature (Szwed, 2019).

Both in China and in California, some authors (Berg and Hall, 2015; Mo *et al.*, 2019) have studied territorially the increase in the frequency of extreme events in relation to the effects of Climate Change.

In the Southern Hemisphere, similar situations are manifested in terms of increased extreme phenomena. Furthermore, spatial rainfall imbalances are witnessed, leading for example southern regions of Australia to have less precipitation than northern regions, which are not showing the same dynamics (Dey *et al.*, 2019).

Studies more inherent to the area of study (Aosta Valley) have shown a decrease in cumulative precipitation and precipitation frequency in the alpine mountain chain (Padulano *et al.*, 2020; Gizzi *et al.*, 2022).

These accounts in the literature give us insight into the reasons for the increasingly frequent hydrogeological catastrophic events and widespread drought phenomena. Increased rainfall intensity with less frequent phenomena in fact, turns out to be less effective in recharging ground water resources, moreover it is more damaging due to rapid saturation of slopes leading to landslides and an increase of surface runoff that generates flooding and damage.

Of course, groundwater resources are directly dependent on what happens at the atmospheric level, as it is the first phase of the hydrological cycle. Several studies show the suffering of groundwater resources in the face of new climatic conditions that do not favor an effective water supply for recharging groundwater receptors (Carvalho-Santos *et al.*, 2017; Wu *et al.*, 2020; Amanambu *et al.*, 2020).

Some authors have shown a direct study of the consequences of decreased precipitation on groundwater fluctuations (Dey *et al.*, 2020).

In addition to liquid precipitation, it is important to consider solid precipitation; as it has been mentioned earlier, snow plays a key role in aquifer recharge. The lower amount of winter accumulation dictated by less precipitation and 'increased temperature results in a negative effect in the environmental utilities that receive this supply (Jepsen *et al.*, 2016).

Some authors also detected a variation in the timing at which the snowpack begins to melt, this due to its lower mass and especially temperatures rising above 0°C earlier than in the past shifting sometime from early spring to late winter (Clow, 2010).

1.4 Shallow Landslides

The spin-off of this thesis paper presents the interaction of cryosphere melting phenomena with possible instability phenomena such as Shallow Landslides.

Shallow landslides are phenomena that include a superficial soil portion, one to few meters, and locate their slip surface above the bedrock substrate as shown in **Fig 4**. Their susceptibility depends on geological, geomorphological and land-use features (Persichillo *et al.*, 2017).

Usually this type of phenomenon is triggered by soil saturation that decreases the cohesive forces that determine the stability of the soil portion. These phenomena are also very dangerous and destructive given the short warning time and their rapid movement dynamics (Marinelli *et al.*, 2022). Therefore it is important to understand their dynamics, predisposing factor, and triggering factor in order to improve the early warning systems and territorial knowledge.

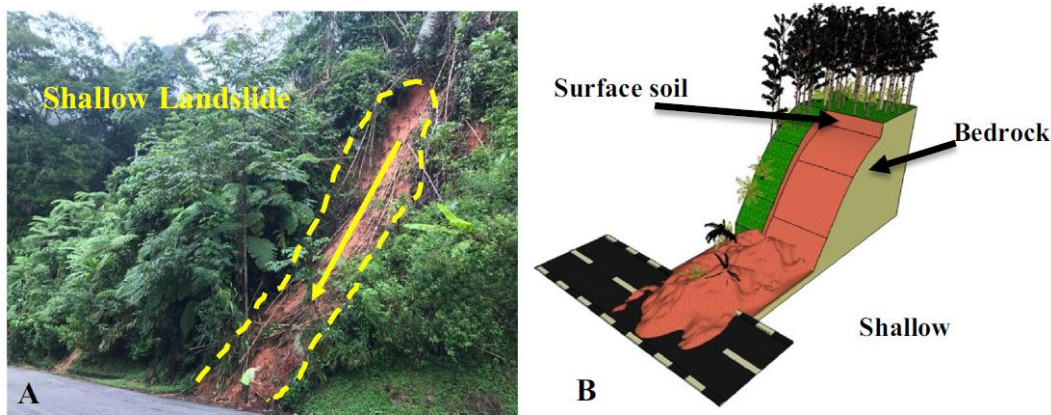


Figure 4. A: Photo of a Shallow Landslide; B: Scheme of a Shallow Landslide (Mezaal and Pradhan, 2018).

Shallow Landslides are usually caused by intense rainfall phenomena, in which the landslide body has not enough time to drain the water, therefore, the porous medium becomes saturated generating the slope failure (Gariano *et al.*, 2015). Given the increasing frequency of extreme rainfall events, these phenomena are becoming more frequent and important to analyze.

For this reason, it is important to understand whether, in addition to the intensity of rainfall phenomena, with the accelerated melting cycles of cryosphere caused by rising temperatures, it is possible for large amounts of melted water to infiltrate rapidly, generating instability.

Down-scale laboratory tests are one way to understand precipitation thresholds in relation of this type of phenomenon. Based on various recreated system parameters such as slope, soil type, soil compaction, some boundary conditions in terms of time, amount and intensity of precipitation are generated to trigger the collapse of the

medium. Several authors including (Huang and Yuin, 2010; Wu *et al.*, 2015) have carried out laboratory tests to simulate the collapse of shallow landslides from rainfall inputs. Nevertheless no one has ever performed a downscaled simulation of a shallow landslide with snowmelt input rather than precipitation.

In this thesis, with the collaboration of Politecnico di Milano, some downscaled experiment have been performed exploiting the University laboratory landslide simulator (Longoni *et al.*, 2022), where an actual snow layer was leaned above a sand soil layer. Process reconstruction by means of a sophisticated equipment is able to investigate the phenomena that affect melting and infiltration-percolation activity between soil and snow.

This analysis has started relying on some authors works, which were aimed to build snow melting triggering landslide thresholds on regional scale maps (Al-Umar, Fall and Daneshfar, 2020; Camera *et al.*, 2021). As they analysed, the importance of understanding not only predisposing factors of this type landslide, but also comprehending the physical and thermal process between snow and soil interaction that might trigger huge amount of infiltrating water and then collapse of the soil.

1.5 The 2030 Agenda

The United Nations has developed the 2030 Agenda for Sustainable Development, which has as its main goal to limit global warming within the limits dictated by the Paris Agreement. In addition to the climate topic, which is the basic one for the Agenda according to the effects it causes from the perspective of ecosystems, there are a whole series of subgoals related to different current issues.

These subgoals are the so-called SDGs (Sustainable Development Goals), they are 17 principles on which Agenda 30 is developed. It is of paramount importance that nowadays in a thesis paper it is specified which topical issues are touched upon in order to ensure a better scientific integration into what are the world's socio-economic needs at this time.

Among the 17 SDGs, this thesis definitely includes SDG number 6 related to the need to ensure water availability for all and its sustainable management, in fact the study of this research offers a basis for understanding the change of the water resource across the Alpine territory in order to then activate those governance systems that can mitigate the water transition and increase the resilience of the integrated water management system in the territory.

Definitely standing out in this thesis is the emergency from the ecosystem perspective, a theme developed with SDG 15, which emphasizes the importance of protecting,

restoring and promoting the sustainable use of terrestrial ecosystems, sustainably managing forests, combating desertification, halting and reversing soil degradation and halting biodiversity loss. Since water availability is one of the most important elements in ensuring ecosystem balance, it is also one of the factors that generates the most ecological and biodiversity changes when it is altered.

Of course, SDG 13 on taking urgent measures to combat climate change and its consequences also comes into play in this manuscript. Effectively, in the proposed research, no decisive systems are directly proposed to combat rising temperatures, but it does raise the need to accelerate countermeasures to stop this change. The consequences of water resources and the cryosphere, in fact are clearly visible as a result of this research, which carries a message of urgency regarding SDG 13, that is, the actions that need to come into play to limit rising temperatures. The consequences of climate change from the point of view of hydrogeological risk, are analyzed in the second part of the thesis where the focus is on how conspicuous melting of the cryosphere can generate slope instability phenomena.

This scientific paper, presenting cause-effect relationships between climate, cryosphere, groundwater resource, and hydrogeological instability, goes a long way toward integrating as many as three principles of the 2030 Agenda for Sustainable Development from environmental and socio-economic perspective.

Wantingly, this research also lays the foundation regarding SDGs 9 and 12, related to building a resilient Infrastructure and ensuring sustainable consumption and production patterns. Thus with regard to the problem analyzed in the thesis, those goals can concern the improvement of aqueduct diversification related to water intake structures and the optimization of water resource consumption adopting models and systems that reduce its waste.

Chapter 2

MATERIAL AND METHODS

2.1 Territorial Frame

The study is mainly carried out throughout the territory of Aosta Valley, which is an Italian region with an extension of 3.263 km² placed North-West of Italy, sharing the border with France and Switzerland.

Physically, Aosta Valley presents large portion of surface above 2000 m.a.s.l, it is the region with highest mountain chains in Italy. In fact, three of the highest mountain in Italy are in this region: Monte Bianco (4.809 m), Monte Rosa (4.609 m) and Cervino (4.478 m).

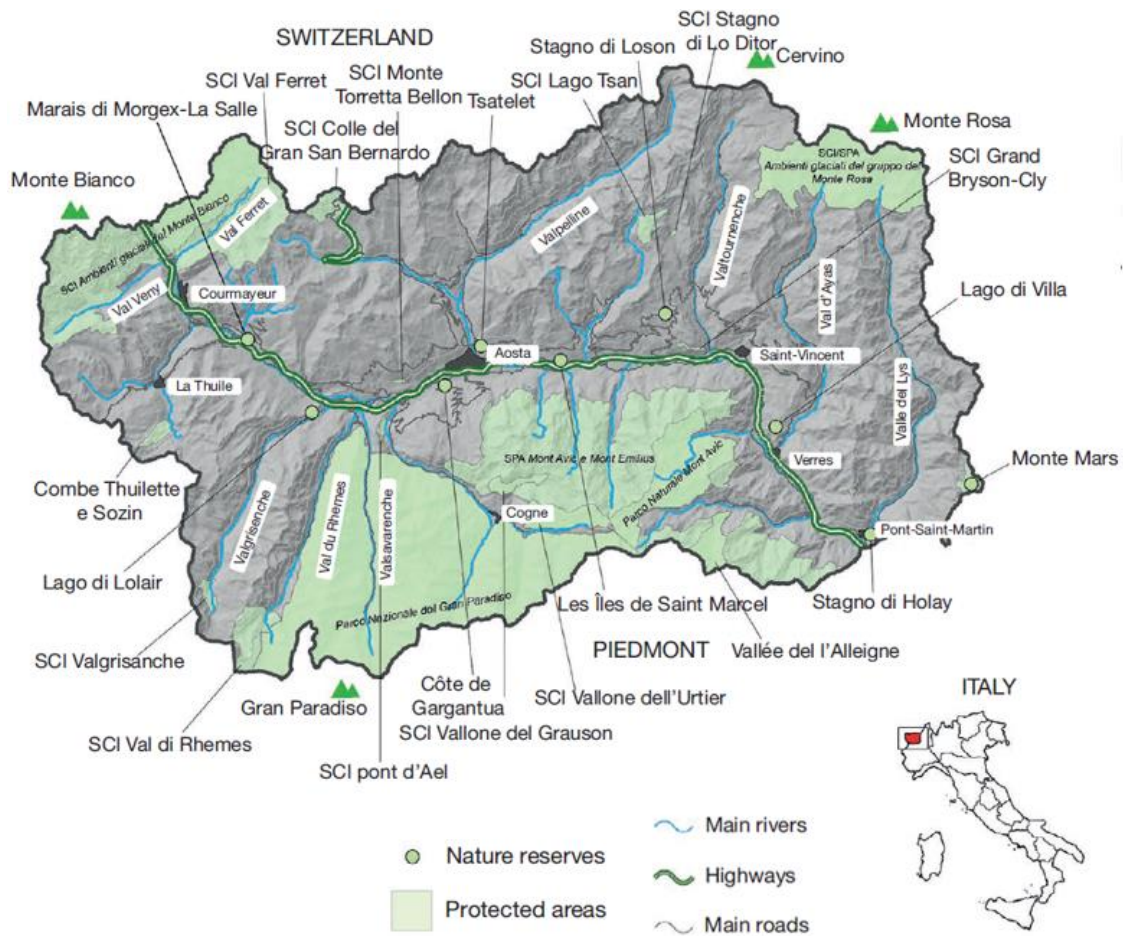


Figure 5. Aosta Valle map by (Paschetta *et al.*, 2016)

Fig. 5 shows a physical, hydrographic and naturalistic map of Aosta Valley presented by the authors (Paschetta *et al.*, 2016), where SCI are the Site of Community Importance, SPA and are the Special Protection Areas.

Along the main valley of the region is flowing the river Dora Baltea that conveys all the water coming from the smaller catchment areas where other valleys has been forms in millions of years (**Fig. 5**).

In Aosta Valley, water resources are abundant but not distributed homogeneously. The complex geology of the area make as well complex the hydrogeological assets of the territory. In fact, it is not easy to understand the evolution of springs associated to water resources, now more than ever because of the meteorological conditions changing in time.

In order to study the behavior of water resources in this territory, Applied Geology team of Politecnico di Torino has installed twelve multiparametric probes in some water intake structures across all the Aosta Valley Territory as presented in **Fig. 6**.

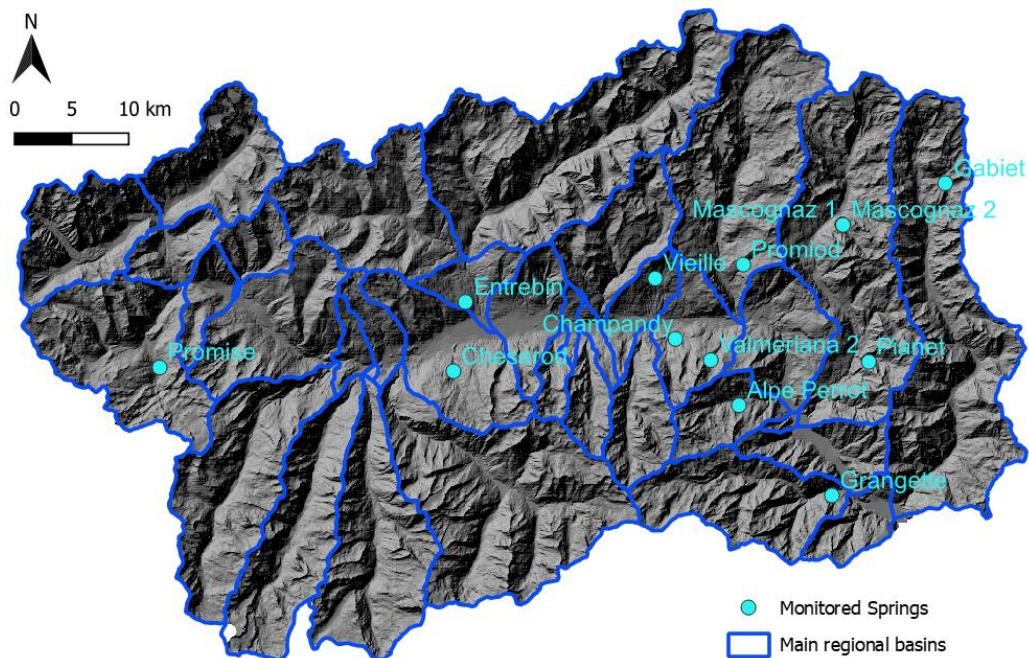


Figure 6. Locations of monitored springs in Aosta Valley.

These monitored springs are positioned along different valleys that are rejoining the main one where Dora Baltea river flows. Springs water is conveyed and transferred to aqueduct system for drinkable water distribution. Therefore, the selected monitored spring have an important role for mountain communities and it is worth to monitor them.

Geologically, the territory of the Aosta Valley is part of the Alpine chain sector called the Western Alps. The Valley cuts through the major structural systems into which the inner side of the European vergence chain is divided: the Austroalpine, Penninic and associated Ophiolitic Units.

In the northwestern marginal sector are present the units of the Ultraelvetic and Helvetic System. The tectono-metamorphic units of Alpine origin form a complex structure of overlapping strata in which features of post-collisional tectonic activity and the activation of neotectonic dislocation systems (e.g., the Aosta-Ranzola Fault) can be recognized. In particular, the Austroalpine System is composed of a system of strata of Paleo-African origin, which show different metamorphic grades, from green schist to granulitic facies; the Sesia-Lanzo Zone (orthogneiss and eclogitic mica schists) and the Dent Blanche stratum (gabbros, metagranites, mica schists, and Mesozoic cover) are recognized in the Aosta Valley.



Figure 7. Regional Geology of Aosta Valley (Bonetto & Gianotti, 1998).

The Piedmont Zone consists of a sector with predominantly oceanic metasedimentary cover (calcescists, marbles and quartzites) and a sector with predominantly metabasites derived from oceanic substrate (serpentinites, amphibolites, metagabbros and prasinites). The Pennitic System is subdivided into the Upper Pennitic Zone (schists, metaconglomerates, metagranites and paragneisses), the Middle Pennitic Zone (gneisses, metagranites, quartzites, calcschists, chalks and dolomites) and the Outer Pennitic Zone (serpentinites, prasinites, mycascites, quartzites, calcschists, flysch). The Ultraelvetic System consists of the Ultraelvetic Escarpment Pits, the Mont Chetif Pits (limestones, porphyroids, calcschists, carnioles) and the Mont Frety Pits. The Helvetian System is represented by the Mont Blanc Massif (parascists, migmatites and

granites) and, subordinately by Mesozoic sedimentary covers (Giardino and Ratto, 2005).

The hydrogeological system of the Aosta Valley has as its major reservoir in the Aosta plain where the region's main water supply resides.

In addition to this, there are more than 500 springs in the Aosta Valley, indicating the presence of water resources distributed throughout the valleys surrounding the main one. These water resources occur within aquifers that may have porous or fractured characteristics. In particular, porous aquifers are generated by the presence of Quaternary deposits within the valleys, while fractured ones, develop within rock masses and tectonic structures.

Among these 12 springs monitored by Politecnico di Torino, in this work, 5 of them have been selected for different analysis according to the quality of their information time series (Alpe Perrot, Cheserod, Mascognaz, Promiod, Promise) **Fig. 8**. Moreover 5 weather station have been chosen to represent spring climatic area based to the proximity of the spring, quality of data and all necessary parameters to analyze: Precipitation, Temperature, Snow Depth.

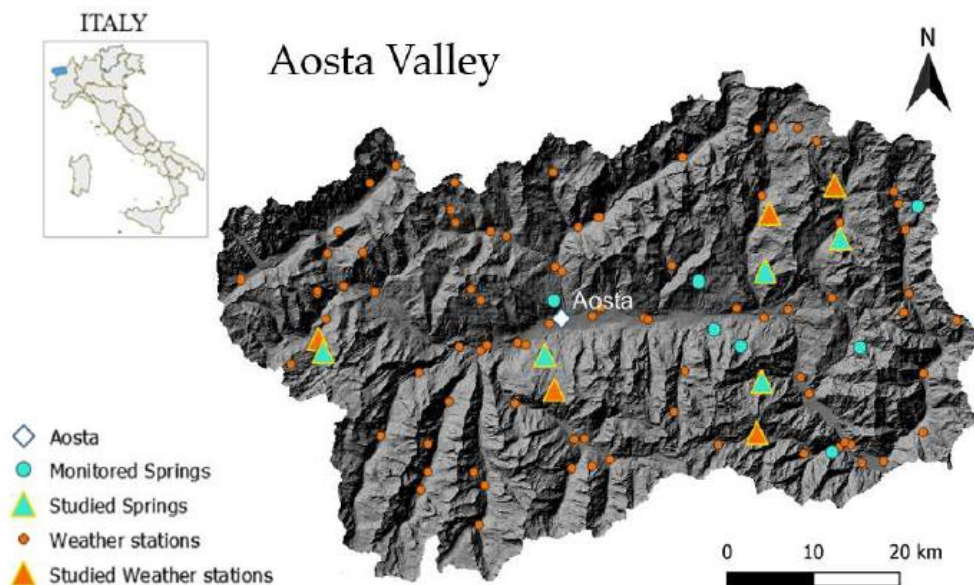


Figure 8. Analyzed springs with related weather stations in Aosta Valley.

2.2 Case studies

2.2.1 Alpe Perrot

The spring of Alpe Perrot is located in the municipality of Champdepraz (717 inhabitants, ISTAT, 2023) whose name comes from the namesake valley. The Champdepraz valley as shown in **Fig. 9** wedges between the Champorcher valley and le val Clavalitè. The main mountains surrounding the valley are Mont Glacier (3185 m a.s.l.), Mont Avic (3003 m a.s.l.) and Mont Ruvic (3006 m a.s.l.).

The spring is located at an elevation of 1280 m a.s.l. within the serpentinite massif of Mont Avic, one of the largest in the Western Alps.

Serpentinized peridotites with intercalations of magnetite and chlorite schists make up the Mont Avic massif, in addition, there are strands and lenses of rodingite and some metagabbro bodies embedded in the massif.

In the study area, the outcrop lithology is dominated by the Zermatt-Saas Unit, which is an ophiolite of Jurassic-Cretaceous age. Ophiolites, are portions of oceanic rock that are uplifted or overlain by continental crust until they outcrop (Dal Piaz, G., 1992).

Alpe Perrot spring flows through the Quaternary cover that characterizes the slope, the latter of which includes Pleistocene glacial deposits (undifferentiated till, ablation or bedrock deposits, landslide deposits with glacial transport and scattered moraine skeletons) and glaciogenic deposits (glacial contact, glacio-lacustrine and fluvio-glacial) (**Fig. 10**).

In **Fig. 9** is also shown a 3D satellite figure that show the morphology of the hydrographic basin where the spring is located. It is on the hydrographic right of Champdepraz valley.

Alpe Perrot is one of the springs type defined by permeability boundary when there is a plane of stratification, well identified, between two lithologically different soils.

Past geological surveys carried out by the Applied Geology team of the Polytechnic University of Turin allowed the identification of two spring feeding area, which are characterized by two Quaternary deposits overlying the bedrock subsystem that, it is hypothesized, constitute the underground spring feeding basin.

The two type of Quaternary deposits, that were mentioned before, are: a glacial deposit with eluvial-colluvial cover and a gravitational accumulation with metric-sized large blocks.

As reported in the map (**Fig. 9**), the closest useful weather station (Champorcher- Petit Mont Blanc, 1640 m a.s.l.) including rainfall, snow, and temperature information, is placed not in the same valley at airline distance of about 6 km from the spring.

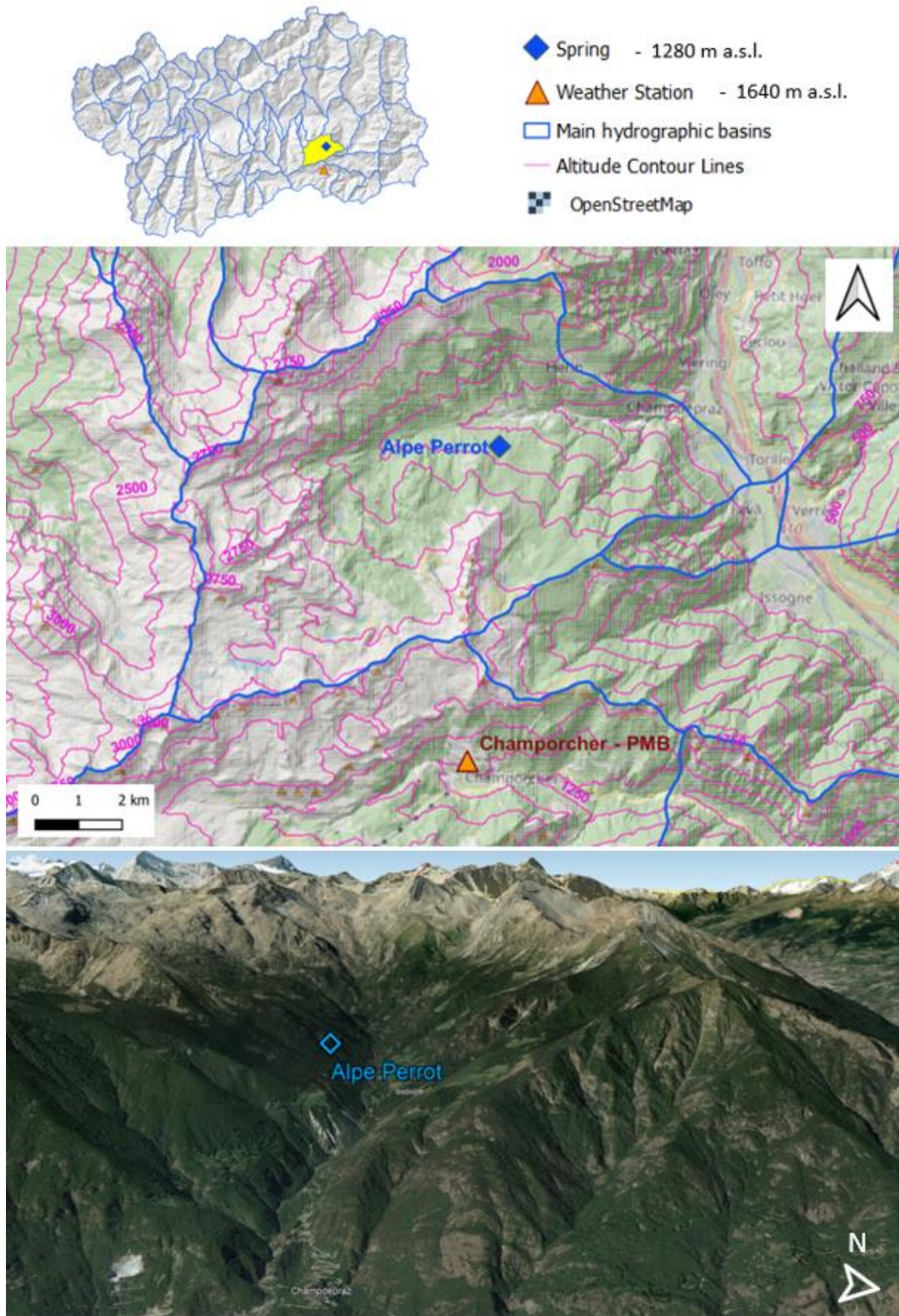






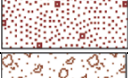






Figure 9. Territorial map with Alpe Perrot spring and Champorcher- PMB weather station; below it is represented a 3D Google Earth Pro image with the spring surrounding area.



Figure 10. Alpe Perrot spring depicted in Geotectonic map of the Aosta Valley, scale 1:100000, (De Giusti, *et al.*, 2003).

45		Calcescists s.l.: Mesozoic heterogeneous carbonate metasediments derived from protoliths of Upper Jurassic and/or Cretaceous age; local manganese quartzites
46		Metabasalts in prasinitic facies, amphibolites, and minor eclogites: metabasalts derived from normal MORB and transitional types with oceanic hydrothermal metamorphism of varying magnitude; prasinites, eclogites, glaucophanic eclogites, and garnetiferous glaucophanites
48		Antigoritic magnetite serpentinites and titanclinohumite-olivina-diopside aggregates
		Glaciers
		Alluvial deposits
		Undifferentiated moraine deposits
		Slope debris
		Main landslide bodies
		Deep gravitational slope deformations
		Main overthrusts
		Main faults

2.2.2 Cheserod

The spring of Cheserod is located at the eponymous village of Cheserod at 1095 m a.s.l., within the municipality of Gressan (3390 inhabitants, ISTAT, 2023).

The subject site is included within the Piedmont Zone sequences. This is a multi-stratum system that continuously separates the Austroalpine units (Sesia-Lanzo Zone and Dent Blanche System) from the underlying and more external Pennine strata of Monte Rosa, Gran Paradiso and Gran San Bernardo. Ophiolitic units with eclogitic metamorphism correlated with the Zermatt-Saas are placed to the south of the Aosta - Col-de-Joux - Ranzola fault, on the orographic right slope of the Aosta Valley, where the spring is located.

There are also several outcrops of soluble Triassic rocks in the area surrounding the spring, such as carbonate breccias, gypsum, and anhydrite. The carbonate clasts are white with a medium-fine grain size. They are immersed in a fine light yellow matrix that becomes yellow ochre on contact with the clasts. The deposit cover is composed of undifferentiated glacial deposits, worked by the eluvial and colluvial action of external agents (Dal Piaz, G., 1992).

The spring, given the lack of knowledge about the intake work, it is not possible to determine what type it is.

As can be seen in the **Fig. 11**, the spring is right next to the valley incision of the slope where the stream flows.

So it can be assumed that given the high flow rate of the spring and the presence of the river close to it, much of the water comes from the drainage of the stream and to a small extent from secondary recharge feeds. Nevertheless, the recharge area of the spring has been found to be larger given that the amount of water is not affected much by seasonal variations in river discharge.

The weather station (Gressan – Pila Leissè, 2280 m a.s.l.) used to study the hydrological inputs feeding the spring is located upstream this one at Pila locality, within the same catchment area of the spring.

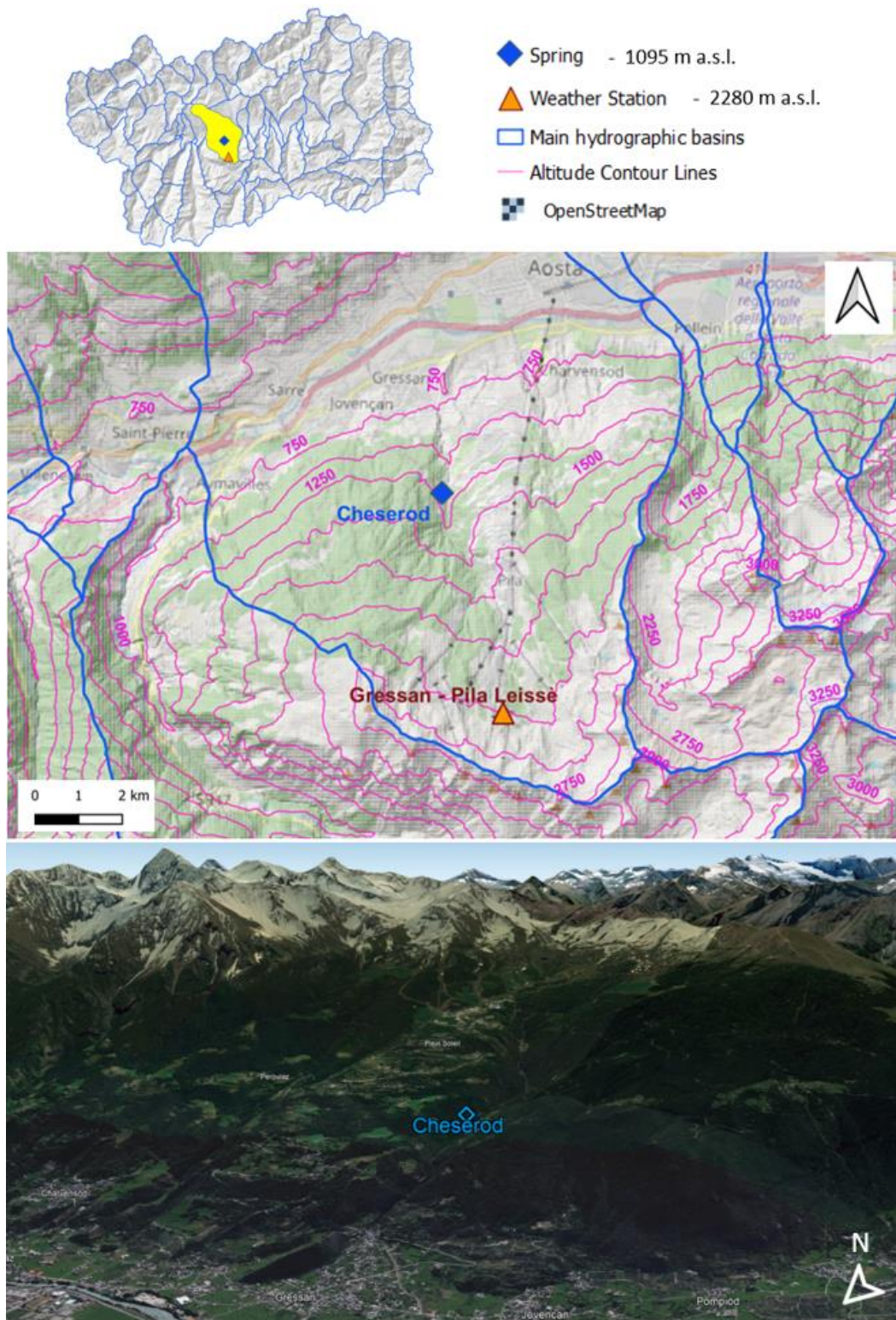


Figure 11. Territorial map with Cheserod spring and Gressan – Pila Leisse weather station; below it is represented a 3D Google Earth Pro image with the spring surrounding area.

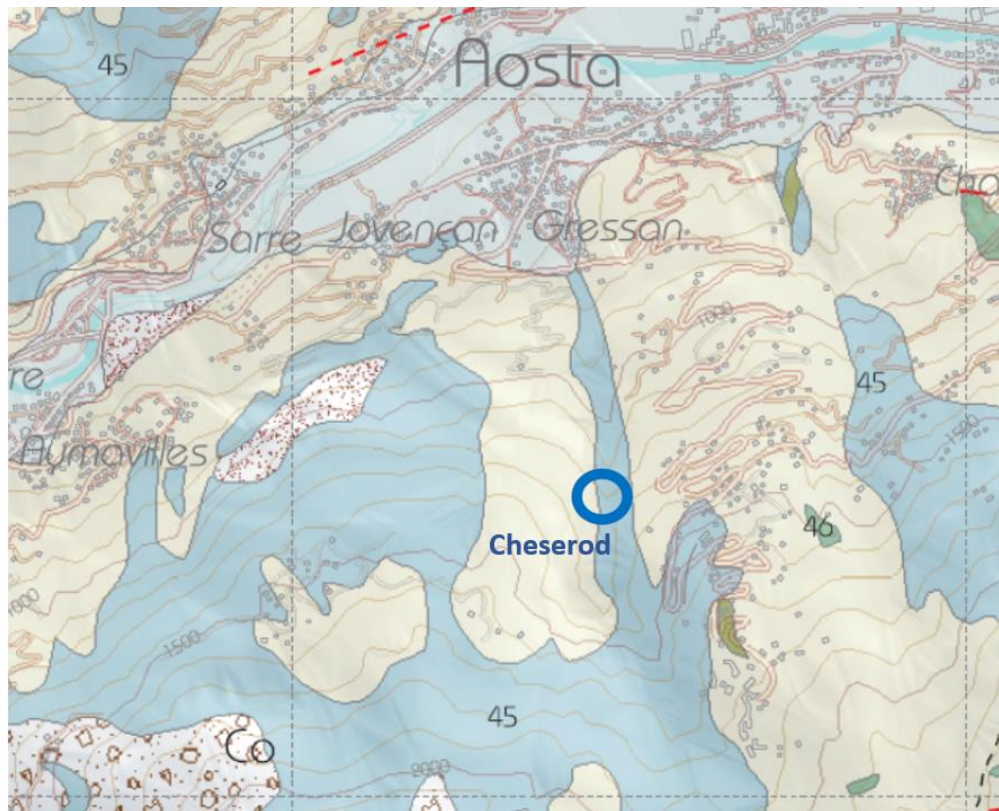
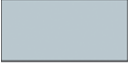


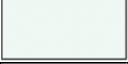

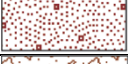






Figure 12. Chäserod spring depicted in Geotectonic map of the Aosta Valley, scale 1:100000, (De Giusti, et al., 2003)

45		Calcschists s.l.: Mesozoic heterogeneous carbonate metasediments derived from protoliths of Upper Jurassic and/or Cretaceous age; local manganese quartzites
46		Metabasalts in prasinitic facies, amphibolites, and minor eclogites: metabasalts derived from normal MORB and transitional types with oceanic hydrothermal metamorphism of varying magnitude; prasinites, eclogites, glaucophanic eclogites, and garnetiferous glaucophanites
		Glaciers
		Alluvial deposits
		Undifferentiated moraine deposits
		Slope debris
		Main landslide bodies
		Deep gravitational slope deformations
		Main overthrusts
		Main faults

2.2.3 Mascognaz

The Mascognaz spring is located within the valley of the same name, in the municipality of Ayas (1359 inhabitants, ISTAT, 2023), fraction of Champoluc. The basin where the spring is located is quite small, about 10 km² in size, oriented in a south-east direction.

The case study site is included within the Piedmont Zone sequences. This is a multi-stratum system that continuously separates the Austroalpine units (Sesia-Lanzo Zone and Dent Blanche System) from the underlying and more external Pennine geological formations of Monte Rosa, Gran Paradiso, and Gran San Bernardo. On the hydrographic left with respect to the Dora Baltea and north of the Aosta-Col-de-Joux-Ranzola fault, the Combin Auct. Zone and the lower ophiolitic unit of Zermatt-Saas are recognized (Dal Piaz, G., 1992). The spring of Mascognaz is located within the Combin Zone, which is represented in the spring surroundings by metabasalts and subordinate Mesozoic metasediments. The geology of the valley is particularly interesting because it is affected by the tectonic contact between the Combin Zone and the Sesia Lanzo Zone afferent to the Austroalpine system.

As far as surface formations are concerned, glacial deposits can essentially be recognized. The valley floor of the Mascognaz basin is characterized by the presence of bodies consisting of detritus that connect the steep slopes with the flat valley floor. As seen in the 3D satellite image (**Fig. 13**), the spring is located near the valley incision, on the hydrographic left, near the basin closure section.

The water intake structure is directly connected to the aqueduct network of the municipality of Ayas. The intake structure, by means of sub-horizontal drains, intercepts the piezometric level of the underlying aquifer, the body of which consists of Quaternary deposits that are mostly gravitational (**Fig. 14**).

The weather station used to study the atmospheric parameters that condition the spring is that of Ayas - Alpe Aventine (2080 m a.s.l.), which is not located within the Mascognaz basin, but within one of the main Aosta Valley catchment area called T. Evançon High Basin where the related spring is located too.

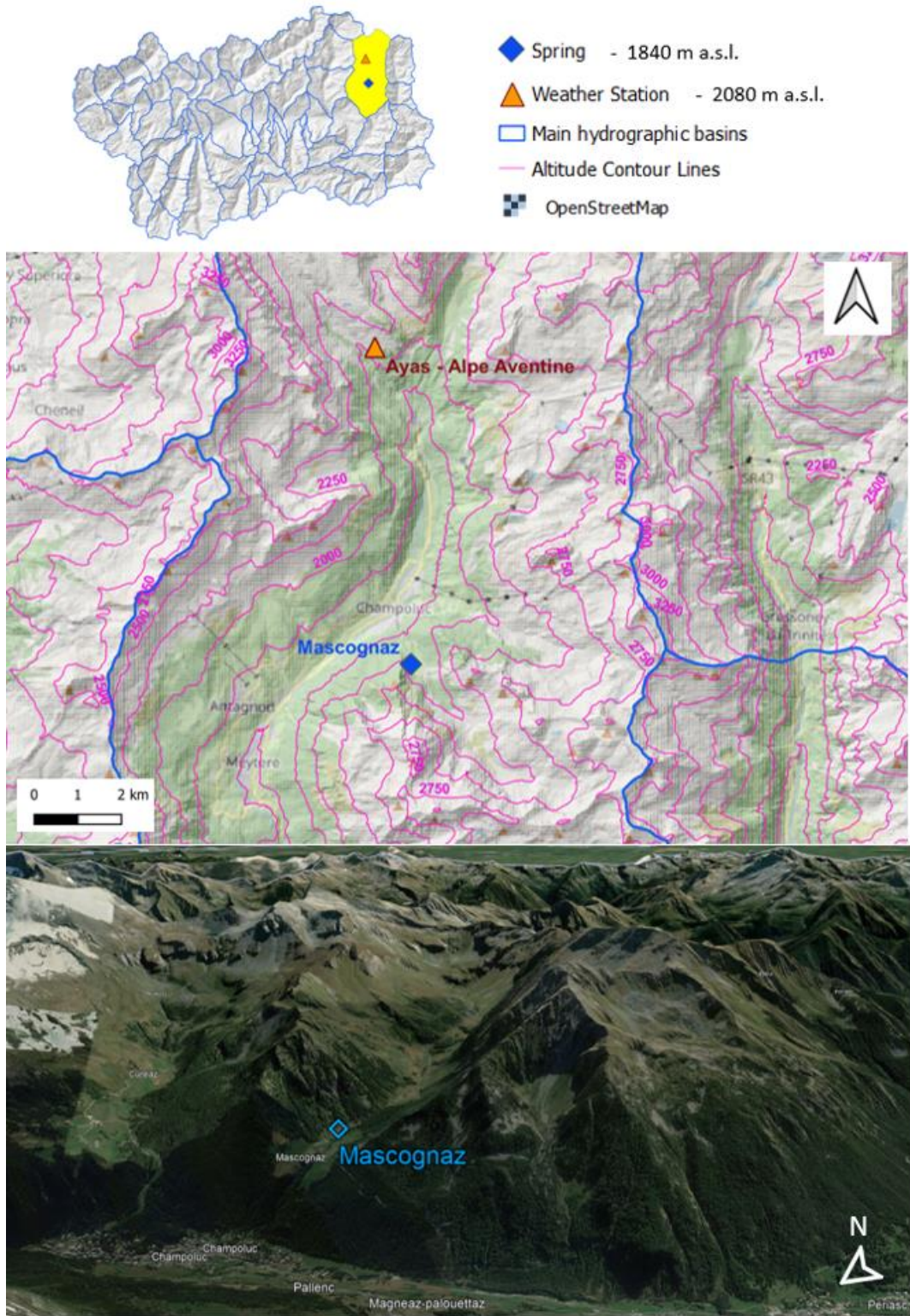




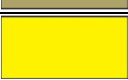





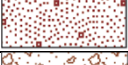






Figure 13. Territorial map with Mascognaz spring and Ayas – Alpe Aventine weather station; below it is represented a 3D Google Earth Pro image with the spring surrounding area.



Figure 14. Mascognaz spring depicted in Geotectonic map of the Aosta Valley, scale 1:100000, (De Giusti, et al., 2003).

45		Calcschists s.l.: Mesozoic heterogeneous carbonate metasediments derived from protoliths of Upper Jurassic and/or Cretaceous age; local manganese quartzites
46		Metabasalts in prasinitic facies, amphibolites, and minor eclogites: metabasalts derived from normal MORB and transitional types with oceanic hydrothermal metamorphism of varying magnitude; prasinites, eclogites, glaucophanic eclogites, and garnetiferous glaucophanites
47		Coarse-grained and solid-textured metagabbri, flaser or milonitic
48		Antigoritic magnetite serpentinites and titanclinohumite-olivine-diopside aggregates
49		Undifferentiated Permo-Mesozoic successions : silvery quartzose-albitic schists, with intercalations of quartzites; rare centimeter-long quartz pebble metaconglomerates (Verrucan); white lathroid quartzites, with microclasts of potassic feldspar in accessory amounts (Eotriassic); calcareous and dolomitic marbles, dark gray marbles, carnioles, microbreccias (Middle-Upper Triassic); bluish-gray pelagic marbles with intercalations of sedimentary breccias to dolomitic elements (Jurassic); brown-patinaI carbonate calcareous, nonlitic.

58		Minute Gneiss complex: granitic orthogneisses, minor parascites, and milonites in green alpine schist facies
67		Ultrapotassium lamprophyric strands and minor andesites of Oligocene age (32-30 Ma)
		Glaciers
		Alluvial deposits
		Undifferentiated moraine deposits
		Slope debris
		Main landslide bodies
		Deep gravitational slope deformations
		Main overthrusts
		Main faults

2.2.4 Promiod

The Promiod spring (1650 m a.s.l.) is located within the Lower T. Marmore Basin and falls within the municipality of Châtillon (4402 inhabitants, ISTAT, 2023). This spring is still used for water supply purposes in the municipality. The spring is located on the hydrographic left of the Valtournenche and close to the incision of a sub-basin facing South-West (**Fig. 15**).

At the geological level, the site in question is included within the Piedmont Zone sequences. This is a multi-stratum system that continuously separates the Austroalpine units (Sesia-Lanzo Zone and Dent Blanche System) from the underlying and more external Pennine unit of Monte Rosa, Gran Paradiso, and Gran San Bernardo. In the Aosta Valley, on the orographic left slope and north of the Aosta - Col-de-Joux - Ranzola fault, the Combin Auct. Zone and the lower ophiolitic unit of Zermatt Saas are recognized (Dal Piaz, G., 1992). The Promiod spring is located within the Combin Zone, represented here by metabasalts and subordinate Mesozoic metasediments. The Quaternary deposits are related to glacial action and subsequent colluvial eluvial reworking. Debris accumulations are also present in the area (**Fig. 16**).

Promiod, like Alpe Perrot, falls into the class of springs by permeability limit defined when there is a plane of stratification, well identified, between two lithologically different soils.

The geological survey highlighted the different nature of the rocks belonging to the Combin Unit. It is assessed that the defined permeability boundary is given by the alternation of more fractured and less fractured calcareous levels.

Thus, the more fractured portion of the rock turns out to be like a porous medium where water can circulate and accumulate creating the aquifer body.

In fact, the Promiod spring is generated at the contact of the most fractured zone with the one below, which acts as an impermeable layer. Two drains are positioned to intercept the piezometric level and convey the water inside the intake structure to be poured into the aqueduct pipeline.

The reference weather station for Promiod spring is Chamois - Lac de Lou station (2020 m a.s.l.) near the municipality of Chamois, further north continuing along the Valtournenche valley.

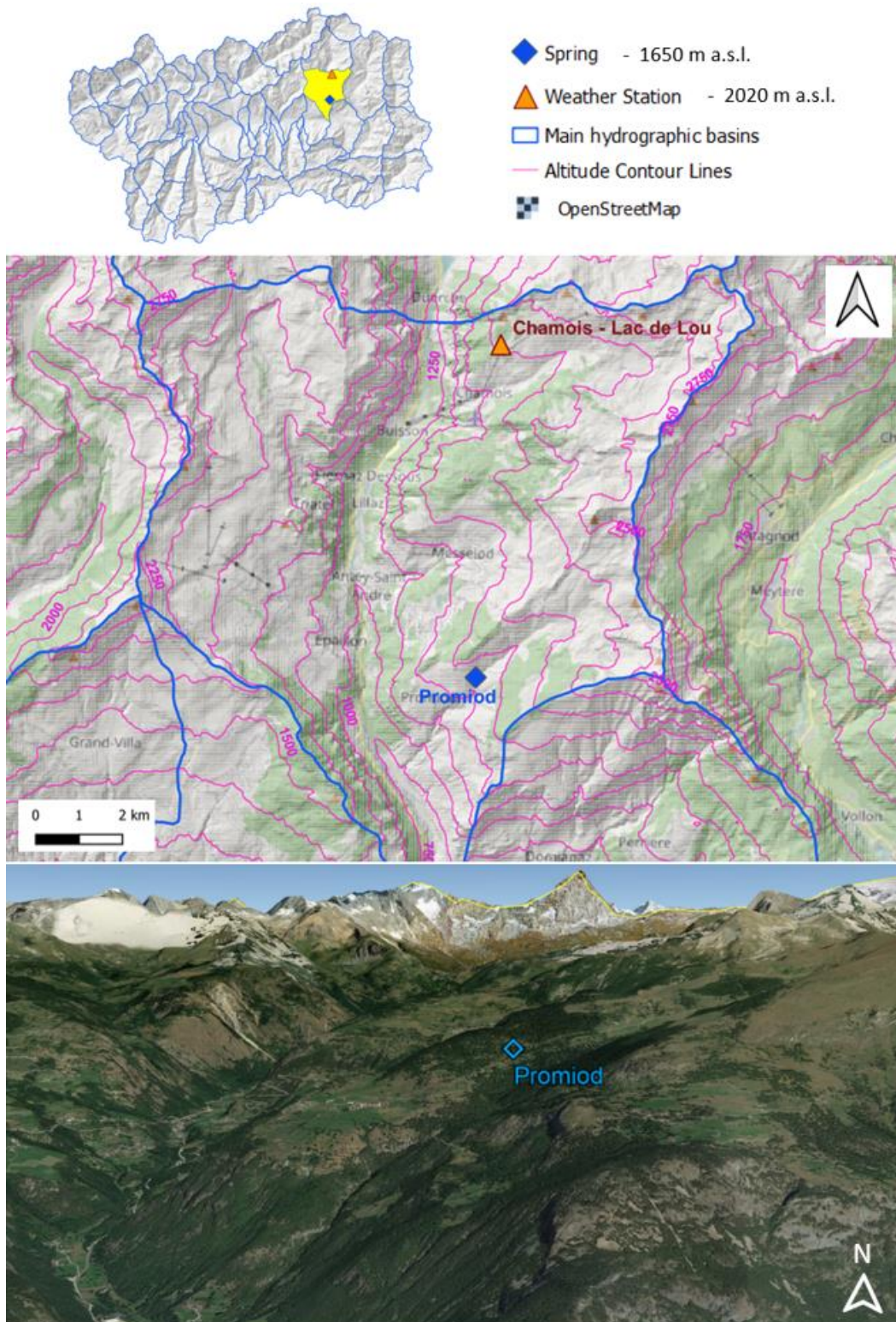
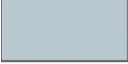





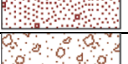






Figure 15. Territorial map with Promiod spring and Chamois – Lac de Lou weather station; below it is represented a 3D Google Earth Pro image with the spring surrounding area.



Figure 16. Promiod spring depicted in Geotectonic map of the Aosta Valley, scale 1:100000, (De Giusti, et al., 2003).

45		Calcschists s.l.: Mesozoic heterogeneous carbonate metasediments derived from protoliths of Upper Jurassic and/or Cretaceous age; local manganese quartzites
46		Metabasalts in prasinitic facies, amphibolites, and minor eclogites: metabasalts derived from normal MORB and transitional types with oceanic hydrothermal metamorphism of varying magnitude; prasinites, eclogites, glaucophanic eclogites, and garnetiferous glaucophanites
48		Antigoritic magnetite serpentinites and titanclinohumite-olivina-diopside aggregates
		Glaciers
		Alluvial deposits
		Undifferentiated moraine deposits
		Slope debris
		Main landslide bodies
		Deep gravitational slope deformations
		Main overthrusts
		Main faults

2.2.5 Promise

The Promise spring (1580 m a.s.l.) is located within the municipality of La Thuile (816 inhabitants, ISTAT, 2023), within the valley named after the latter one. The spring is located just below the Rutor Glacier (**Fig. 17**), one of the largest in the Aosta Valley, on the hydrographic right with respect to the Rutor Torrent.

The Aosta Valley basin, where Promise spring is located, is called the T. du Rutor Basin after the glacier, it is joined to the main Aosta valley where the Dora Baltea river rises. The hydrographic basin has as its highest point the Testa del Rutor (3486 m a.s.l.) which is the peak just above the glacier.

Specifically, the structure where the spring is located was part of a former Anthracite mine of the so called "Colle Croce" mining complex . Currently this structure has the effect of a drainage tunnel that brings water to the Promise spring. The intake work consists of a tunnel that brings water to a calm reservoir. That reservoir ends in a rectangular weir, which made the spring suitable for instrumentation. Following that reservoir there is the loading reservoir. The intake structure is in a good state of preservation. To date the spring is closed given the high levels of arsenic (As) present in the water.

The spring named Promise is located at the outcrop area of the Houllère Zone sequence, a Unit of the Outer Brianzese Dominion , belonging to the Middle Penninic System. The Houllère Zone, also called the Axial Permo-Carboniferous Zone, owes its name to the fact that it consists of clay-arenaceous-conglomeratic metasediments with lenses of anthracite of Upper Carboniferous age. Around the spring the outcropping rocks are Conglomerates, metapsammites and metapelites, shales and micaceous sandstones with anthracite beds (**Fig. 18**).

Difficult to understand the water origin of the spring, in this case the spring is not belonging to the permeability boundary class. But rather considering the geological and tectonic setting of the area, it seems that the water circulates in the fractured rock mass generated by the sub-vertical fault flowing under the glacier with North-North-East direction, and the rock layers of the anti-dip slope with the South-East dip direction and 35°-39° inclination.

Therefore, the spring could receive some nearby water by rapid infiltration and water from more distant areas such as those of the glacier. In fact, the fault that reaches near the spring cuts upstream the Rutor Stream acting hypothetically as a water collector between the spring and the melt processes of the Rutor Glacier.

The representative weather station for the spring is that of La Thuile - Villaret (1488 m a.s.l.), located near the municipality of La Thuile.

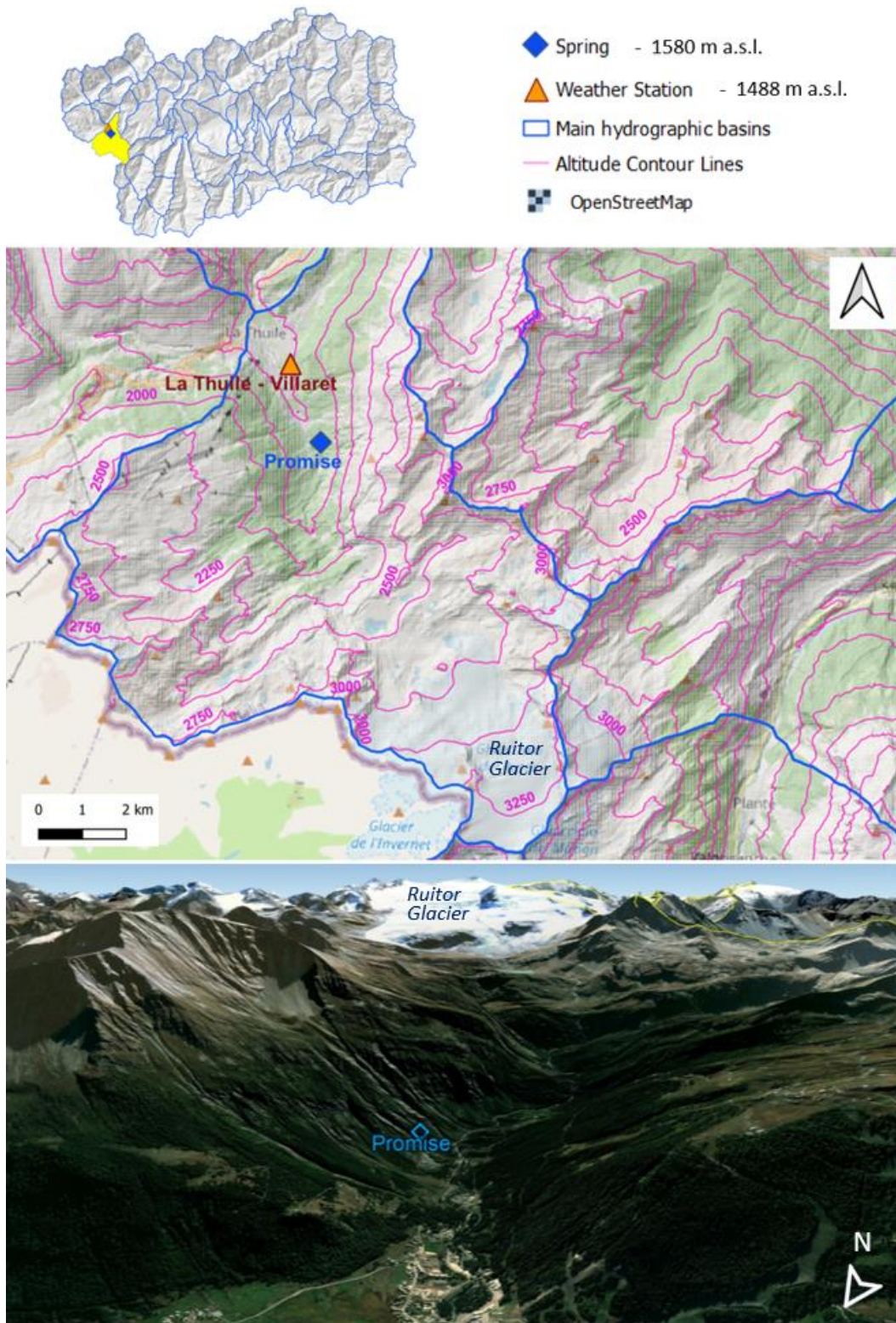


Figure 17. Territorial map with Promise spring and La Thuile - Villaret weather station; below it is represented a 3D Google Earth Pro image with the spring surrounding area.

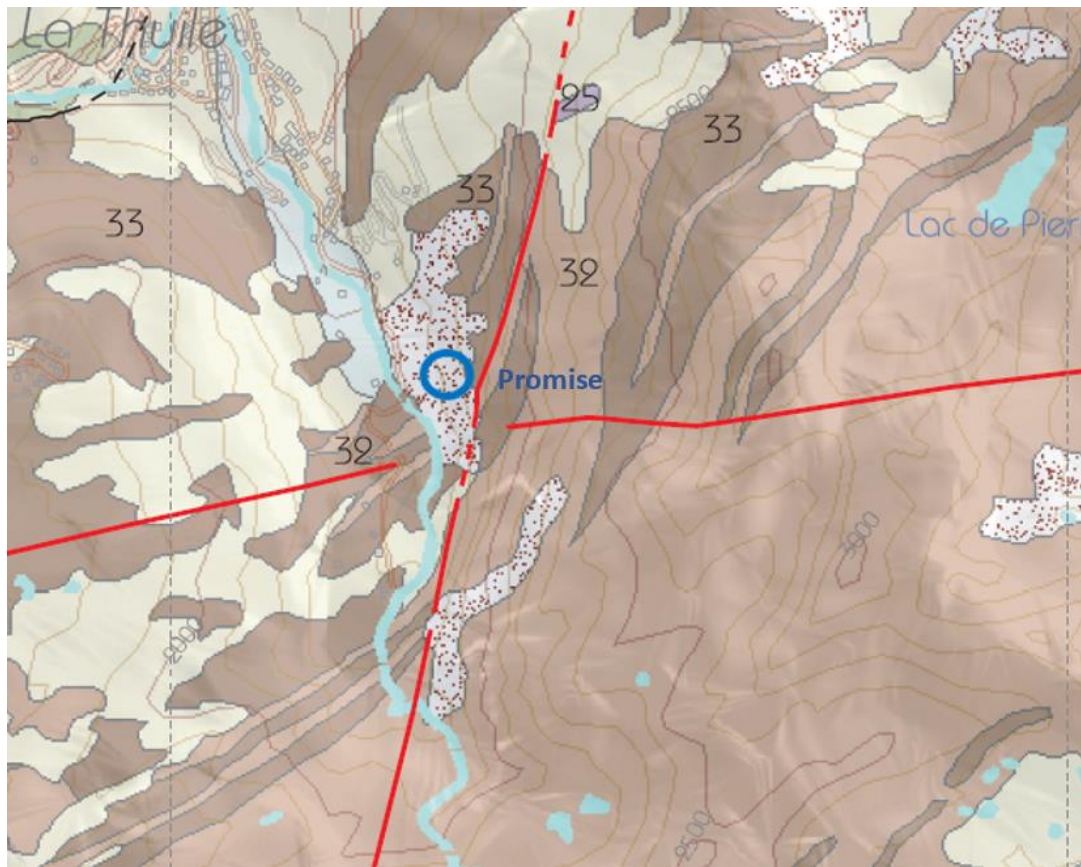






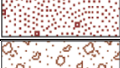

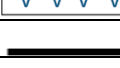




Figure 18. Promise spring depicted in Geotectonic map of the Aosta Valley, scale 1:100000, (De Giusti, et al., 2003).

25		Calcareous and siliceous limestones: dark gray crystalline limestones with flint lists
32		Conglomerates, metapsammites and metapelites (Stephanian-Eopermian)
33		Anthracite-bedded micaceous shales and sandstones: powerful metaderivate succession, with lenses of fossil coal (Westphalian-Stephanian)
		Glaciers
		Alluvial deposits
		Undifferentiated moraine deposits
		Slope debris
		Main landslide bodies
		Deep gravitational slope deformations
		Main overthrusts
		Main faults

2.3 Meteorological analysis

Weather conditions for each spring case study are monitored using weather stations whose data are maintained by the Aosta Valley Hydrographic Service (Centro Funzionale Regione Autonoma della Valle D'Aosta). The historical data series are old enough to cover the same time interval as the spring data series.

The data are downloadable with hourly or daily time steps; daily data were taken as the spring data. Spring time series, in fact, has been converted from hourly to daily in order to simplify the reading of the parameter (Machiwal and Jha, 2006; T.O.Olatayo and Taiwo, 2014).

Time series, in general are defined as a set of observations ordered with respect to time and express the dynamics of a certain phenomenon over time. Time series are studied both to interpret a phenomenon, identifying components of trend, cyclicity, seasonality and/or accidentality, and to predict its future trend.

The parameters downloaded to evaluate the evolution of hydrological inputs of atmospheric conditions are: Air Temperature, Precipitation, and Snow Depth on the ground.



Figure 19. a: Bascule Rain Gauge conveying mouth; b: Bascule Rain Gauge heating system; c: Thermo-igrometer measuring Temperature and Relative Humidity; d: Ultrasonic sensor for Snow depth recording.

Precipitations are often monitored by means of a heated bascule rain gauge that allows both liquid rainfall in mm and solid rainfall in terms of Snow Water Equivalent (mm) by melting the snow falling inside it. **Fig. 19a** shows the mouth of the rain gauge where precipitation is collected, while **Fig. 19b** represents the heating system inside the pluviograph metallic coverage. Temperature is often monitored by a thermo-hygrometer (**Fig. 19c**), which also has a relative humidity sensor inside it. The depth of the snow on the ground is monitored by an ultrasonic sensor (**Fig. 19d**), which, thanks to the principle of the time interval in which the sound wave is reflected from snow surface, is able to derive the height of the snowpack. This sensor should be calibrated according to the atmospheric temperature, since the wave speed also depends on the variation of this parameter.

Occasionally the time series of these parameters have gaps that are caused by sensor malfunctions or electrical voltage drops. Therefore, adjustment of the parameter time series is done by making a linear interpolation between the gaps using present data or by integrating the parameter information using the nearest weather station sensor (Ruane, Goldberg and Chryssanthacopoulos, 2015).

The evolution of the variables are evaluated by calculating trends of these parameters over time. Trends are carried out finding out the slope of the straight line having performed the linear regression of the time series. It is important to understand whether there is a decrease or increase in a parameter such as temperature, snow and precipitation in the studied time interval in order to understand the evolution of the hydrogeological processes that outcome in the spring output. The regression method exploited in this thesis is the Ordinary Least Squares of y regression ($OLS_{y,x}$), which minimizes the summatory of the quadratic deviation $\sum(\delta y)^2$ on the y-axis to construct the regression line as shown in **Fig. 20** (Ludbrook, 2010).

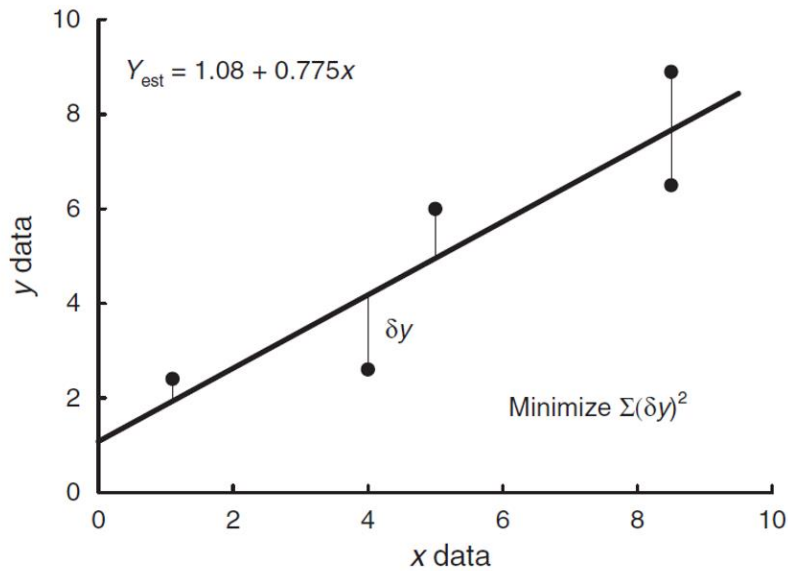


Figure 20. Ordinary Least Squares of y regression (Ludbrook, 2010).

Once the regression line is obtained, its coefficients can be derived, including the most important one in the study of a time series, namely the angular coefficient, which is the slope of the line and determines whether a parameter data series is increasing or decreasing.

Other features of rainfall are performed such as intensity (amount of rainfall over time) and frequency (number of events in a time interval) to characterize the pluviometric regime evolution and to understand a series of consequences this variations might induce (Mo *et al.*, 2019).

These other two elaborations from the raw data of precipitation per day are calculated by computing in the first case the number of rainy days per month (frequency) and in the second case by dividing the monthly cumulative rainfall by the number of rainy days in the same month. An example of the processing of these other two parameters is shown in **Fig. 21**, which represents graphs from a paper recently published by the authors (Gizzi *et al.*, 2022), who sought to understand the evolution of Aosta Valley water resources from the evolution of climatic and rainfall conditions.

Because, in addition to the amount of rainfall, the type of rainfall dictated by the intensity of the event can also play a key role in aquifer recharge. In fact, it is studied that very heavy rainfall is often ineffective in recharging groundwater given the rapid saturation of the hydrogeological circuit (Dourte *et al.*, 2013).

This aspect makes climate change very influential for aquifer recharge as it has been lately experienced less frequent rain events, but with higher intensity. Therefore, in

addition to quantity, there is also the issue of rainfall quality, which leads to an increase in the percentage of water runoff respect to the infiltrated amounts.

Then of course it depends on the type of aquifer and its drainage system. If the aquifer has a very open fracture system it will be more difficult to saturate rapidly. Whereas if a system has low porosity, it will prefer prolonged but low intensity rainfall so that less water is lost by runoff after saturation.

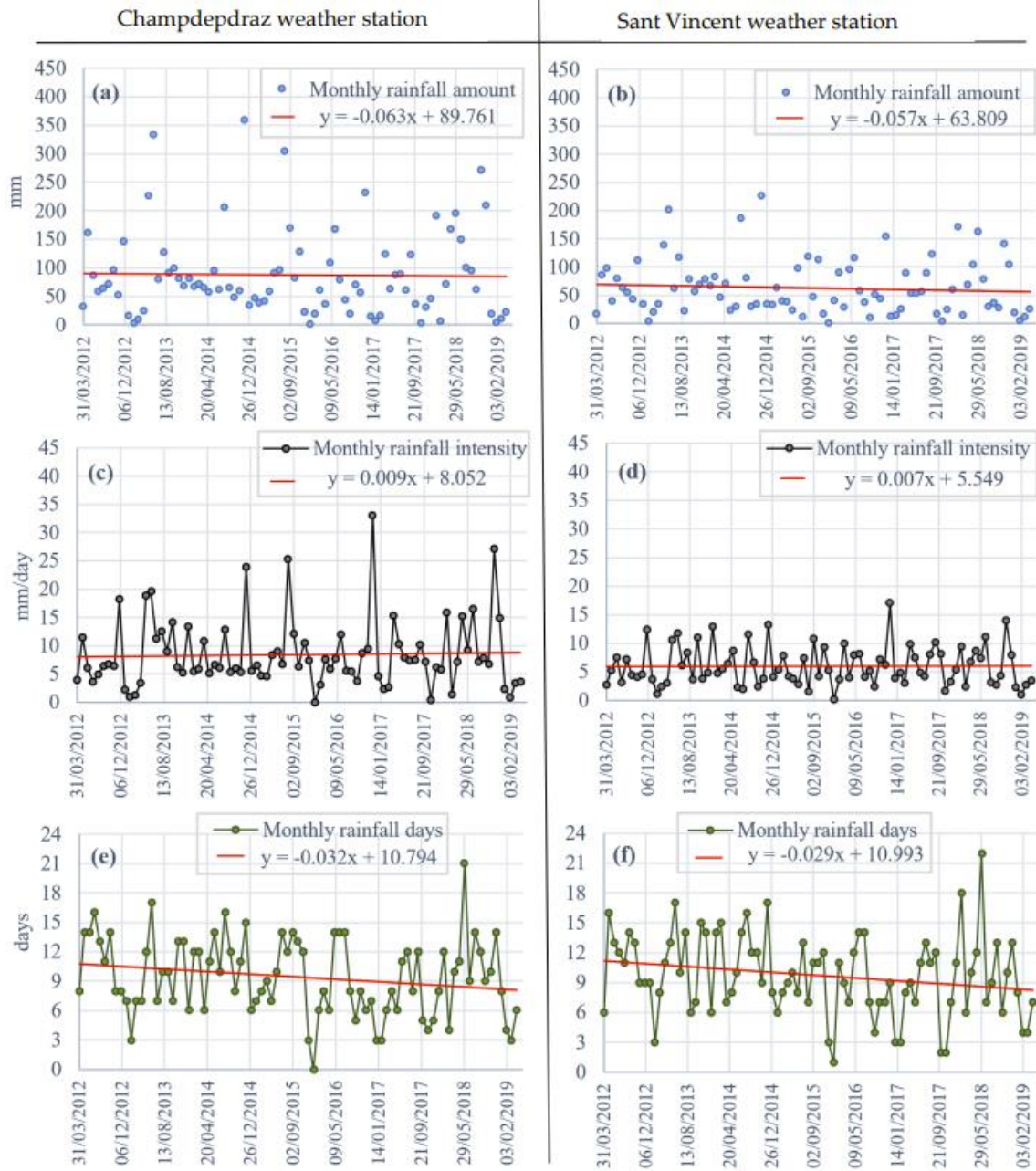


Figure 21. Rainfall time series characterization for two different weather station in Aosta Valley (Gizzi et al., 2022).

2.4 Spring analysis

The springs described in the previous chapter have the following parameters hourly monitored: Flow Rate (Q), Electrical Conductivity (EC) and Water Temperature (T), these data gathered so far had fed the studied time series from 2011 to 2022.

The instrument that monitors these parameters all together is the multi-parameter probe from OTT CTD (OTT HydroMet GmbH) (**Fig. 22b**). A classic schematic of installation of these probes inside the water intake structure is shown in the **Fig. 22** The probe consists of two metal cylinders connected by a cable, inside one cylinder there are the 3 detectors of Flow Rate, Temperature and Electrical Conductivity, this cylinder is submerged in the intake tub of the spring usually anchored inside a plastic PVC pipe as shown in **Fig. 22d**. In the second cylinder, connected to the first one and anchored outside the intake tub, there is the data logger that reads the sensor records and saves them (**Fig. 22c**).

The multi-paramant probe, not being equipped with a SIM card, does not transmit the data in real time to the server, so it is necessary to periodically go to the spring intake structure and download the data.



Figure 22. Typical set-up of a monitored spring (Mondani, Gizzi and Taddia, 2022).

2.4.1 Hydrograph analysis

The Hydrograph is the discharge function in time that characterizes a particular outflow from a section, or from underground in case of springs.

Therefore, the hydrograph is the signal over time of the flow rate that allows to analyze different elements of the water resource contained within the aquifer. In fact, several indicators and parameters will be shown below that allow an accurate analysis of the spring behavior that reflects the behavior of the hydrogeologic system after being altered by the hydrologic inputs.

Let's start by introducing what are the Hydrogeological years (**Fig. 23**), they are the time frames of the hydrograph contained by the lowest value of the water discharge, which are considered the extremes that include the hydrogeological year period. Therefore, the hydrogeological years are different from calendar years, they might be longer or shorter according to the length of the recharging limb (upward segment) and the length of the recession limb (downward segment).

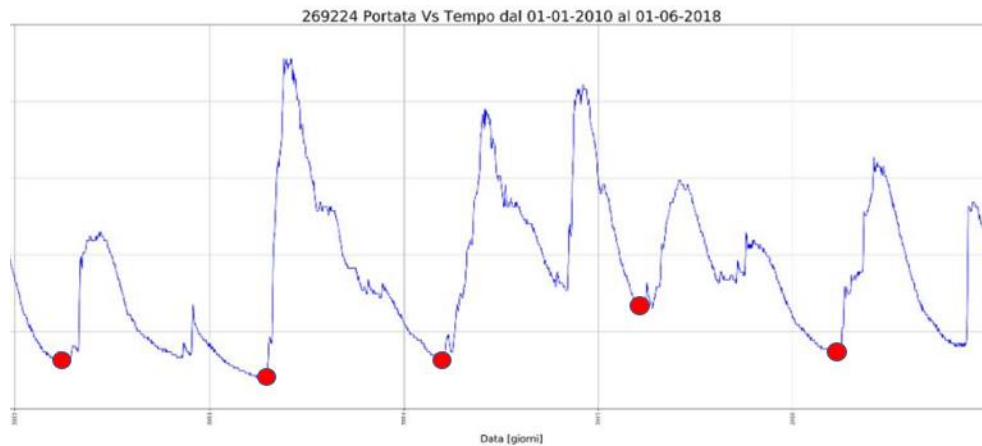


Figure 23. Four Hydrogeological years represented for the Alpe Perrot spring.

Clearly in each hydrogeological year there can be more than one recharge and recession phenomenon. Usually in a mountain hydrograph there is the highest peak in spring as a result of snowmelt and other less significant peaks caused by rainfall throughout the year. In any case regardless of the hydrogeological year it can be referred to what is the elementary hydrograph study as shown by (Kresic and Bonacci, 2010).

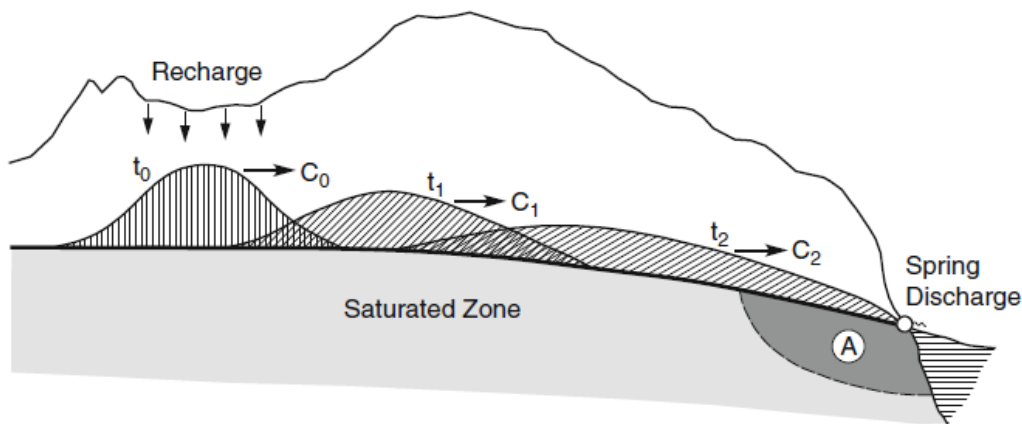


Figure 24. Formation and movement of a groundwater "wave" generated by a localized recharge event.

As these authors report, the zone that influences the spring regime is the so-called vadose zone, which can saturate and dry out depending on infiltrative conditions. It, in fact, lies above the perennially saturated zone. Precipitation events generate a chain reaction as shown in **Fig. 24**, which then lead to the variation of the spring regime with these perturbations in time driven by a “wave effect”.

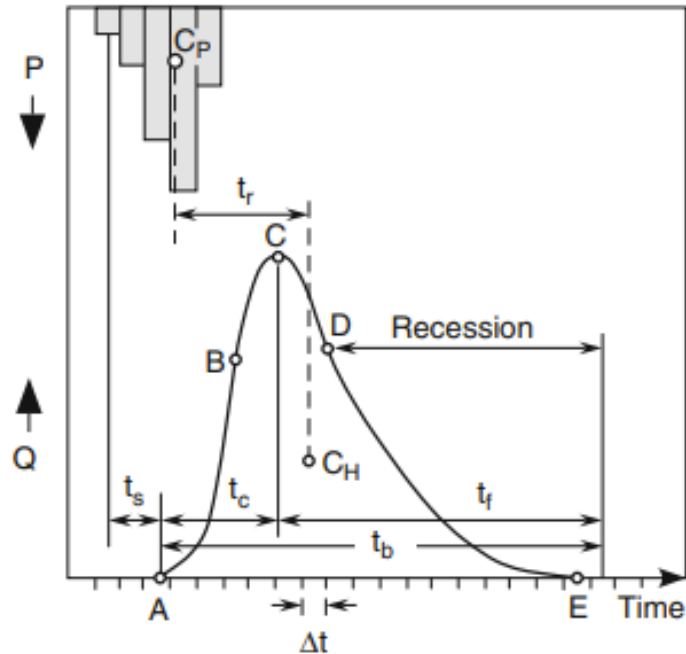


Figure 25. Components of a discharge hydrograph

The beginning of discharge after a rainfall or melting input is marked with point A, and the time between the beginning of rainfall and the beginning of discharge is called the starting time, t_s .

The time in which the hydrograph raises to its maximum (point C), is called the concentration time, t_c . The time from maximum discharge until the end of the hydrograph, when the discharge theoretically equals 0 (point E), is the falling time, t_f . (**Fig. 25**)

Together, the concentration time and the falling time are called the base time of the hydrograph, t_b . The time between the centroid of the precipitation episode (CP) and the centroid of the hydrograph (CH) is called the retardation time, t_r .

The time interval for recording the amount of precipitation and the flow rate at the spring is Δt . The shape of the hydrograph is defined by its base (AE), the rising limb (AB), the crest (BCD), and the falling limb (DE) (**Fig. 25**).

Analysis of the falling hydrograph limb shown in **Fig. 25**, which corresponds to a period with no significant precipitation, is called the recession analysis. Knowing that the spring discharge is without disturbances caused by a rapid inflow of new water into the aquifer, the recession analysis provides good insight into the aquifer structure.

By establishing an appropriate mathematical relationship between spring discharge and time, it is possible to predict the discharge rate after a given period without precipitation and to calculate the volume of discharged water.

$$Q_t = \frac{Q_0}{[1 + \alpha(t - t_0)]^2} \quad (1)$$

$$Q_t = Q_0 * e^{-\alpha(t-t_0)} \quad (2)$$

(1)(2) equations represents the Boussinesq and Maillet equations that interpolate the recession limb. Boussinesq shows that the recession limb can be represented with a parabolic relation and Maillet with an exponential relation implying a linear relation between the hydraulic head and flow rate. The dimensionless parameter α in both equations represents the coefficient of discharge (or recession coefficient), which depends on the aquifer's transmissivity and specific yield. As shown by authors (Lo Russo *et al.*, 2021) recession coefficient can be determined by knowing Q_0 and Q_t as follow:

$$\alpha = \frac{\sqrt{Q_0} - \sqrt{Q_t}}{\sqrt{Q_t} t} \quad (3)$$

$$\alpha = \frac{\log Q_0 - \log Q_t}{e^{(t-t_0)}} \quad (4)$$

(3) equation to determine the recession coefficient α with Boussinesq method and (4) with Maillet method. This coefficient, in both cases is used to find out an important parameter: W_0 , which is the groundwater stored above spring level at the end of recharging season and for both method can be found by the following equations:

$$W_0 = \frac{Q_0}{\alpha(1 + \alpha t)^2} * 86400 \quad (5)$$

$$W_0 = \frac{Q_0}{\alpha} * 86400 \quad (6)$$

Besides eq. (5) of Boussinesq and eq. (6) of Maillet, the other important volume that can be derived is W_d , which is the groundwater volume discharged from a time t_0

(beginning of recession) and at time t. W_d is calculated as follow by Bussinesq and Maillet approach respectively (7)(8):

$$W_d = \left[\frac{Q_0}{\alpha} - \frac{Q_0}{\alpha(1 + \alpha t)} \right] * 86400 \quad (7)$$

$$W_d = \frac{(Q_0 - Q_t)}{\alpha} * 86400 \quad (8)$$

So finally, knowing the volume at the beginning of recession and the volume flowed at time t, it can be known the volume remaining above the spring elevation at the end of recession ($W_t = W_0 - W_d$), if t is the time relative to the end of recession. In addition, a number of other parameters can be calculated from these mathematical relationships such as the: Renewal rate and Renewal time rate (Trin), which refer to the time it would take to replenish the water resource.

Summarizing, let's say that the recession coefficient (α) represents the slope of the curve, the larger the coefficient the greater the slope of the recession. In fact, this coefficient, the larger it is, the greater the discharge peak and discharge rate will be. It is not necessarily the case that if the recession coefficient is larger, more volumes of water will flow out from the beginning to the end of the period.

The parameter that illustrates the evolution of the water resource is the stored volume at the end of recession (W_t), calculated through the difference between the volume at the beginning of recession (W_0) and the volume discharged along the recession (W_d). W_t is indicative of aquifer wellbeing, showing the stored resources at the end of the hydrogeological year that contribute to the saving amount for the following year.

The recession interval shown in the table was previously illustrated when analyzing the hydrogeological years divided into the two phases of recharge and discharge.

The spring Renewal rate (Rr) is the ratio of the volumes flowed out during the recession (W_d) to the volumes at the beginning of the recession (W_0). It is an index that reflects the loss of the water resource relative to the maximum volume at the beginning of the recession.

The lower this ratio, the smaller the volumes lost in the recession period from the initial volume, so less water inputs are needed as a percentage to renew the initial volume.

The Renewal time rate (Trin), on the other hand, is inversely proportional to the renewal rate (Rr), because it indicates the time it would take the resource to return to current-year conditions from a null volume above the spring elevation. The longer the

renewal time rate, the better the health of the water resource, because it shows that at the end of recession there are still many cubic meters available in the aquifer.

For each case study, the interpolation method between Bussinesq and Maillet will be chosen, based on the one that best represents the behavior of the spring discharge. So that the output parameters, which will be shown in the table, will refer to the method used.

To select the model, the cleanest recession phases are taken for each spring, that is where there are no oscillations due to the response of other hydrological inputs, including melt and rainfall. In addition, the Root-Mean-Square Error (RMSE) is looked at to see which of the two functions has the least margin of error. Usually a spring keeps one of the two functions optimal for all years due to its aquifer endogen characteristics, hard to find a spring which the subsequent recession is best interpolated by the other method.

To perform this analysis, a semi-automatic software based on the Python programming language is used. This package, named SOURCE, improved by the authors: Lo Russo Stefano, Suozzi Enrico, Gizzi Martina, Taddia Glenda, is open-source and can be downloaded via links: <https://zenodo.org/records/6257321#.YheM3ZbSKUI>. Furthermore, the explanation of this software is shown in the paper: Lo Russo, S., Suozzi, E., Gizzi, M., & Taddia, G. (2021). SOURCE: a semi-automatic tool for spring-monitoring data analysis and aquifer characterization. *Environmental Earth Sciences*, 80, 1-13.

2.4.2 System classification

Study of hydrogeological relationship between input impulses such as rainfalls and snow melting can be made on the basis of literature background (Banzato *et al.*, 2020). Aquifers are recharged from precipitation and surface waters that percolate through the land surface and generate an hydric impulse in the aquifer system that might be more or less hampered according to the aquifers features. The aquifer drainage system can be characterized by an impulse function that transforms the input (e.g., rainfall or snowmelt) into spring hydrograph responses in terms of discharge, temperature, and EC variations. The impulse functional analysis can then be related to the drainage “effectiveness”.

Qualitative analysis of the hydrographs and observed correlations between the flow rate and EC as a function of infiltration input reveals three broad behavioral categories (types A–C), based on the drainage system effectiveness (Lo Russo *et al.*, 2021).

In the highly effective drainage system (type A) during high water levels (e.g., flood or snow melting period), most of the freshly infiltrated water reaches the spring very

quickly, due to the presence of open fracture systems, well-developed karst conduits, or highly permeable horizons, according to the local hydrogeological situation. Freshly infiltrated water of low salinity tends to replace the groundwater supplying the spring during the baseflow. Therefore, the water chemistry response is usually characterized by a fast and intense reduction in mineralization, highlighted by decreased EC values corresponding to the flood peaks. The behavior of the groundwater temperature is relatively similar to that of the EC: its intense variability is almost synchronous with the flood peaks, and it recovers rapidly after the end of the infiltrative processes.

In the moderately effective drainage system (type B), the spring hydrodynamic response can display impulsive behaviors. Freshly infiltrated water increases the hydraulic head in the saturated zone, and induces a pressure increase in the saturated fractured portions of the rock mass (fractures and/or karst conduits). This pressure increase and the corresponding pushing effect tend to mobilize the resident groundwater. The groundwater is near thermal equilibrium with the aquifer and is characterized by a higher salinity than the freshly infiltrated water. Therefore, an increase of flow discharge, EC, and temperature is observed by monitoring the spring (piston effect). After the infiltrative peak, the system is dominated by a mixing process between the resident pre-event groundwater and the freshly infiltrated water.

In a low effective drainage system (type C), the hydrodynamic impulsive response to the infiltrative processes is almost absent. The discharge flow displays slow and modest fluctuations that are delayed up to several months relative to the main rainfall events. Chemical parameters (salinity) and the discharge water temperature usually display a similar trend, with slow and minor variations. Freshly infiltrated water moves slowly in the unsaturated and saturated zones, thereby reaching equilibrium with the aquifer and the resident pre-event circulating groundwater. Homogenization occurs due to the aquifer characteristics, and the external output due to the infiltrative process (low salinity and cold water) is strongly reduced.

Here below are shown the intervals spanned by the correlation coefficient and correlation factor for the three basic types of spring described above:

- Type A: Replacement; $-1 \leq \rho \leq -0.2$; $0.2 \leq c(\rho) \leq 1$
- Type B : Piston; $0.2 \leq \rho \leq 1$; $0.1 \leq c(\rho) \leq 0.5$
- Type C: Homogenization; $-0.2 \leq \rho \leq 0.2$; $0 \leq c(\rho) \leq 0.2$

Then these coefficients will be utilized to evaluate the influence of precipitation and snowmelt phenomena on spring output. Because it is important to understand whether at least the spring responds to the hydrologic input within the hydrogeological year. If not, a study of a 10-year time series could also cover precipitation and melt phenomena from even years prior to the time interval studied. Therefore, it is important to evaluate

the time lag of input and output characterized by the aquifer system structure, size and geometry.

2.4.3 Statistical Characterization

Statistical characterization of the spring flow data set can be useful in understanding some of its behaviors over time. Two statistical analysis will be shown below, the first one (BoxPlot) related to the discharged volumes populations for each month of the year with the information obtained over the whole interval of the time series. While the second statistical characterization is used to have an interpretation of the water flow signal over the entire time series (Standard Discharge Index).

The BoxPlot is a graphical representation of a population of parametric or not parametric individuals, graphically showing the data population distributed in quartiles. The box is enclosed within the Lower quartile (25% Percentile) and the Upper quartile (75% Percentile), while the Lower Tail and Upper tail are calculated respectively: Lower Tail = Lower quartile - 1.5*Box Length, Upper Tail = Upper quartile + 1.5*Box Length, they represents the "wings" of population distribution. The median is represented with a line within the Box Length, and outliers are those values that are above or below the Upper Tail and Lower Tail (Praveen *et al.*, 2018).

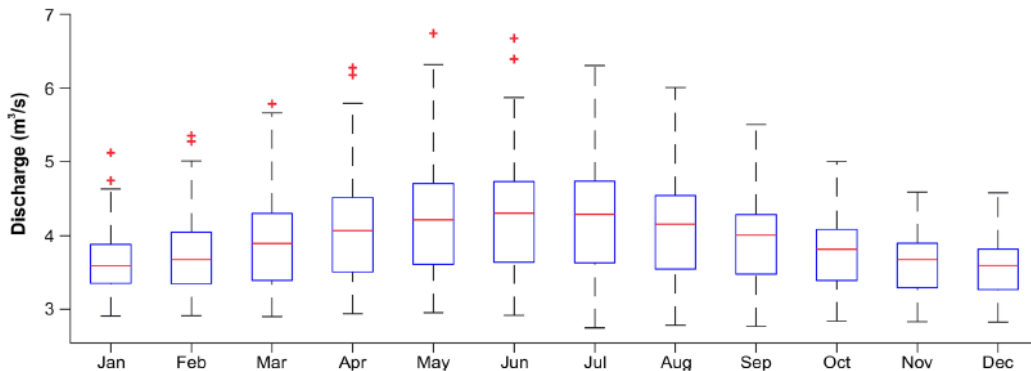


Figure 26. Monthly Discharge BoxPlot population example by (Leone *et al.*, 2021).

As shown by the authors (Leone *et al.*, 2021) in **Fig. 26**, the BoxPlots related to the monthly flow population show us which months are the most prosperous in terms of runoff flows, especially corresponding to the most rainy months per year or seasonal melt processes. In fact, it can also tell whether the spring regime and hydrograph is most influenced by rainfall scattered throughout the year or influenced by a particular hydrogeological input concentrated at one time of the year. However, generally, the BoxPlot intrinsically represents the hydrogeological input-output system relative to the

time interval under consideration. Thus it returns the precise information of how the spring flow behaves during the year. Of course, the more years are available, the more realistic monthly discharge population distribution estimates will be.

The other important characterization that can be made statistically, is the Standard Discharge Index (SDI) which is important to find out what are the drought or wet period calculated on a time interval. This approach is widely used also to characterized the drought and wet period in term of precipitation regimes as witnessed by the authors (Khan, Gabriel and Rana, 2008; Cheval, 2015; WMO, 1987).

SDI is based on accumulated discharge and it is used to quantify the deficits or surpluses on different time scales. For example as time scale become longer, monthly precipitations affect less on the total amount (Wang *et al.*, 2017). The SDI can be calculated starting from different probability distribution. The one that will be used for our case studies is the Gamma distribution, which is one of the most used. The probability density function of the gamma distribution is defined as:

$$g(x) = \frac{1}{\beta^\alpha \Gamma(\alpha)} x^{\alpha-1} e^{-\frac{x}{\beta}} \quad \text{for } x > 0 \quad (9)$$

In (9) equation there is α which is a shape parameter, β which is a scale parameter, $x > 0$ is the discharge amount and $\Gamma(\alpha)$ is the gamma function (Guenang and Mkankam Kanga, 2014).

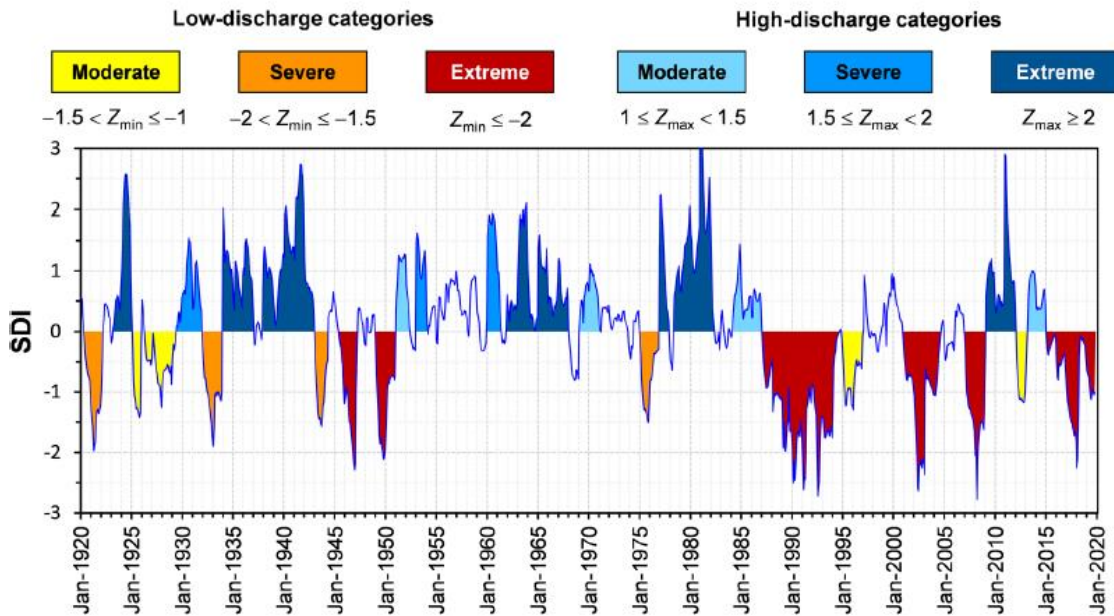


Figure 27. Standardized Discharge Index example as reported by (Leone et al., 2021).

In Fig. 27 is represented a study with SDI with a 100 year time series and a yearly scale of distribution (Leone *et al.*, 2021). In this research work, having a shorter time series, it has been used higher resolution scales, one of 1 month and the other one of 3 months. After characterized SDI values it is important to associate them with the drought magnitude scale that describe the time series condition in term of prosperity or scarcity of the value according to the probability distribution. The drought magnitude is shown in Table 2.

Table 3. SDI values.

2.0+	extremely wet
1.5 to 1.99	very wet
1.0 to 1.49	moderately wet
-.99 to .99	near normal
-1.0 to -1.49	moderately dry
-1.5 to -1.99	severely dry
-2 and less	extremely dry

2.4.3 Trend analysis

The dense amount of data acquired from mountain spring spots are largely sufficient to perform statistical tests and elaboration to assess the increasing or decreasing behavior. Multiparametric probes started to register during 2011 year and the dataset has a time interval of 1 hour. Nevertheless, to reduce the computational cost, it has used the daily time step, that is traduced in about 4120 values for each spring from the beginning up today.

With this datasets, it is possible to run statistics with an high level of significancy. The most used one for spring trend evaluation is the Mann-Kendal that Sen's Slope which are usually combined together (Machiwal and Jha, 2006; T.O.Olatayo and Taiwo, 2014).

The Mann–Kendall test is a rank-based non-parametric method, whose purpose is to assess the sign and the significance of monotonic trends in time series. It does not need to satisfy the assumption of normality of the data; its statistic is based on the signs of the variables. The mathematical equations for calculating Mann–Kendall statistics, i.e., S , $\text{Var}(S)$, and standardized test statistics Z_{mk} are:

$$S = \sum_{i=1}^{n-1} \sum_{j=i+1}^n \text{sgn}(Y_j - Y_i) \quad (10)$$

$$\text{sgn}(Y_j - Y_i) = \begin{cases} +1 & \text{if } \text{sgn}(Y_j - Y_i) > 0 \\ 0 & \text{if } \text{sgn}(Y_j - Y_i) = 0 \\ -1 & \text{if } \text{sgn}(Y_j - Y_i) < 0 \end{cases} \quad (11)$$

$$\text{Var}(S) = \frac{1}{18} \left[n(n-1)(2n+5) - \sum_{p=1}^q t_p(t_p-1)(2t_p+5) \right] \quad (12)$$

$$Z_{mk} = \begin{cases} \frac{S-1}{\sqrt{\text{Var}(S)}} & \text{if } S > 0 \\ \frac{S+1}{\sqrt{\text{Var}(S)}} & \text{if } S < 0 \end{cases} \quad (13)$$

where Y_j and Y_i are data at time points j and i ($j < i$), n is the length of the time series, t_p is the number of ties for the p th value and q is the number of tied values. The sign of the trend is represented by the sign of standardized test statistic Z_{MK} .

The true slope of the trend detected by the Mann–Kendall test was then computed by using Sen's slope test. Sen's test assumes that trend is linear; the slope, b_{Sen} , and the intercept, a_{Sen} , of the trend line, are given by:

$$b_{sen} = \text{median} \left(\frac{(Y_j - Y_i)}{(j - i)} \right) \quad (14)$$

$$a_{sen} = \text{median}(Y_i - b_{sen}t_i) \quad (15)$$

where Y_i is the data point at time t_i .

Furthermore, the Mann-Kendal and Sen's slope outputs are also combined with the linear regression angular coefficients for each time series, in order to strengthen the validity of the statistic tests. OLS Linear Regression has been explained in meteorological analysis sub-chapter.

2.4.3 Hydrogeochemical analysis

After having analyzed hydrogeological input (precipitation and snow melting) and hydrogeological output (spring discharge) it is important to add some qualitative analysis on aquifer in order to understand what are the water path and circulation before the outflow section.

The main widespread approach is the hydrogeochemical one, which analyzing the amount of cations, anion and metals helps to understand the rock mass containing the water aquifer and so to discover the catchment area of the spring.

Moreover, the time series of this information are useful to verify variation of aquifer structure in time and to assess the variation in water input type along time.

In fact, this method of analysis can be fundamental to check along time if water is coming from glacier and permafrost melting, which it is the most important issue of this research.

Variation of water salts are usually plotted on Schoeller diagram, which is adopted to show the relative concentrations of anions and cations typically expressed in milliequivalents per liter (Balestra, Fiorucci and Vigna, 2022).

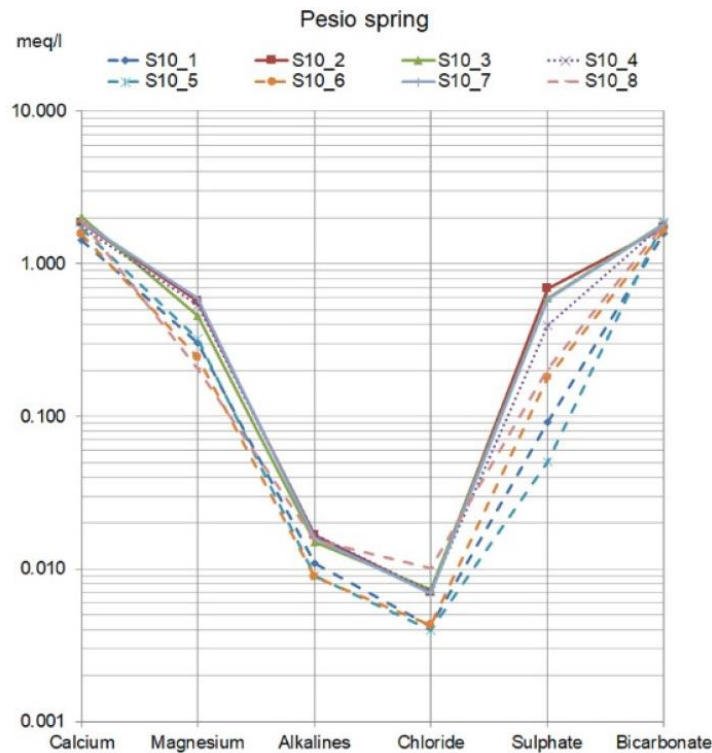


Figure 28. An example of Schoeller diagram by authors (Balestra, Fiorucci and Vigna, 2022).

From the diagram (**Fig. 28**) the chemical type of water can be determined, they according to the concentrations and the Shoeller diagram are divided into main categories: Bicarbonate-Calcic, Sulfate-Calcic, Bicarbonate-Alkaline, Chloride-Alkaline. Then if there are three prevalent salts it can be also classes like: Bicarbonate-Calcic-Magnesium, Bicarbonate-Sulfate-Calcic.

According to this salts classifications of water, back analysis can be performed to identify the rock lithologies of provenience and so try to assess the geometry of the aquifer.

The hydrochemical analysis is often combined with the physical parameters of Temperature and Electric Conductivity of spring water. They are useful to understand how long the water travelled inside the rock mass and also help to understand which kind hydric input the aquifer is influenced.

An other chemical representation is the PIPER diagram, that will be used to understand the ratios among anions and cations in order to assess the ion prevalence independently from the absolute concentration (meq/l) of them (Karmegam, et.al., 2011)

2.5 Annual precipitation and discharge

The volumes discharged from the springs and the precipitation regimes in addition to being analyzed independently are also related to each other. This will make it easier to understand the interaction between hydrogeological inputs and outputs of the studied groundwater resources (Williams and King, 2020; Adji and Bahtiar, 2016). Also, with this type of analysis in this research, it will be easier to understand whether there are inputs aimed to the spring different from those generated by the seasonal solid precipitation and the liquid precipitation.

This analysis is carried out by considering the annual volumes of water discharged with regard to springs and the annual mm of precipitation calculated by the relevant weather station. Given the geographic and morphological situation of the case studies, it is important to distinguish between liquid and solid precipitations. Since the latter ones, if they fall during the last months of the year, knowing that the hydrogeological input occurs at the melting of solid precipitation, they need be added to the precipitation amount of the following year and be taken off from the precipitations of the previous one (Gizzi *et al.*, 2022).

Therefore, precipitations were processed on the basis of atmospheric temperatures measured by the weather station and based on the elevation difference between the spring location and the weather station. Indeed, temperatures were calibrated according to the tropospheric vertical thermal gradient (-0.6 °C/+100 m a.s.l.) (Limet, 2023). For example, in case the weather station is 200 meters lower than the spring, the temperature measured by the station of 1.2 °C is chosen as the thermal zero of the spring. Of course this is a simplification because the thermal gradient then undergoes seasonal effects that result from different atmospheric conditions (Lu *et al.*, 2009).

In addition, calendar years instead hydrogeological years were considered in order to have a constant time steps and thus have a consistent reading of the graphs especially from the point of view of trends reconstruction and visual interpretation. Then having calculated the annual budget of input and output, Linear Regression (OLS) of the two variables, as explained in sub-chapter 2.3, was carried out to obtain the coefficient of determination R^2 to define the relationship degree of annual hydrogeological input and output. R^2 is defined by the equations (17,18,19):

$$R^2 = \frac{ESS}{TSS} \quad (17)$$

$$ESS = \sum_{i=1}^n (\hat{y}_i - \bar{y})^2 \quad (18)$$

$$TSS = \sum_{i=1}^n (y_i - \bar{y})^2 \quad (19)$$

In which ESS is the Explained Sum of Squares and TSS represent the Total Sum of Squares, y_i are the observed values, \bar{y} is the mean of the population and \hat{y}_i are the estimated values obtained from the linear regression shown previously. the coefficient of determination measures the link between the variability of the data and the correctness of the statistical model used. R^2 varies between 0 and 1, when it is equal to zero it means that the model (Linear Regression) does not explain the relationship of the two variables at all, when R^2 instead is equal to 1 it means that the model perfectly explains the relationship between the variables (Draper *et al.*, 1998).

Furthermore, to understand the correlation between the two variables, it can be considered the R index also known as the Pearson correlation index, which is a coefficient expressing any linearity relationship between the variables. It is calculated by taking the square root of the coefficient of determination or by dividing the covariance by the product of the standard deviations of the two variables as defined in eq (20):

$$R = \frac{\sigma_{xy}}{\sigma_x \sigma_y} \quad (20)$$

Where σ_{xy} is the covariance and σ_x , σ_y are the standard deviations of the two variables. When $R \leq 0.35$ there is a weak correlation, if $0.35 < R < 0.68$ there is a moderate correlation, while if $R \geq 0.68$ there is a strong correlation (Taylor, 1990).

2.6 Mascognaz weather station

This subchapter presents the Mascognaz nivo-meteorological station, a station belonging to the applied geology group of the Politecnico University of Turin. Given the state-of-the-art instruments installed at this station, studies have been carried out of what atmospheric and nivometric factors most influence snowmelt. The Mascognaz nivo-meteorological station is located in the same catchment area as the Mascognaz spring (Fig. 29), a few hundred meters further upstream. It had been installed to study the effect of nival melt on the spring discharge rate downstream. It is not used in this research to describe the climatic-pluviometric regime of the spring because the datasets of this weather station for several parameters are very fragmented. Rather, it will be

used to study snow melt phenomena of few seasons where there are continuous and good quality data.

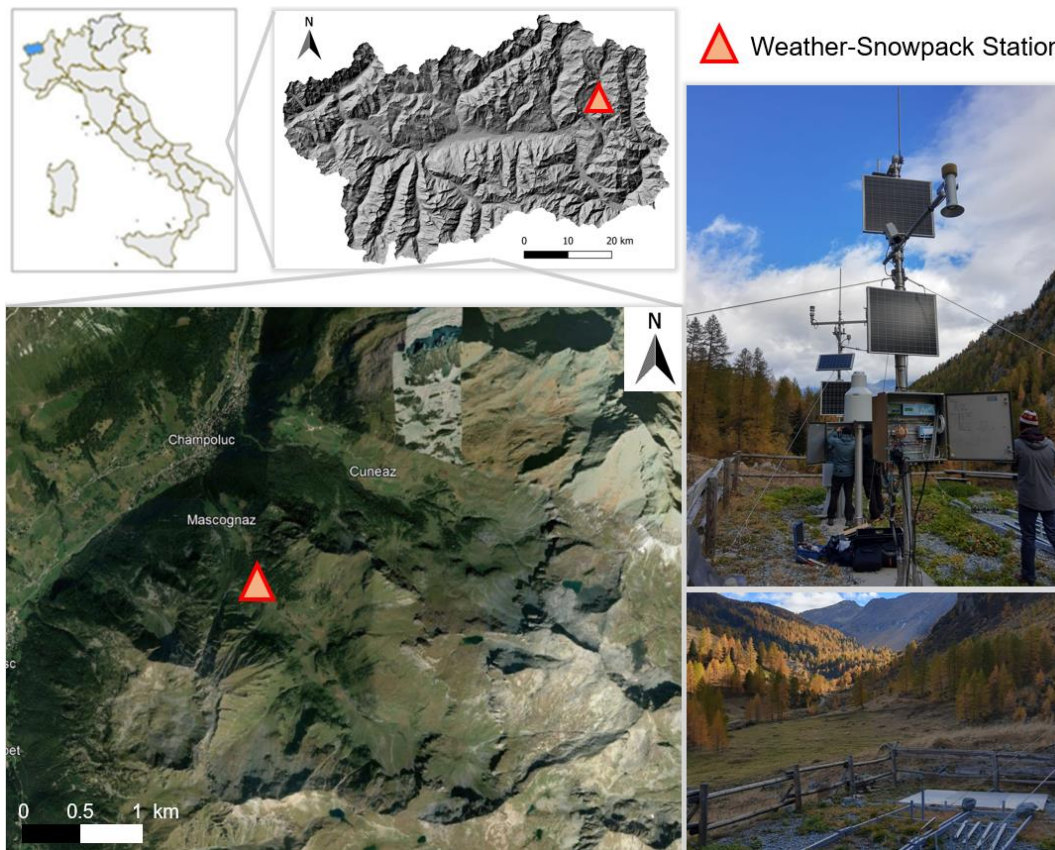


Figure 29. Mascognaz nivo-meteorological station geographic location and photos (Panzeri and Mondani, 2022).

This station, in fact, can be subdivided into a meteorological station and a snow station, the latter equipped with a series of sensors designed precisely to monitor parameters such as Snow Depth, Snow Weight, and Snow Density. The Meteorological Station is instead equipped with sensors that monitors: Air Temperature, Relative Humidity, Direct and Inverse Radiation, Air Pressure, Winds and Rainfalls. From these parameters, an attempt will be made to establish a relationship between the melting process in which the mantle loses weight and the snow and atmospheric conditions that caused the melting phenomenon, this in order to be able to understand how the evolution of atmospheric conditions given by Climate Change may also influence ablation processes leading to aquifer recharge or potential instability phenomena.

After introduced snow characteristics and metamorphisms, the most important aspect is to evaluate the snow melting water amount.

The approached used so far is statistical-based, data acquired from Mascognaz weather station are elaborated and averaged. Then, they are statistical implemented to

understand what are the correlation between atmospheric parameters (Temperature, Direct Radiation, Inverse Radiation, Absorbed Radiation, Relative Humidity, Atmospheric pressure, Wind) and snowpack parameters (Snow Weight, Snow Depth, Snow Density) with the melted water which is calculated as the loss of Snow Water Equivalent (SWE).

It has been preferred to perform a statistical analysis rather than physical relations to assess snow melting rate according to atmospheric and snowpack variables monitored by Mascognaz weather station. This decision was made on the basis that the snowpack-weather station records many parameters that usually are not monitored all together in the same spot.

In fact, besides the classic atmospheric and pluviometric sensors, this station was equipped with Laser/Ultrasonic sensor and Scale to record snow depth, weight and density evolution.

It has been considered the value recorded by the Snow Scale (Snow Water Equivalent) to assess the quantity of water melted ($\Delta SWE < 0$) within a different simulated time step. Moreover, all the other aforementioned variables have been put in the statistical analysis to find out the strength of correlations.

The approach used is the Multiple Linear Regression (MLR) with Ordinary Least Square (OLS) capable to find a linear relation between depending variable (ΔSWE) and all the other independent variables (Hutcheson, 2011) as follow:

$$y' = a_0 + a_1x_1 + a_2x_2 + \dots + a_nx_n \quad (16)$$

Where y' is the predicted dependent variable, and x are all the independent variables used to describe the model, $a_{0...n}$ are all the variables coefficients found with the OLS in order to find the best interpolation with biggest value of R^2 .

An overview of the instruments with which the station is equipped is shown in the **Fig. 30** as reported by authors (Mondani, Gizzi and Taddia, 2022), as it can be recognized, the sensors are installed on two main towers, tower 1 is equipped with atmospheric instruments, tower 2 with snowpack monitoring sensors.

Besides towers equipment, there is the Snow Scale, Underground Pluviograph and Weight Pluviograph instruments, which are spread out within the ranch delimited by the fences.

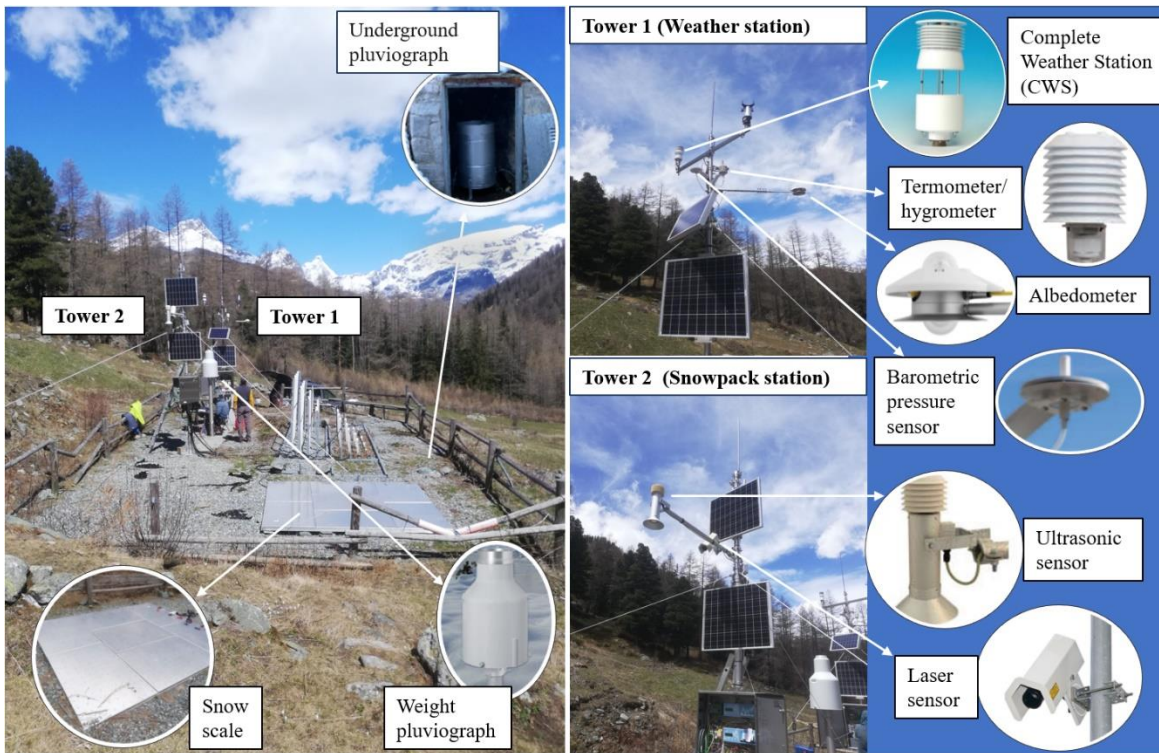


Figure 30. Nivo-Meteorological station set-up. Tower 1 is equipped with atmospheric sensors, Tower 2 with Snowpack sensors (Mondani, Gizzi and Taddia, 2022).

Among all these instruments, some of them will be exploited to carry out the aforementioned variables to perform the statistical test (MLR) and establish statistical correlations. Those sensors are better described below in **Table 3**.

Table 3. Sensors used for the statistic tests.

Parameter	Sensor	Characteristics
Air temperature (°C)	CWS All-In-One (AIO) Weather Sensor (Climatronics Corporation, NY, U.S.)	range of application: -40 to 50°C operating temperature: -50 to 70°C overall uncertainty: +/- 0.2°C
Relative humidity (%)	CWS All-In-One (AIO) Weather Sensor (Climatronics Corporation, NY, U.S.)	range of application: 0 - 100 % rh operating temperature: -50 to 70°C overall uncertainty: +/- 3 % on measured value

Direct and inverse radiation (W/m ²)	Albedometer model CMA6 (Kipp&Zonen, Delft, Netherland)	range of application: 0 - 2000 W/m ² operating temperature: -40 to 80 °C overall uncertainty: +/- 20 W/m ²
Atmospheric pressure (hPa)	CWS All-In-One (AIO) Weather Sensor (Climatronics Corporation, NY, U.S.)	range of application: 600 to 1100 hPa operating temperature: -50 to 70 °C overall uncertainty: +/- 0.35 hPa
Snow water equivalent (mm)	Snow scale Snow pillow (Sommer GmbH & Co KG, Koblach, Austria)	range of application: 0 to 2500 mm operating temperature: > -30°C material: fabric thickness PVC-foil resolution: 1 mm overall uncertainty: 0.25 % +/- on measured value
Snow depth (mm)	Ultrasonic sensor USH - 8 (Sommer GmbH & Co KG, Koblach, Austria)	range of application: 0 to 8000 mm operating temperature: -35 to 60 °C housing: aluminum resolution: +/- 1 mm overall uncertainty: +/- 0.10 % on measured value

Temperature and relative humidity are monitored by both the hygrometer and the multi-sensor CWS (All-In-One Complete Weather Sensor), only the CWS is considered for the statistical study of these parameters for the quality and continuity of information recorded. Temperature is detected by a triple thermistor element inside the CWS, while for relative humidity there is inside the CWS a capacitive polymer sensor very resistant to wetting, dust, dirty and environmental chemicals.

Barometric Pressure is monitored both by the 61302 Barometric Pressure Sensor and by CWS which characteristics are visible in **Table 3** and within which there is a piezoresistive pressure sensor that measure this parameter.

Inverse and direct radiation are both detected by the CMA 6 albedometer, it includes in one container two pyranometers. A glare screen prevents direct radiation from lower domes during sunrise and sunset. a drying cartridge absorb humidity inside the instrument keeping dry the pyranometers.

Absorbed Radiation is the indirect parameter that is calculated from the subtraction of Direct Radiation and Reverse Radiation, this will be an important parameter to consider in statistical tests, since the greater the absorbed radiation of snow, the greater the latent heat transmitted to the snowpack. In fact according to the albedo effect, fresh snow has

a very high coefficient that increases the reflection of solar radiation by decreasing the absorbed heat.

The weight of the snow and thus its Snow Water Equivalent (SWE), that is the height in millimeters of water equivalent to the weight of the snow, is monitored by the Snow Scale. This large system consists of 7 adjacent perforated panels generating an area of 2.8 x 2.4 meters. All panels allow water to percolate through the sensor into the ground. The load sensor is placed only in the middle panel, the other panels have the utility of minimizing edge effects by creating the continuity of the snowpack above the panel that measures weight. This system ensures accurate measurement even when there are conspicuous snow accumulations, although as noted in **Table 3**, the overall uncertainty increases as the mm of SWE above the scale increases.

Snow height (Snow Depth), is measured through two instruments: the SHM 30 Laser sensor and the Ultrasonic Sensor (USH-8), of the two only the latter will be used for statistical processing, because the laser sensor does not have continuous and accurate time series. The Ultrasonic Sensor (USH-8) uses sound waves to determine the time in which that wave is reflected from the surface back to the sender. Of course, depending on the height of the snow, that wave will take longer or shorter to return to the sensor, so the time parameter, depending on the height of the sensor above the ground, is transformed into the Snow Depth parameter (Varhola *et al.*, 2010). Air temperature measurement is also recorded inside this instrument, because this parameter affects the propagation of the sound wave in the air. So based on the temperature values, the sensor automatically calibrates the wave propagation speeds.

The only parameter calculated indirectly is Snow Density, which is nothing but the ratio of the SWE measured with the Snow Scale and the Snow Depth measured with the Ultrasonic Sensor, the ratio multiplied by 1000 gives back the kg/mc of the snowpack.

Data acquisition of all the sensors of the nivo-meteorological station is carried out by the OTT net DL1000 data logger, which is installed inside the OTT MetSystem lockable control cabinet. The data logger is a versatile unit that can be used in hydrometry as well as meteorology and agrometeorology (Dombrowski, Franssen and Brogi, 2021). It has a small size that allows it to be convenient in installation, plus it is a very durable unit even in extreme temperatures such as -70°C and 40°C, making it perfect even for high mountain areas.

The datalogger includes several standard ports, which communicate with the sensors through different interfaces. It includes several transmission protocols (HTTPS, HTTP, SMTP, FTP, XML). In addition, it is equipped with SIM, which allows data to be sent in real time to the parent company's server and to the Politecnico di Torino. The mobile internet network systems with which the SIM can transmit are: GSM, GPRS and 3G (Djordjevic and Dankovic, 2019).

Currently, data are transmitted using the General Packet Radio Service (GPRS) network, with a frequency of 10 minutes (Harris *et al.*, 2020). Actually, the sensors take multiple values in 10 minutes; the data logger takes an average of the values taken in these 10 minutes and sends them.

Such an accurate temporal resolution makes it possible not only to conduct daily and seasonal analyses, but also to analyze the behaviors of parameters and the interactions between them on a sub-hourly scale. Therefore, this makes it possible to increase the significance of statistical correlation tests, the results of which will be shown later.

The statistical model built on the data collected from the sensors described above is compared with an experiment performed in Applied Geology Laboratory a at the Lecco Territorial Pole in which snowpack melting activity, with monitored atmospheric conditions, was monitored by photogrammetric survey. The set-up is presented in **Fig. 31**.



Figure 31. Snow melt experiment on the Laboratory Landslide simulator. GoPro cameras attached on the frames above the snow.

Three GoPro cameras have been placed on the top of simulator, attached to the steel frame, in order to reconstruct a 3D model by means of Cloud Compare Software that reveal the thinning rate of snow melting on all the simulator surface (Girardeau-Montaut, 2016). On the snow are placed 3 markers (**Fig. 31**) to reference the 3D reconstruction.

2.7 Rutor Glacier mass balance

Rutor Glacier will be used to understand the interaction between mountain springs and the cryosphere, in fact its conditions, unlike rock glaciers, are certainly easier to monitor. In fact it has been kept under observation by ARPA Valle d'Aosta for about 17 years.

Very important information has been obtained every year about Rutor in relation to the Promise spring, which is only a few thousand meters from the glacier. In fact, every year the glacier accumulation is calculated, that is the snowpack generated by all the solid precipitation above the glacier in a season. The measurement of accumulations so far has been done by local surveys of the snowpack, which are then interpolated to obtain the total mass of glacier accumulation in terms of SWE (Snow Water Equivalent) (**Fig. 32**).

While regarding glacier mass loss, thus glacier ablation, point measurements at fixed references are not possible. Therefore, geodetic methods based on the difference of digital surface models (DSMs) are applied; these have recently been compared with aero-photogrammetric surveys acquired by the Politecnico di Torino as part of Glacier Lab activities (ARPA VDA, 2022).

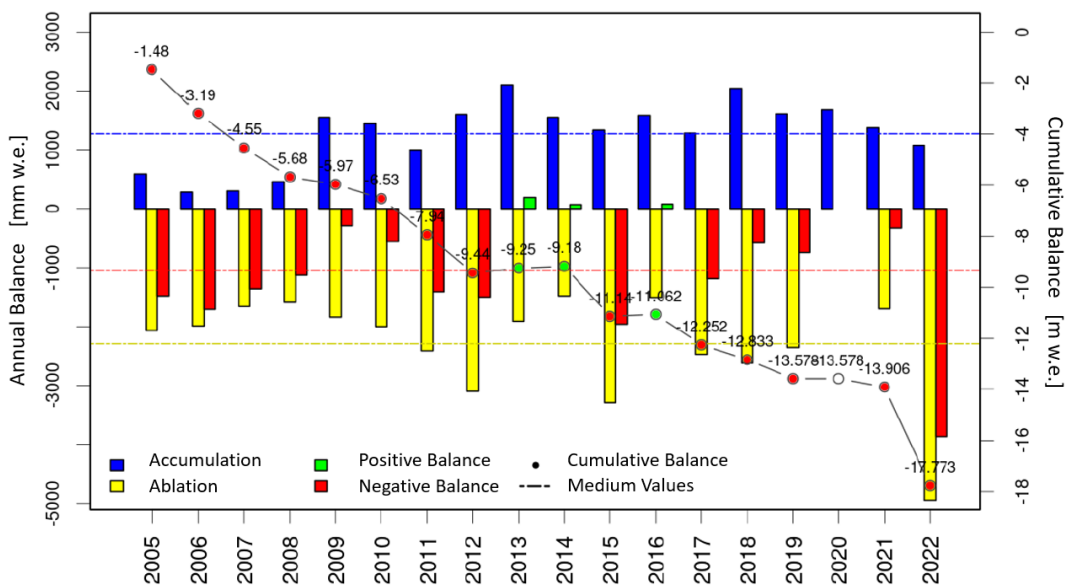


Figure 32. Rutor Glacier mass balance. Observation period (2005, 2022). (ARPA VDA, 2022).

Thus the total melting of the glacier in a year is equal to the sum of the melting of the snow mantle accumulated in winter and possibly the underlying glacier accumulated the years before. Clearly, if the total melt does not exceed the winter accumulation, the glacier will have a positive balance; if the total melt exceeds the winter accumulation, there will be melting of what had accumulated prior to the current year, so there will be a negative balance (**Fig. 32**). It can be seen that the last year (2022) was particularly

disastrous for the glacier, with little winter accumulation and intense ablation phenomena in summer leading to a far negative mass balance compared to the glacier's usual. While unfortunately missing is the budget for the year 2020 related to the pandemic and the inability to operate in the field.

This information was then juxtaposed with spring information in terms of discharge time series, with La Thuile-Villaret information about hydrogeological input affecting spring discharge and the La Thuile - La Grande Tete meteorological station (2430 m a.s.l.) (**Fig. 33**), in order to analyze the correlation between air temperature time series and the Rutor ablation activity.

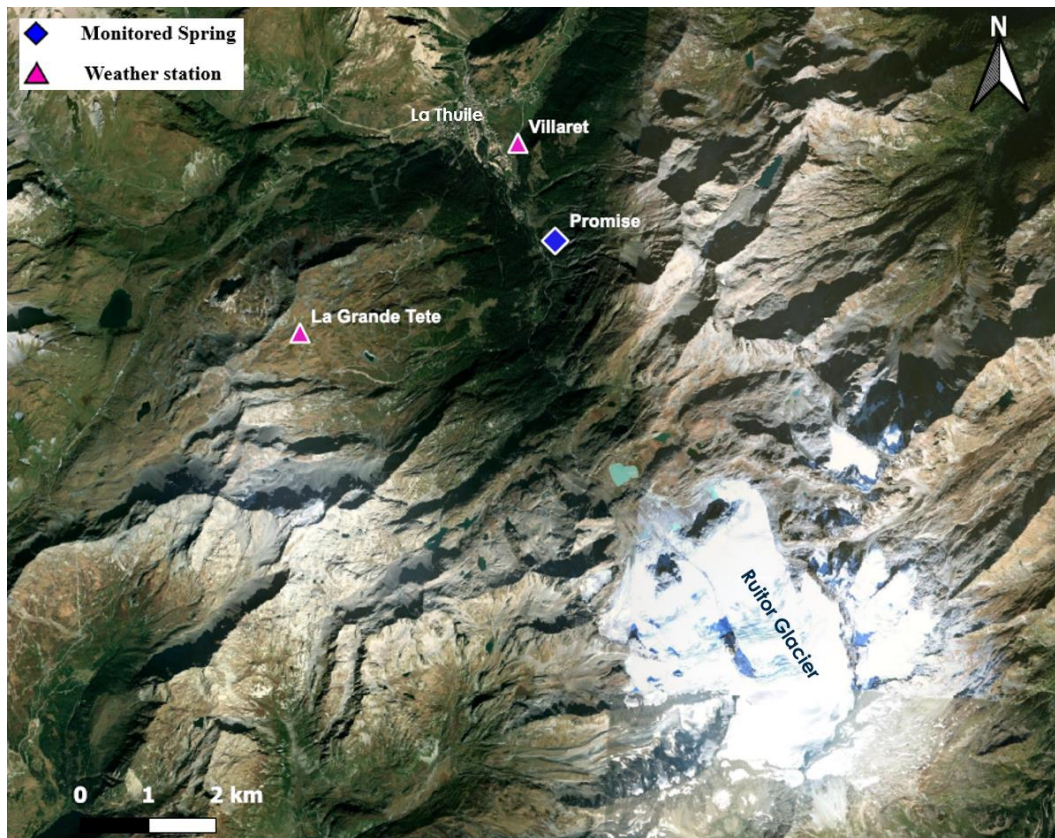


Figure 33. Location of Rutor Glacier, weather stations and Promise spring.

This station is located closer to the glacier and at a higher elevation than La Thuile Villaret, so it was chosen as more representative in terms of the climatic regime of Rutor. To understand the influence that glacier ablation has on the spring, it was necessary to reconstruct the annual hydrological input determined by snowmelt and rainfall in order to subtract the annual discharged volume with total precipitation contributions and obtain values correlated to the Rutor mass balance.

To do this, it has been used the total precipitation calculated as presented in subchapter 2.6, with the shift of last months solid precipitations to the following year.

The only shortcoming of this analysis will be the lack of accurate information regarding the Promise spring aquifer recharging area to obtain detailed annual volumetric balances of what comes in from rain, snow, or glacier melt. So the problem lies in the inability to transform mm of rain and snowmelt into cubic meters by missing the areal parameter. What is done, then, to make the elements of the hydrological budget: spring discharge, glacier budget, snowmelt and rainfall, comparable to each other is to make the parameters dimensionless by normalizing the annual values. Two normalization methods will be compared, which are the two most widely used. The first one is the min_A, max_A method (The minimum and maximum values of the attribute A) described as follow (16):

$$a' = (high - low) * \frac{a - min_A}{max_A - min_A} + low \quad (16)$$

where high and low are the limits of the range of values to be obtained, in our case it has been kept between 0 and 1. a' is the normalized value, a is the actual value, min_A and max_A are the smallest and largest value of the population named A. The main problem with using the min-max normalization method in time series prediction is that the minimum and maximum values of the out-of-sample data series are unknown (Ogasawara *et al.*, 2010).

So the second normalization method is used to check the validity of the first, this is the method $\mu(A)\sigma(A)$ (Mean and Standard Deviation of attribute A) described in the equation (17):

$$a' = \frac{a - \mu(A)}{\sigma(A)} \quad (16)$$

Where a and a' are always the normalized value and the actual value, while $\mu(A)$ is the population mean and $\sigma(A)$ is the standard deviation of the population. This method is useful when the true value of the minimum and maximum of the population is unknown (Ogasawara *et al.*, 2010).

Once the values are normalized, it will be plotted on the same graph the annual spring discharge subtracted by the annual snowmelt and the glacier mass balances of the same years. This is done to observe any relationship between the surplus of water given by the negative balance of Glacier and the Promise spring discharge.

The analysis is performed with the negative mass balance and not the total ablation, because the latter will be included of the snowmelt, which instead will be calculated already through the La Thuile-Villaret weather station recorded data.

2.8 Shallow landslide experimental setup

The Hydrogeology laboratory of Lecco is provided with a landslide simulator, which can be employed to perform downscaled experiments with different slope inclination covered by the studied material layers (Longoni *et al.*, 2022; Ivanov *et al.*, 2020; Ivanov *et al.*, 2021).

Usually the tests are carried out to estimate rainfall thresholds that trigger soil failure under a given inclination (Huang and Yuin, 2010; Wu *et al.*, 2015).

A scheme of the experimental set up is shown in **Fig. 34**. The steel frame supports a slab where the soil is positioned. Then the system is equipped with different sensors in order to reconstruct the entire process.

The Time Domain Reflectometer (TDR) is put within the soil and measure the volumetric water content evolution of the soil (**Fig. 34b**).

Geoelectric method is then employed to reconstruct the resistivity profile of the soil through which is possible to understand the water amount and water front progress into the soil. This one is applied by means of 42 electrodes anchored on the soil surface according to the Wenner scheme (**Fig. 34d**) (Tresoldi *et al.*, 2019).

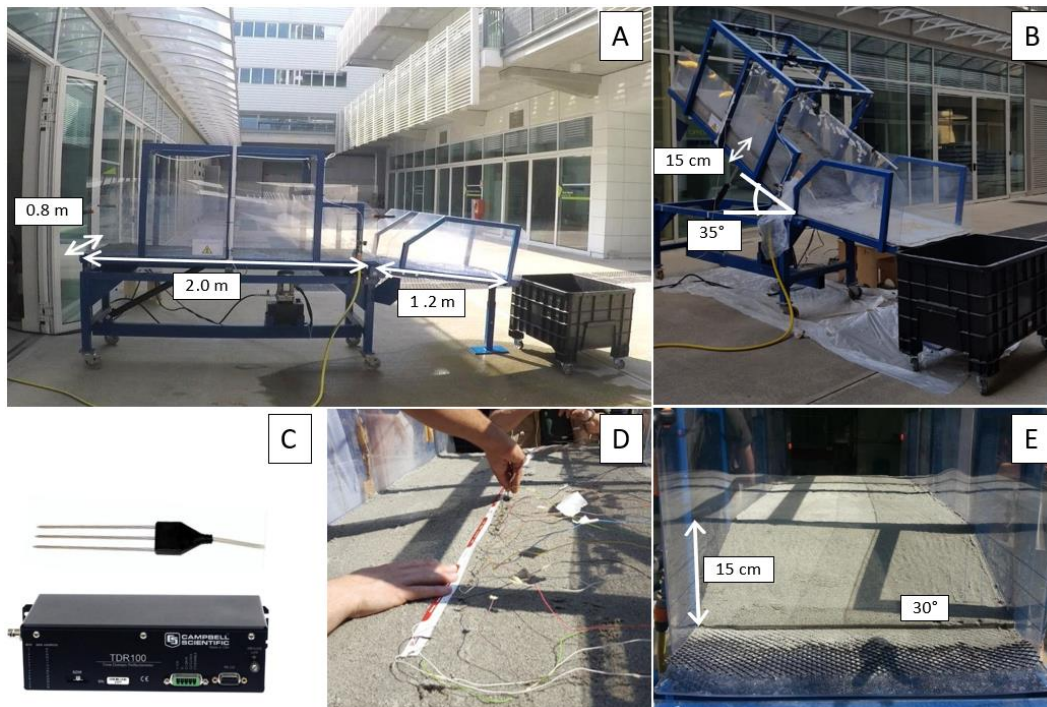


Figure 34. A: Simulator geometry without soil and in horizontal position. B: Simulator inclined of 35° with a soil layer of 15 cm positioned on the slab; C: TDR probe; D: electrodes array of geo-resistivity survey; E: soil foot frontal view (Panzeri and Mondani, 2022).

Three pressure transmitters, are positioned at different levels and depths, they record both pressure and temperature, nevertheless in this case they have been used to record just soil temperature to understand the thermal evolution coming from the interaction between soil and snow.

In this research project, the landslide simulator has been used to analyze the interaction of soil and snow layers, precisely, the soil infiltration process induced by the snow melting. In order to do that, it has chosen a 15 cm sand soil layer and 7.5 snow layer to simulate almost 1 meter thickness of soil and 0.5 meter thickness of snow with a scale factor of six (**Fig. 35**).

The simulation was expected to be carried out until the failure occurrence induced by saturation of the soil caused by snow melting. During the test, some fundamental parameters leading the infiltration and percolation process have been investigated.

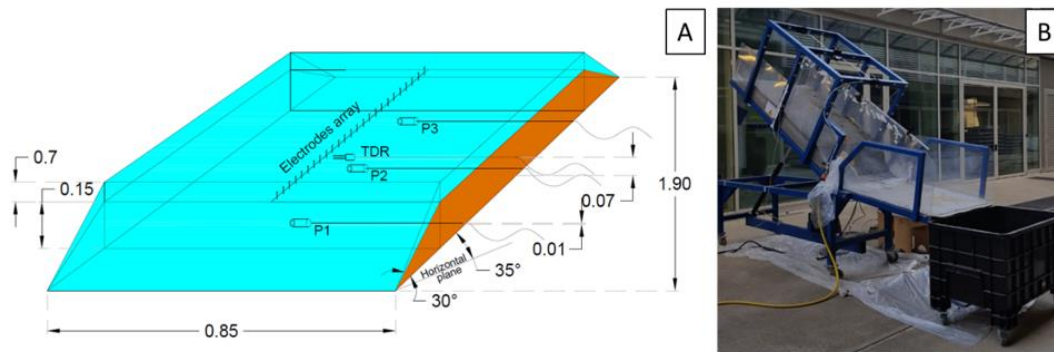


Figure 35. Left side: frontal view of snow melting simulation; right side: conceptual scheme of the simulation with geometries and sensors positions (Panzeri and Mondani, 2022).

Afterwards, an experiment was conducted without the presence of snow, but simulating the upstream filtration that any landslide body would undergo with the snow/glacial melting activity occurring upstream of it.

Therefore, without the direct presence of snow on the ground, a perforated water hose was therefore applied at the upstream perimeter of the soil placed on the simulator. It has been covered with gravel mixed with sand soil in order to dissipate less water and create more continuity near the boundary condition (**Fig. 36**).

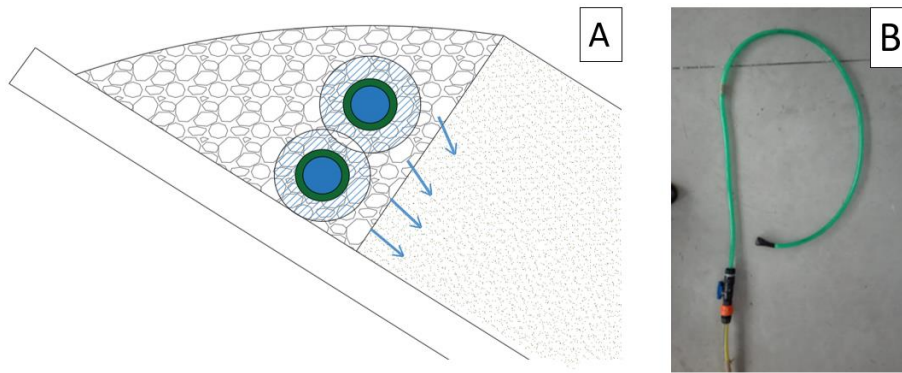


Figure 36. A: Position of the bended hose on the simulator, it is within a portion of gravel and sand soil; B: Photo of the drilled hose .

Water was released with a constant rate and the process of water circulation within the soil portion was studied with the same instruments explained for the previous experiment.

Chapter 3

RESULTS

3.1 Weather station results

The results derived from the weather stations of each spring are summarized below. The time series of the analyzed parameters were taken with the same time interval as the spring time series.

As described in the Methods chapter, the parameters analyzed to describe atmospheric conditions and hydrological inputs are: precipitation, temperature and snow depth. Of these, precipitation includes snowfalls, transformed into equivalent millimeters of water, notwithstanding, the snowpack depth is shown to give a better representation of what is the evolution of snow mantles over the years.

These three parameters are plotted as taken from the Aosta Valley portal with information corrections and integration added to fix the time series where there are discontinuities in the dataset.

For each of these, the recession line was constructed showing the upward or downward trend of the parameter along the time series.

Three other factors were elaborated from the stations daily precipitation, they are: monthly rainfall, dictated by the sum of millimeters of precipitation per month, rainfall intensity, equal to monthly rainfall divided by rainy days, and rainfall frequency relative number of rainy days per month. These three derived parameters also make it possible to add information from the qualitative point of view of the precipitation regime evolution.

From **Fig. 37** to **Fig. 46** are presented all the parameters aforementioned described for all studied weather stations.

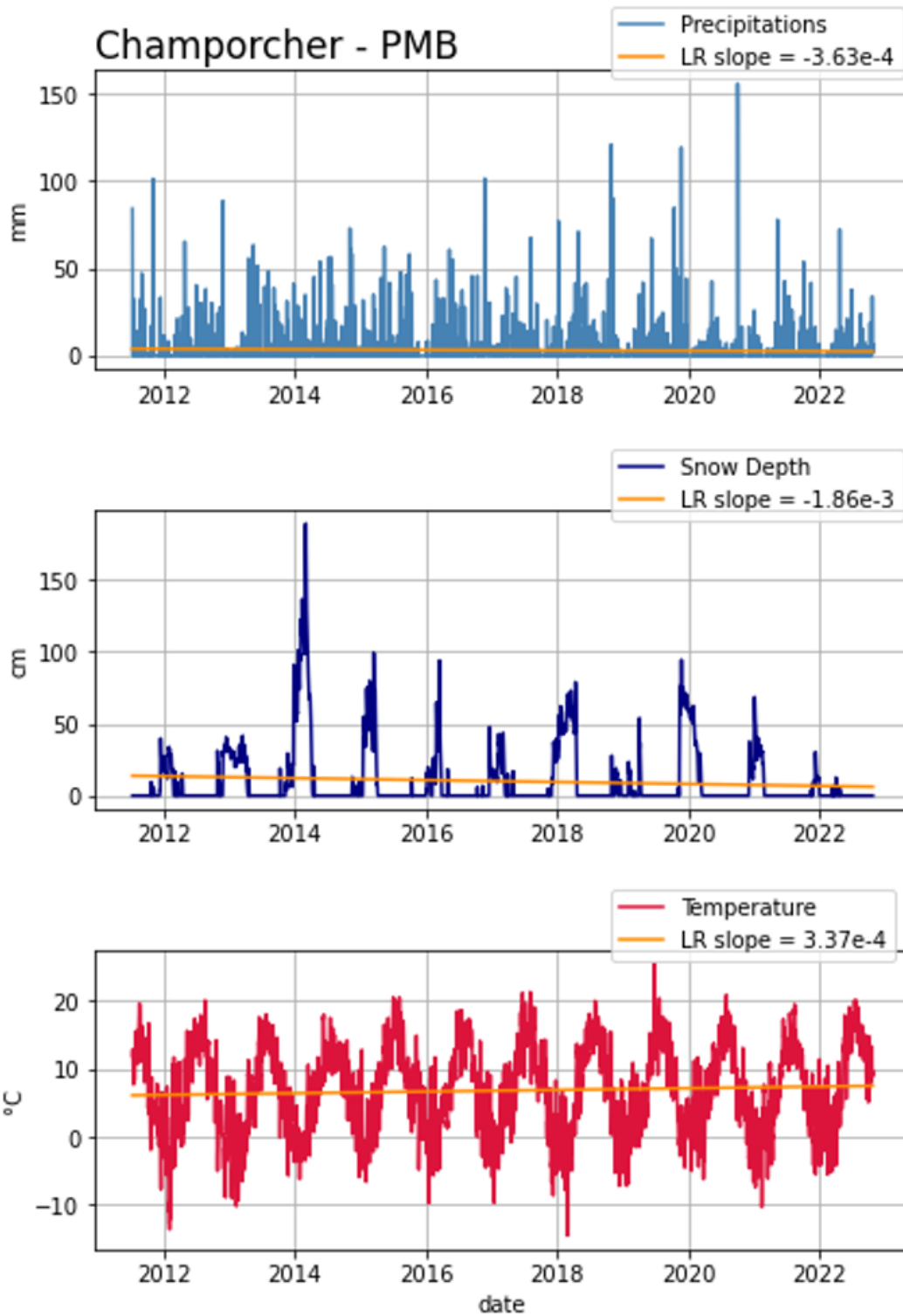


Figure 37. Time series of Precipitations, Snow Depth and Temperature of Champorcher - Petit Mont Blanc weather station.

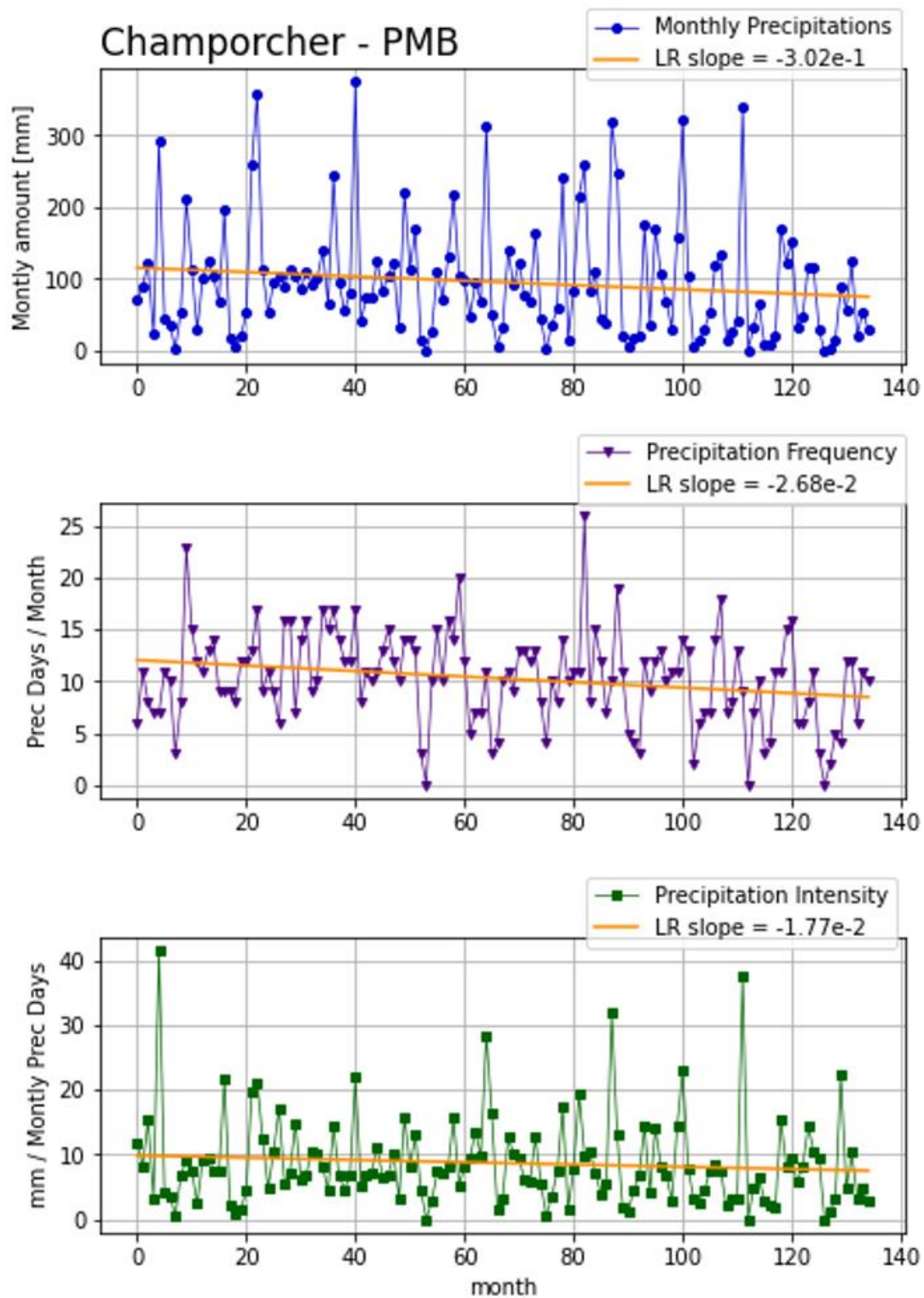


Figure 38. Time series of Monthly Precipitation, Precipitation Frequency and Precipitation Intensity of Champorcher - Petit Mont Blanc weather station.

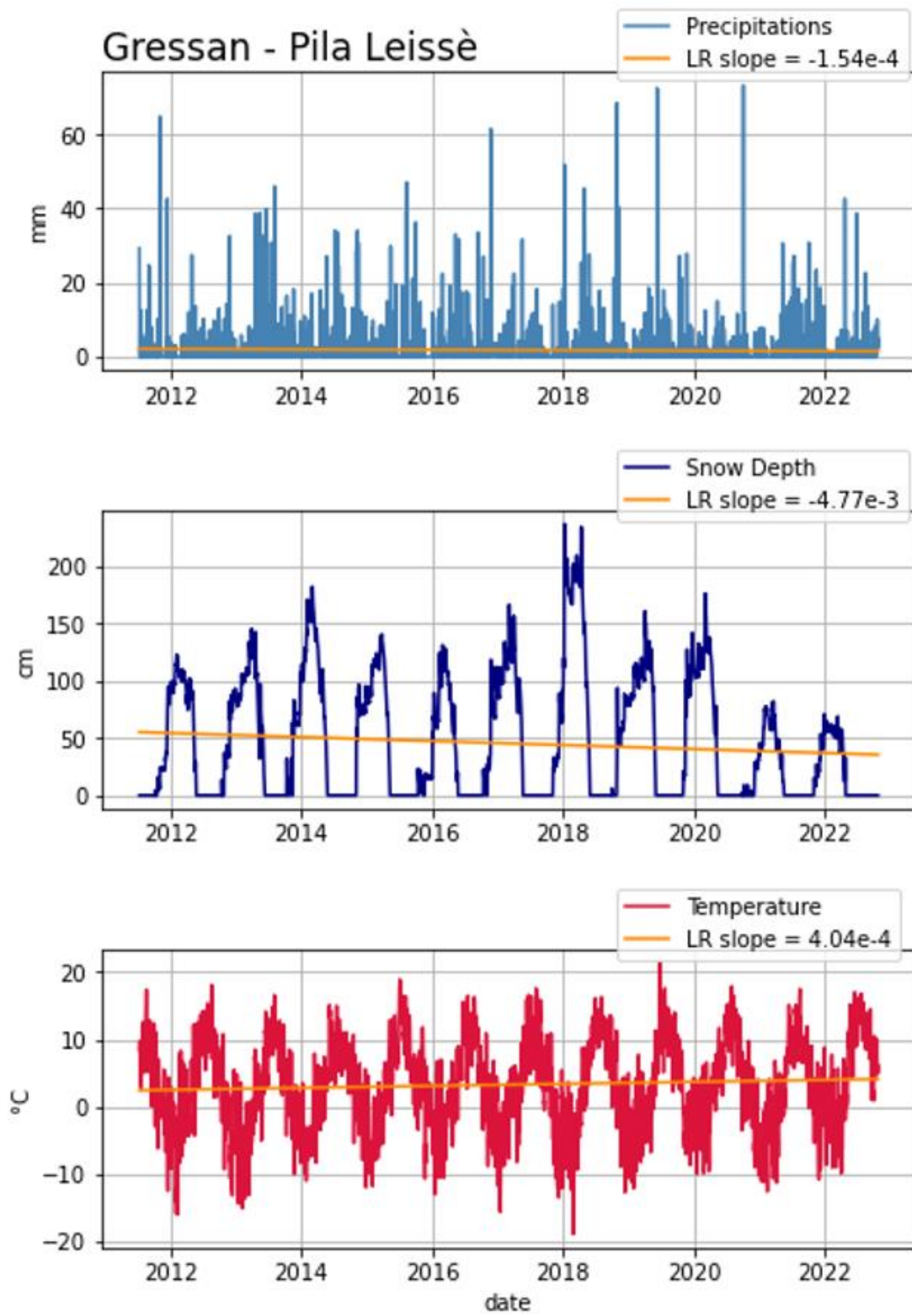


Figure 39. Time series of Precipitations, Snow Depth and Temperature of Gressan - Pila Leissè weather station.

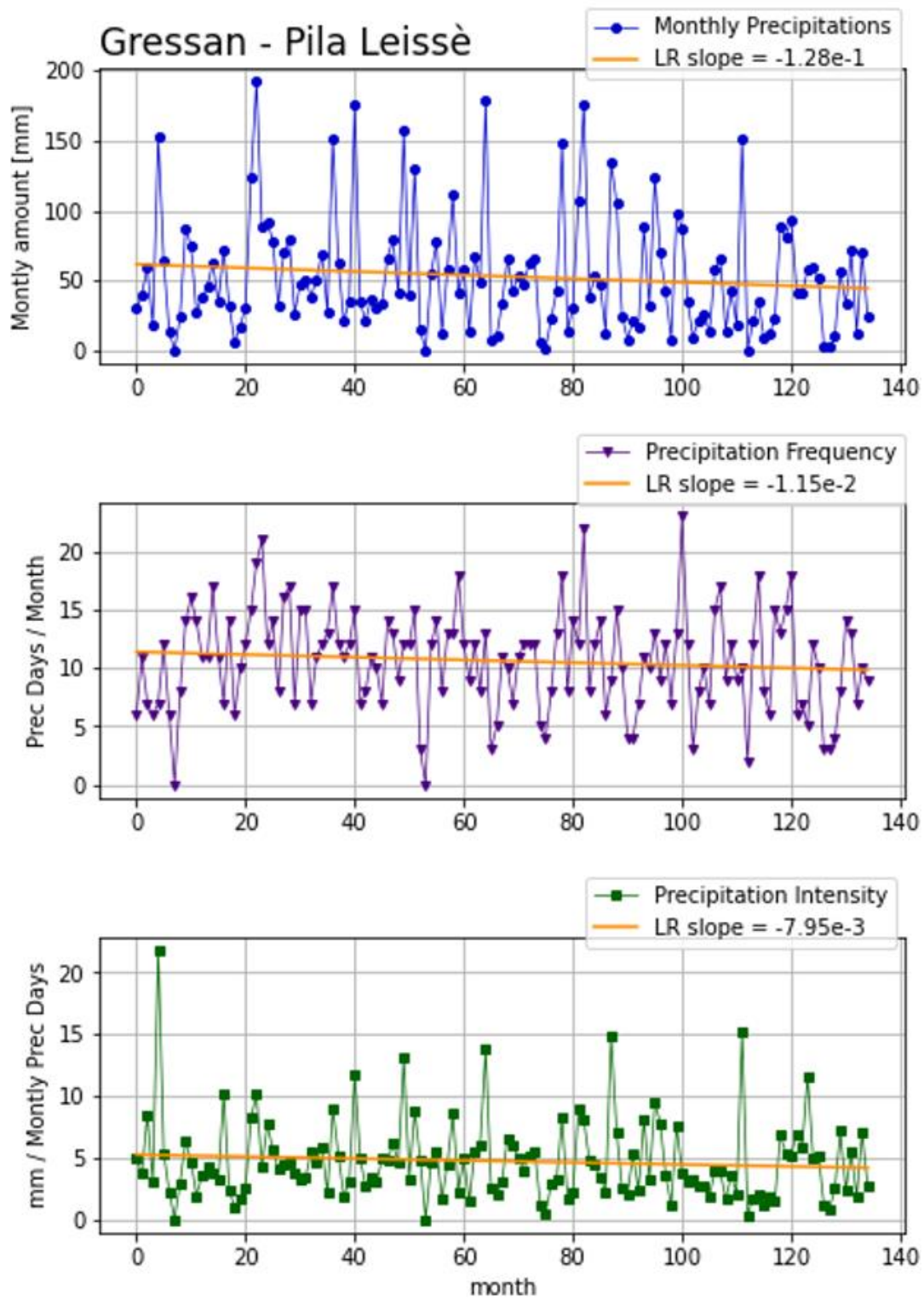


Figure 40. Time series of Monthly Precipitation, Precipitation Frequency and Precipitation Intensity of Gressan - Pila Leissè weather station.

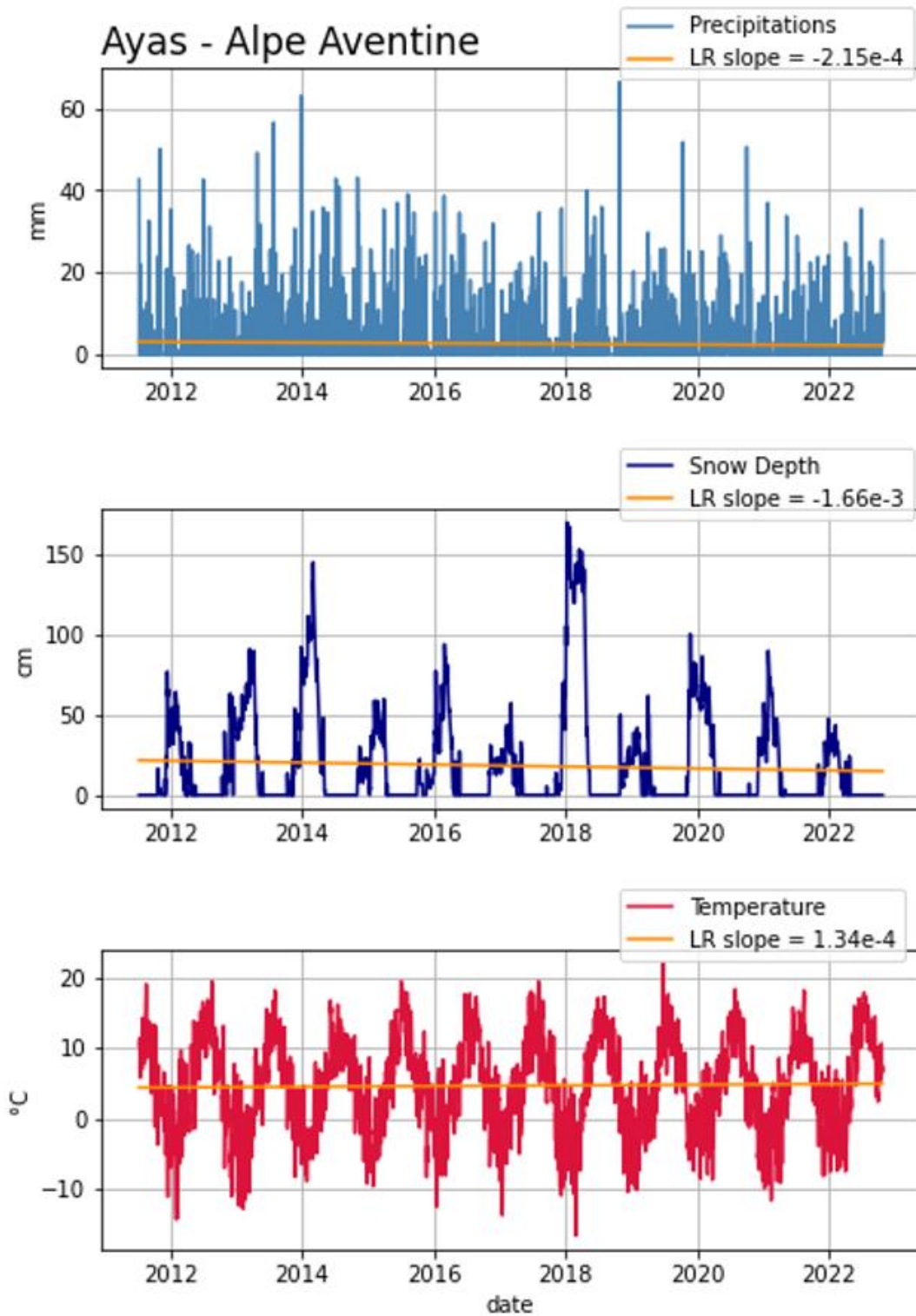


Figure 41. Time series of Precipitations, Snow Depth and Temperature of Ayas - Alpe Aventine weather station.

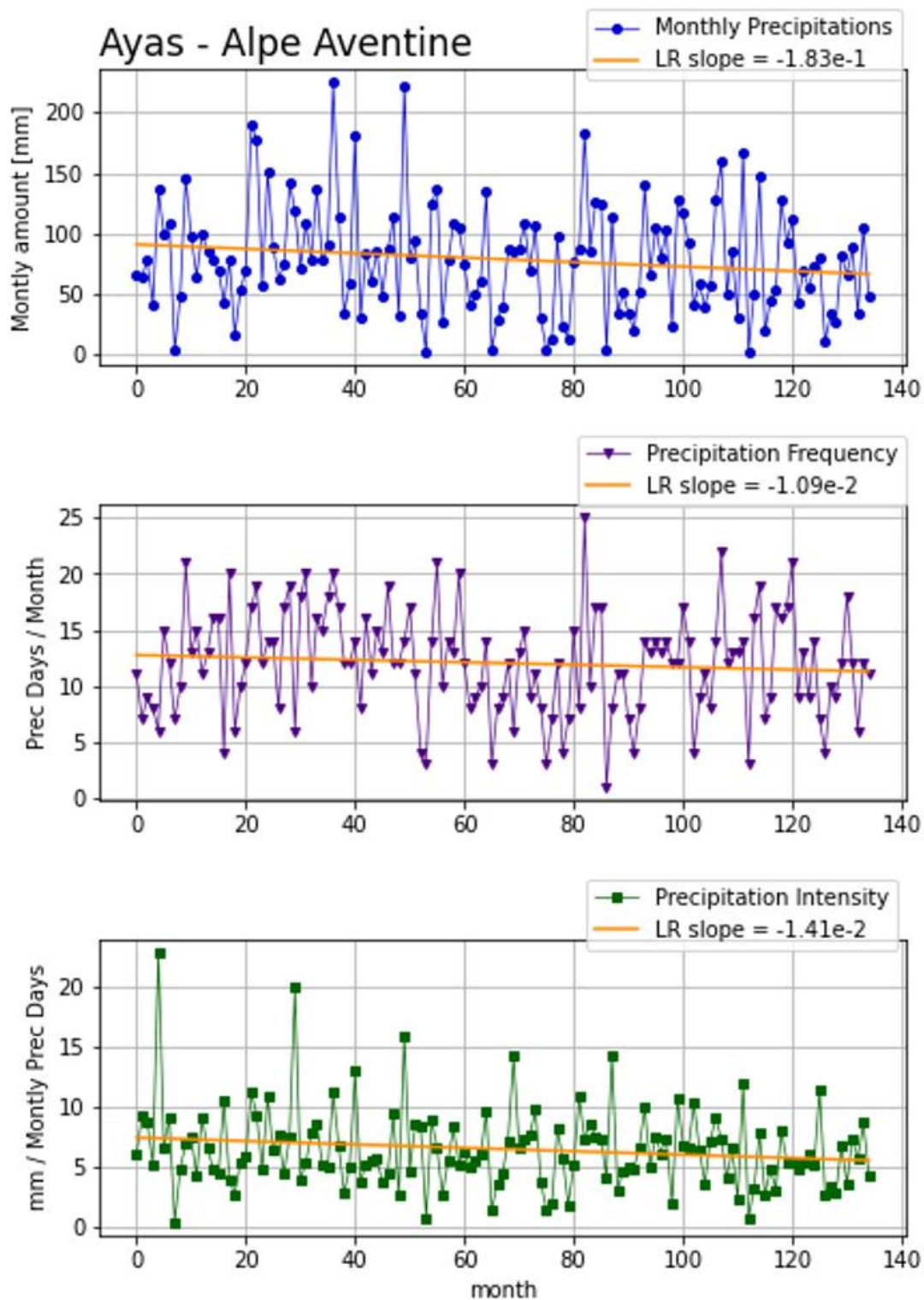


Figure 42. Time series of Monthly Precipitation, Precipitation Frequency and Precipitation Intensity of Ayas - Alpe Aventine weather station.

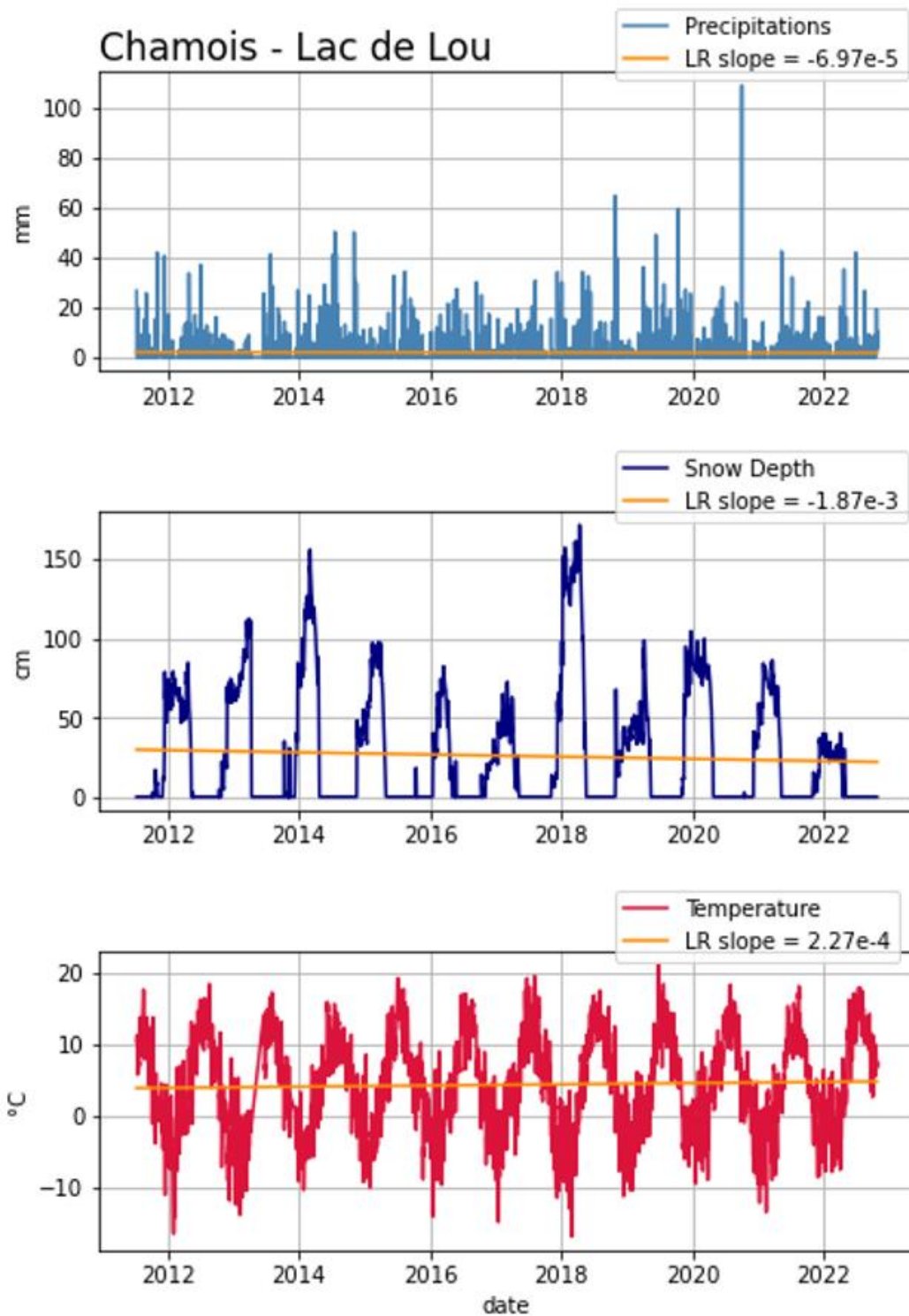


Figure 43. Time series of Precipitations, Snow Depth and Temperature of Chamois - Lac de Lou weather station.

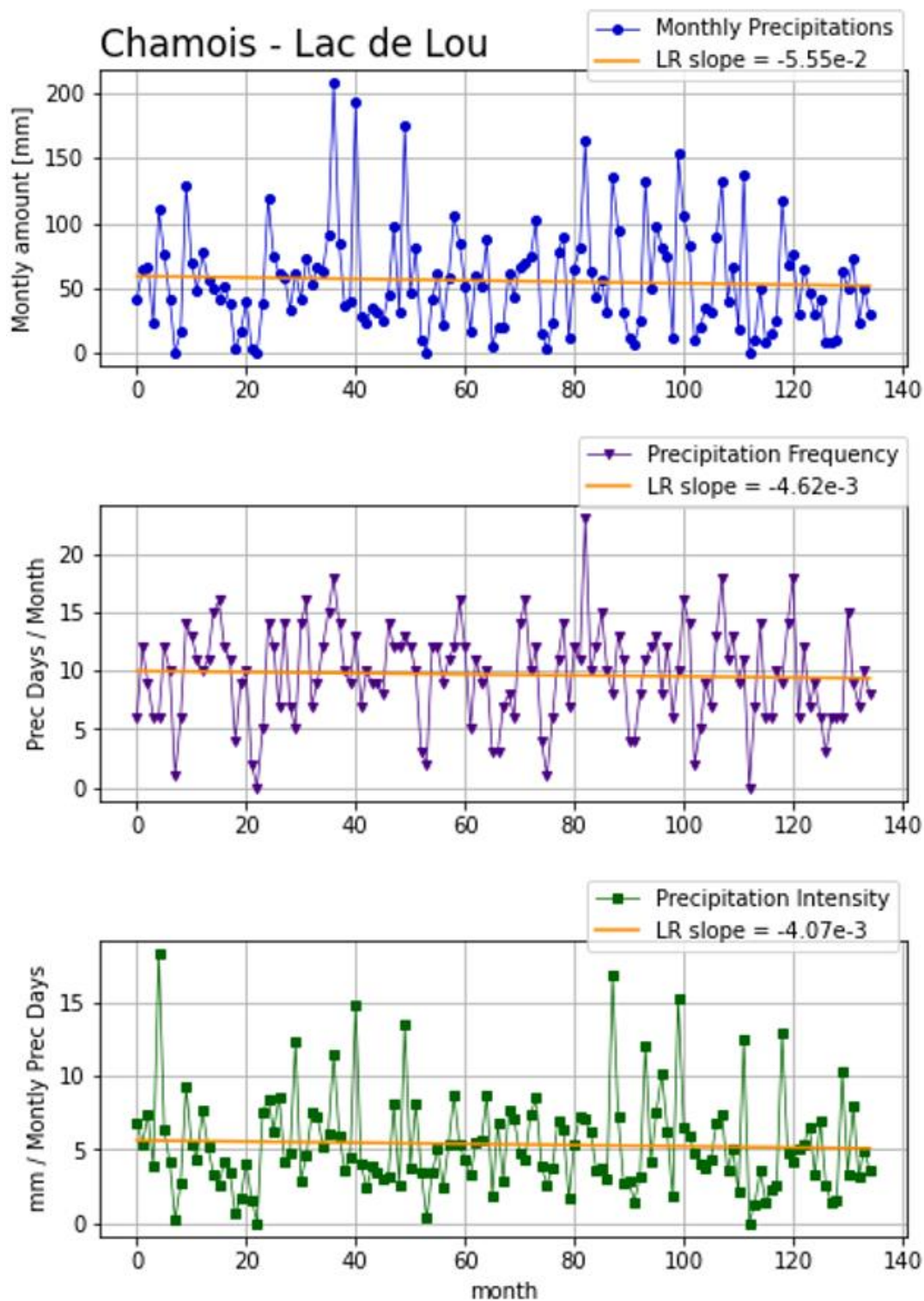


Figure 44. Time series of Monthly Precipitation, Precipitation Frequency and Precipitation Intensity of Chamois - Lac de Lou weather station.

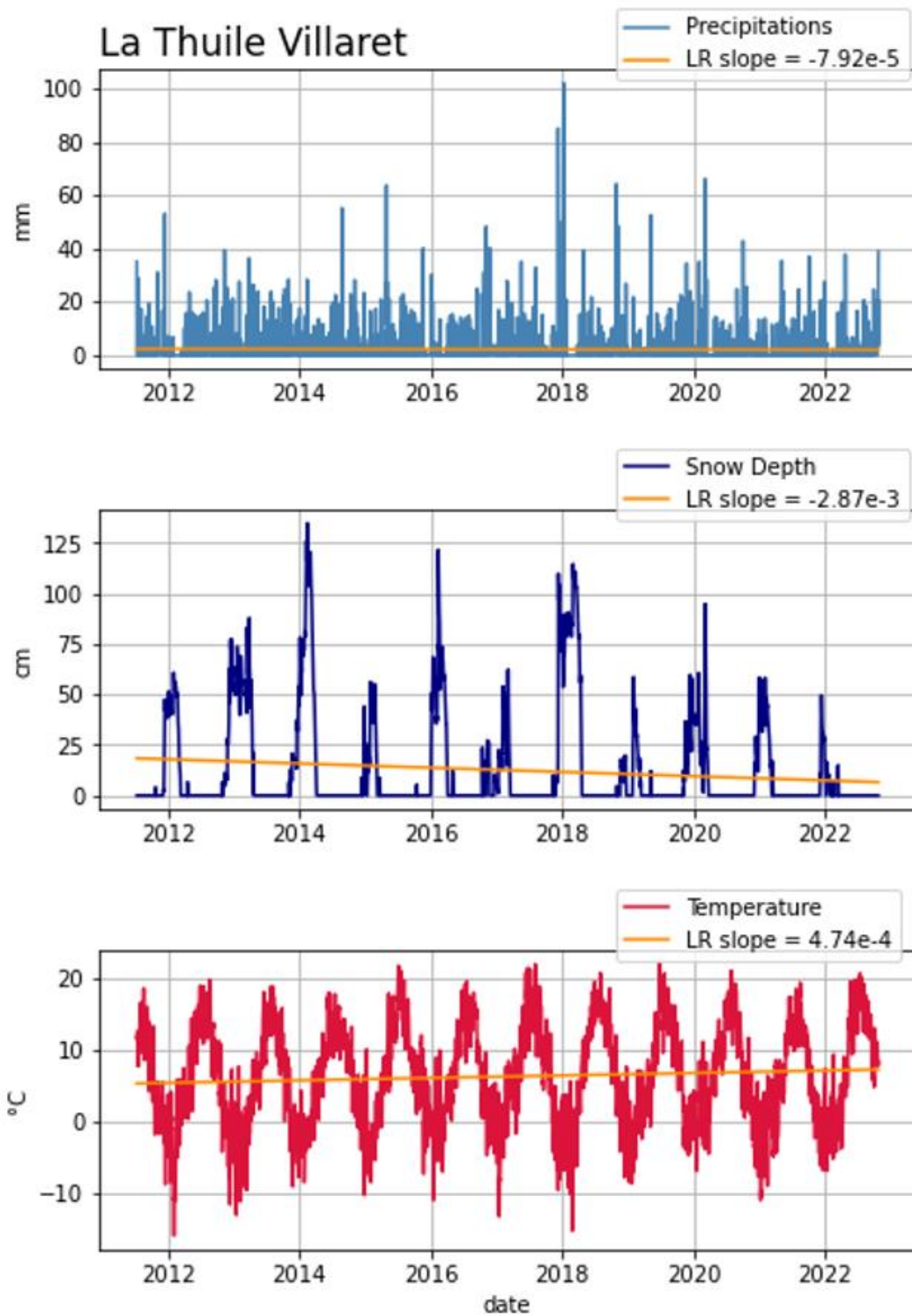


Figure 45. Time series of Precipitations, Snow Depth and Temperature of La Thuile - Villaret weather station.

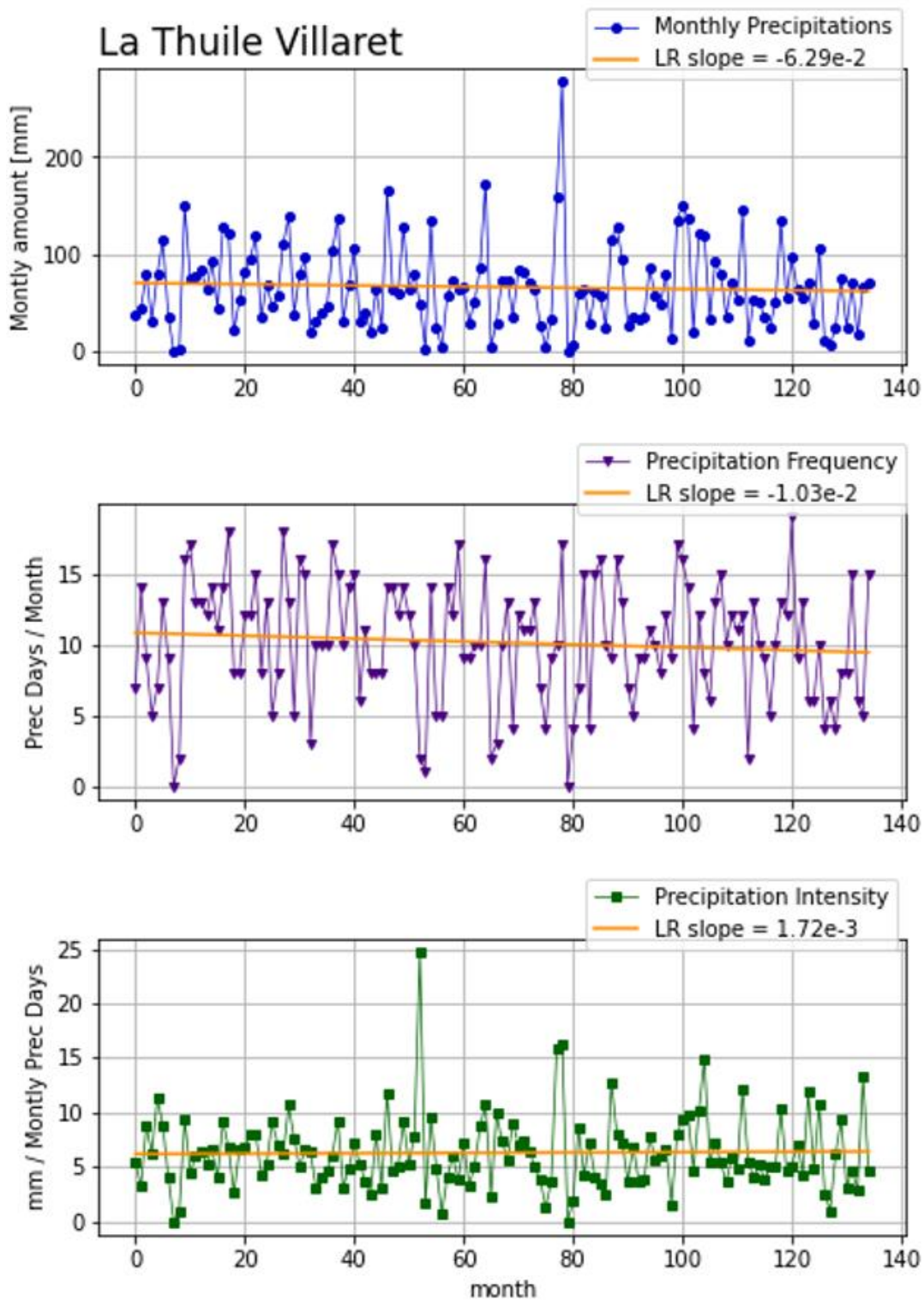


Figure 46. Time series of Monthly Precipitation, Precipitation Frequency and Precipitation Intensity of La Thuile - Villaret weather station.

Table 4. Meteorological results summary, positive trend in green and negative trend in red.

	Champorcher - Petit Mont Blanc	Gressan - Pila Leissè	Ayas - Alpe Aventine	Chamois - Lac de Lou	La Thuile - Villaret
Daily Precipitation trend slope	-3.63E-04	-1.54E-04	-2.15E-04	-6.97E-05	-7.92E-05
Average increased/decrea sed Daily precipitation [mm]	-1.50	-0.63	-0.89	-0.29	-0.33
Daily Snow Depth trend slope	-1.86E-03	-4.77E-03	-1.66E-03	-1.87E-03	-2.87E-03
Average increased/decrea sed Dayly Snow Depth [cm]	-7.67	-19.66	-6.84	-7.71	-11.83
Daily Temperature trend slope	3.37E-04	4.04E-04	1.34E-04	2.27E-04	4.74E-04
Average increased/decrea sed Daily Temperature [°C]	1.39	1.67	0.55	0.94	1.95
Monthly Precipitation Frequency slope	-2.68E-02	-1.15E-02	-1.09E-02	-3.62E-03	-1.03E-02
Average increased/decrea sed Rainy Days per Month [days/month]	-3.62	-1.55	-1.47	-0.49	-1.39
Monthly Precipitation Intensity slope	-1.77E-02	-7.95E-03	-1.41E-02	-4.07E-03	1.72E-03
Average increased/decrea sed Monthly Precipitation per Rainy Days [mm/rainy days]	-2.39	-1.07	-1.90	-0.55	0.23

The summarized results from the graphs shown above are summarized in the **Table 4**. For each trend slope value, the average increase or decrease value for the analyzed step is associated. That is, how much that parameter on average increased or decreased from the beginning of the time series to its end after about 11 years.

For the first 3 parameters analyzed: precipitation, snow depth, and temperature, concordant results are obtained for the various weather stations. In fact, in addition to having the same negative trend (precipitation, snow depth) or positive trend (temperature) it has obtained approximately the same order of magnitude for the mean angular coefficients and increments.

These results show the spatial compliance of the evolution of weather conditions during the period analyzed. Precipitation includes both rainfall and snowfall, the generic trend is decreasing. Of course, the trend in seasonal snowpacks attests that there is also a specific decrease in solid precipitation.

With both liquid and solid precipitation decreasing, there is an increase in temperature in the Aosta Valley, evidenced by the rising trends at all weather stations.

Gressan and La Thuile stations witness the largest increase, between 1.5 and 2 °C, which for an 11-year period is definitely a warning increase. Champorcher notes an increase of 1.39 °C while the other two stations remain below the degree.

Considering that the altitudinal temperature gradient is about 0.65 °C/100 m, the average increasing values found may be alarming given the possibility of raising temperatures at higher altitudes where the permanent cryosphere could previously preserve itself. An additional 1.95 °C would mean raising generally the average thermal zero by about 300 meters.

In addition to the described parameters, rainfall frequencies and intensities are also analyzed. In all cases there is an average decrease in rainy days per month during the interval. In the case of intensity, however, they are all decreasing except for La Thuile station. This is because since in this area the amount of rainfall is not so lossy compared to the others (LR slope = -7.92E-05) and since there is a pronounced decrease in rainfall frequency, there is an increase in precipitation intensity.

Thus, it's worth to notice an approximately concordant climatic and precipitation regime evolution throughout the region, where there are no marked divergences from a local point of view. This evolution is certainly not favorable to the recharge of springs, which are faced with less water amounts with a lower inputs frequency and sometimes intense precipitation that are inefficient in recharging them because they quickly saturate the hydrogeological system. In addition to the snows, which are considered crucial for recharge given their slow but continuous water release, are abruptly decreasing in time.

3.2 Spring analysis results

The time series of the five springs: Alpe Perrot, Cheserod, Mascognaz, Promiod, and Promise, are constructed through continuous monitoring activity since 2011, which allows to gather the hourly discharge data. These five springs were analyzed for continuity of the dataset with respect to the other monitored springs. In fact, the time series, shown in **Fig. 47**, didn't need any reconstruction or interpolation to fill the gaps. The spring flows are then transformed from hourly to daily time steps to reduce the computational cost during statistical analyses including: Mann-Kendal and SDI, and to facilitate comparison with rainfall and climate data from weather stations.

The spring time series illustrated below, besides showing the quantitative discharge amounts, shows also the quality of the signal understood as its temporal variations. These ones are dictated by the seasonal and annual cyclicities that make up the frequency domain of the flow signals. In fact, it can be seen in **Fig. 47** that some springs such as Mascognaz, Promiod and Promise are punctuated by a signal whose maximum amplitude occurs with annual periodicity. While Cheserod shows peaks with lower frequency and thus on multi-year time scales. In contrast, Alpe Perrot has a main oscillation frequency that has a seasonal period.

All five are characterized by periods of recharge and discharge. In springs dominated mainly by snow melting, the two periods cover an annual interval, where recharge almost always occurs in conjunction with the spring or summer months. While the discharge, also called the recession period, begins at the peak and generally ends in winter. In springs such as Alpe Perrot, there can also be two periods of recharge and recession per year, one mainly dictated by snow melting and the other one between late summer and autumn generated by rainfalls.

There are anomalous years as shown by the last segment of the Cheserod spring hydrograph in which recharge and recession last more than a two and a half years. This is certainly driven by the water scarcity of recent years that generate a very long recession period in which no new recharge activities occurs.

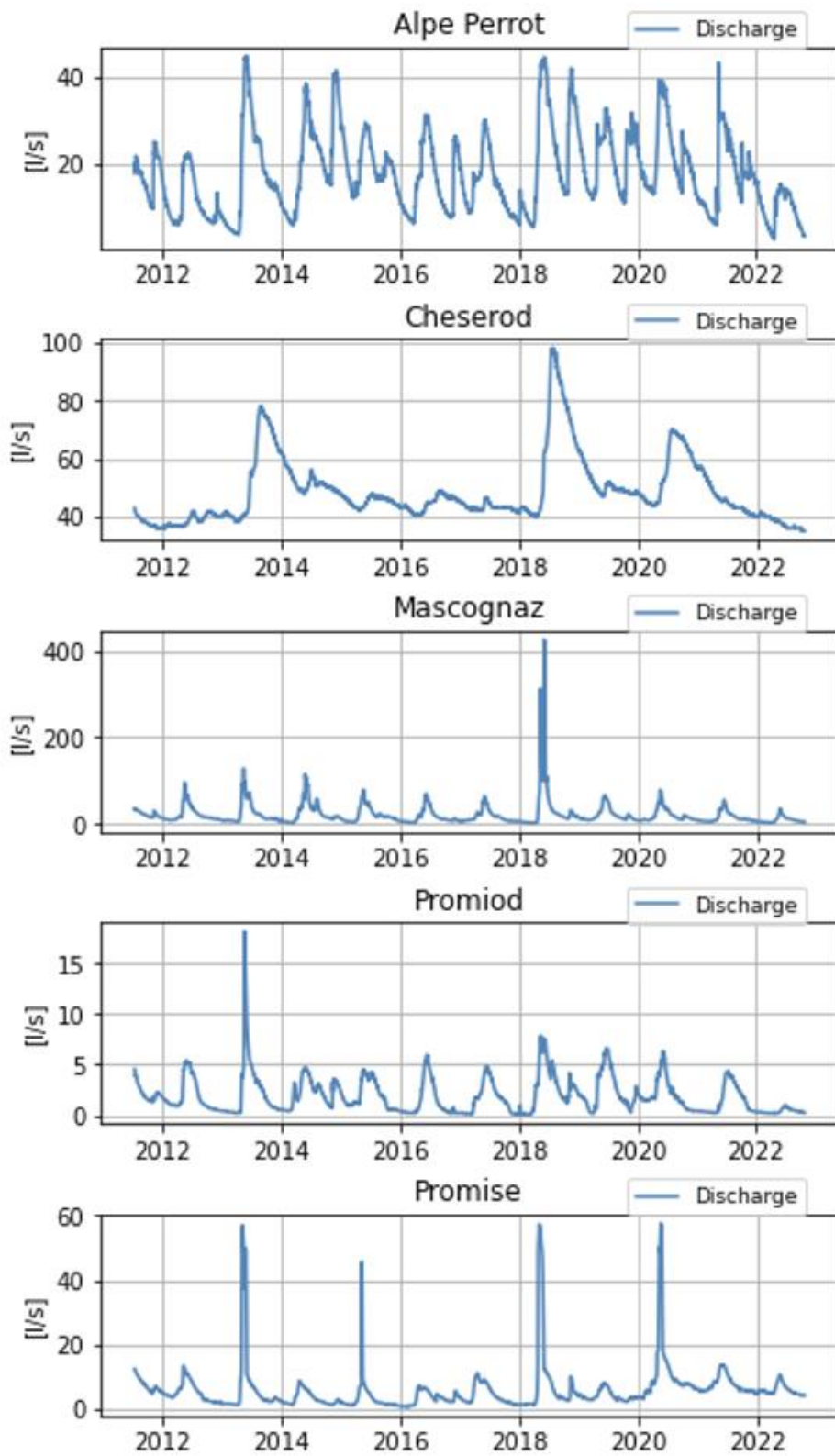


Figure 47. Hydrographs of the five springs analyzed.

It can be seen that in the cases of Cheserod, Mascognaz and Promise there are years with very pronounced peaks compared to the usual, these occur during the years 2013, 2018, 2020. These seasons, in fact, are characterized by heavy snowfall leading to the melting of large amounts of water in the spring season.

In addition to the usual seasonal pattern of springs, there is an increase in lows after 2016 for Alpe Perrot, Cheserod, and Promise springs. This increase at the end of recession, which occurs in late autumn-winter, may indicate an input of water from glacier or permafrost. However, this hypothesis needs to be tested in deep by analyzing precipitation and snowfall data from the same time interval. Therefore, afterwards, more sophisticated analysis will be performed to find a more clear trace of this assumption.

Basically, under generalized weather conditions, where it has been shown approximately the same hydrogeological inputs features for the five springs, it will be easier to note the discordance in recent years between the behaviors of springs that receive inputs from the permanent cryosphere (glaciers and permafrost) from those that do not receive these type of inputs.

As explained in the methods, the characterization of hydrogeologic years, meaning the temporal discretization of the spring hydrograph into sub-periods delineated by the discharge minima, is certainly important for understanding specific aspects of the aquifer in response to hydrologic inputs.

In the following **Table 5**, the hydrogeologic years of all springs are shown, in addition these sub-intervals were divided in turn into recharge and recession periods denoted with the beginning date and the end date of each one.

Table 5. Hydrogeological years of the analyzed springs. Charge and Discharge seasons are also presented.

	Alpe Perrot	Cheserod	Mascognaz	Promiod	Promise
1° h.y. (charge season; discharge season)	12/03/2012 - 25/03/2013 (12/03/2012 - 05/06/2012; 06/06/2012 - 25/03/2013)	17/12/2011 - 26/03/2013 (17/12/2011 - 06/07/2012; 07/07/2012 - 26/03/2013)	19/02/2012 - 15/04/2013 (19/02/2012 - 13/05/2012; 13/05/2012 - 15/04/2013)	29/02/2012 - 19/04/2013 (29/02/2012 - 21/05/2012; 22/05/2012 - 19/04/2013)	09/03/2012 - 12/04/2013 (09/03/2012 - 08/05/2012; 09/05/2012 - 12/04/2013)

2° h.y. (recharge season; discharge season)	26/03/2013 - 14/03/2014 (26/03/2013 - 24/05/2013; 25/05/2013 - 14/03/2014)	27/03/2013 - 23/05/2014 (27/03/2013 - 25/08/2013; 26/08/2013 - 23/05/2014)	15/04/2013 - 16/03/2014 (15/04/2013 - 12/05/2013; 12/05/2013 - 16/03/2014)	20/04/2013 - 08/02/2014 (20/04/2013 - 18/05/2013; 19/05/2013 - 08/02/2014)	13/04/2013 - 09/03/2014 (13/04/2013 - 06/05/2013; 07/05/2013 - 09/03/2014)
3° h.y. (recharge season; discharge season)	15/03/2014 - 13/03/2015 (15/03/2014 - 30/05/2014; 31/05/2014 - 13/03/2015)	24/05/2014 - 02/05/2015 (24/05/2014 - 08/07/2014; 08/07/2014 - 02/05/2015)	16/03/2014 - 15/03/2015 (16/03/2014 - 25/05/2014; 25/05/2014 - 15/03/2015)	09/02/2014 - 13/03/2015 (09/02/2014 - 23/05/2014; 24/05/2014 - 13/03/2015)	10/03/2014 - 15/03/2015 (10/03/2014 - 21/04/2014; 22/04/2014 - 15/03/2015)
4° h.y. (recharge season; discharge season)	14/03/2015 - 20/03/2016 (14/03/2015 - 17/06/2015; 18/06/2015 - 20/03/2016)	03/05/2015 - 09/04/2016 (03/05/2015 - 11/07/2015; 12/07/2015 - 09/04/2016)	15/03/2015 - 24/03/2016 (15/03/2015 - 21/05/2015; 21/05/2015 - 24/03/2016)	14/03/2015 - 17/02/2016 (14/03/2015 - 21/05/2015; 22/05/2015 - 17/02/2016)	16/03/2015 - 26/02/2016 (16/03/2015 - 08/05/2015; 09/05/2015 - 26/02/2016)
5° h.y. (recharge season; discharge season)	21/03/2016 - 09/03/2017 (21/03/2016 - 06/06/2016; 07/06/2016 - 09/03/2017)	10/04/2016 - 13/05/2017 (10/04/2016 - 07/09/2016; 08/09/2016 - 13/05/2017)	24/03/2016 - 13/01/2017 (24/03/2016 - 10/06/2016; 10/06/2016 - 13/01/2017)	18/02/2016 - 11/02/2017 (18/02/2016 - 10/06/2016; 11/06/2016 - 11/02/2017)	26/02/2016 - 10/03/2017 (27/02/2016 - 27/04/2016; 28/04/2016 - 10/03/2017)
6° h.y. (recharge season; discharge season)	10/03/2017 - 24/03/2018 (10/03/2017 - 01/06/2017; 02/06/2017 - 24/03/2018)	14/05/2017 - 12/04/2018 (14/05/2017 - 07/06/2017; 08/06/2017 - 12/04/2018)	13/01/2017 - 12/04/2018 (13/01/2017 - 01/06/2017; 01/06/2017 - 12/04/2018)	12/02/2017 - 17/02/2018 (12/02/2017 - 12/06/2017; 13/06/2017 - 17/02/2018)	11/03/2017 - 05/04/2018 (11/03/2017 - 20/04/2017; 21/04/2017 - 05/04/2018)
7° h.y. (recharge season; discharge season)	25/03/2018 - 31/03/2019 (25/03/2018 - 04/06/2018; 05/06/2018 - 31/03/2019)	13/04/2018 - 06/06/2019 (13/04/2018 - 23/07/2018; 24/07/2018 - 06/06/2019)	12/04/2018 - 06/03/2019 (12/04/2018 - 01/06/2018; 01/06/2018 - 06/03/2019)	18/02/2018 - 31/03/2019 (18/02/2018 - 11/05/2018; 12/05/2018 - 31/03/2019)	05/04/2018 - 02/04/2019 (06/04/2018 - 02/05/2018; 03/05/2018 - 02/04/2019)

8° h.y. (recharge season; discharge season)	31/03/2019 - 13/10/2019 (31/03/2019 - 18/06/2019; 18/06/2019 - 13/10/2019)	06/06/2019 - 15/04/2020 (06/06/2019 - 07/07/2019; 07/07/2019 - 15/04/2020)	06/03/2019 - 17/01/2020 (06/03/2019 - 15/06/2019; 15/06/2019 - 17/01/2020)	31/03/2019 - 23/11/2019 (31/03/2019 - 02/07/2019; 02/07/2019 - 23/11/2019)	02/04/2019 - 01/10/2019 (02/04/2019 - 04/06/2019; 04/06/2019 - 01/10/2019)
9° h.y. (recharge season; discharge season)	09/04/2020 - 30/04/2021 (09/04/2020 - 15/05/2020; 15/05/2020 - 30/04/2021)	15/04/2020 - 24/10/2022 (15/04/2020 - 02/08/2020; 02/08/2020 - 24/10/2022)	17/01/2020 - 01/04/2021 (17/01/2020 - 15/05/2020; 15/05/2020 - 01/04/2021)	23/11/2019 - 02/04/2021 (23/11/2019 - 06/06/2020; 06/06/2020 - 02/04/2021)	01/10/2019 - 20/02/2021 (01/10/2019 - 19/05/2020; 19/05/2020 - 20/02/2021)
10° h.y. (recharge season; discharge season)	30/04/2021 - 22/04/2022 (30/04/2021 - 12/05/2021; 12/05/2021 - 22/04/2022)		01/04/2021 - 10/04/2022 (01/04/2021 - 11/06/2021; 11/06/2021 - 10/04/2022)	02/03/2021 - 18/04/2022 (02/03/2021 - 13/07/2021; 13/07/2021 - 18/04/2022)	20/02/2021 - 25/12/2021 (20/02/2021 - 06/06/2021; 19/05/2021 - 25/12/2021)

The results depicted in the table are summarized in the graphs below, which naturally enhance their interpretation and understanding.

The hydrogeological year trends of Alpe Perrot are displayed in **Fig. 48**, it shows a very stable behavior for the first 7 years, that is during the period from 12/03/2012 until 31/03/2019. In this interval, the hydrogeological years are very close to the calendar years, meaning that there is a regularity in the period of aquifer recharge and recession. On the contrary, the last three hydrogeological years, between 31/03/2019 and 22/04/2021, it shows anomalous variations both in terms of the hydrogeological year, which finds an unusual shortening in 2019, and in terms of the recharge period, which decreases significantly to a very small time span of 12 days.

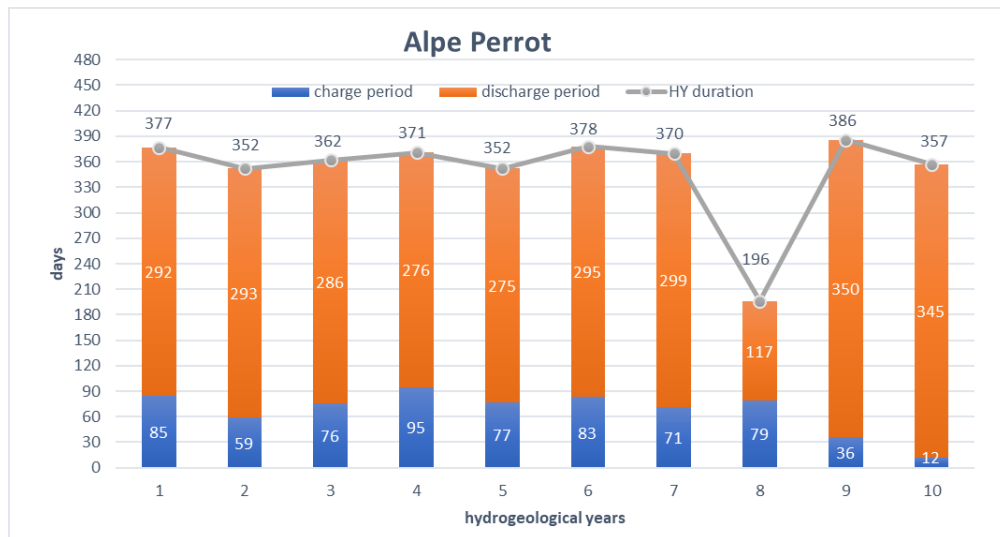


Figure 48. Alpe Perrot hydrogeological years duration series (grey dots and lines), discretized in recharge period (blue bars) and discharge period (orange bars).

Cheserod trends are shown in **Fig. 49**. Compared to Alpe Perrot in this case there is greater discontinuity in terms of both hydrogeological years and periods of recharge and recession. In fact, there are years with a full-bodied and prolonged recharge as in conjunction with the 1st, 2nd and 5th years that bring considerable water inputs and very short recharge periods as in the 3rd and 8th years. Clearly, the anomaly of the last year emerges, where there is a recession period that lasts for 813 days, that is from 02/08/2020 to where the data were retrieved on 24/10/2022. This information is indicative of the water scarcity of the last two years that result in a progressive depletion of the Cheserod aquifer that does not receive sufficient inputs to be able to begin a recharge phase.

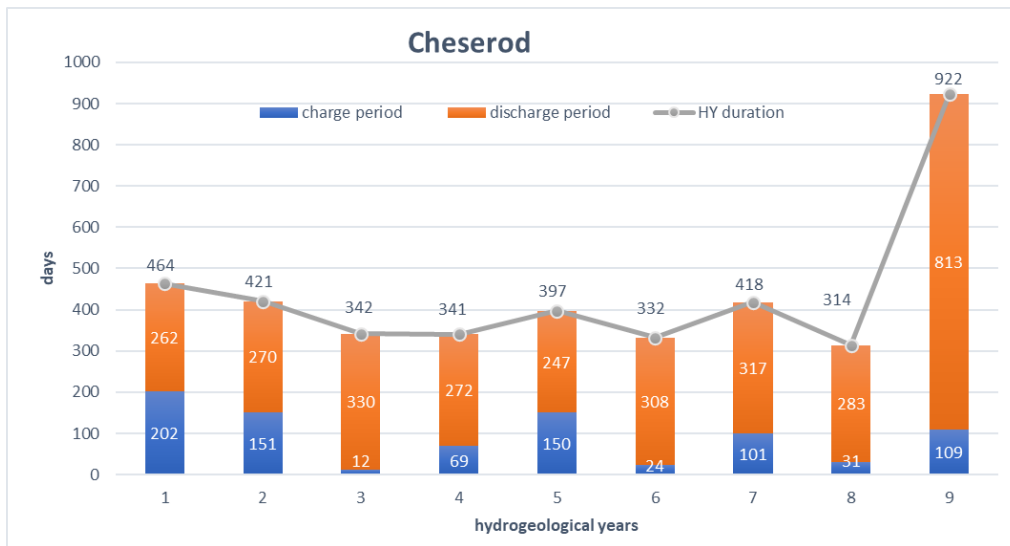


Figure 49. Cheserod hydrogeological years duration series (grey dots and lines), discretized in recharge period (blue bars) and discharge period (orange bars).

Mascognaz spring, on the other hand, shows a kind of regularity of hydrogeological periods throughout the studied interval. Shortenings and lengthening of the hydrogeological year and the two phases are noted, despite that in recent years there are no major anomalies as noted in Alpe Perrot and Cheserod.

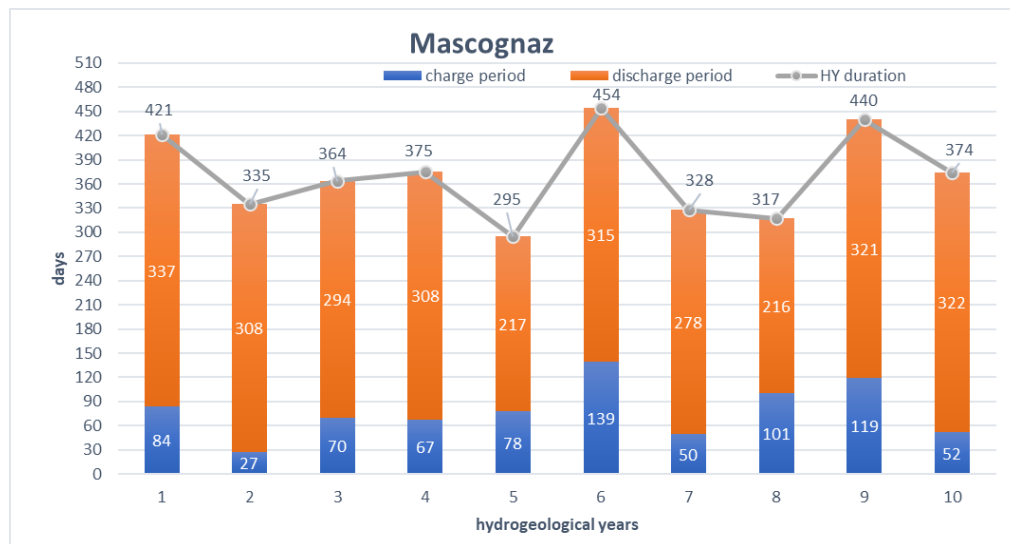


Figure 50. Mascognaz hydrogeological years duration series (grey dots and lines), discretized in recharge period (blue bars) and discharge period (orange bars).

The Promiod spring (**Fig. 51**), does not appear to be a constant spring in the recharge and recession phases, this due to the very small spring flow regimes, indicating a reduced recharge area with a rapid spring response to infiltrative phenomena.

Having said that, it also seems to deviate from the time average of hydrogeological years in concurrence with the last three years ranging from the period 31/03/2019 to 18/04/2022. Above all, the 8th year shows a shortening dictated by the preventive start of recharge in the following year (9th) that extends to 196 days. The last year seems to return to steady state with a longer than average recharge period.

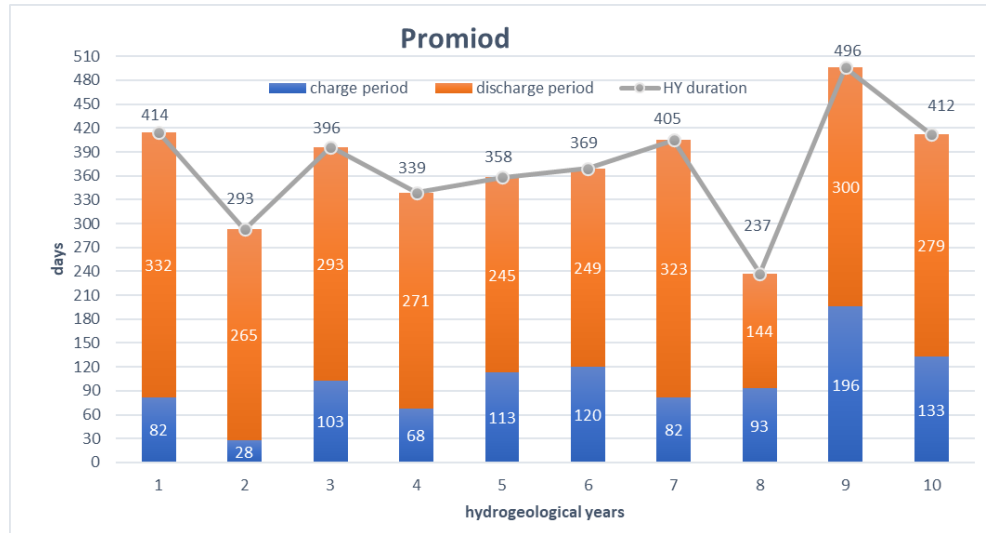


Figure 51. Promiod hydrogeological years duration series (grey dots and lines), discretized in recharge period (blue bars) and discharge period (orange bars).

The hydrogeologic years of Promise, displayed in **Fig. 52**, also show similar behaviors to those of Promiod regarding the last three years. In this case, the first 7 years the recharge and recession phases are more constant than the spring described above. While in the last three, like Promiod, there is a shortening of the 8th year with the recharge of the next one anticipating the 9th year extending to a year and a half. The last year returns on average with a more pronounced reloading phase.

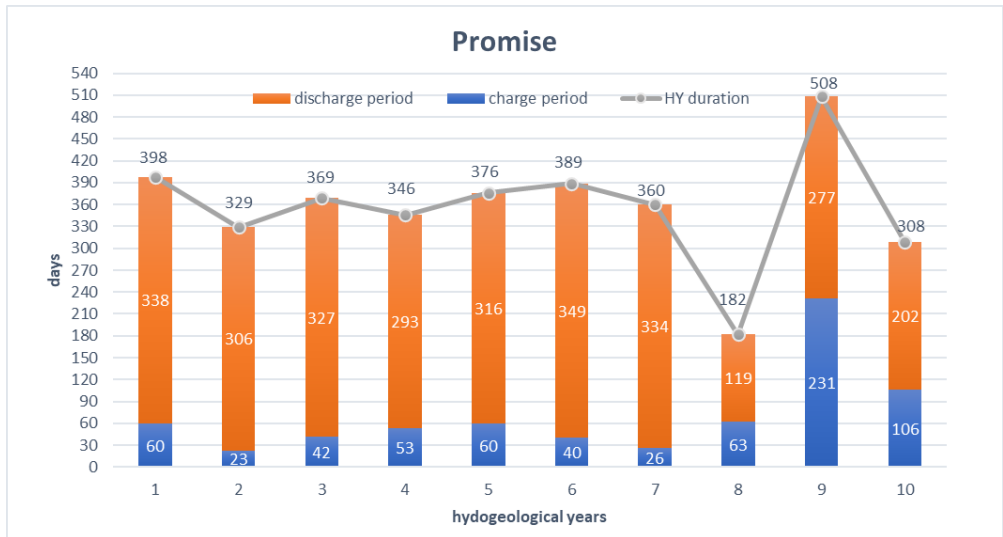


Figure 52. Promise hydrogeological years duration series (grey dots and lines), discretized in recharge period (blue bars) and discharge period (orange bars).

Generally, the last period analyzed show anomalous recharge and recession behaviors for most of all the studied springs. The only spring that does not show major variations for this period is Mascognaz, which maintains a certain regularity of the two phases.

The variations in recent years may be due to a number of causes that unbalance the seasonality and quantity of water supplies. In detail, a decrease in both solid and liquid precipitation and reduced snow cover go to destabilize the rhythms with which the spring reacts. In addition, the eventual contribution of the permanent cryosphere for some springs modifies the summer recession by turning it into a recharge phase.

To gain a better understanding of the variation in the volumes discharged and remaining in the various aquifers, the recessive analysis explained in Methods Chapter is carried out below. That is, the study of the phase of the hydrograph from the peak to the time of lowest discharge at the end of the hydrogeological year. The interpolation of this branch is carried out by the Bussinesq and Maillet methods shown in paragraph 2.4.1, the parameters listed then later in tables as the aquifer volumes of the beginning of recession and the end of recession are derived by choosing the method that best interpolates the curve of each spring.

In fact, only two examples of recessions from two different years of the same spring will be shown in **Fig. 53-57**. In **Fig. 53-57** it will also be displayed Maillet and Bussinesq functions that interpolate the recession showing the RMSE.

Once the model is chosen, the interpolation of the recession curve is done for all hydrogeological years of each spring. In fact, the parameters that are derived with the recession analysis for each year are shown in the **Table 6-10**, so that it can be understood how some characteristics of the water resource vary over time.

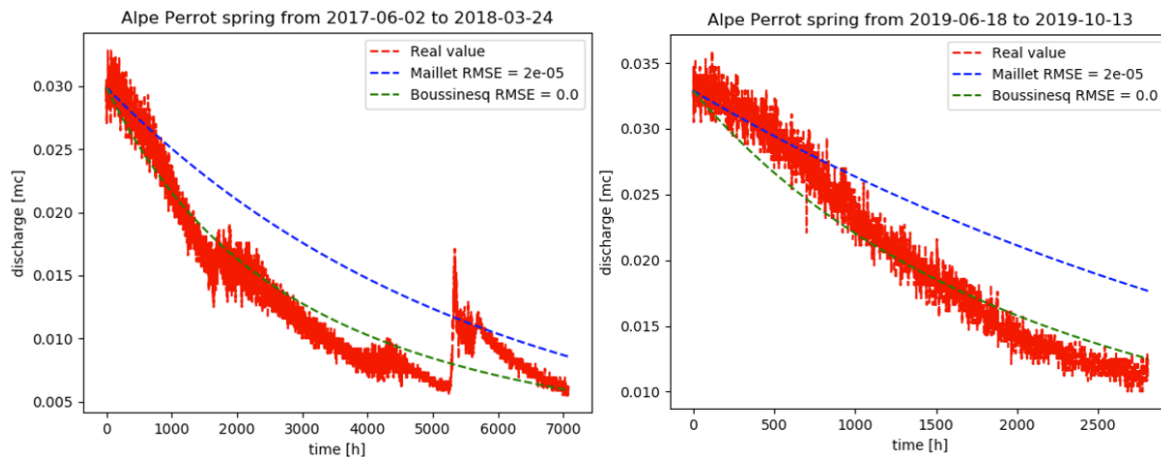


Figure 53. Alpe Perrot recession with Bussinesq and Maillet interpolation (SOURCE).

Table 6. Alpe Perrot recession parameters summarized for every hydrogeological year.

ALPE PERROT (method: Bussinesq)	1° h.y.	2° h.y.	3° h.y.	4° h.y.	5° h.y.	6° h.y.	7° h.y.	8° h.y.	9° h.y.	10° h.y.	<i>m.u.</i>
Flow rate at the beginning of the recession (Q0)	0.0227	0.043	0.0378	0.0282	0.0305	0.0299	0.0436	0.0329	0.0384	0.0333	<i>mc/s</i>
Flow rate at the end of the recession (Qt)	0.0043	0.0059	0.0134	0.0069	0.0104	0.0059	0.0125	0.0125	0.0062	0.0028	<i>mc/s</i>
Groundwater volume at the beginning of the recession (W0)	441341	640456	1374513	658236	1017080	609100	1298203	534398	780028	405377	<i>mc</i>
Groundwater volume discharged at the end of the recession (Wd)	249255	403220	556132	332638	423168	338530	603091	204999	466598	287829	<i>mc</i>
Remained Groundwater volume at the end of the recession (Wt)	192086	237236	818381	325598	593912	270570	695112	329399	313430	117548	<i>mc</i>
Recession interval (dt)	292	293	286	276	275	295	299	117	350	345	<i>Day</i>
Recession coefficient (α)	0.0044	0.0058	0.0024	0.0037	0.0026	0.0042	0.0029	0.0053	0.0043	0.0071	
Renewal rate (Rr)	56.5	63.0	40.5	50.5	41.6	55.6	46.5	38.4	59.8	71.0	<i>%</i>
Renewal time rate (Trin)	1.8	1.6	2.5	2.0	2.4	1.8	2.2	2.6	1.7	1.4	<i>Year</i>

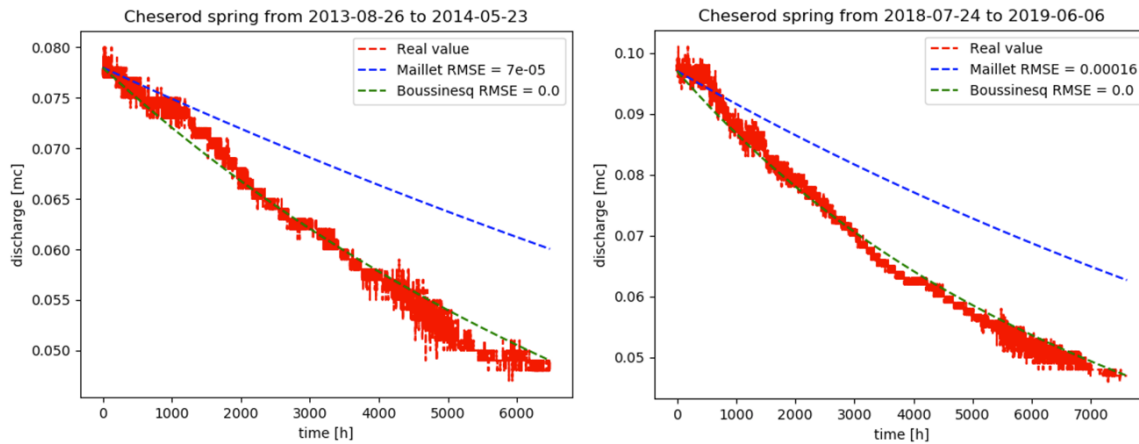


Figure 54. Cheserod recession with Boussinesq and Maillet interpolation (SOURCE).

Table 7. Cheserod recession parameters summarized for every hydrogeological year.

CHESEROD (method: Boussinesq)	1° h.y.	2° h.y.	3° h.y.	4° h.y.	5° h.y.	6° h.y.	7° h.y.	8° h.y.	9° h.y.	<i>m.u.</i>
Flow rate at the beginning of the recession (Q0)	0.041	0.078	0.056	0.047	0.049	0.049	0.046	0.097	0.052	<i>mc/s</i>
Flow rate at the end of the recession (Qt)	0.038	0.049	0.043	0.041	0.042	0.042	0.04	0.047	0.044	<i>mc/s</i>
Groundwater volume at the beginning of the recession (W0)	23967330	6953467	10211730	15628767	13051101	16912217	6084956	14595283	11994735	<i>mc</i>
Groundwater volume discharged at the end of the recession (Wd)	893509	1442191	1263451	1031629	968129	1141493	1849302	1169575	3451937	<i>mc</i>
Remained Groundwater volume at the end of the recession (Wt)	23073821	5511276	8948279	14597138	12082972	15770724	4235654	13425708	8542798	<i>mc</i>
Recession interval (dt)	262	270	298	272	247	308	317	283	813	<i>Day</i>
Recession coefficient (α)	0.0001	0.001	0.0005	0.0003	0.0003	0.0002	0.0014	0.0003	0.0005	
Renewal rate (Rr)	3.7	20.7	12.4	6.6	7.4	6.7	30.4	8.0	28.8	<i>%</i>
Renewal time rate (Trin)	26.8	4.8	8.1	15.1	13.5	14.8	3.3	12.5	3.5	<i>Year</i>

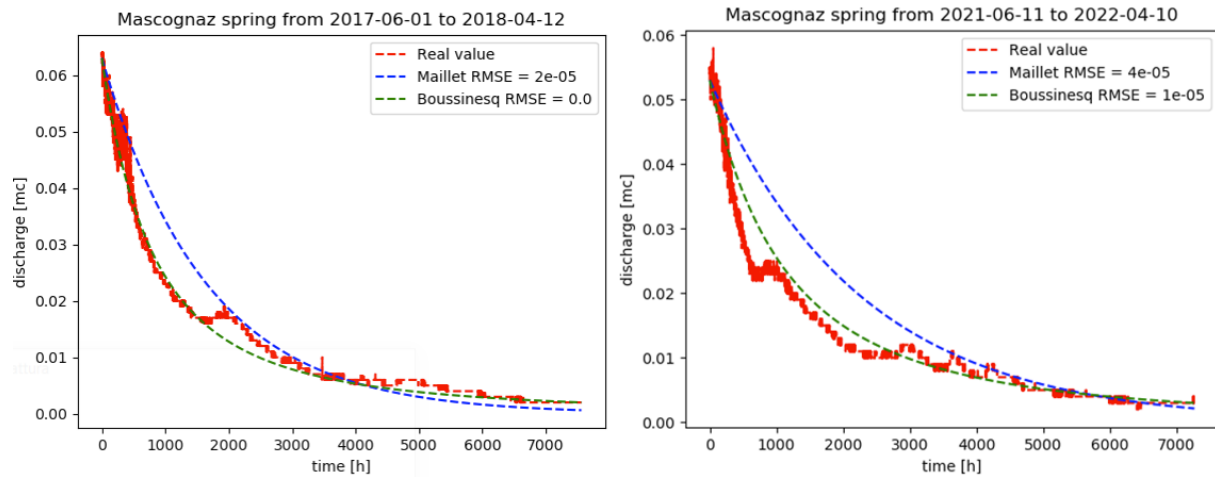


Figure 55. Mascognaz recession with Boussinesq and Maillet interpolation (SOURCE).

Table 8. Mascognaz recession parameters summarized for every hydrogeological year.

MASCOGNAZ (method: Boussinesq)	1° h.y.	2° h.y.	3° h.y.	4° h.y.	5° h.y.	6° h.y.	7° h.y.	8° h.y.	9° h.y.	10° h.y.	<i>m.u.</i>
Flow rate at the beginning of the recession (Q0)	0.092	0.117	0.108	0.077	0.066	0.063	0.426	0.063	0.081	0.053	<i>mc/s</i>
Flow rate at the end of the recession (Qt)	0.005	0.003	0.004	0.003	0.004	0.002	0.008	0.007	0.005	0.003	<i>mc/s</i>
Groundwater volume at the beginning of the recession (W0)	814327	593615	651559	503922	404119	371732	1624862	587866	742659	433163	<i>mc</i>
Groundwater volume discharged at the end of the recession (Wd)	624486	498561	526167	404455	304632	305499	1402195	391910	558144	330107	<i>mc</i>
Remained Groundwater volume at the end of the recession (Wt)	189841	95054	125392	99467	99487	66233	222667	195956	184515	103056	<i>mc</i>
Recession interval (dt)	337	308	293	308	217	315	278	216	321	303	<i>Day</i>
Recession coefficient (α)	0.0098	0.017	0.0143	0.0132	0.0141	0.0146	0.0227	0.0093	0.0094	0.0106	
Renewal rate (Rr)	76.7	84.0	80.8	80.3	75.4	82.2	86.3	66.7	75.2	76.2	<i>%</i>
Renewal time rate (Trin)	1.3	1.2	1.2	1.2	1.3	1.2	1.2	1.5	1.3	1.3	<i>Year</i>

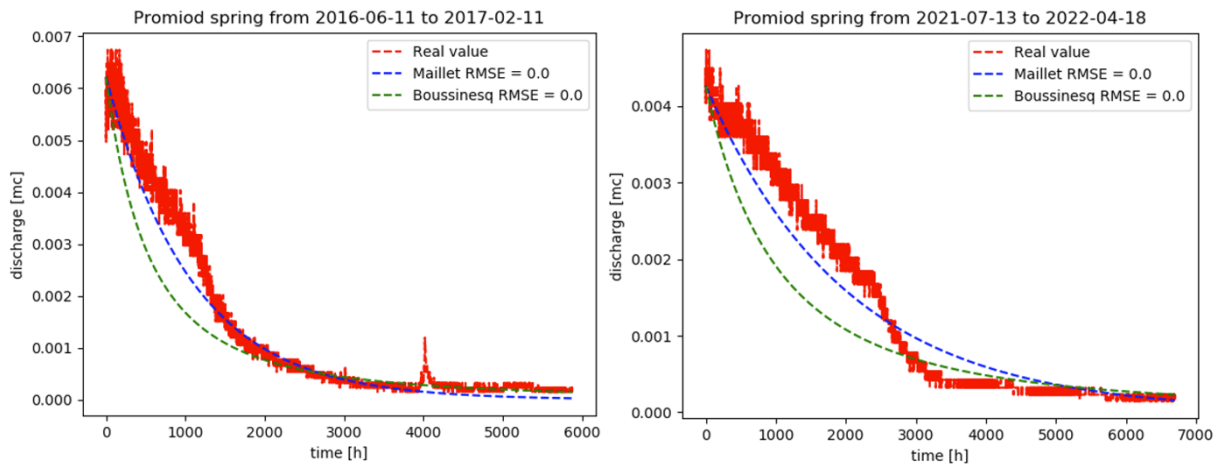


Figure 56. Promiod recession with Bussinesq and Maillet interpolation (SOURCE).

Table 9. Promiod recession parameters summarized for every hydrogeological year.

PROMIOD (method: Maillet)	1° h.y.	2° h.y.	3° h.y.	4° h.y.	5° h.y.	6° h.y.	7° h.y.	8° h.y.	9° h.y.	10° h.y.	<i>m.u.</i>
Flow rate at the beginning of the recession (Q0)	0.0055	0.0111	0.005	0.0045	0.0062	0.0045	0.0084	0.0067	0.0067	0.0043	<i>mc/s</i>
Flow rate at the end of the recession (Qt)	0.0002	0.0004	0.0011	0.0002	0.0001	0.0001	0.0001	0.0003	0.0002	0.0002	<i>mc/s</i>
Groundwater volume at the beginning of the recession (W0)	40432	59327	107016	30765	24199	14993	36156	23457	39587	31094	<i>mc</i>
Groundwater volume discharged at the end of the recession (Wd)	32130	47747	57813	23805	20440	12980	31324	18330	32275	23872	<i>mc</i>
Remained Groundwater volume at the end of the recession (Wt)	8302	11580	49203	6960	3759	2013	4832	5127	7312	7222	<i>mc</i>
Recession interval (dt)	332	255	293	271	245	249	323	144	300	279	<i>Day</i>
Recession coefficient (α)	0.0117	0.0162	0.004	0.0126	0.0222	0.0259	0.0201	0.0248	0.0147	0.0118	
Renewal rate (Rr)	79.5	80.5	54.0	77.4	84.5	86.6	86.6	78.1	81.5	76.775	<i>%</i>
Renewal time rate (Trin)	1.3	1.2	1.9	1.3	1.2	1.2	1.2	1.3	1.2	1.3	<i>Year</i>

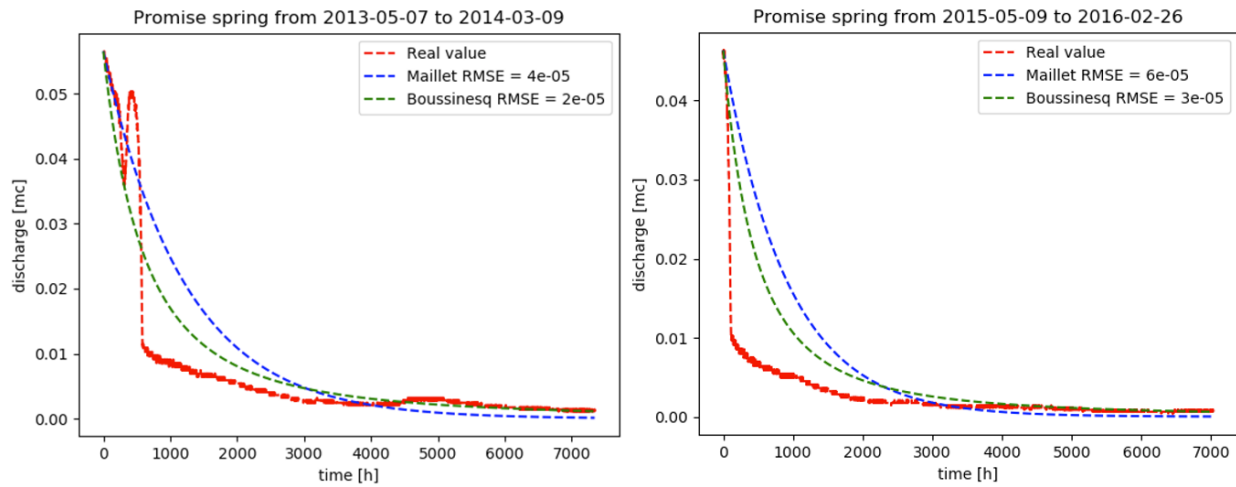


Figure 57. Promise recession with Boussinesq and Mailliet interpolation (SOURCE).

Table 10. Promise recession parameters summarized for every hydrogeological year.

PROMISE (method: Boussinesq)	1° h.y.	2° h.y.	3° h.y.	4° h.y.	5° h.y.	6° h.y.	7° h.y.	8° h.y.	9° h.y.	10° h.y.	<i>m.u.</i>
Flow rate at the beginning of the recession (Q0)	0.0127	0.0565	0.008	0.0464	0.0069	0.0109	0.0575	0.008	0.0575	0.0134	<i>mc/s</i>
Flow rate at the end of the recession (Qt)	0.0011	0.0011	0.0011	0.0006	0.0014	0.0011	0.0028	0.0025	0.0054	0.0041	<i>mc/s</i>
Groundwater volume at the beginning of the recession (W0)	158627	247107	136913	153429	157979	156847	472782	101930	610623	303263	<i>mc</i>
Groundwater volume discharged at the end of the recession (Wd)	111186	212021	85243	135686	86092	106082	367986	45503	423016	136203	<i>mc</i>
Remained Groundwater volume at the end of the recession (Wt)	47441	35086	51670	17743	71887	50765	104796	56427	187607	167060	<i>mc</i>
Recession interval (dt)	338	306	327	293	316	349	334	119	277	214	<i>Day</i>
Recession coefficient (α)	0.0069	0.0197	0.005	0.0261	0.0038	0.006	0.0105	0.0068	0.0081	0.0038	
Renewal rate (Rr)	70.1	85.8	62.3	88.4	54.5	67.6	77.8	44.6	69.3	44.9	<i>%</i>
Renewal time rate (Trin)	1.4	1.2	1.6	1.1	1.8	1.5	1.3	2.2	1.4	2.2	<i>Year</i>

For the parameters described above, it is important to differentiate between how much water has flowed over the years, thus the discharge trend, and the volume stored in the aquifer at the end of each hydrogeologic year. In fact Mascognaz for example shows a decrease in the flow trend but keeps the volume stored at the end of the recession period constant. This means that the aquifer for now is not reducing the volumes at the base of the water supply.

Cheserod, Alpe Perrot and Promiod, on the other hand, are found to have the volume of water at the end of recession less than that in the first hydrogeological year, with moreover a decreasing trend in the stored reserve at the end of recession. This results in a gradually increasing renewal rate (R_r) and a decreasing renewal time rate (T_{rin}). Clearly the renewal time rate of the resource is a parameter dependent on the ratio of the initial volume W_0 to the outflow volume W_d , in fact it gives an idea of how long it would take to return to having the same resource stored at time t i.e. at the end of recession. If it is bigger, the greater will be the water stored at time t with respect to the initial volume.

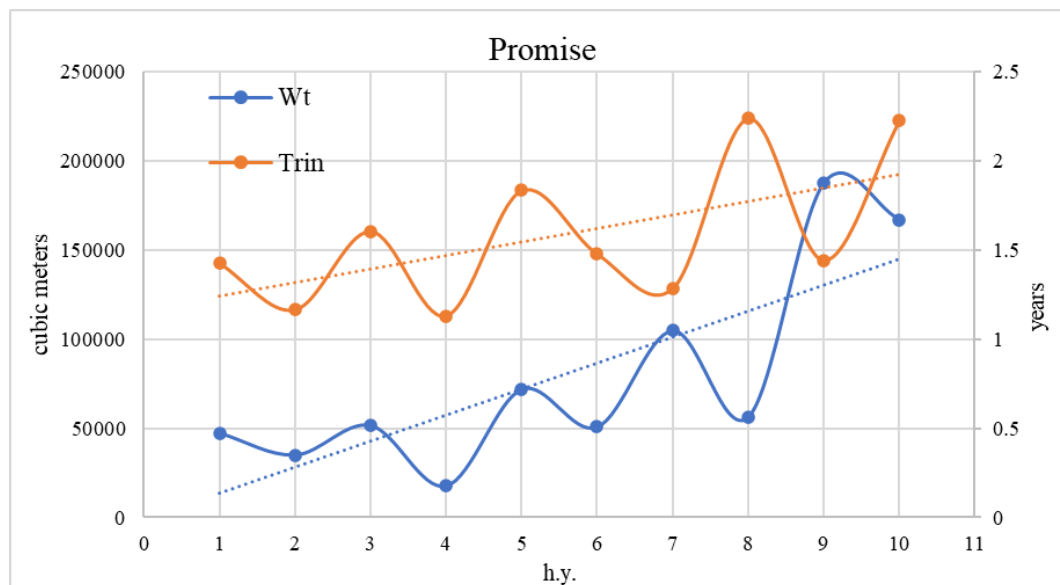


Figure 58. Annual time series of Water stored at the end of recession (W_t) and Renewal time rate (T_{rin}) of Promise spring.

The Promise spring is the only one that shows a steady rise in end-of-recession W_t volume (**Fig. 58**), so net of seasonal fluctuations, it is the only one that is storing more and more water resources. This is evidenced by the increasing W_t volumes till the 10th hydrogeological year that has tripled compared to the first one. In fact, this

phenomenon is accompanied by a decrease in the Renewal rate (R_r) and an increase in the Renewal time rate ($Trin$) of the spring.

The parameter Q_t is also an index of how much the resource is discharging at the end of recession. When this approaches zero, it means that the piezometric level of the aquifer is leveling off with the spring elevation.

Q_0 and W_0 show fluctuations for all springs that depend greatly on the amount of precipitation/snowpack height during that season. Recession, which is usually in summer, on the other hand, can be faster or slower depending on whether other inputs come into play during that phase including other precipitation or cryosphere melting (glacier/permafrost). In fact, the latter factor acts precisely on the recession curve in the case of these springs where the peak is almost always following the spring season snowmelt.

This is demonstrated by the recession coefficient of Promise which is progressively decreasing, so it shows the lower slope of the curve between the beginning and the end of the recession. Clearly this is not a diagnostic factor for understanding upstream glacier melt, but it is a good indicator of how the mountain aquifer is behaving.

An additional analysis that is done is the correlation factor analysis, shown by the Methods chapter, to understand what kind of drainage the spring aquifer has. Since the spring trend may show divergences from the precipitation trend, it is important to understand whether the aquifer can somehow keep track of previously stored inputs and through homogenization processes showing behaviors that do not conform to those of precipitation regimes.

In fact, especially Promise showed anomalous behaviors in terms of volumes runoff and remaining at the end of recession compared with the other springs. Therefore, it is important to understand whether this spring has a different drainage system type from the others that therefore does not respond directly to the rainfall regimes of the same period.

The classification of the drainage system based on the three classes A (Replacement), B (Pistoning) and C (Homogeneization), ensures to have some more information related to the behavior of the system following in response to the hydrologic input. This is done by correlating the change in flow rate to the change in electrical conductivity (EC). Since the hydrologic input is not mineralized it has $EC = 0$, and as fast as it reaches the spring output as the EC value monitored at the source decreases sharply. This phenomenon can be seen in **Fig. 59** showing the relationship between the flow rate and electrical conductivity of a hydrogeological year of each spring.

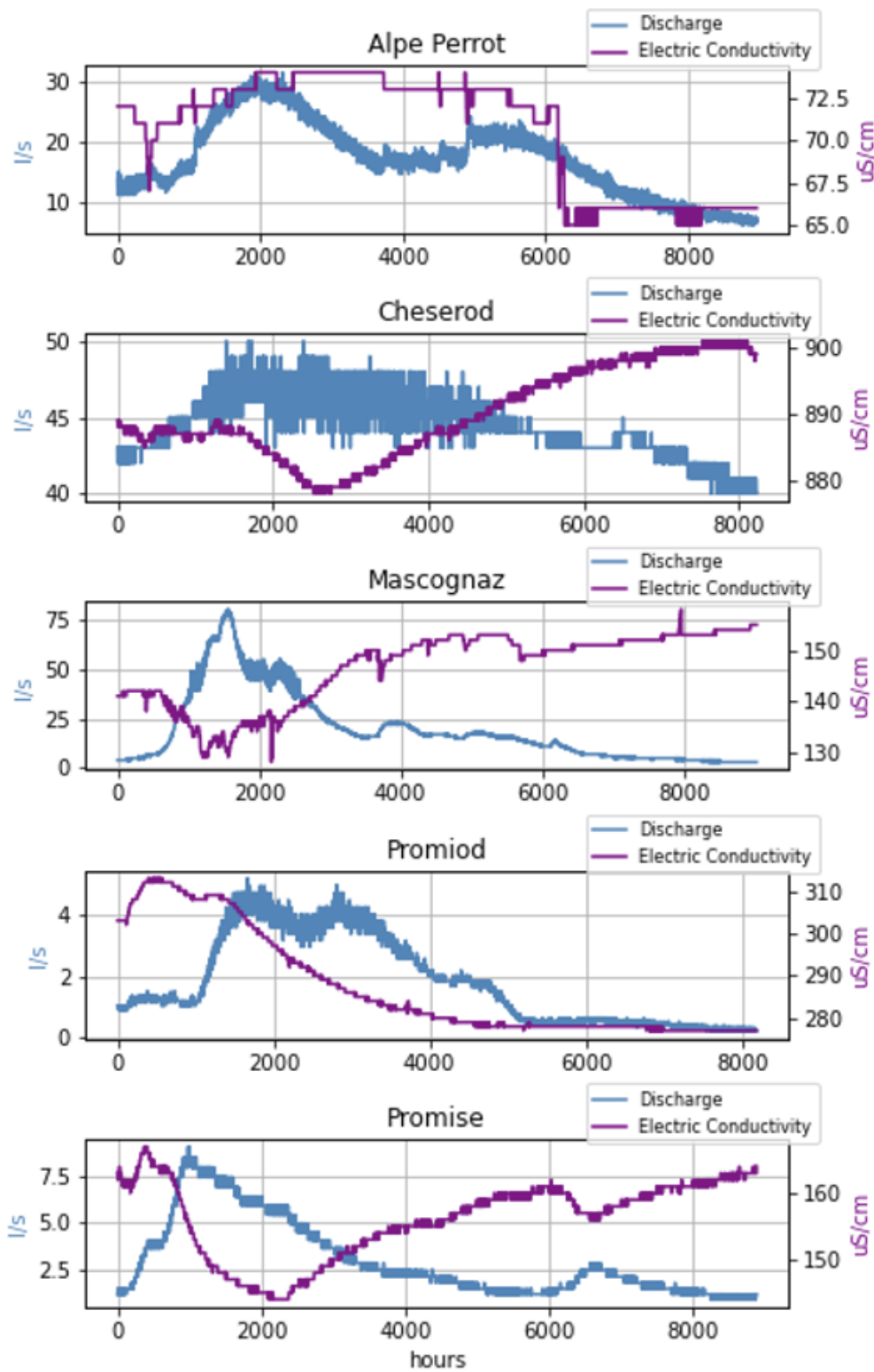


Figure 59. Hourly time series of Discharge and Electric Conductivity (EC) for each spring along an hydrogeological year.

In the first case (A), the hydrological input abruptly turns into output showing the simultaneous decrease in electrical conductivity as the flow rate increases. In case (B), the hydrological input pushes the pre-existing water resource in aquifer to outflow from the spring section, this is seen by the decrease in electrical conductivity with a clearly visible delay from the peak flow rate.

Finally the case (C), in which the system input dictated by precipitation and snowmelt has no effect on the discharge output, this is manifested by a homogenization of the input with the pre-existing water resource in the aquifer. The correlation here would be zero since at an increase in flow rate there would be no difference in electrical conductivity (EC).

Table 11. Table that summarize the Correlation Factor results from each spring

	Correlation Factor	System Classification	Description
Alpe Perrot	0.766	B	Pistoning
Cheserod	-0.802	A	Replacement
Mascognaz	-0.826	A	Replacement
Promiod	0.409	B	Pistoning
Promise	-0.673	A	Replacement

The **Table 11** shows that none of the springs under consideration are type C, hence homogenization, this is also seen in **Fig. 59** where the change in spring flow rate is also followed by the change in electrical conductivity. Based on the lag of the change in EC with respect to the change in flow rate, type A and type B springs are differentiated.

As can be seen from Cheserod and Mascognaz, there is a practically specular pattern of the time series of flow rate and Electrical Conductivity, resulting in a correlation factor of almost -1 which is the maximum. As for Promise there is a specular behavior

with a slight lag of the Electrical Conductivity, which, however, still makes the Correlation score fall within the type A drainage

In contrast, for Alpe Perrot and Promiod, the response of the Electrical Conductivity signal arrives with a longer delay, such that these springs fall into category B, that is the piston system type.

Overall, the springs can be said to respond well to precipitation and snowmelt regimes making them excellent for understanding the possibility of additional inputs from melting glaciers and permafrost.

So having the opportunity to use these springs to understand what role the melting processes of the cryosphere are playing, further statistical analyses of the spring flow regime were performed.

The one presented below is the Standard Discharge Index which shows, according to the characterization of the values population within the time series using the Gamma Distribution (paragraph 2.4.3), the SDI scores redistributed on the time axis with the chosen time scale. The scores, shown in the methods chapter, range from values less than two (extremely dry) to values greater than two (extremely wet), this is used to understand along the time frame which periods are marked by water scarcity and water abundance to look for correlations.

Fig. 60 shows the graphs of the SDI for each spring, with the default layout of the Python `standard_precip.spi` library in which below zero is pre-set to a red color, while values above zero have a blue color.

From fig's SDI with a monthly resolution, similarities and peculiarities of each spring can be seen. For example, Mascongaz and Promiod seem to have very similar periods of scarcity and abundance, where after a fairly flourishing period between 2018 and 2020 there is a major decline in the last two years marking by far the worst score of the time interval studied.

Alpe Perrot and Cheserod also show similarities; before 2014 they both have a period of scarcity, followed soon after by a couple of flourishing years that end leaving room for a three-year period slightly below zero. From 2018 there is a flourishing period that ends later than Mascognaz and Promiod, extending until almost the end of 2021. This flourishing period partly mitigates the drop of the last period that causes the SDI index to collapse to values around -2 (Extremely Dry), which are worrisome but less drastic than those of the springs described first.

Promise certainly turns out to be the most anomalous spring compared to the others, it shows a fluctuation of the score that starts from positive values for the first two years and then gradually decreases until it finds the negative peak in 2016 and then goes back up and from 2018 returns to be positive. From this time it turns out to be the most flourishing period for the spring, which even after 2022, which is the least rainy year Promise turns out to have values above zero.

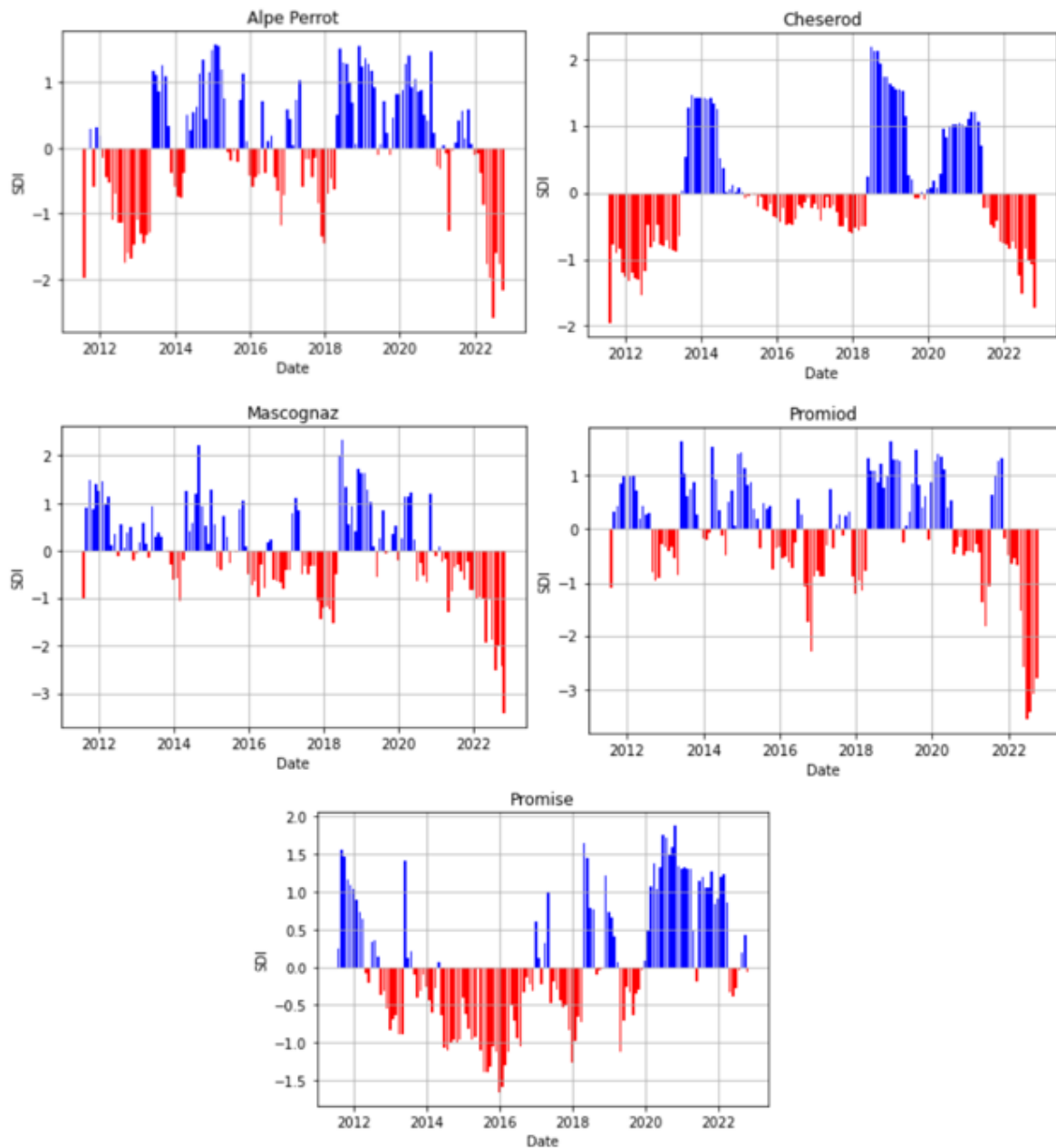


Figure 60. Standard Discharge Index of the 5 springs, using 1 month discharge resolution and gamma distribution.

As seen above, since Promise is a Type A spring, it is unlikely to accumulate reserves that then manifest late. So the anomaly recorded from 2020 onward compared to the other springs points to other clues regarding the upstream glacier melting respect the Promise spring itself.

Clearly being the SDI, an index based on the populations of each individual spring, it should not be taken as an absolute index in order to make any kind of relationship

between the springs themselves and future predictions. Though, It is good information to be able to relate the periods of each spring to the values of the same spring for the whole interval.

Fig. 61 shows the same analysis as in the previous figure with a three-month scale in which the values collected to construct the distribution are of three months instead of one. This makes a sharper representation, with more pronounced periods of abundance or scarcity. Despite this, no major differences are noticeable respect to the graphs shown earlier.

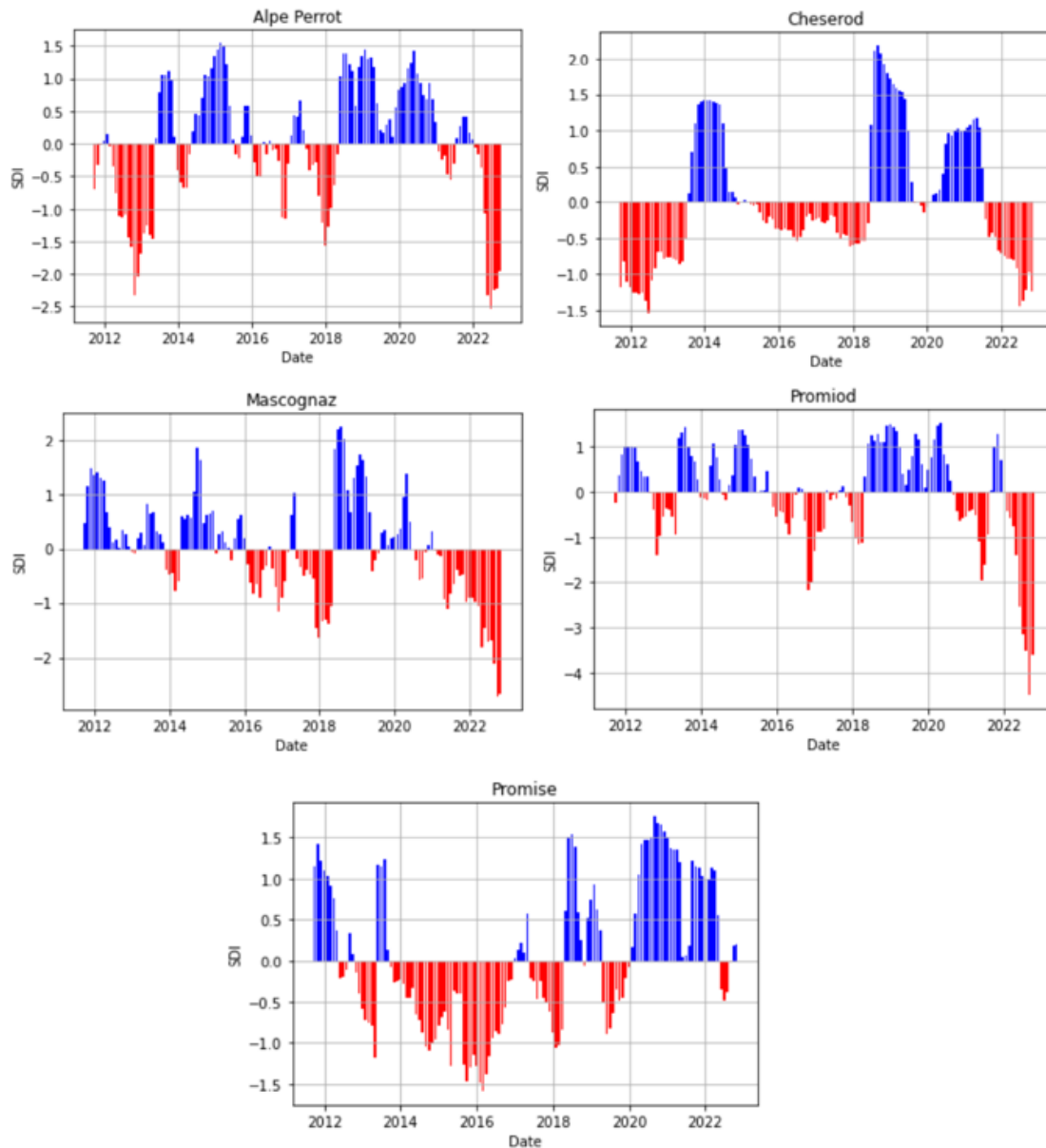


Figure 61. Standard Discharge Index of the 5 springs, using 3 months discharge resolution and gamma distribution.

A further analysis to understand the nature of the aquifers under consideration, is that of BoxPlots, which as explained in the Methods is useful to characterize the main discharge regime during the course of the years. In fact it shows the populations of monthly flowed volumes in the eleven years in which the historical series was considered.

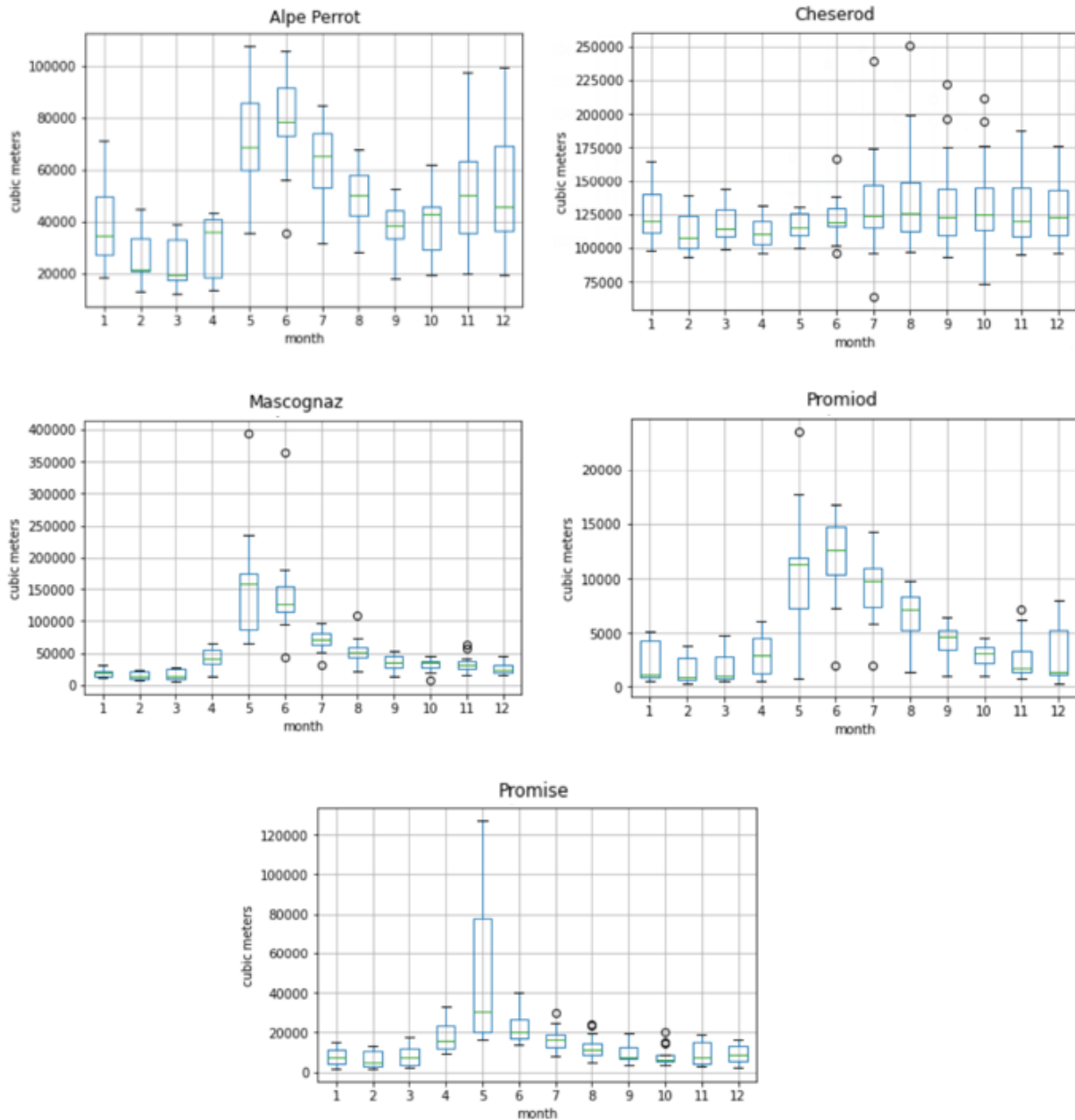


Figure 62. Box Plot representing the monthly population of discharge for every spring analyzed.

As seen in **Fig. 62**, the Alpe Perrot spring shows higher average monthly populations for May, June and July, and later for November and December. From this behavior, it can be deduced that the spring is definitely dominated by spring snowmelt, spring-summer rains and late autumn rains.

Examining the Cheserod spring, on the other hand, there is an increase in average population values from the summer months to the winter months. This suggests, that compared to Alpe Perrot, it is dominated mainly by summer and autumn rainfall and less by snowmelt.

For Mascognaz, Promiod, and Promise, on the other hand, there is an increase in average flow rates in conjunction with spring season, so spring discharge is dominated mainly by melt processes at the end of the winter season. This behavior appears to be more pronounced for Promise and Mascognaz, where there is a marked peak for the month of May and for the other months a return to low discharge. While for Promiod the high average flows in May are complemented by those in June and July, summer rains certainly also come into play in these two months to influence flow regimes.

The **Fig. 62** results just described, are helpful in understanding therefore to which hydrological inputs the springs respond most, as far as Promise and Mascognaz are concerned, snowmelt turns out to be of paramount importance for spring recharge. While rainfall certainly feeds the spring but does not generate other recharge phases during the year.

After the various analyses described so far to characterize the springs from a drainage system and flow domain point of view, statistical analyses are carried out on the discharge time series to check the upward or downward trend along the time interval, and possibly check its conformity with the rainfall assessed in the previous subchapter. The results of the statistical tests performed by the Mann-Kendal/Sen's Slope and Linear Regression methods are shown in **Table 12**. Mann Kendal, through the + or - sign of the ZMK returns qualitatively the trend of the series, while Sen's Slope (bsen) and the angular coefficient of Linear Regression (bLSLR) return a quantitative estimate of the upward or downward trend. the p-value represents the significance of the statistical test performed (Mann Kendal/Sen's Slope), which represent the relevant chance that a given value will appear, usually when the p-value is less than 0.05 it is considered statistically significant, when it is less than 0.01 it is highly significant.

The statistical results for the various springs are consistent with each other. Mann Kendall tests for Promise and Cheserod indicate an increasing trend underlined by Sen's Slope and Linear Regression, which give a quantitative estimate of the increase.

Table 12. Summary of statistic tests performed for each spring, in green are those results that confirm the increasing trend, in red for the decreasing trend.

	A Perrot	Cheserod	Mascognaz	Promiod	Promise
MK test trend	no trend	Increasing	decreasing	decreasing	Increasing
MK * Standardized Test Statistic (ZMK); Day Interval Time Series (l/s)	1.363	7.874	-12.813	-12.633	16.06
Sen's Slope Test (bsen); Day Interval Time Series (l/s)	0.000156	0.000855	-0.00153	-0.000176	0.000665
p-Value	0.173	0.00	0.00	0.00	0.00
Linear Regression (bLSLR); Average Daily Discharge Time Series (l/s/day)	0.0003	0.0012	-0.002	-0.0002	0.0007
Linear Regression (bLSLR); Daily Water Volume Discharged (m ³ /day)	0.029	0.1011	-0.173	-0.0164	0.0604
m ³ of water lost or gained on average by day	119.393	416.2287	-712.241	-67.5188	248.6668

While for Mascongaz and Promiod there is a decrease for all tests performed. For these four springs there is a p-value below 0.01 confirming the significance of the tests performed.

While for Alpe Perrot there is a p-value of 0.173 which makes the Mann-Kendal statistical test insignificant returning in fact as a result of the test "No trend". Despite this, both Sen's slope and Linear Regression returned an increasing values for this spring.

Although for Alpe Perrot there is no overwhelming confirmation dictated by the statistical test, for the other springs, it can be said that the results obtained are strong in confirming the increase or decrease in the flow rates discharged during the years analyzed. In addition to the quality of the observations regarding the trend, the results are also proportionate in quantitatively describing the slope of the trend. Promise is the spring that shows more growth than the others from the point of view of scores, Mascognaz and Promiod show very similar decreasing scores between them. Cheserod has growth equivalent to about half that of Promise, and Alpe Perrot has very tenuous growth such that it is not significant for Mann Kendal.

From Linear Regression the average cubic meters that were lost or gained on average each day were calculated, of course these values are not to be compared between the different springs because each has different flow regimes from the others, for example Cheserod has much higher flow rates on average than the other springs.

It is important to point out, as mentioned earlier, that the trends in flowed discharge may be independent of the values of volumes stored in the aquifer. in fact as seen for Mascognaz the volume values at the end of the recession W_t shown earlier turns out to be fairly constant over time despite the fact that runoff volumes have decreased. For Alpe Perrot and Cheserod there is a countertrend as volumes outflowed have increased over the series but volumes stored have decreased. Promise and Promiod are the only ones that show conformity between trends in outflow and stored volumes at the end of the recession, the former showing an increase for both values and the latter a decrease in both values.

That said, although there are different trends for the springs, there are conforming climatic and precipitation regimes among them. In fact, Mascognaz and Promiod seem to react sensibly to the lesser rainfall and snowfall along the considered time interval, while the other springs do not seem to suffer from the decrease in rainfall but rather increase their discharge. This is a sign of different input from that analyzed by the weather stations whose results are shown in the sub-chapter 3.2.

Next, the table containing the main chemical parameters for each spring recovered from monitoring campaigns from the year 2011 through 2021 is shown. It can be seen in the **Table 13** that the sampling period was mainly carried out during the summer months

Table 13. List of chemical parameters gathered in different sampling campaigns for each analyzed spring.

Spring	Sampling date	Ca [meq/l]	Mg [meq/l]	Na + K [meq/l]	Cl [meq/l]	SO4 [meq/l]	HCO3 [meq/l]	NO3 [meq/l]
ALPE PERROT	11/07/2011	0.205	0.781	0.014	0.008	0.058	0.782	0.049
ALPE PERROT	02/08/2012	0.186	0.832	0.016	0.005	0.037	0.917	0.034
ALPE PERROT	12/06/2019	0.151	0.785	0.013	0.006	0.029	0.793	0.028
ALPE PERROT	01/07/2020	0.152	0.829	0.014	0.005	0.054	0.839	0.036
ALPE PERROT	03/09/2021	0.168	0.71	0.015	0.006	0.045	0.81	0.038
CHESEROD	12/07/2011	5.779	4.504	0.11	0.089	6.3	4.216	0.068
CHESEROD	01/08/2012	5.779	4.577	0.191	0.022	5.895	4.371	0.007
CHESEROD	10/06/2019	6.804	4.688	0.063	0.036	7.386	4.001	0.008
CHESEROD	02/09/2021	6.693	4.117	0.103	0.043	6.704	3.912	0.012
MASCOGNAZ 1	11/07/2011	1.562	0.124	0.055	0.003	0.236	1.5	0.036
MASCOGNAZ 1	30/07/2012	1.576	0.134	0.063	0.005	0.213	1.575	0.02
MASCOGNAZ 1	12/06/2019	1.578	0.1	0.051	0.003	0.176	1.444	0.018
MASCOGNAZ 1	01/07/2020	1.559	0.124	0.05	0.002	0.34	1.454	0.02
MASCOGNAZ 1	17/05/2021	1.563	0.118	0.056	0.004	0.336	1.36	0.035
PROMIOD	15/07/2011	2.684	0.559	0.052	0.014	0.32	2.973	0.021
PROMIOD	01/08/2012	2.676	0.656	0.064	0.008	0.277	3.053	0.006
PROMIOD	10/06/2019	2.849	0.545	0.055	0.01	0.259	3.143	0.007
PROMIOD	01/07/2020	2.602	0.602	0.052	0.011	0.352	2.902	0.009
PROMIOD	03/09/2021	2.281	0.492	0.054	0.012	0.344	2.46	0.01
PROMISE	12/07/2011	1.644	0.167	0.127	0.008	0.433	1.492	0.022
PROMISE	28/08/2012	1.729	0.19	0.179	0.006	0.432	1.686	0.005
PROMISE	10/06/2019	1.658	0.173	0.117	0.004	0.333	1.574	0.007
PROMISE	01/07/2020	1.506	0.161	0.111	0.005	0.458	1.476	0.008
PROMISE	02/09/2021	1.526	0.169	0.139	0.006	0.482	1.338	0.007

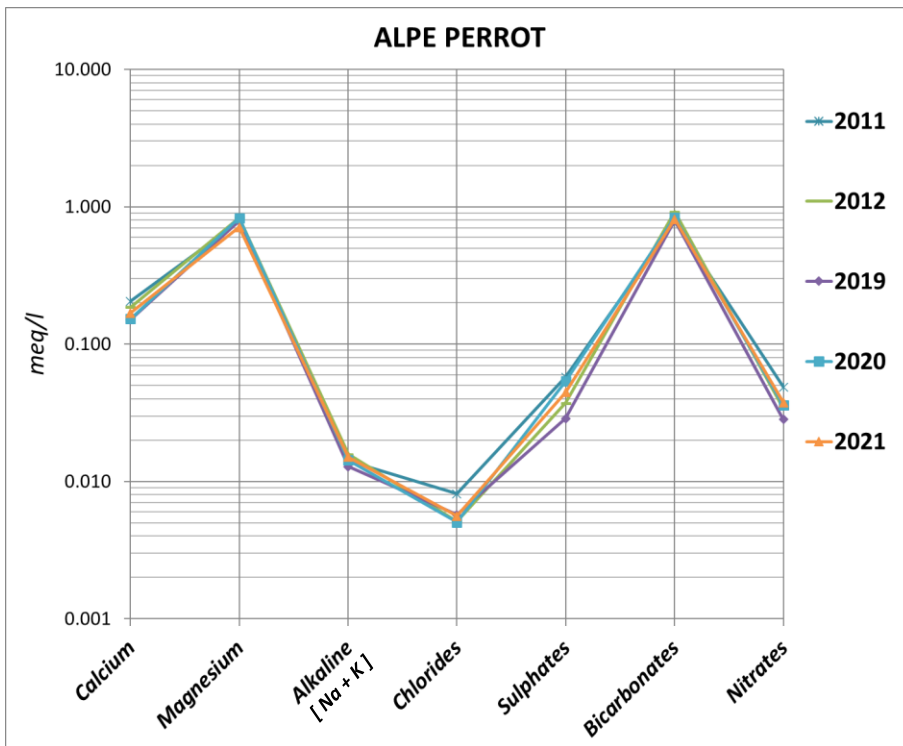


Figure 63. Alpe Perrot spring Schoeller Diagram.

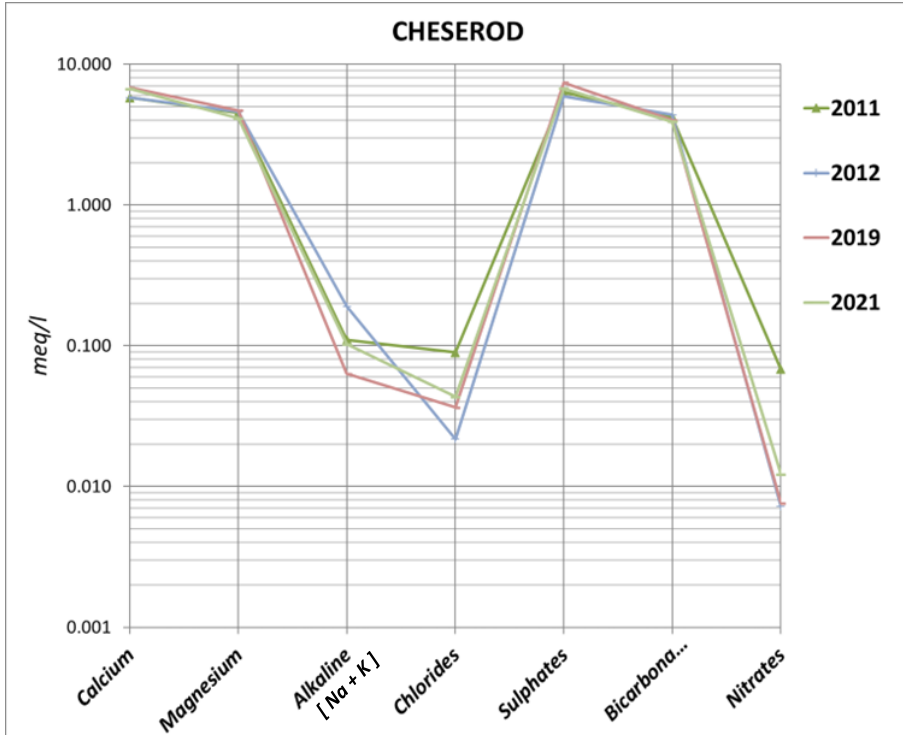


Figure 64. Cheserod spring Schoeller Diagram.

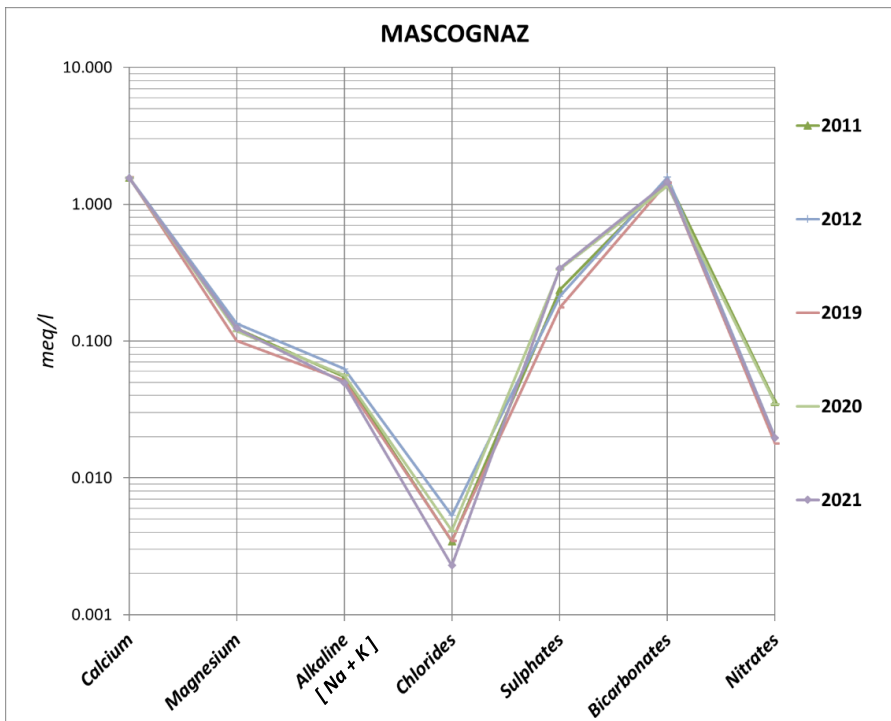


Figure 65. Mascongaz spring Schoeller Diagram.

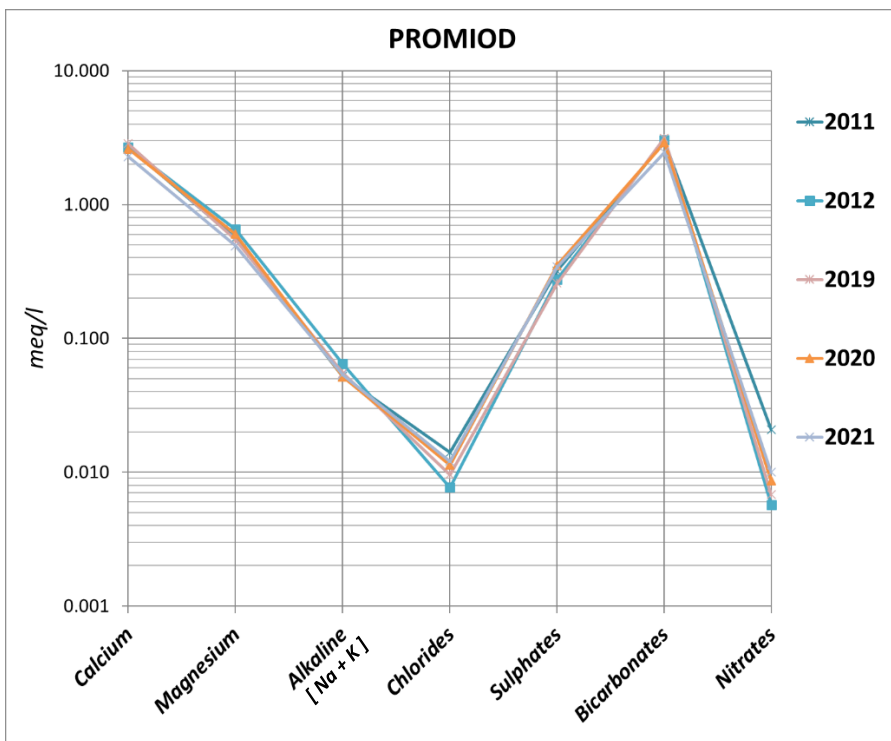


Figure 66. Promiod spring Schoeller Diagram.

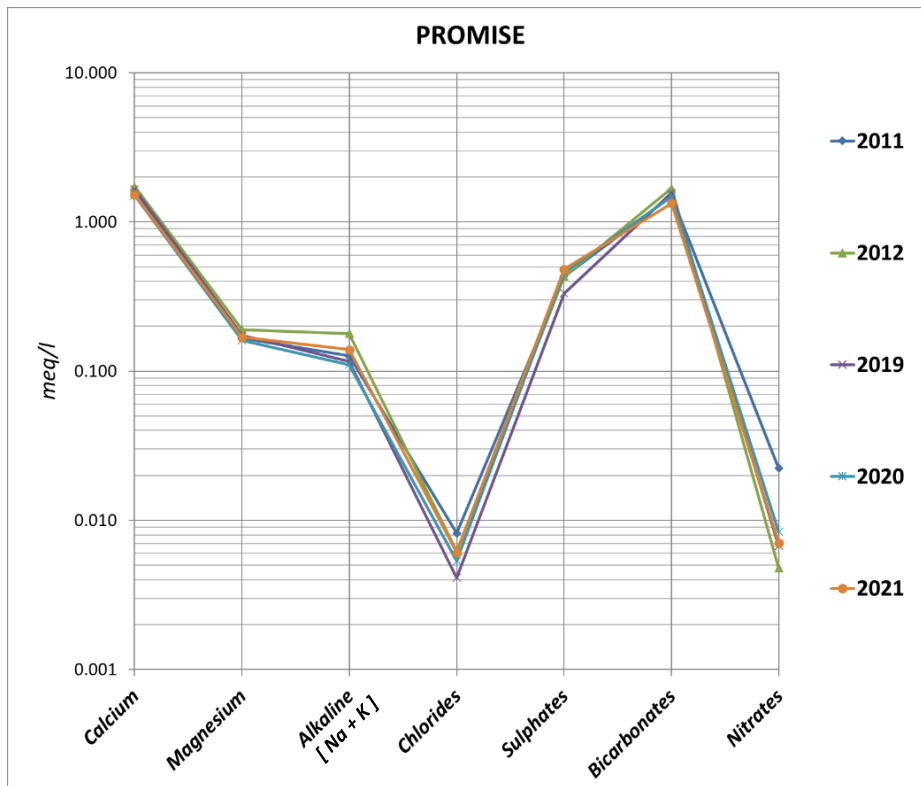


Figure 67. Promise spring Schoeller Diagram.

Shown in **Fig. 63-67** are the chemical analyses for samplings taken during the summers of the years marked in the legend. All springs show 5 samples from different years, the only one with less sampling is Cheserod which has 4. The time series is not uniform but shows two "old" samples related to the years 2011 and 2012 and recent samples related to the years 2019-2020-2021, with a seven-year data gap. This should more easily point out whether the hydrochemistry of the water had visibly changed during the time interval between the old and new samples.

Fig. 63 shows the Schoeller diagram of Alpe Perrot, where can be noted the prevailing concentrations of Bicarbonate, Magnesium and Calcium falling into the hydrochemical facies of Bicarbonate-Calcic-Magnesian type. Cheserod on the other hand based on the concentrations of salts falls within the Sulfate-Calcium-Magnesian type. Mascognaz and Promise have a very similar hydrochemistry that is characterized by a predominantly Bicarbonate-Calcic facies and a Sulfate-Alkaline sub-facies. Promiod, instead, has a simple hydrochemical facies of the Bicarbonate-Calcium type.

The distributions of the concentrations listed above with the facies of each spring show small variations in dissolved salts, despite that in these variations no upward or

downward trend is identified, they seem more like variations resulting either from the sampling period or the level of uncertainty of the chemical analyses conducted.

So hydrochemistry in this case does not help to understand whether there are different water inputs, i.e. from glacier or permafrost. This is because most likely the lithology characterizing the hydrogeological circuit from where the rain and nival meltwater comes is the same as that from which the glacier and permafrost meltwater comes.

Next, the PIPER diagram (**Fig. 68**) of all springs is shown, according to which the concentrations of anions and cations are shown in percentage rather than absolute terms.

It can be seen that in addition to the stability of absolute meq/l concentrations shown by Schoeller, there is also an incredible stability of ratio of ion concentrations.

This outlines a constancy from the point of view of the hydrogeological circuits serving the springs.

The Piper diagram of Alpe Perrot delineates an ionic prevalence of Magnesium and Bicarbonate, probably resulting in the first case from the serpentine lithology, rich in Mg, characterizing the area (**Fig. 10**), and in the second case (HCO_3) from the dissolution of calcium carbonate present in the calcschists and moraine deposits of the area.

The Cheserod spring, according to the diagram, falls into the Calcium Chloride type. While the origin of the Ca^+ cation is easily associated with the dissolution of calcium carbonate from deposits and calcschists characterizing the area, for Cl^- it is not easy to understand its origin. It may be that metabasalts and calcschists in the area (**Fig. 12**), contain halite lenses, or that moraine deposits are rich in this mineral.

Promiod and Mascognaz show similarity in Piper's diagram from the point of view of predominant ions in water. They have a Bicarbonate-Calcium prevalence, this rather than coming from the lithologies that characterize the area (serpentine and metabasalts, (**Fig. 14**; **Fig. 16**)) are mostly derived from the dissolution of calcium carbonate present in alluvial and slope deposits for Mascognaz, and morainal and slope deposits for Promiod.

Promise also has an ionic prevalence of Calcic and Bicarbonate, although the lithology of the area is different from that of Mascognaz and Promiod (**Fig. 18**). Promise, as a spring that gathers circulating water in fractures, it is more likely to mineralize from flow through the fracture system than from deposits. In fact, sandstone and limestone formations favor the phenomenon of karstification that leads to enriching the water with Calcium and Bicarbonate.

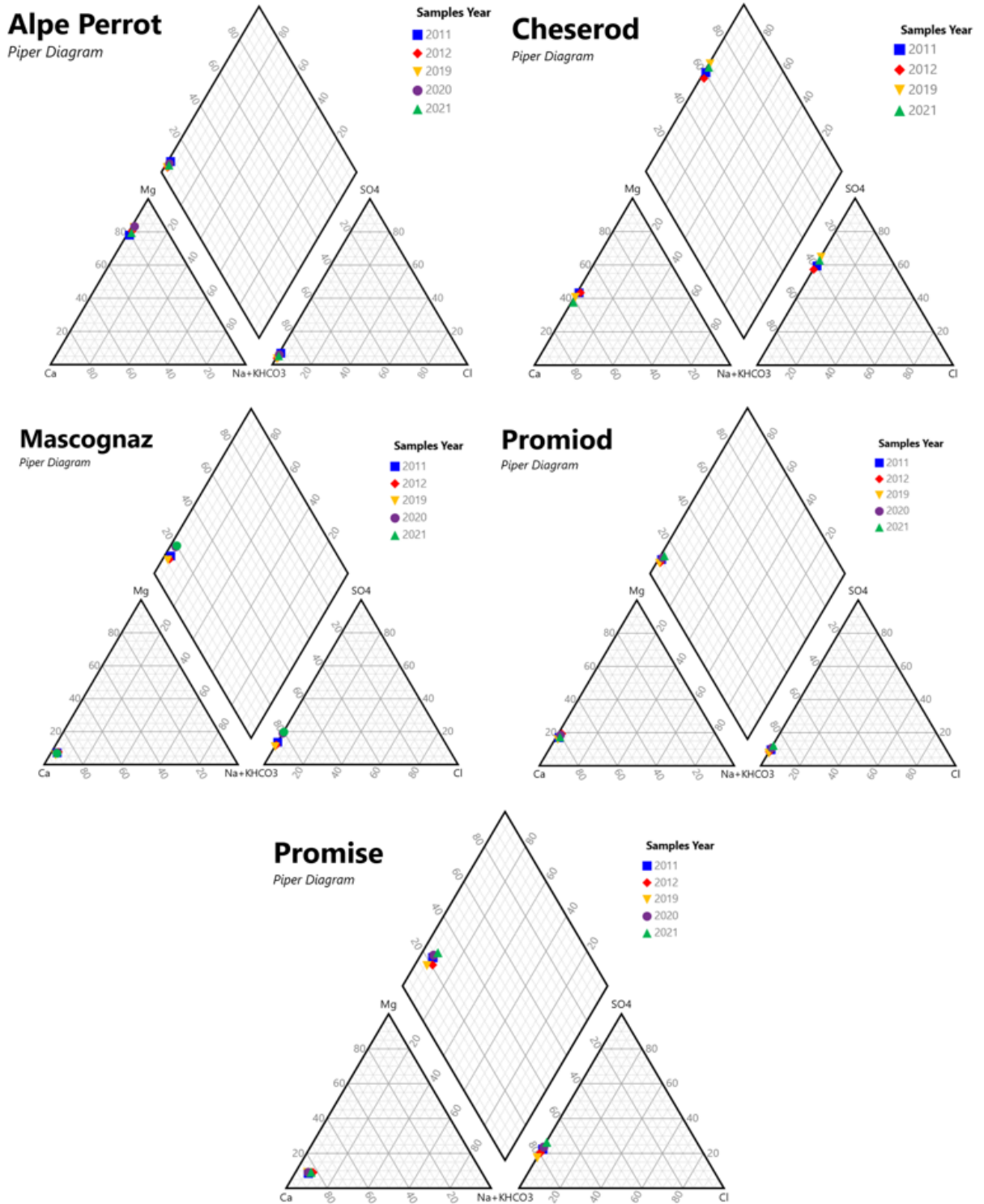


Figure 68. Piper Diagram of the five monitored spring, each symbol refers to a different year of sampling.

3.3 Precipitation and discharge correlation

After nearly analyzing the spring flows and precipitation independently, in this section of the results, the time series of precipitation and spring flows will be shown so that they can be compared.

To do this, it is essential that the precipitation is processed in such a way as to shift the snowfall that fell during the months of October November and December into the following year, since the aquifer perceives the water input only once snowmelt occurs, thus in the spring period.

Since heated bascule rain gauges that convert snow into millimeters of rainfall are installed at the 5 weather stations, it is important to distinguish between solid and liquid precipitation in order to translate the equivalent snow millimeters to the following year. In **Fig, 69**, the part of the code used to distinguish rainfall and snowfall based on atmospheric temperature is shown. Temperature parameter recorded by the weather station, is then made representative by shifting it using temperature gradient according to the spring elevation respect to the temperature sensor elevation .

Since the spring are lower or higher than where the temperature is detected, the temperature shift (0.6 °C per 100 meters) makes the type of precipitation involving the spring more realistic.

In fact, as noted in the piece of code for the Promise spring, which is associated with the La Thuile weather station located at a lower elevation, respectively, the solidification temperature is shifted from 0 °C to 2 °C.

```

8 import pandas as pd
9 import numpy as np
10 import plotly.express as px
11 import matplotlib.pyplot as plt
12
13 # SOMMA PIOGGIA GIORNALIERA
14
15 sorgente = pd.read_csv('Promise_Q_Day_T_New.csv', sep=';', encoding='UTF-8')
16 stazione = pd.read_csv('SM_LaThuile_Extended.csv', sep=';', encoding='UTF-8')
17
18 PL = []
19 PS = []
20
21 for i in range(len(stazione.prec)):
22     if stazione.temp[i] < 2:
23         PS.append(stazione.prec[i])
24         PL.append(0)
25     else:
26         PS.append(0)
27         PL.append(stazione.prec[i])
28
29 PrecSolida = np.array(PS)
30 PrecLiquida = np.array(PL)

```

Figure 69. Python code for Solid and Liquid precipitation separation.

In **Fig. 70**, the results of the annual budgets for the Alpe Perrot spring are shown. From the image on the left, it can be discerned that there is a good similarity between the annual rainfall series and the annual runoff volumes, this up to the year 2019, where up to 2021 a strong divergence is seen.

This is confirmed by the correlation shown in the figure on the right, which makes the very good correlation stand out net of the three years 2019-2020-2021 (black dots), while correlating the whole time series, including the above three years (gray dots), the correlation drops to 50 percent.

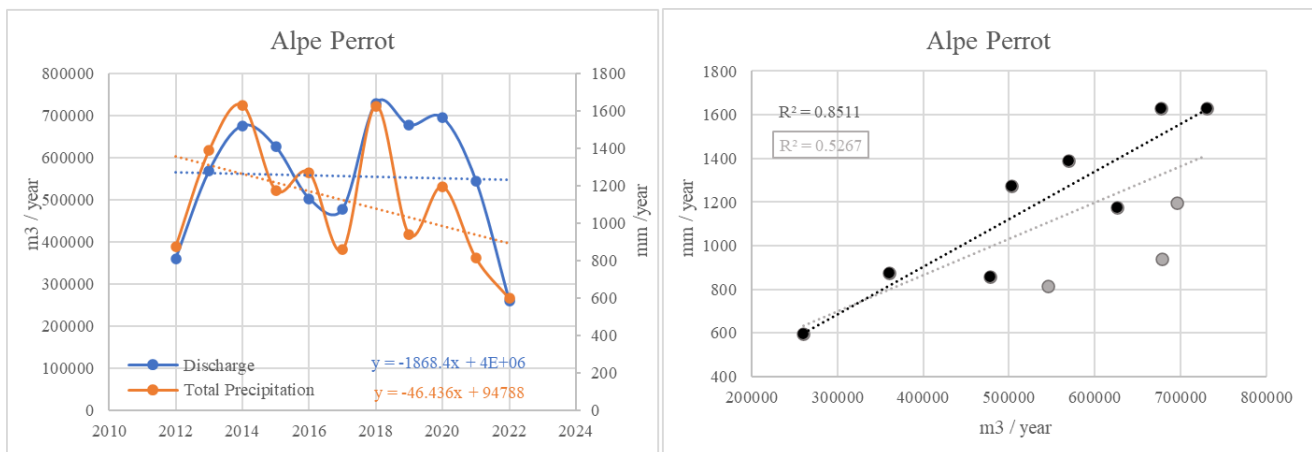


Figure 70. Left: Alpe Perrot annual discharge and annual total precipitation comparison. Right: Annual discharge and precipitation correlation, best correlation with black dots and total correlation with black and grey dots.

The behavior of Alpe Perrot is similar to that of Cheserod (**Fig. 71**), which for the same years 2019-2020-2021, shows decorrelation from precipitation,

As seen in the right figure, the spring flow rate, in the calendar year seems to precisely follow the amount of rain and melted snow within the same year. There is a remarkable disparity especially in the 2020s, where against a considerable amount of runoff volume there is a very low amount of hydrological input. In fact, this divergence, leads the Cheserod time series to have an 'increase over time, while the precipitation series to decrease over the years. As in Alpe Perrot, the correlations shown in the right graph were divided into correlation net of the 3 years 2019-2020-2021 (81%), and a full one to show how much the three years mentioned before make the overall correlation worse (43 %).

This may explain the fact that in those years the aquifer received inputs not only from rainfall and seasonal snowmelt, but also from glacier or permafrost.

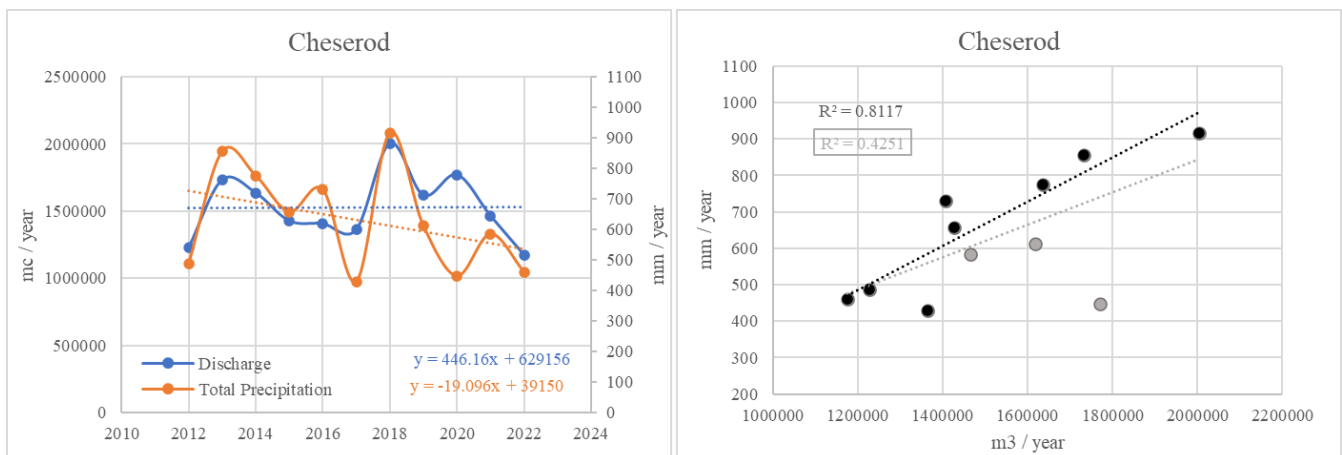


Figure 71. Left: Cheserod annual discharge and annual total precipitation comparison. Right: Annual discharge and precipitation correlation, best correlation with black dots and total correlation with black and grey dots.

The results of the annual Mascognaz budgets are shown below (**Fig. 72**). Unlike the two cases shown above, the spring shows good correlation throughout the period, even in recent years.

The only year in which the hydrogeological inputs processed by the weather station and the runoff volumes deviate are in the year 2018, where the spring flow is very abundant compared to precipitation moving away from the regression line. This is shown in the adjacent figure (grey dot), where the correlation with or without the 2018 budget is shown.

This may be due to errors in capturing rainfall during the year that therefore underestimate the actual amount of precipitation, or a misrepresentation of snowfall/rain for that year by the Ayas weather station that is located near the spring but in a different basin. Due to local climatic factors, it is therefore possible that the station did not represent the weather aquifer condition very well.

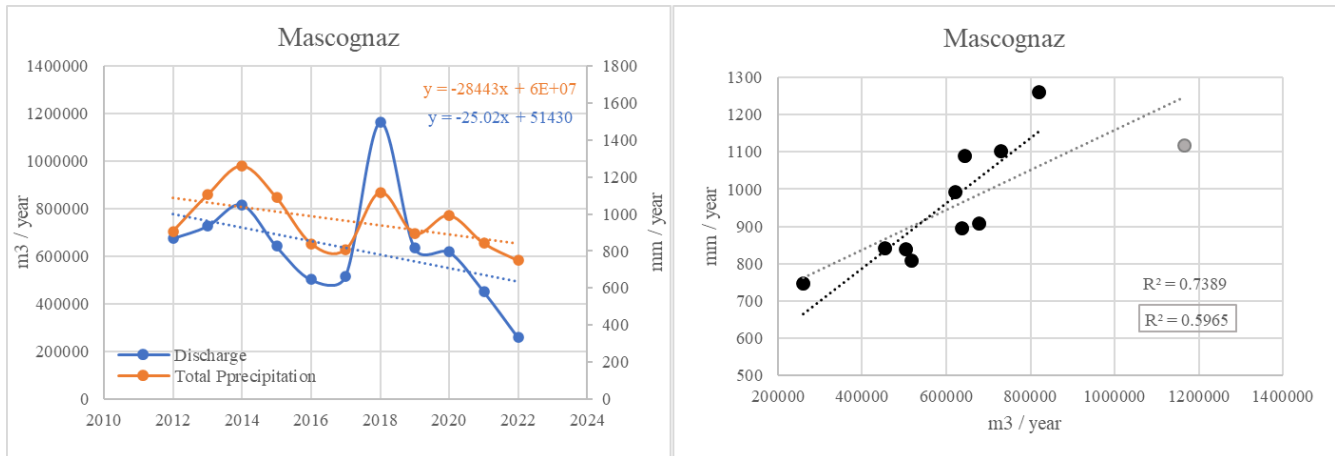


Figure 72. Left: Mascognaz annual discharge and annual total precipitation comparison. Right: Annual discharge and precipitation correlation, best correlation with black dots and total correlation with black and grey dots.

What the Mascognaz spring and Ayas precipitation time series certainly have in common are the decreasing trends.

This can also be discerned with regard to the case of Promiod (**Fig. 73**), where there is a marked negative trend of precipitation followed by the marked negative trend of the spring. In fact, this case perfectly represents the condition in which the aquifer consistently responds to the spring inputs, also showing that it does not receive any other input from the semi-permanent cryosphere.

Therefore, in this case a single correlation is shown with all years of precipitation and water runoff from the spring, reaching a correlation of almost 70 percent. As in all the others, but especially for Promiod, the 2022 water crisis is noted, at very low annual rainfall the spring almost goes to depletion.

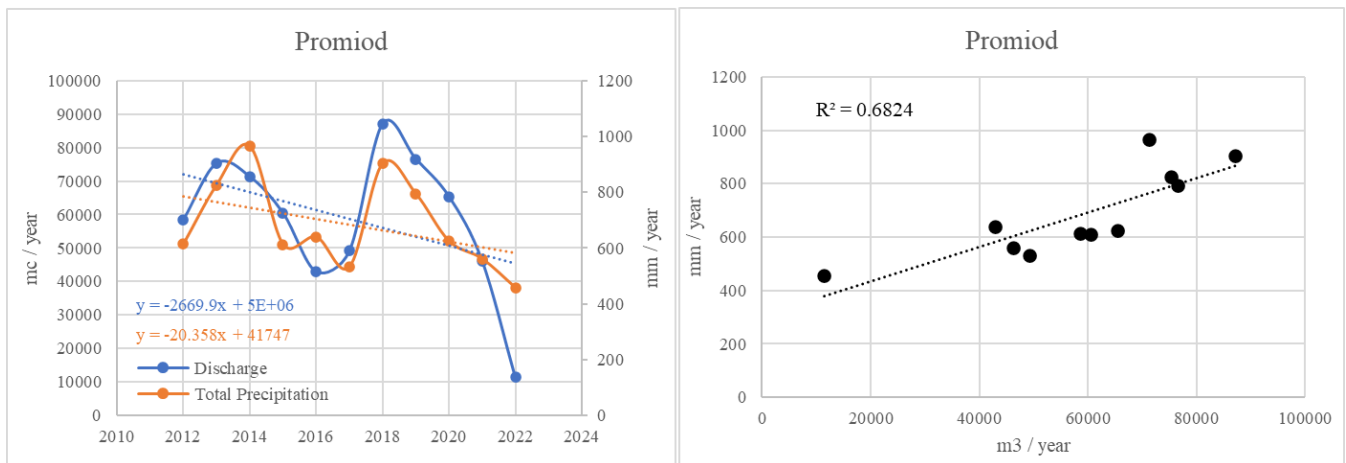


Figure 73. Left: Alpe Perrot annual discharge and annual total precipitation comparison. Right: Annual discharge and precipitation correlation, best correlation with black dots and total correlation with black and grey dots.

Last is shown the Promise spring in **Fig. 74**. Which compared to all the others has a clearly increasing trend with respect to rainfall during the period studied. Especially evident is the growth in runoff volumes from 2020 through 2022, which although maintaining the same basic rainfall shape, show a contribution of water input from additional sources. This can also be seen in the correlation graph on the right, where the gray dots shift the correlation to a regression line parallel to the original one, indicating that the system is still influenced by rainfall but has an additional support base. Emblematic, in fact, is the lower gray dot related to 2022, indicating an abundance of spring discharge relative to the worst annual precipitation.

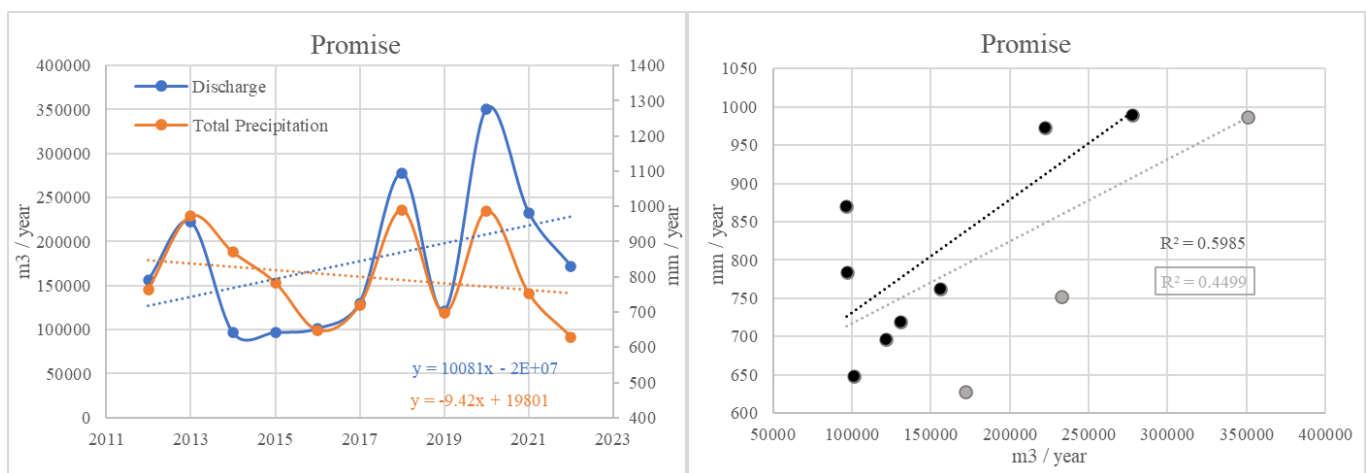


Figure 74. Left: Promise annual discharge and annual total precipitation comparison. Right: Annual discharge and precipitation correlation, best correlation with black dots and total correlation with black and grey dots.

3.4 Snowmelt statistical analysis

With the 10-minute frequency weather station data, several Multiple Linear Regression analyses were performed to evaluate the correlation between the parameters: Temperature, Barometric Pressure, Relative Humidity, Reverse and Direct Radiation, Absorbed Radiation, Snow Density, Snow Weight, Snow Depth with the melting rate calculated by the loss of SWE ($\Delta\text{SWE} < 0$). Of course, in this analysis, an attempt was made to calibrate the time-step Δt according to what seems to be the best model, since the 10-minute values have fluctuations due to instrumental errors and since in 10 minutes it is difficult to capture what is a cause-and-effect relationship between the agent parameters triggering the snowmelt and the melting itself. Also for the same reason, only melting values $\Delta\text{SWE} > 1$ mm are considered also considering the accuracy of the instrument (Snow Scale). In addition, the model was trained by removing outliers and looking for the best population distribution for the dependent variable to improve stochasticity.

So after several MLR simulations using the softwares IBS, SPSS together with Python, it was brought to light that the best model is the one that includes only Temperature as a parameter, with a time-step of 2 hours, which means averaging the values of all parameters over this interval. The model shows an R^2 index of determination for this

model of 76.4%, which is equal to a Pearson's index of 88% signifying a very strong correlation between snowmelt and temperature (**Fig. 74**).

OLS Regression Results						
Dep. Variable:	y	R-squared:	0.764			
Model:	OLS	Adj. R-squared:	0.757			
Method:	Least Squares	F-statistic:	103.6			
Date:	Tue, 21 Feb 2023	Prob (F-statistic):	1.47e-11			
Time:	11:12:18	Log-Likelihood:	-33.026			
No. Observations:	34	AIC:	70.05			
Df Residuals:	32	BIC:	73.10			
Df Model:	1					
Covariance Type:	nonrobust					
	coef	std err	t	P> t	[0.025	0.975]
x1	0.7499	0.074	10.179	0.000	0.600	0.900
const	-3.4269	0.663	-5.165	0.000	-4.778	-2.075
Omnibus:	0.657	Durbin-Watson:	2.199			
Prob(Omnibus):	0.720	Jarque-Bera (JB):	0.754			
Skew:	-0.230	Prob(JB):	0.686			
Kurtosis:	2.433	Cond. No.	53.5			

Figure 75. Summary of MLR regression result in Python (Statsmodel). The model is described by coefficient column where x1 is Temperature independent variable and const is the constant of the model relation.

Multiple models with multiple variables were tested, also considering the square and cube of the independent variables to see if there were also nonlinear relationships. One of the best models ($R^2 = 80.6\%$) is the one in which there is Temperature (T), Snow Density and Absorbed Radiation. In this case Snow Density and Absorbed Radiation individually show a moderate correlation with snow melting, $R = 42\%$ and 50% , respectively. Nevertheless, the model is inefficient because it shows rather high multicollinearity values as shown in **Fig. 76** in the bottom red box. This happens when two parameters taken as independent variables show in turn a correlation between them; this certainly happens with regard to Temperature and Absorbed Radiation. This cannot be said for Snow Density, whose value is derived from the metamorphism processes that take place before the two hours considered as timestep. Certainly this parameter shows a moderate correlation given that the closer the ultimate state of the snow related to the maximum density (800-1000 kg/mc) is reached, the less the snow has capacity to hold water through metamorphisms and thus begins to release water.

OLS Regression Results						
Dep. Variable:	y	R-squared:	0.806			
Model:	OLS	Adj. R-squared:	0.786			
Method:	Least Squares	F-statistic:	41.49			
Date:	Tue, 21 Feb 2023	Prob (F-statistic):	8.54e-11			
Time:	11:05:20	Log-Likelihood:	-29.715			
No. Observations:	34	AIC:	67.43			
Df Residuals:	30	BIC:	73.54			
Df Model:	3					
Covariance Type:	nonrobust					
	coef	std err	t	P> t	[0.025	0.975]
x1	0.0008	0.000	1.879	0.070	-7.11e-05	0.002
x2	0.0041	0.002	1.926	0.064	-0.000	0.008
x3	0.6412	0.081	7.868	0.000	0.475	0.808
const	-4.1641	0.838	-4.967	0.000	-5.876	-2.452
Omnibus:	0.321	Durbin-Watson:	2.336			
Prob(Omnibus):	0.852	Jarque-Bera (JB):	0.496			
Skew:	0.141	Prob(JB):	0.780			
Kurtosis:	2.480	Cond. No.	3.86e+03			
Notes:						
[2] The condition number is large, 3.86e+03. This might indicate that there are strong multicollinearity or other numerical problems.						

Figure 76. Summary of MLR regression result in Python (Statsmodel). The model is described by coefficient column where x1 is Temperature, x2 is Snow Density, x3 is Absorbed Radiation and const is the constant of the model relation.

The model that gives back the highest coefficient of determination is the one in which these first-order independent variables are taken: Temperature, Relative Humidity, Snow Density, Snow Weight, Absorbed Radiation) and the same second-order ones (T^2 , RH^2). Getting a model with R^2 of 84.4 %, but with an even higher condition number than before ($1.79e+07$).

However in any case, the most effective and simple model is characterized by the simple snow melting - air temperature correlation. Moreover, it is the easiest model to reproduce in the absence of instruments that measure snow parameters and other less usual atmospheric parameters such as Absorbed Radiation. So these aspects make it the strongest model from a statistical and practical point of view.

The statistical model just described is then compared to a downscaled experiment at the Applied Geology Laboratory of the Lecco Campus University in which the cm lost from the snowpack as a result of certain weather conditions was measured.

The snow in this case, transported from Montespluga in polystyrene containers, was of the Firn type (**Table 1**) and had an average density of 450 kg/mc. It was placed on the inclined landslide simulator, which is described in subchapter 2.8, above a compacted

soil to improve environmental conditions and ensure the absorption of melted snow below the snow layer. The atmospheric conditions monitored during the experiment found an almost constant air temperature around 15 °C and fairly high relative humidity (RH = 70 - 80%) with overcast sky.

According to the most efficient statistical model listed above, at this temperature the snowpack should melt at a rate of 3.91 mm/h of Snow Water Equivalent. The millimeters of SWE calculated in this way, knowing that the mantle has an average density of 450 kg/m³, can be transformed into the value of cm/h, centimeters of snowpack that are lost per hour (Δ SnowDepth/h). Therefore, this value is estimated to be 0.87 cm/h. So this value will be kept checked during the experiment to see whether the model is satisfied by the experimental evolution of snowpack depletion.

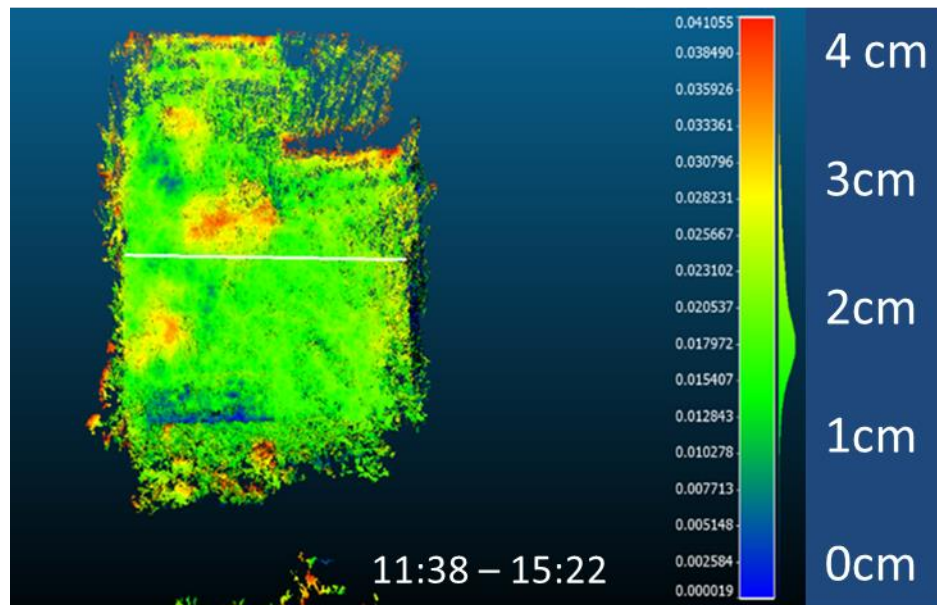


Figure 77. Photogrammetric evolution of snow surface which loses thickness along time

The photogrammetric reconstruction by Cloud Compare is represented in **Fig. 77**, showing at the surface level the evolution of the snowmelt. During the time span denoted in the **Fig. 77**, about 3 hours and 44 minutes, there are areas where the melt stopped at 2 cm and other spots where it reached up to 4 cm. With the statistical prediction of 0.87 cm/h shown above, during the time frame of 3 hours and 44 minutes it should have shown a generalized melt of about 3.25 cm, which is a fairly good average of what the 3D reconstruction shows. Perhaps the model turns out to be slightly abundant in this case, however, it detects a melt rate that is still within the melt range within the analyzed surface.

Of course, this is still a simplistic statistical model based only on the air temperature parameter, despite that it approximately represented the experiment carried out in the laboratory. These results encourage the continuation of atmospheric and nival monitoring of the Mascongaz station to obtain more samples and be able to refine the model.

3.5 Rutor Glacier mass balance

The Glacier Mass Balance data, shown in the Method sub-chapter 2.7, are in this section confronted with atmospheric temperatures taken from the La Thuile - La Gran Thete weather station, and then analyzed according to the Promise spring discharge response.

Glacier mass balances are available from the year 2005 to 2022. As mentioned earlier the year 2020 is lacking in glacier data given the pandemic.

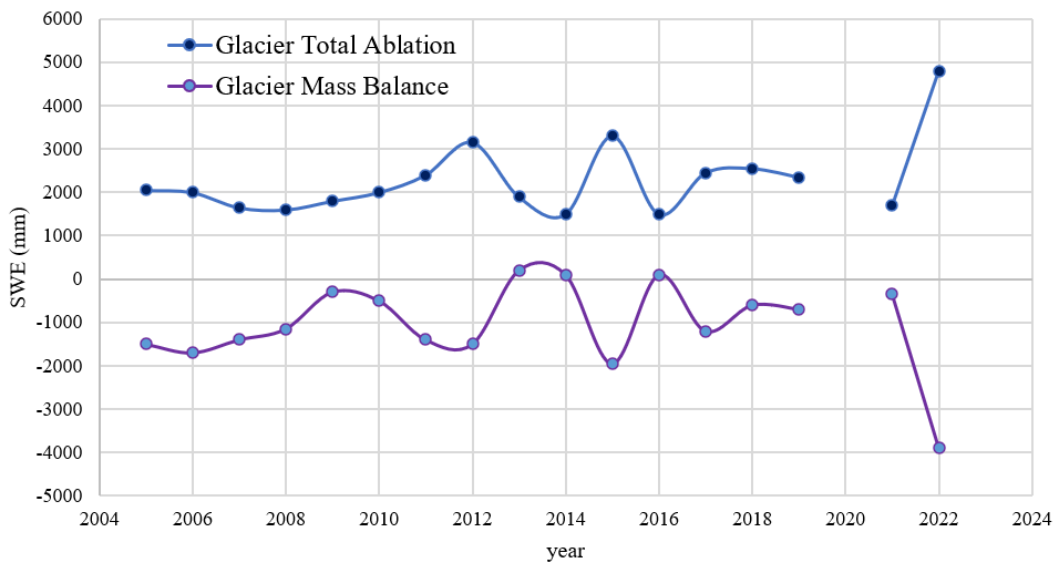


Figure 78. Annual Ablation and Mass Balance of Rutor Glacier.

Fig. 78 shows the Snow Water Equivalent (SWE) values related to the total melt activity of the glacier year by year and the Mass Balance of the glacier again in terms of SWE. Of course the two behaviors are mirror-image, as the annual melt increases, the negative balance of the glacier will also increase, although this depends very much on the seasonal snow accumulation, in fact the behaviors are not perfectly symmetrical. Indeed, the thicker is the seasonal snowpack, the greater will be the protection on the glacial mass, especially during particularly warm years.

The air temperature time series, which has been provided with the same time interval as the Rutor mass balances (2005-2022), is correlated with the total ablation activity of the glacier for each year, thus the melting of the seasonal accumulation plus possibly melting of the portions accumulated the years before.

For temperature, a selection was made by considering the summer average of 4 months from the first of May to the first of September, this choice was calibrated using the Moving Average method over several time intervals (2-3-4 months) of each year, the best correlation was found by using the average for the interval listed above (1 May - 1 September).

The annual Rutor total melting and summer average temperature values are shown in **Fig. 79**.

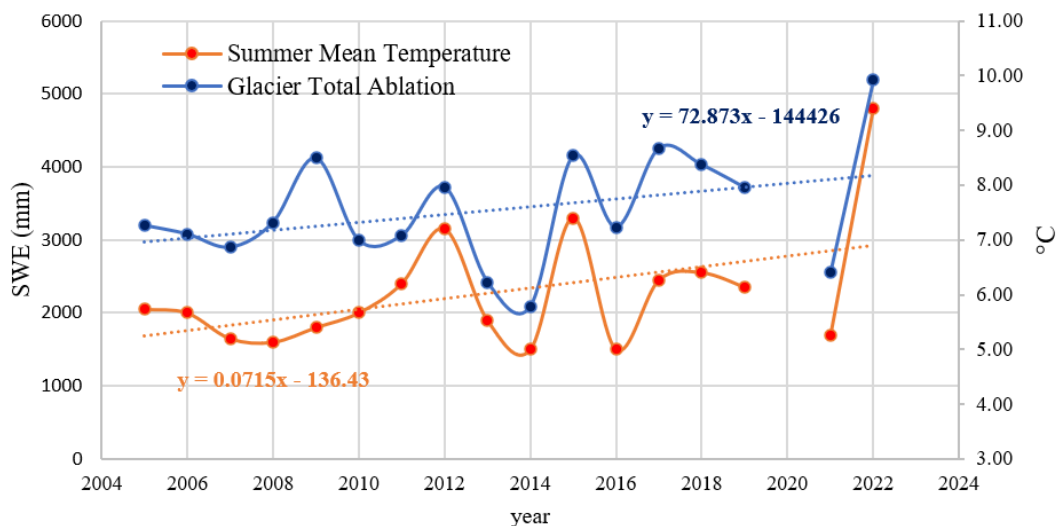


Figure 79. Annual time series of Summer Mean Temperature and Glacier Total Ablation from 2005 to 2022.

It can be seen that there is an affinity between these variables; the summer temperature trend turns out to be probably the parameter that most influences Rutor's melting processes. The only year in which there is a discrepancy between the two parameters is 2009, in which the peak of glacier melting is not followed by an increase in summer temperatures in the same year. This behavior may be due to an incorrect estimation of mass balances for that year, or to the misrepresentation of average summer temperatures for that year in which perhaps melting was concentrated in a particular month.

However in any case, it's worth to notice an increasing trends for both variables, almost synchronously are the interpolating recession lines in the **Fig. 80**, which rise to mark an average increase of 1.3 °C in temperature and 1300 mm(SWE) in melting from the beginning to the end of the period.

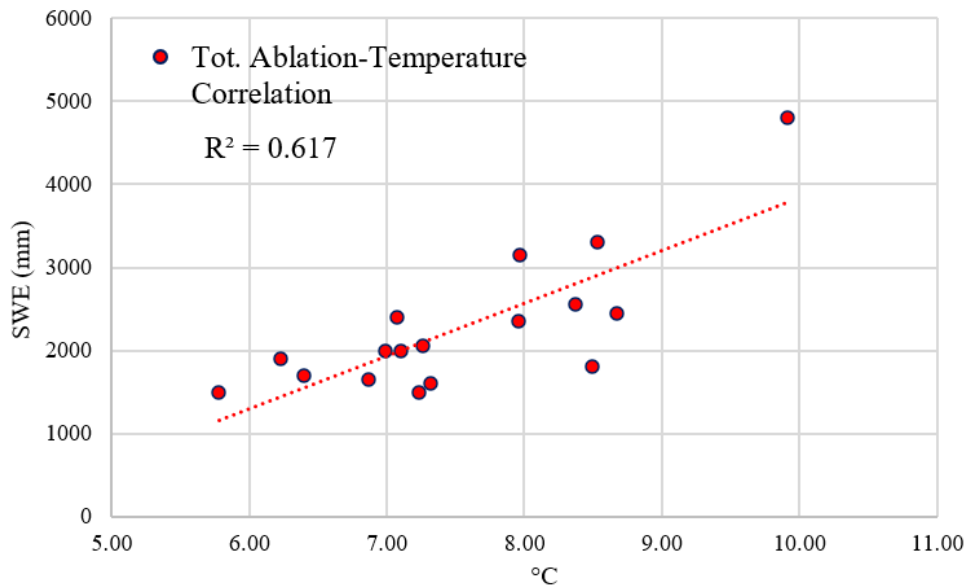


Figure 80. Correlation between Summer Mean Temperature and Glacier Total Ablation with coefficient of determination R^2 .

The **Fig. 80** shows the relationship between the two variables depicted above, it can be seen that there is a strong correlation between the two (Pearson's index $R = 0.79$) as shown in Method section 2.5. this result shows the strong relationship between melting and atmospheric temperature, also in glacial broad context and not only in punctual seasonal snow context.

This result is quite in line with the indices of determination of the statistical model shown above (sub-chapter 3.4), clearly the results are carried out based on completely different time scales, the model is based on snowmelt processes on a 2-hour time step, while the correlation between glacier and temperature are made on seasonal time step. This absolutely must become urgently relevant regarding the issue of Climate Change and how temperatures affect both snow and glacial melt cycles in Alpine context.

Next, the behaviors of Rutor glacier and Promise spring were analyzed graphically to ascertain possible relationships between them. In detail, after calculating the annual discharge and annual precipitation values characterizing the spring, these were transformed into normalized values becoming adimensional. These two were subtracted to find out the normalized residual discharge to be compared to the normalized Rutor mass balance values. In Methods sub-section 2.7, it was explained why mass balance values were used rather than total ablation values. Also, to make the comparison visible between the residual discharge and the mass balance, the sign to the latter was changed to make the glacier mass loss directly proportional to the increase in flow rates. Of course, the years in which the balance is positive have been set to zero since they do not result in a water supply for the spring.

Table 14. Normalized time series of: Spring Discharge (Q), Total Precipitation (Ptot), Residual Discharge (Q-Ptot) and Glacier Mass Balance (GMB), using two different normalization methods.

	Min Max		Normalization		Mean,Std		Normalization	
	Q	Ptot	Q-Ptot	GMB	Q	Ptot	Q-Ptot	GMB
2012	0.235	0.372	-0.137	0.385	-0.270	-0.298	0.028	0.715
2013	0.495	0.952	-0.457	0.000	0.559	1.344	-0.785	-1.520
2014	0.000	0.668	-0.668	0.000	-1.020	0.540	-1.560	-1.520
2015	0.001	0.429	-0.428	0.500	-1.017	-0.136	-0.881	1.386
2016	0.018	0.054	-0.035	0.000	-0.961	-1.198	0.237	-1.520
2017	0.134	0.252	-0.119	0.308	-0.594	-0.636	0.042	0.268
2018	0.713	1.000	-0.287	0.154	1.253	1.480	-0.227	-0.626
2019	0.098	0.188	-0.090	0.179	-0.706	-0.818	0.111	-0.477
2021	0.535	0.341	0.194	0.090	0.688	-0.385	1.073	-0.998
2022	0.287	0.000	0.287	1.000	-0.103	-1.350	1.247	4.291

The parameters analyzed for the juxtaposition of annual spring regimes and glacier melt processes are listed in the **Table 14**. The time series reconstructed by normalization are Discharge (Q), Total Precipitation (Ptot) and Glacier Mass Balance (GMB) while the difference between Q and Ptot, which determines the residual discharge, is directly calculated from the difference of normalized values given the impossibility of relating the two variables of discharge in cubic meters and precipitation in millimeters. Normalizations were calculated using both the MinMax and Mean,Std methods as explained in the Methods chapter. Graphs of the time series: GMB and Q-Ptot, normalized by mean of the two methods, are shown in **Fig. 81**.

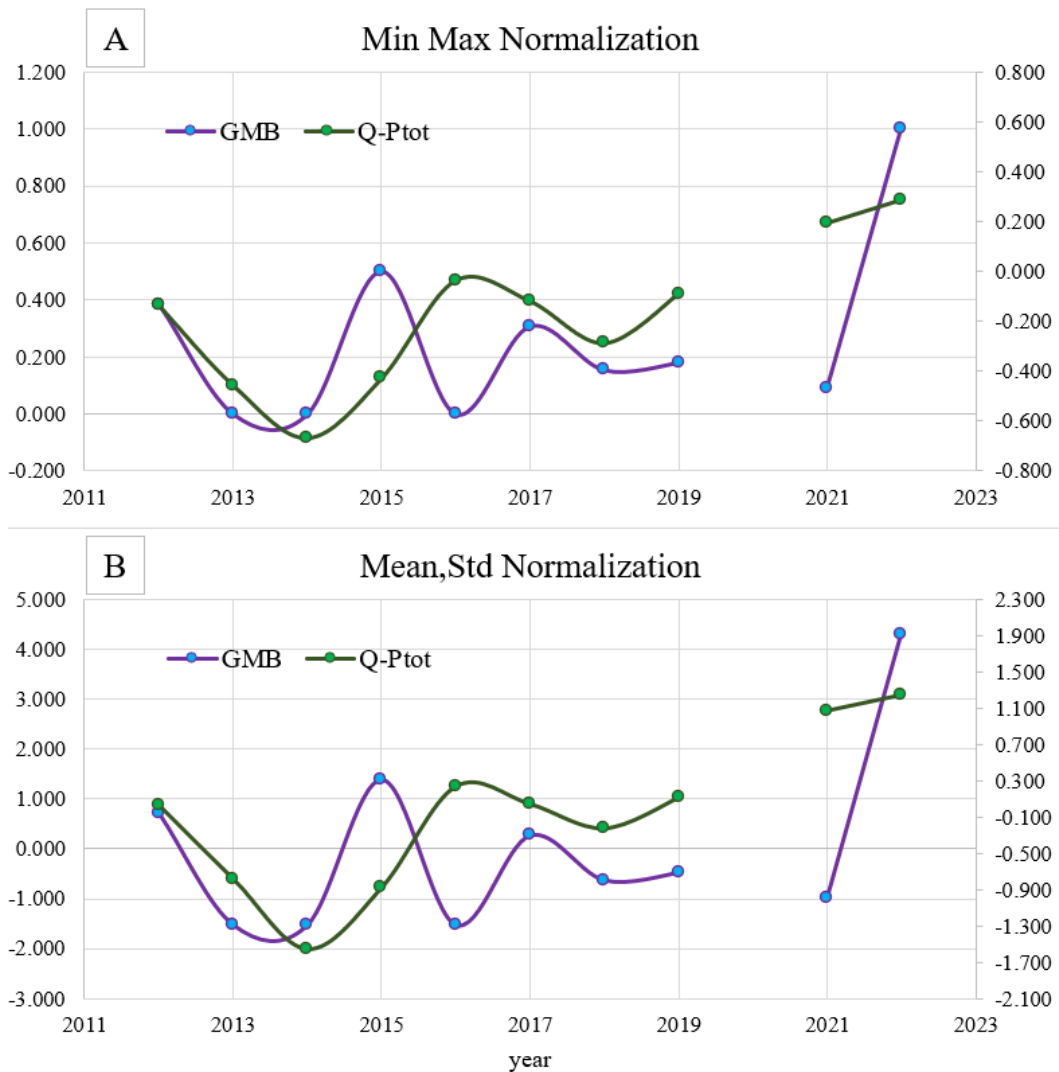


Figure 81. A: Graph representing normalized Residual (Q-Ptot) and Glacier Mass Balance (GMB) with Min Max method; B: Graph representing the same normalized variables with Mean,Std method.

The results from the two normalizations are presented in **Fig. 81**. The comparison between the discharge residuals (Q-Ptot), showing the changes in what have not been affected by solid and liquid precipitation input, and the GMB Mass Balance, changed in sign with initial values greater than zero, is plotted.

It can be seen that the two series are not perfectly correlated, but there seems to be a phase shift between what are the peaks of the mass balance and residual discharge. In fact, the residual discharge responds to the first decrease in the mass balance with a time-lag and increases its lag when the balance shows a change in trend by pointing upward. Thereafter, the residual (Q-Ptot) decreases but still remains with values close to the first peak. It then increases again after 2019 until it finds its maximum in 2022.

This behavior of the residual, which appears to be a dampened upward oscillation in response to the Mass Balance, surely indicates that glacier melt does not generate an immediate reaction in the spring, this surely dictated by the distance between the two. This leads us to infer that the spring responds to more than one hydrogeologic system, a neighboring circuit that gets water rapidly shown by the hydrograph response to seasonal melting processes, and a more distant circuit that recharges the aquifer with water from the glacier. Being more distant, the latter may arrive with a delay and act with a cumulative action in the aquifer, which shows progressive recharge over the years.

3.6 Shallow landslide simulations

As mentioned in the methods chapter, two experiments were carried out on the landslide simulator to evaluate soil instability conditions as a result of infiltrative inputs. So with the set up consisting of the TDR, georesistimeters, and soil temperature sensors, the parameters of water content and temperature within the soil were kept monitored.

The first experiment involved placing the soil layer overlain by a less thick layer of compacted snow with a density of 350 kg/m³, which was transported from the village of Montespluga (province of Sondrio) using polystyrene insulating containers.

The weather conditions during the experiment were fairly constant, 19°C air temperature and 35 % humidity with clear skies.

Experiment 1 starts as soon as the snow is put on the soil layer and the simulator is tilted 35°. Three photography shots showing the progress of the experiment, which has a duration of almost 4 hours, can be seen in **Fig. 82**.

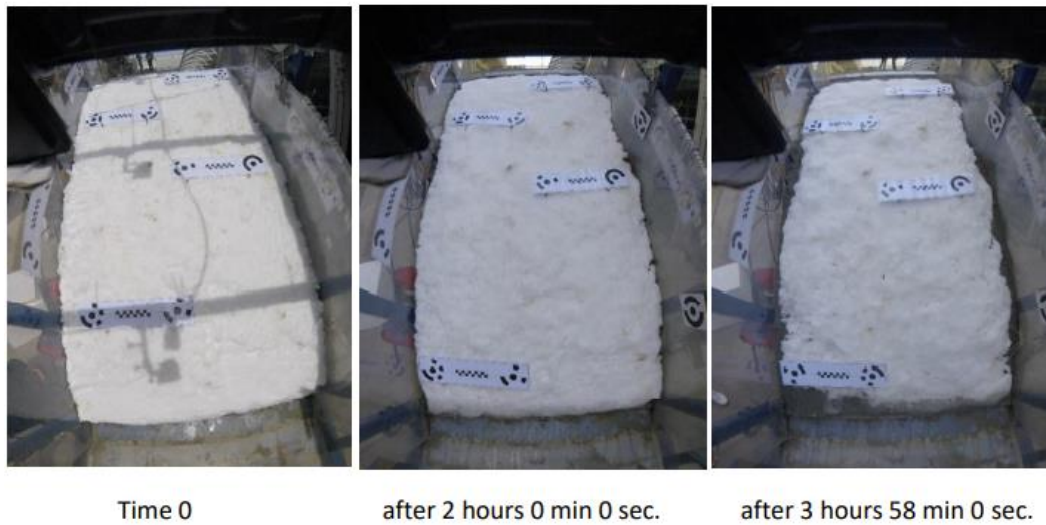


Figure 82. Top view photos from the GoPro cameras in different moments during the Experiment 1.

As can be seen in **Fig. 82** at the end of Experiment 1, there were no instabilities that led to collapse, nor did fractures open along the slope. This is due to the evolution of the infiltrative process between snow and soil, which will be explained by showing sensor records.

The snowpack thinning values are shown in **Fig. 83a**, in this case they are not taken to evaluate the previous statistical model because they are acquired in a localized arrangement at the edge of the snowpack. Moreover these values are gathered with a ruler, so they are less precise and less representative measurements than the three-dimensional survey measurements.

In addition to the snow thinning values, there are those related to soil water content (**Fig. 83c**) and those related to soil temperature upstream downstream and in the center of the simulator (**Fig. 83d**).

It can be seen from the TDR that the water content, initially at 6 %, begins to detect infiltration from the snow after about 100 minutes from the start of the experiment. Being in the middle of the ground, at a depth of 7 cm, and taking time for the snow to melt, it is legitimate for some time to pass before it detects an increase in water content. The water content is found to increase to 12 percent at minute 200, and from that point it stabilizes.

Concurrently, ground temperatures that start at 14 degrees gradually drop to between 8 and 10 degrees Celsius. This is due to heat exchange with the snowpack on the surface, which in turn exchanges heat with the ground and transforms it into latent heat by releasing water. Since the temperature sensors are at the bottom of the ground, 14 cm depth, it must be considered that the layer most in contact with the snow may have

reached temperatures near zero after about 200 minutes reaching a situation of thermal equilibrium with the snow.

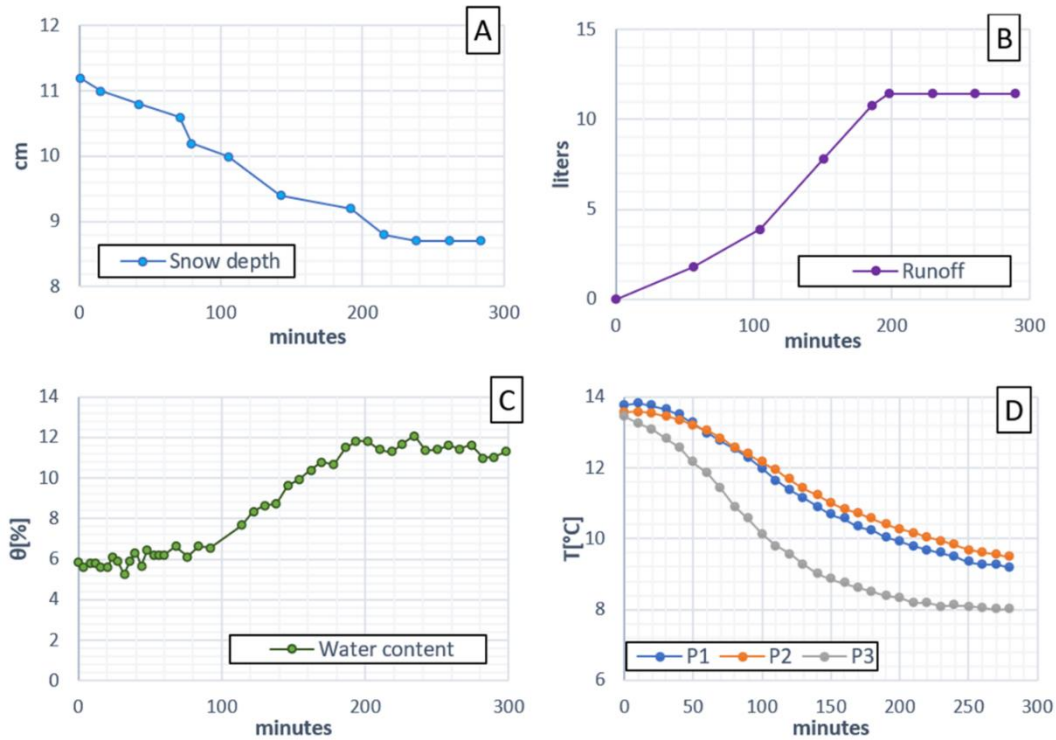


Figure 83. A: snow depth evolution recorded by observation; B: cumulated runoff water gathered inside the bawl along the experiment; C: volumetric water content recorded during the experiment; D: temperature registered by the three sensors placed along the landslide simulator located at the maximum depth of soil layer.

This assumption is also validated by graph **Fig. 83b**, which shows the calculated runoff rate at the foot of the landslide simulator. In fact, it can be seen that in the first 100 minutes, faced with significant thinning of the mantle, there is less runoff, so the amounts of water infiltrated into the soils are greater. Between 100 and 200 minutes, runoff increases, because the soil as it cools reduces the infiltration phenomenon by acting as a barrier. And finally found the thermal equilibrium between snow and soil the heat exchange ends and the snow near the interlayer no longer melts.

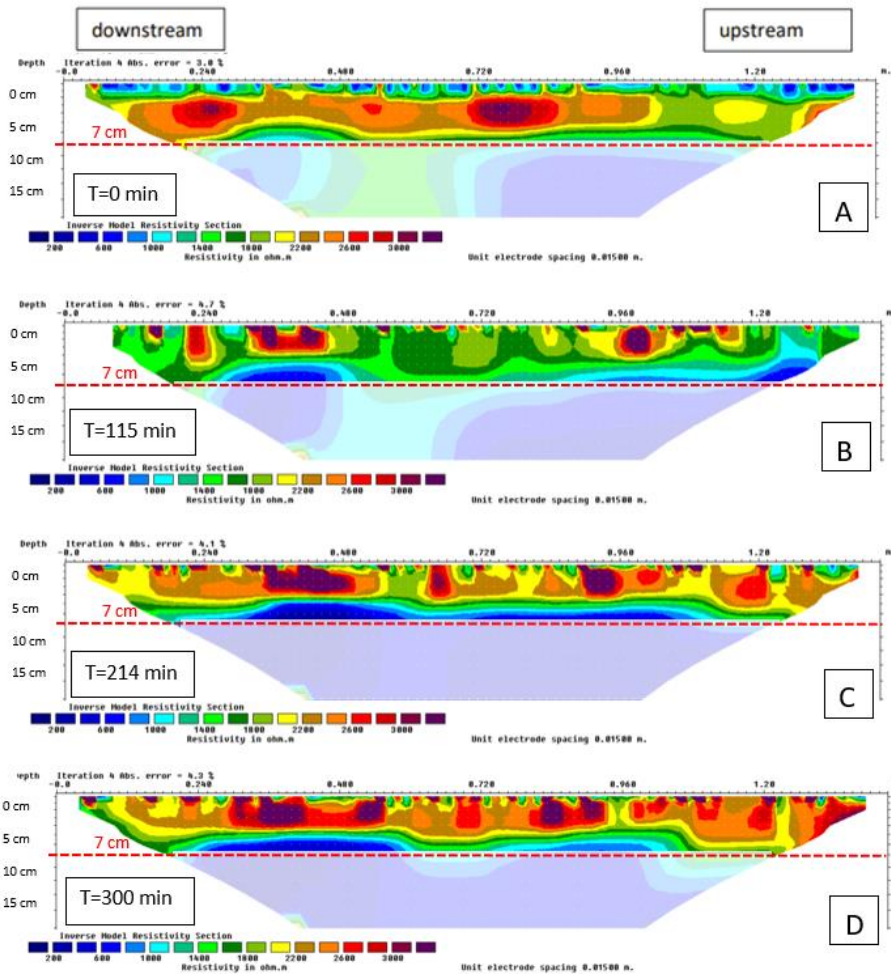


Figure 84. A,B,C,D,E: tomography results at different moment during the experiment.

Certain aspects described above from the other measured parameters can also be verified in geophysical tomography sections. The color scale seen in **Fig. 84** indicates the water content calculated from the resistivity of the soil medium, the more water the higher the electrical conductivity (toward blue: high electrical conductivity; toward red/purple: low conductivity). The geophysical section is to be considered reliable only in the top half, as below the metal temperature sensors alter the electrical conductivity parameter, in fact below portion of the section has been obscured.

At time zero (**Fig. 84a**), low conductivity is seen in most of the layer, with the presence in the surface part of small blue dots where there is high conductivity representing the beginning of infiltration from the snow layer. Then, in section at 115 minutes from the beginning (**Fig. 84b**), it can be seen that most of the layer tends to green tone colors, signifying that from the surface, water is transitioning throughout the layer by infiltration. In the following sections (**Fig 84c-d**), at 214 and 300 minutes from

beginning, it's worth to notice a decrease in the presence of water in the layer, getting back to yellow-orange shades for the 214 minutes section and orange-red shades for the 300 minutes one. This means that the transition of water in that band decreases and then ends moving into the lower layers close to the impermeable bottom.

This information is very important because it verifies the observations made in describing the **Fig. 83**, especially the TDR values that tell us a transition of water for a range of time and then stabilizing again. This then may be dictated by the cooling of the soil that gradually becomes less and less vulnerable to infiltration until it is in thermal equilibrium with the snow. So as seen in the runoff results, that increases as the soil temperature decreases. This indicates that the water, having snow cooled the soil, finds preferential pathways through the snow or in the interlayer between snow and soil.

Basically, it does not result in failure of the soil, because as shown by other experiments and the experiment shown below, a volumetric water content between 35 percent and 40 percent must be reached for saturation of the porous medium and therefore for landslide collapse triggering. Whereas in this case, a water content of 12 percent was reached by increasing only 6 percent from the initial volumetric water content.

The evolution of the second experiment on the landslide simulator is shown in next figure (**Fig. 85**). As can be seen, in this case there is no presence of snow, and snow melting acts from upstream simulated with the drains placed at the upper end of the soil.

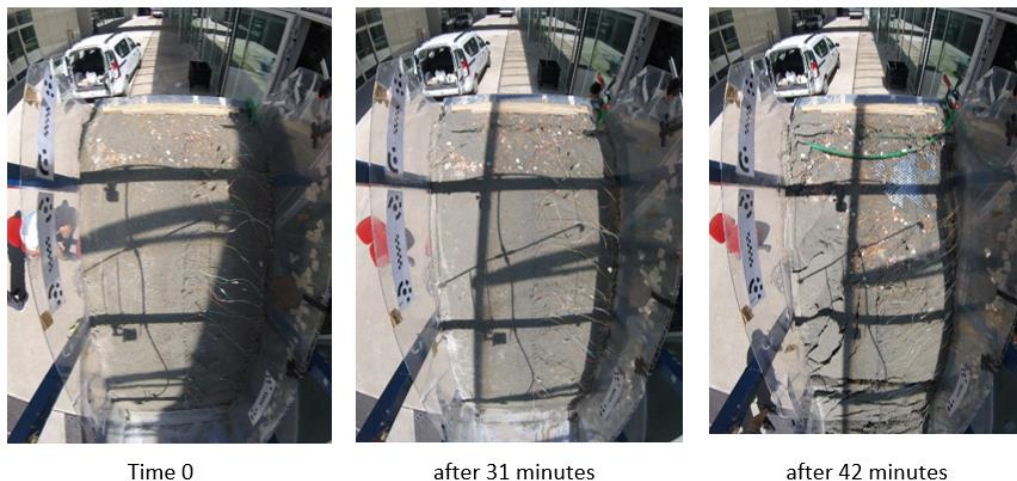


Figure 85. Top view photos from the GoPro cameras in different moments during the Experiment 2.

In this case, unstable conditions due to saturation of the porous medium are reached. After only 31 minutes the first fractures begin to appear, and after 42 minutes there is soil collapse

The results collected from the TDR and geophysical sections during the experiment are shown in **Fig. 86**.

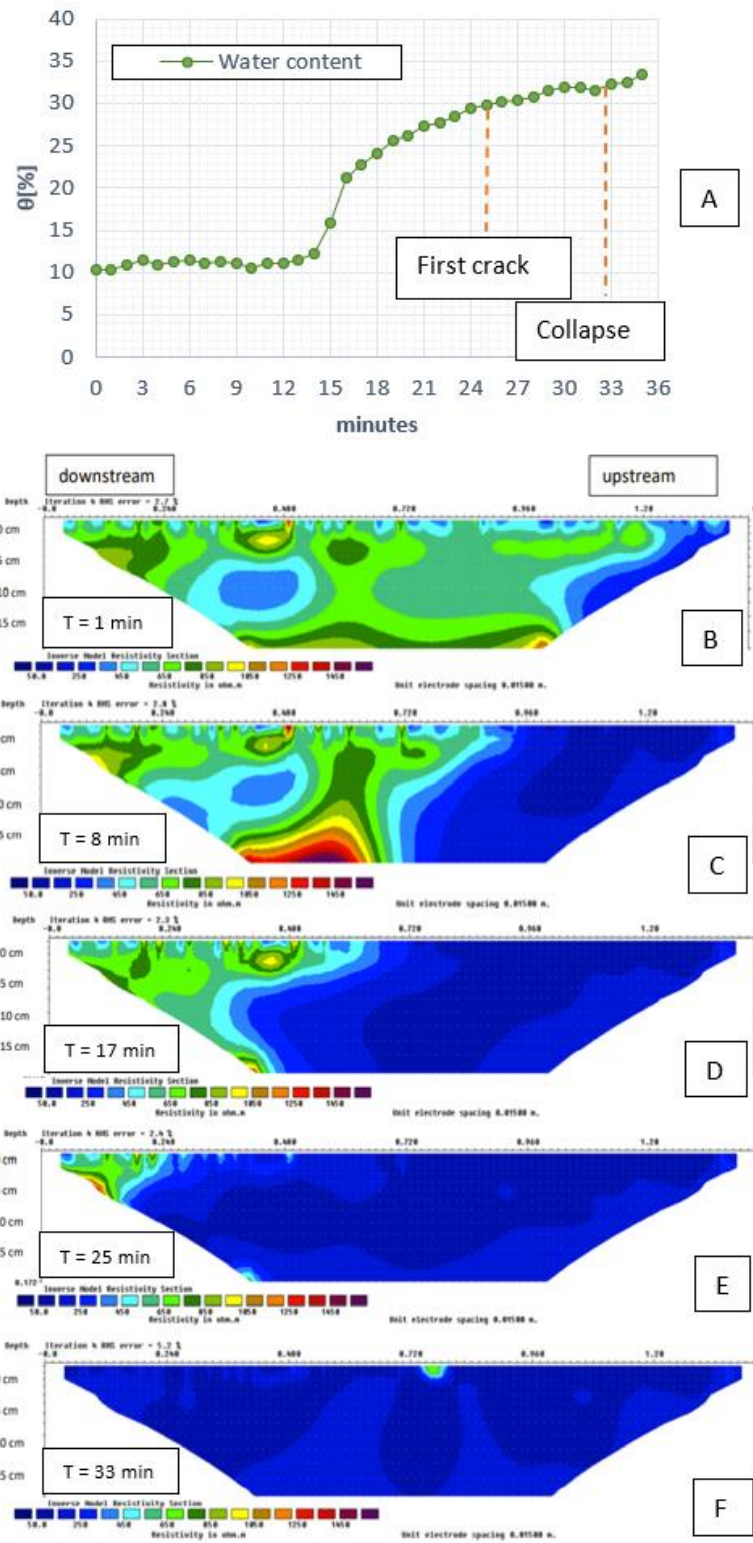


Figure 86. A: Water content detected by TDR during the simulation. B, C, D, E, F: tomography results at different moment during the experiment.

Water seeping from upstream takes 13 minutes to arrive at the TDR sensor located in the center of the simulator. Once it arrives to TDR, the water causes the violent rise of volumetric content with a "wave" effect, quickly reaching saturation conditions.

Geophysical sections (**Fig. 86**) better delineate the transition of water within the porous medium; without thermal barriers generated by snow, water easily pours into the ground and by gravity migrates downstream between the underlying impermeable surface and the ground surface.

Progressively, as can be seen from the blue-colored area indicating high electrical conductivity, the area with low water content (green) changes to an area with high water content (blue), until the section becomes totally of this color (**Fig. 86**). At this point, the saturation of the porous medium is completed and the first fracture appears in the last section (33 min), which is the only non-blue area indicating the opening of the soil medium by lowering the electrical conductivity value.

The collapse achieved by this experiment is total and rapid, involving all portions of the soil simultaneously increasing the speed of the dynamics and the power of impact. This deduction is made on the comparison made with other experiments where the water input was given by simulated rainfall, leading to slower collapse mechanisms with partialization of movement.

Chapter 4

DISCUSSION

4.1 Mountain aquifer discussion

From the conducted analyses, the results of which are shown in the previous Chapter, it is normal to wonder how some springs have an increasing discharge trend despite there is a decrease in liquid and solid precipitation over the same time period. As it has been shown, the hydrogeological circuits studied respond quite quickly to meteorological inputs, so it is expected that over the multi-year period studied the springs will show a decreasing trend in accordance with rainfall regimes.

Moreover through the statistical model on nival melting and the correlations between temperature and melting of Rutor Glacier, the importance of atmospheric temperature in driving the processes of wet metamorphism and thus to the transformation from solid to liquid state of the cryosphere has emerged. Given the marked rise in temperatures over the time span studied, it is immediate to infer that ablation occurs even for those elements that were previously perennally frozen.

From this consideration it is worth to reflect on the interaction of permafrost and glaciers with the mountain hydrogeological system of the Aosta Valley. In fact, analyzing the regional territory, it is important to highlight the morphology and the altimetry of the region. In fact, the average altimetry of the Aosta Valley is the highest in all of Italy, consider only that 59 % of the territory is located at an altitude greater than 2000 m a.s.l., above this altitude in the Alps the periglacial domain is already defined as far as the northern slopes are concerned. While for the southern slopes the periglacial domain generally lies above the altitude of 2300 m.a.s.l. Generally, permafrost is found in the Alps diffusely above the altitude of 2500 m. a.s.l.

In **Fig. 87** it is shown a probability map of the presence of permafrost in the Alps from the University of Zurich UZH made by the authors (Boeckli *et al.*, 2012), which represent in the Aosta Valley region the areas with the most probable presence of permafrost in blue and the least probable areas in yellow. However, it is worth to notice the extensive cryosphere coverage between glaciers and permafrost in this region.

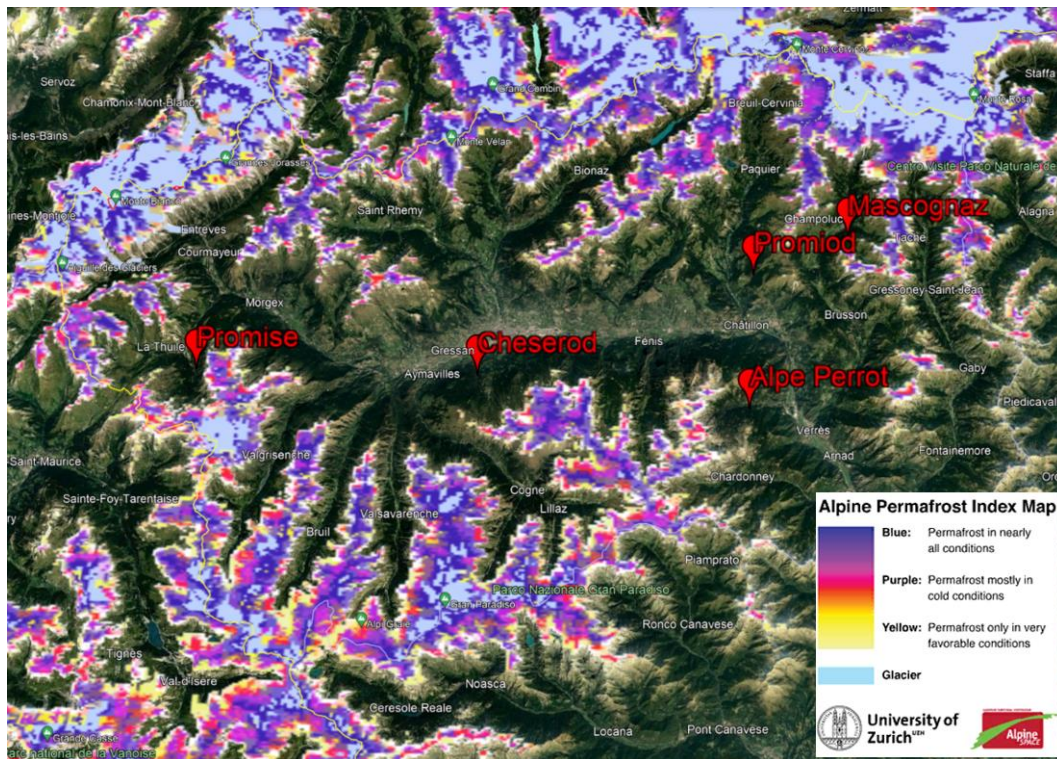


Figure 87. Alpine Permafrost Index Map (Boeckli et al., 2012) with springs location.

Of course, it must be understood what portions of permafrost actually contain water reserves. For as it has been described in Introduction Chapter, the definition of permafrost indicates portions of soil below 0°C but does not necessarily include an ice matrix.

For this reason, it is not easy to understand, with climate change, what the new water supplies from these frozen portion of land might be.

In the analysis of the springs, it is immediately evident which ones are those where there are no external inputs other than rainfall and snowfall, while noting on the other hand the springs that have experienced surplus inputs over meteoric inputs. In particular, this is pointed out in sub-chapter 3.3, where the annual precipitation and flow balances are made. Here in fact, it is understood that there are springs whose balances are correlated, annual discharged volumes with annual mm of precipitation, while there are springs whose balances are less correlated in conjunction with some specific years.

In this regard, the springs that never seem to be affected by permafrost or glacier melt are those of Mascognaz and Promiod, while those where distorted balances are discernible are Alpe Perrot, Chesserod, and Promise. In fact, among the latter, especially after 2019 there is a clear disparity between the increasing spring discharge in contrast to lower precipitation.

It will be now considered the updated information from RAVdA, 2022 related to the census of rock glaciers and glaciers throughout the Aosta Valley in order to understand the behaviors obtained from each spring by integrating some information from their surrounding area.

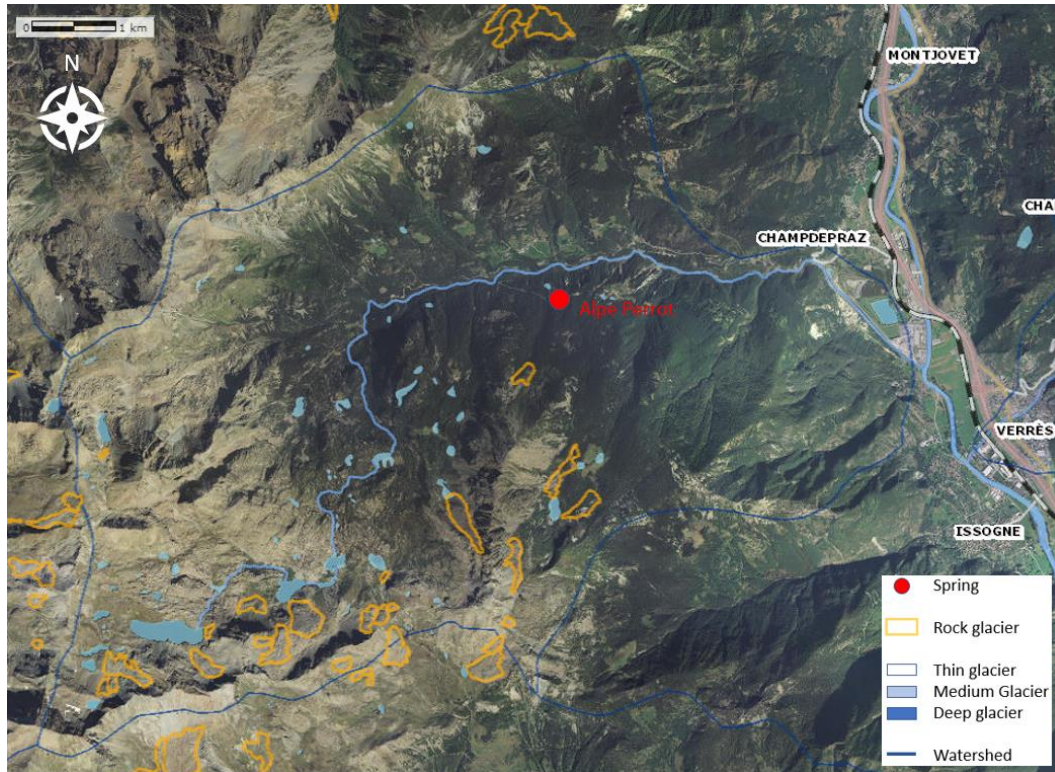


Figure 88. Alpe Perrot territory with RAVdA, 2022 information about glaciers and rock glaciers.

As noted in **Fig. 88**, Alpe Perrot lies in a hydrographic basin exposed mainly to the North-East with the highest point at elevation 3145 m a.s.l. There are no glaciers in the basin; near the apex of it are periglacial lakes formed by the semi-flat morphology of this area.

The N-E exposure along with the North is certainly one of the coldest, and the elevations of the basin certainly make the site suitable for permafrost formation. In fact, several rock glaciers have been surveyed in **Fig. 88**, they are distributed over different elevations starting from those immediately above the spring at 1800 m. a.s.l. to those near the top of the basin at elevations close to 2800 meters. Almost all of the mapped rock glaciers are located on the hydrographic right of the basin, such as the Alpe Perrot spring, so the possibility that the melt of one of them will go to intercept the spring is quite high.

As noted by the data from the reference weather station, Champorcher - Petit Mont Blanc, it measures an average temperature increase over the period of 1.32 °C, which means a rise in the thermal zero of about 200 meters in elevation. This rise in the thermal range above zero, may have affected a rock glacier in the basin that was still intact, causing its melting and releasing water that subsequently has been recorded by the spring sensor especially for the years 2019-2020-2021 where there are significant spring discharged volumes compared to the low rainfall.

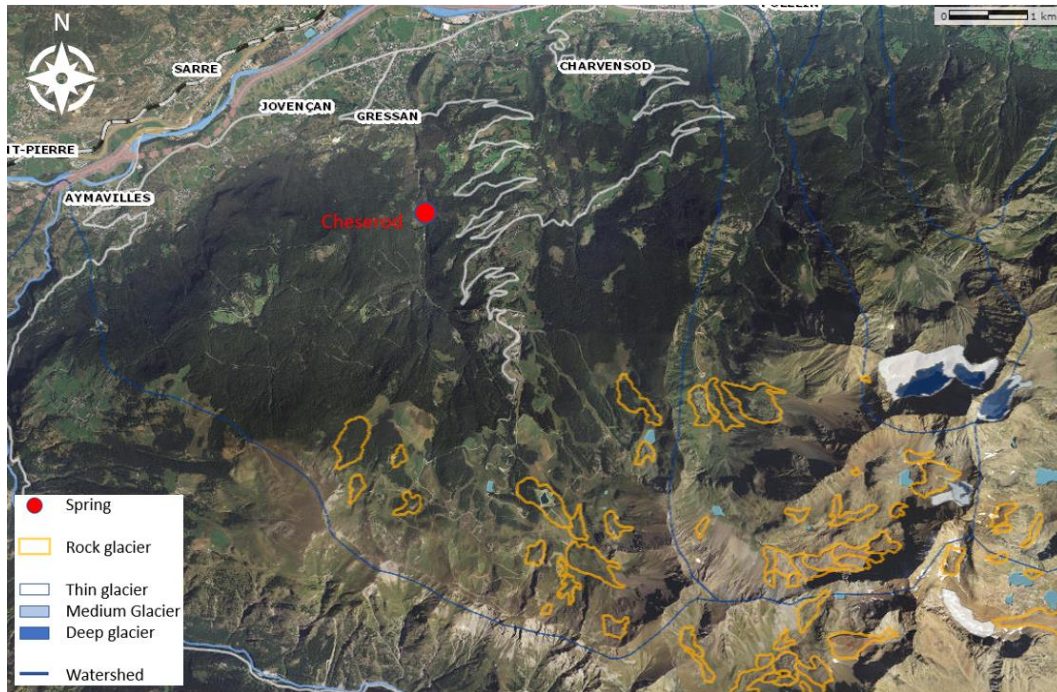


Figure 89. Chéséród territory with RAVdA, 2022 information about glaciers and rock glaciers.

The Chéséród spring is located in a hydrographic basin whose closing section culminates at the conjunction of the Dora Baltea, which is the main river of the region. In this case, the basin has a predominantly northern exposure, with elevation ranging from the bottom of the valley (550 m a.s.l.) to the highest point at an elevation of 3041 m a.s.l.. In the basin as in the one of Alpe Perrot, several rock glaciers are present and illustrated in **Fig. 89**. These also range over different elevations from 2200 meters to near the summit at 2750 meters.

Three of these rock glaciers have significant dimensions reaching lengths of nearly 900 meters with widths between 250 and 350 meters. It is very likely, given the exposure of the slope, that the rock glaciers higher up are still intact and still retain water resources. This cannot be said for the rock glaciers present at the lower elevations, which, as in the previous case, given the temperature increase recorded by the Gressan

Pila-Leissè reference station of 1.67°C shown in the Results Chapter, are very likely to have been impacted by losing water reserves previously conserved in a solid state. This would result in the increase in spring flow detected at Cheserod in the years 2019-2020-2021 compared to the calculated rainfall in the respective years. It is no coincidence that these anomalies occur in the very same years as they do for Alpe Perrot. In fact, they have similarities from the point of view of basin exposure, permafrost-populated elevations, and atmospheric temperature increase detected by weather stations.

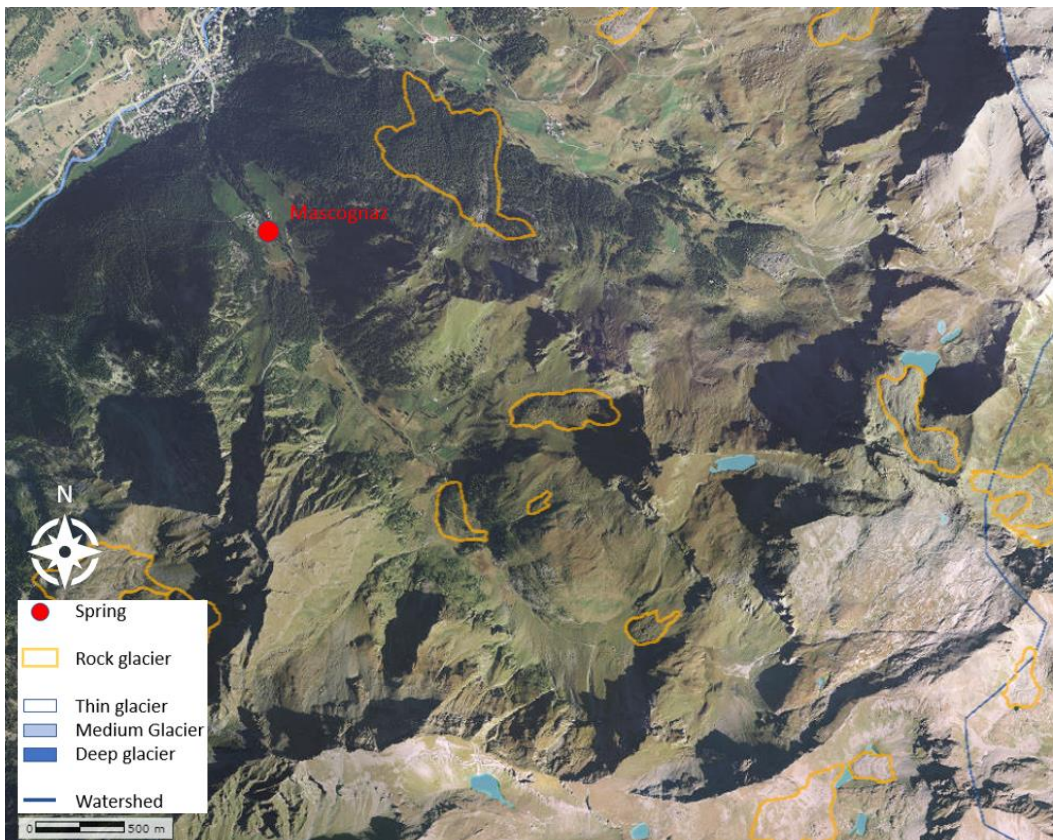


Figure 90. Mascognaz territory with RAVda, 2022 information about glaciers and rock glaciers.

The Mascongaz spring basin is shown in **Fig. 90**. It is significantly smaller than those shown previously and has a North-West exposure. It develops from an elevation of 1550 m to a maximum elevation of 3023 m a.s.l.

Inside the basin 4 rock glaciers of small size are mapped, the largest one to the right of the spring falls in the neighboring catchment area so it does not affect the spring. These rock glaciers are all located between the elevations of 2000 and 2300 m. a.s.l., thus at a lower elevation range than illustrated above for Cheserod and Alpe Perrot. Thus

despite the exposure of the basin being quite favorable for ice preservation, it is possible that the lower elevation of these elements has already played a key role in their preservation and therefore these have already lost their water content in the past. The hypothesis that they are relict rock glaciers is to be juxtaposed with the hypothesis that these deposits never had a matrix of water in the solid state.

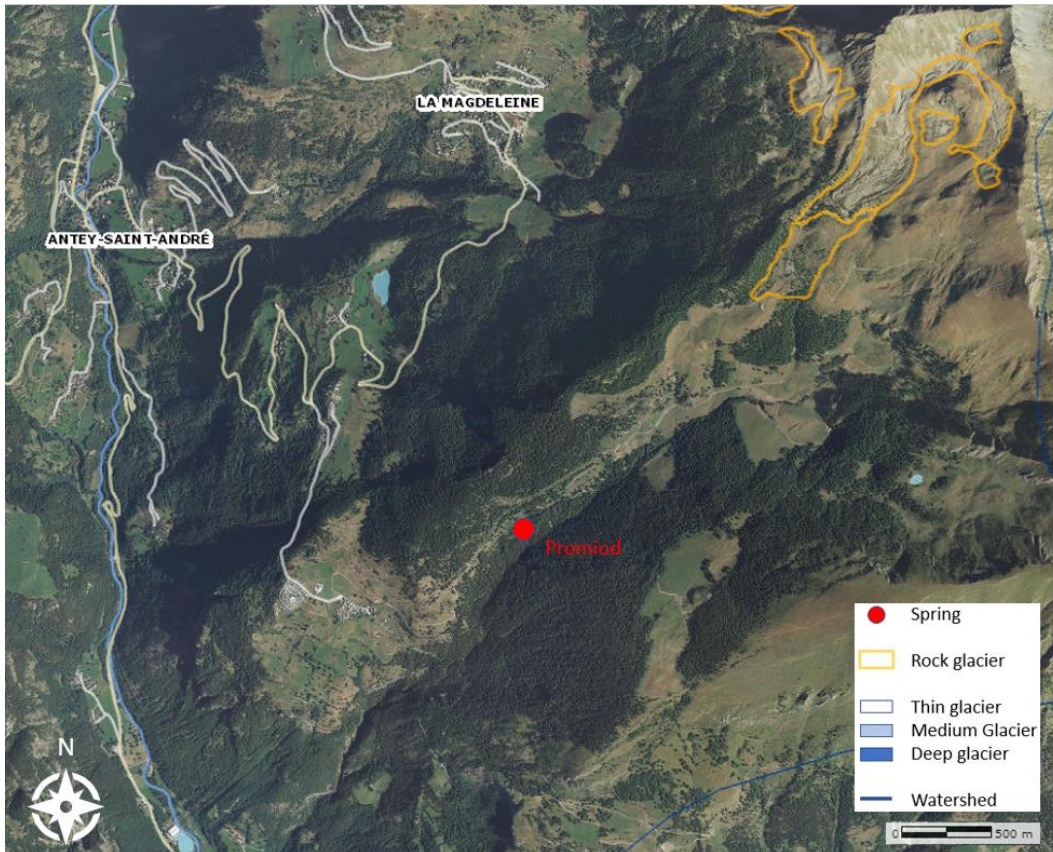


Figure 91. Promiod territory with RAVdA, 2022 information about glaciers and rock glaciers.

Promiod is located within a fairly small hydrographic sub-basin, the development of which ranges from 740 m a.s.l. to a maximum elevation of 2652 m a.s.l. In addition to being lower than the others, the Promiod basin also has a South-West exposure that is not favorable for the generation and maintenance of permafrost.

In **Fig. 91** it can be seen that within this hydrographic basin a single rock glacier has been cataloged, developing from the top of the basin along the watershed determined by the ridge. Although the latter has a considerable size of about 1900 meters, it is unlikely that it still retains large portions of ice matrix, given the basin's exposure and its low elevation ranging from 2100 to 2500 m a.s.l.

Certainly the Promiod spring, turns out to be in line with precipitation regimes, not experiencing extra amounts from permafrost melting. This may be associated either

with the absence of "active" and icy rock glaciers in the spring basin or with the fact that the spring has a hydrogeological circuit that does not go to intercept cryosphere melting processes. In fact given the small discharge rates of the spring, it is likely that its inputs are derived from a much smaller recharge area than the size of the catchment area shown in the map (**Fig. 92**).

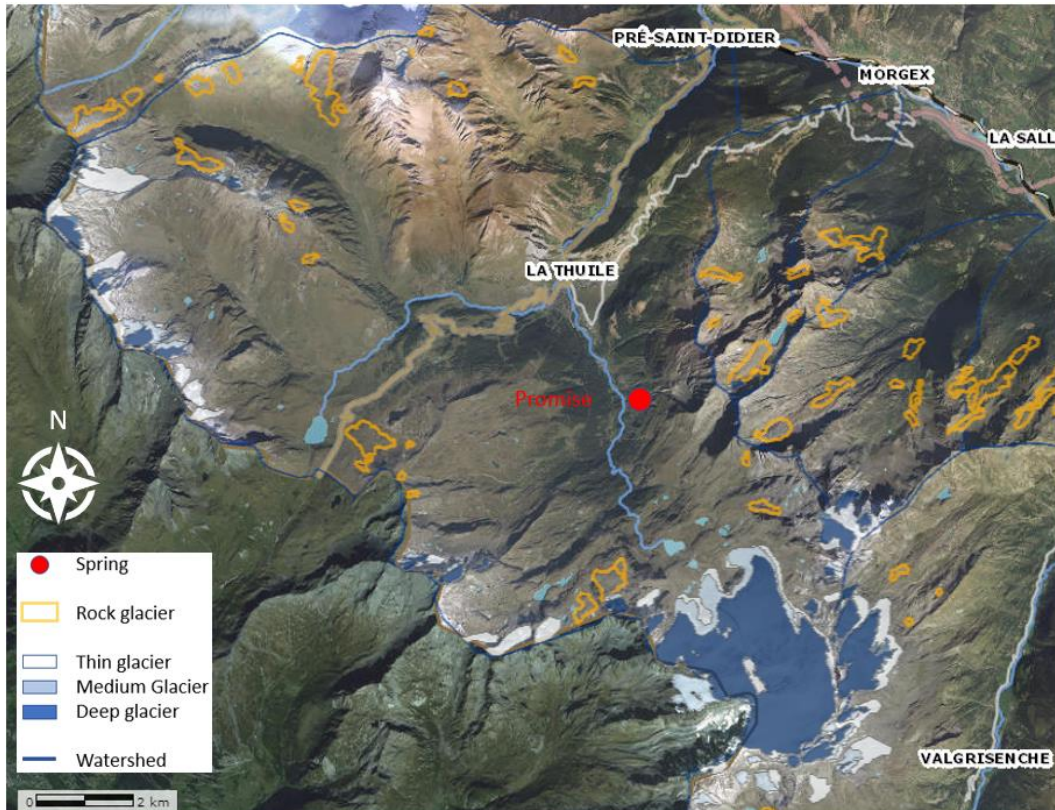


Figure 92. Promise territory with RAVdA, 2022 information about glaciers and rock glaciers.

The Promise hydrographic basin, depicted in **Fig. 92**, has a North-West exposure and develops from the valley floor where the Dora Baltea river flows (1000 m a.s.l.) to the summit of Testa del Rutor (3486 m a.s.l.). Below the main peak there is the Rutor glacier accurately described in sub-chapter 2.7; it is one of the largest in the region and, as seen from Arpa mass balances, it has been suffering from abruptly rising temperatures in recent years. The fact that summer melting processes exceed those of winter accumulation generates a loss of the glacier's total mass, which releases huge amounts of water.

There are also scattered rock glaciers in the basin that are not very relevant to the spring, which hardly interacts with them given their geographical locations. In fact, the

increase in Promise flow rate for simplicity's sake is to be matched entirely with the increase in glacier melt processes.

Of course, compared to Alpe Perrot and Cheserod, this case is much more glaring about the correlation between cryosphere and the hydrogeological system examined. In the previous cases, rock glacier elements are assumed generally to be water-depleting but there is no certainty about which ones are specifically losing water, while in this case the source of surplus water arriving at the spring is known.

Table 15. Summary of spring hydrographic basin information.

	m.a.s.l of the highest point of the hydrographic basin	Basin Exposition	Presence of Permanent Cryosphere inside the hydrographic basin of the spring
Alpe Perrot	3145	N-E	Many rock glaciers
Cheserod	3041	N	Many big rock glacier (3 of them massive), Glacier body in the adjacent valley
Mascognaz	3023	N-W	3 small rock glacier
Promiod	2652	S-W	Presence of a big Rock glacier close to the peak of the basin, it is possibly relict according to the exposition and altitude
Promise	3486	N-W	Presence of Rutor Glacier and two small rock glaciers

In **Table 15**, the spatial characteristics described above are listed. It is easy to find the similarities between the Alpe Perrot and Cheserod basins, both of which are similar in size with the same exposure and with many permafrost features within them. In addition, the identified permafrost spreads over different elevations also making the melting of new ice sectors in recent years more plausible. In addition, the water supply in spring that can be correlated with permafrost melting occurs during exactly the same

years between 2019 and 2021, which are the same years where the Promise discharge also increases significantly.

Therefore, there is also a temporal correlation between what happens between the three springs that are affected by the cryosphere, indeed, they show just in recent years discharged volume values no longer justified by precipitation values.

In contrast, the Promiod and Mascognaz basins, although different in exposure, show conditions in which the ice matrix in the rock glacial bodies is probably already reduced to small portions or even relict long ago.

4.2 Shallow landslide discussion

Experiments conducted in the laboratory were able to show us the dynamics of the interaction between soil and snow from the point of view of thermodynamics and water circulation. Effectively, the temperature of the snow, which is always in thermal equilibrium and never exceeds 0°C, in turn cools the surface layers of the soil by decreasing its absorption capacity.

The dynamics of the process is depicted in **Fig. 93** and shows the main stages found in the laboratory experiment. In the first stage, as soon as the snow is placed on the ground, there is a marked thermal gradient between the two porous media, the heat exchange between the snow and the ground results in the cooling of the ground, and the energy absorbed by the snow is transformed into latent heat, which therefore leads the release of water by means of the melting of the mantle (**Fig. 93a**). At this early stage much of the water infiltrates into the ground, because the ground temperature is not yet low enough, and some of water runs off to the soil surface.

At a later stage (**Fig. 93b**) the thermal gradient between the two media decreases due to the cooling of the soil, the still presence of a temperature difference generates the melting of the mantle in the interlayer, at this point however since the soil temperature has decreased, there will be less water infiltrating while there will be more runoff as shown in **Fig. 93d**.

In the last phase depicted in **Fig. 93c**, a situation is reached where the thermal gradient is set to zero and thermal equilibrium between snow and soil is achieved. In this phase, most likely an icy film of soil in contact with snow is generated, preventing further infiltrative inputs. This thermal barrier ensures that the soil is protected from potential instability phenomena resulting from saturation of the soil.

It can be inferred that once thermal equilibrium is reached, the processes of mantle melting leads to circulation by percolation through the snow layers or by runoff that occurs in the interlayer between soil and snow, but no more soil infiltration into the soil takes place.

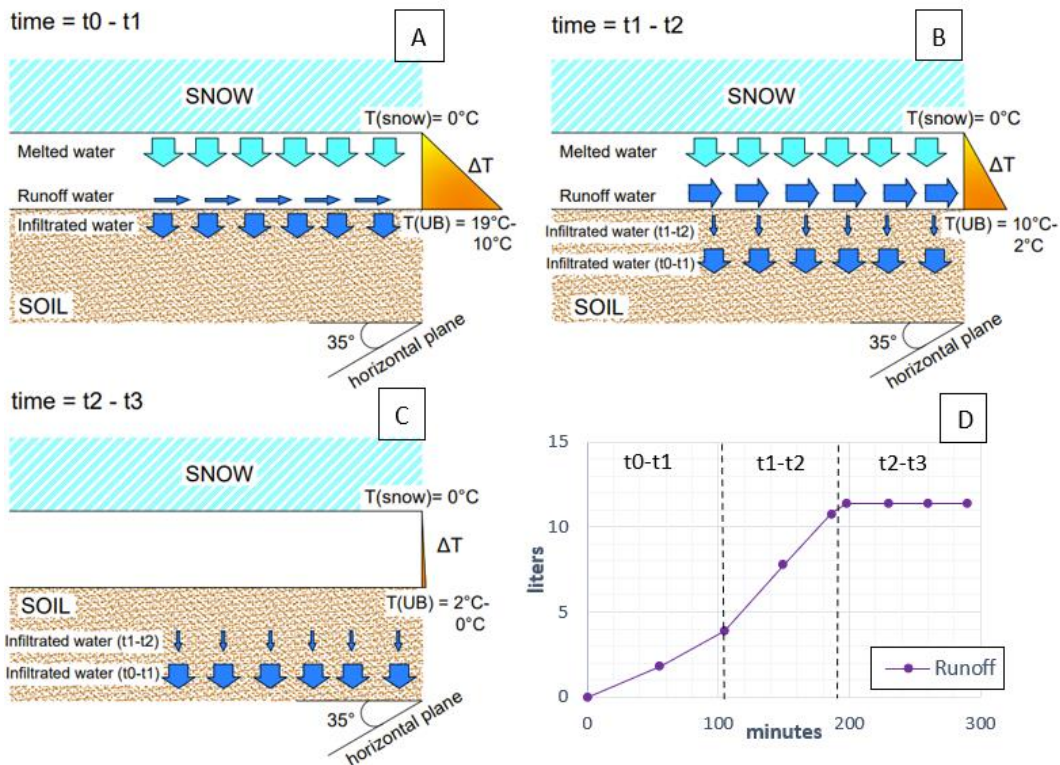


Figure 93. A, B, C: sketches representing the three phases of the Experiment 1. The size of arrows indicates qualitatively the amount of water in each of its component; Heat flux and temperature variation are represented with the temperature gradient symbol on the right side. D: Cumulative runoff graph obtained during the simulation divided in the three phases.

While the soils directly covered by the snow cover are thus protected, the same cannot be said for those that turn out to be downstream of the snow covers. In fact, as shown by Experiment 2, the lack of thermal barriers does not prevent the circulation of water within the soil.

Therefore, one must keep in mind the susceptibility of slopes that are downstream of very intense melt processes. Especially in key Climate Change where there are conspicuous inputs from snowmelt and glaciers that can lead to saturation of slopes occupied by poorly cohesive soils.

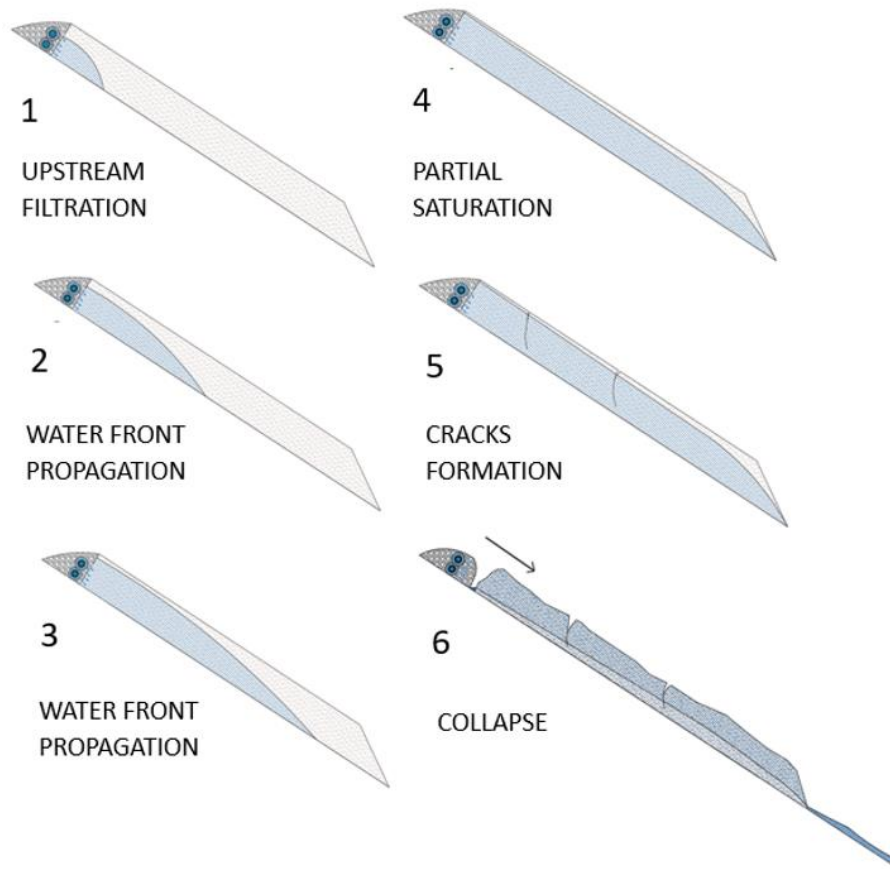


Figure 94. Six phases sketch representing the evolution of Experiment 2

Shown in **Fig. 94** are sketches describing in a simplifying way the dynamics of collapse by the progressive saturation of the soil portion. As it has been also mentioned in the Results chapter, this type of water circulation parallel to the impermeable layer generates a different collapse mechanism than the classical one, involving the whole soil portion in the movement. In this way, the velocity of the mass involved turns out to be greater along with the destructive force of the phenomenon. Therefore, future studies should analyze in more detail the hazard of this specific phenomenon to improve risk management in mountain areas affected by climate change.

Chapter 5

CONCLUSION

In conclusion, the proposed thesis paper brings innovation to the study of water resources and how they are affected by climate change. Until now, especially in northern Italy, there has never been serious problems of water availability, since in winter there has always been conspicuous solid precipitation and in spring, summer and autumn, rainfalls distributed over the time span.

Now more than ever, we are faced with periods of heavy rainfall followed by periods of drought such as the one that occurred in 2022. Therefore, it is important to take advantage of methods that allow us to understand the influence of atmospheric phenomena have on high mountain water resources.

For this, the combination of classical methods, such as Bussinesq and Maillet, recent methods (Cross-Correlation) and statistical methods, together with a spatial and geomorphological analysis, is definitely the best way to verify the trends of the analyzed aquifers.

First, however, it was necessary to characterize the bodies containing the resources of the 5 springs, because in a 12-year temporal analysis, it is appropriate to understand whether hydrogeological inputs and outputs condition themselves in the short term. This is because it is especially the case in large karst systems that the phenomenon of homogenization of the resource by the aquifer drainage system shifts the spring response considerably forward in time relative to the weathering phenomena that determined it.

So the aspect of the interaction between precipitation and spring flow rate had to be analyzed in a first step exploiting the Cross-Correlation between the time series of Flow Rate and Electrical Conductivity of the spring. With this, it was found that the 5 springs, having a high Cross-Correlation value, are well influenced by precipitation and snow melting by being part of the drainage categories of the " Replacement " or " Pistonage " type. This made it possible to put the water resources assessed through the springs in dialogue with the weather phenomena occurring in the Aosta Valley.

Another characterization of the aquifers comes from the hydrochemical analysis, which is important to determine the lithologies that structure the aquifer but especially whether there has been a change in water sources over the years, that is, whether the hydrogeological circuit belonging to a spring has been changed in any way. In the case of the springs analyzed, the hydrochemistry has remained almost constant over the years, this signifying a consistency of hydrogeological circuit over the years. This

information is important in order to be able to focus only on the quality of the water inputs and not the origin of them.

In fact, in light of the fact that the aquifer structure does not change, the divergence from precipitation phenomena may be due to melting of glaciers and permafrost.

A real important indication, comes from the analysis of the recession curve for all the springs, it expresses several information related to the well-being of the aquifer. Above all, it is crucial to see over the years the base volume of the water body net of flow peaks resulting from intense precipitation or nival melt events. In fact, as noted for all the cases analyzed, seasonally flow peaks occur, which in the case of the Aosta Valley springs are mainly caused by spring nival melt phenomena. In contrast to this, the oscillatory behavior between peaks during the time series hides the well-being of the spring, i.e., how much volume it has stored at the time when the spring has the minimum discharge of the year, this usually occurs when the winter season begins.

That said, the aquifer that seems to be increasing its resource the most is the Promise aquifer, which increases the availability of dischargeable water at the end of each recession period. This, it would be inexplicable only looking at the liquid and solid precipitation from the associated weather station (La Thile-Villaret), which has shown a decrease over the years, visible from both the daily, monthly and annual time series. The Standard Discharge Index (SDI) statistical method, allowed us to verify this phenomenon of spring abundance of the last period of the Promise spring, which unlike the other springs, closes the year 2022 with a still positive SDI value, despite the fact that the lowest rainfall in the historical series occurred.

In addition, trend analysis was performed with Linear Regression, Mann Kendal and Sen's Slopes, to point out the discordance with what is happening at the solid and liquid precipitation levels. Of course, Promise is the most striking case in terms of the interaction of water resources and rising melt of Ruitor glacier over time. However, it served as an example in order to understand the behaviors of springs whose water supply could be derived from water sources more difficult to recognize.

In this case we are talking about permafrost, the characteristics of which are explained in the first chapter. Permafrost is found widely above 2000 meters, but its appearance is hardly discernible. Certainly, in high mountains, a sign of the presence of permafrost are rock glaciers, mostly gravitational debris bodies with an elongated shape. The shape determined by plastic deformation, is an indication of the presence of ice matrix. This does not guarantee to know whether this matrix has melted over the years or is still present in the body, which differentiates active or relict permafrost.

This uncertainty related to permafrost water availability usually makes spring analysis very complicated, which when the resource shows a conspicuous amount of water in the face of reduced rainfall, may mean that the aquifer has been soaked with meltwater from portions of the permafrost.

This situation, thanks to the analyses carried out, most likely occurred for the Alpe Perrot and Cheserod springs, which until the year 2019 showed a very good correlation with rainfall, both in terms of trends and least squares correlation between annual rainfall and annual runoff volumes. While it has been shown in the three years 2019-2020-2021 an increase in runoff flows respect to modest rainfall, leading the good correlation of previous years to deteriorate significantly.

The SDI of these springs also shows for these three years a significant prosperity from the point of view of runoff volumes and then returns in 2022 to worsen significantly consistent with the low precipitation in the same year.

In fact, the spatial analysis of these two springs shows us the presence of large traces of permafrost in the form of Rock Glacier; the northern exposure of these basins favors the maintenance of the ice matrix, which, however, in recent years with rising temperatures has begun to disintegrate.

In fact, as has been shown in previous chapters, an increase in temperature of about 1.5 °C over the past twelve years has been matched by a rise in elevation 250 of the thermal zero, going on to interact with new portions of permafrost that were previously intact, releasing water into the environment.

Knowledge of the territory, combined with high-frequency monitoring of high mountain springs, promotes an understanding of the evolution of the semi-permanent cryosphere interacting with water resources. This, without having to make use of invasive and expensive tools that result from deep drilling of soil and ice to monitor permafrost and glacier melt.

It is only necessary to have the ability to process valuable data using classical and modern approaches with the support of programming languages such as Python that allow even those who are not computer specialists, to have access to advanced mathematical and statistical processing.

The simplicity of the Python language, lies in being able to download entire modules that already possess the useful mathematical structure in order to obtain the result from a time series of raw values. Furthermore, since Python is an opensource language improves the ease of consultation even on different websites and blogs.

This, should be a means used by those who manage, monitor territorial water resources such as, Regions, Area Authorities, ARPA and Water Service Managers. They must ensure the availability and quality of water to every citizen, providing themselves with advanced tools for analyzing the resource in order to better plan and manage economic and environmental resources.

In addition to the research conducted in the Aosta Valley, mainly related to the interaction between the water resource and the cryosphere, an analysis was conducted in the laboratory of Politecnico di Milano and at Mascognaz case study to understand

how increased temperature and thus faster melting phenomena can generate slope instability phenomena.

First, it was understood through the statistical analysis conducted at Mascognaz through the support of the state-of-the-art nivo-meteorological station, which parameters most influence snow melting. It was understood that it is safe to rely on melt models that consider only atmospheric temperature as an independent variable.

In the University laboratory, it was instead understood that soils directly covered by snow/ice mantle have a sort of thermal barrier, which prevents melted snow from infiltrating approaching saturation conditions and thus slope collapse.

Differently, it is necessary to treat those portions of ground that are downstream from cryosphere covers, since they no longer have the protection of thermal barrier formed in the upper layer of the soil, therefore, they have no way to protect themselves from infiltration. For this reason, downstream of large snow and glacial melt events, there are soils that are more susceptible to saturation and thus collapse.

To conclude, this preliminary analysis of which parameters are most likely to play a crucial role in landslide phenomena caused by cryosphere melting has brought with it the need to foreground atmospheric temperature and soil temperature. In fact, they are crucial dynamic factors that drive infiltration within porous soil media, besides the non-dynamic predisposing elements that characterize a slope including: slope, soil composition, and presence of vegetation.

So, the empirical analysis shown, is a key supplement for making susceptibility and landslide risk maps in high mountain environments where climate change is modifying the rates at which water quantities are released into the environment.

This is a fundamental requirement for stakeholders and territorial authorities, who need to be increasingly aware of the evolution of hydrogeological risk, which plays a fundamental role for economic and social growth in mountainous territories.

5.1 Further and future research developments

Some analyses could bring to light more in-depth knowledge regarding the influence of hydrogeological inputs on the spring regime of the five case studies analyzed.

One of these is the isotopic characterization of water, which is exploited to understand the share of water derived from the cryosphere. In fact, several studies have already been carried out on how atmospheric processes that generate solid and liquid precipitation, snow metamorphism, and the hydrogeological cycle affect the concentrations of Tritium, Oxygen 18 and Deuterium isotopes in water.

To do this, the Applied Geology Team of the Politecnico di Torino University has already made funds available to be able to conduct this analysis, particularly in the Promise spring case study, where the discordance between spring regime and precipitation is greater, so the glacier contribution is more plausible. Therefore, it will be necessary to take different water samples on different elevation levels of the case study, from the spring to the glacier, via the Rutor torrent, taking samples of the snowpack on the spring slope and on different elevations up to the ice samples to be taken on the glacial front in the summer periods.

In addition, more frequent (one every 4 months) sampling of chemical data: EC, ions and metals, would also help to understand the seasonality of hydrological behaviors influenced by rainfall, glacier melt, permafrost and temporary cryosphere such as snowpack.

REFERENCES

Adji, T. N. and Bahtiar, I. Y. (2016) 'Rainfall–discharge relationship and karst flow components analysis for karst aquifer characterization in Petoyan Spring, Java, Indonesia', *Environmental Earth Sciences*, 75(9), pp. 1–10. doi: 10.1007/s12665-016-5553-1.

Al-Umar, M., Fall, M. and Daneshfar, B. (2020) 'GIS-based modeling of snowmelt-induced landslide susceptibility of sensitive marine clays', *Geoenvironmental Disasters*, 7(1). doi: 10.1186/s40677-020-0142-8.

Al, J. B. et (1987) 'Standardized Precipitation Index User Guide', *Journal of Applied Bacteriology*, 63(3), pp. 197–200.

Amanambu, A. C. et al. (2020) 'Groundwater system and climate change: Present status and future considerations', *Journal of Hydrology*, 589(May), p. 125163. doi: 10.1016/j.jhydrol.2020.125163.

Anderson, D. M., & Morgenstern, N. R. (1973). *Physics, chemistry and mechanics of frozen ground: A review*. In *Proceedings of the Second International Conference on Permafrost* (pp. 257-288). National Academy of Sciences Washington, DC.

Balestra, V., Fiorucci, A. and Vigna, B. (2022) 'Study of the Trends of Chemical–Physical Parameters in Different Karst Aquifers: Some Examples from Italian Alps', *Water (Switzerland)*, 14(3). doi: 10.3390/w14030441.

Balzan, F. (2013). *Proprietà fisiche e metamorfismi della neve al suolo*. Gruppo Natura Bellunese, 39.

Banzato, C. et al. (2020) 'POLITECNICO DI TORINO Repository ISTITUZIONALE Application of the Vulnerability Estimator for Spring Protection Areas (VESPA index) in mountain Application of the Vulnerability Estimator for Spring Protection Areas (VESPA Index) in mountain Quaternary', (August).

Beniston, M. et al. (2018) 'The European mountain cryosphere: A review of its current state, trends, and future challenges', *Cryosphere*, 12(2), pp. 759–794. doi: 10.5194/tc-12-759-2018.

- Berg, N. and Hall, A. (2015) 'Increased interannual precipitation extremes over California under climate change', *Journal of Climate*, 28(16), pp. 6324–6334. doi: 10.1175/JCLI-D-14-00624.1.
- Boeckli, L. et al. (2012) 'Permafrost distribution in the European Alps: Calculation and evaluation of an index map and summary statistics', *Cryosphere*, 6(4), pp. 807–820. doi: 10.5194/tc-6-807-2012.
- Bonetto, F., & Gianotti, F. (1998). *Carta geologico-strutturale della Valle d'Aosta*.
- Boon, S. and Sharp, M. (2003) 'The role of hydrologically-driven ice fracture in drainage system evolution on an Arctic glacier', *Geophysical Research Letters*, 30(18), pp. 3–6. doi: 10.1029/2003GL018034.
- Camera, C. A. S. et al. (2021) 'Introducing intense rainfall and snowmelt variables to implement a process-related non-stationary shallow landslide susceptibility analysis', *Science of the Total Environment*, 786, p. 147360. doi: 10.1016/j.scitotenv.2021.147360.
- Carvalho-Santos, C. et al. (2017) 'Climate Change Impacts on Water Resources and Reservoir Management: Uncertainty and Adaptation for a Mountain Catchment in Northeast Portugal', *Water Resources Management*, 31(11), pp. 3355–3370. doi: 10.1007/s11269-017-1672-z.
- Cazcarro, I., López-Morales, C. A. and Duchin, F. (2016) 'The global economic costs of the need to treat polluted water', *Economic Systems Research*, 28(3), pp. 295–314. doi: 10.1080/09535314.2016.1161600.
- Chenoweth, J. (2008) 'A re-assessment of indicators of national water scarcity', *Water International*, 33(1), pp. 5–18. doi: 10.1080/02508060801927994.
- Chersich, S. et al. (2015) 'Climate change impacts on the Alpine ecosystem: An overview with focus on the soil - A review', *Journal of Forest Science*, 61(11), pp. 496–514. doi: 10.17221/47/2015-JFS.
- Cheval, S. (2015) 'The Standardized Precipitation Index – an overview', *Romanian Journal of Meteorology*, 12(1–2), pp. 17–64.

Chiaudani, A., Di Curzio, D., & Rusi, S. (2019). The snow and rainfall impact on the Verde spring behavior: A statistical approach on hydrodynamic and hydrochemical daily time-series. *Science of the Total Environment*, 689, 481-493.

Clow, D. W. (2010) 'Changes in the timing of snowmelt and streamflow in Colorado: A response to recent warming', *Journal of Climate*, 23(9), pp. 2293–2306. doi: 10.1175/2009JCLI2951.1.

Cuffey, K. M., & Paterson, W. S. B. (2010). *The physics of glaciers*. Academic Press.
Dal Piaz, G. (1992). *Guide Geologica Vol. 2/1: Le Lpi dal Monte Bianco al lago Maggiore. BeMa*, Vol. 3/1. ISBN-13: 9788871431239.

De Giusti, Fabio, et al. (2003) 'Carta geotettonica della Valle d'Aosta.' Università di Padova.

Dey, R. et al. (2019) 'A review of past and projected changes in Australia's rainfall', *Wiley Interdisciplinary Reviews: Climate Change*, 10(3), pp. 1–23. doi: 10.1002/wcc.577.

Dey, S. et al. (2020) 'Potential impact of rainfall variability on groundwater resources: a case study in Uttar Pradesh, India', *Arabian Journal of Geosciences*, 13(3). doi: 10.1007/s12517-020-5083-8.

Djordjevic, M. and Dankovic, D. (2019) 'A smart weather station based on sensor technology', *Facta universitatis - series: Electronics and Energetics*, 32(2), pp. 195–210. doi: 10.2298/fuee1902195d.

Dobinski, W. (2011) 'Permafrost', *Earth-Science Reviews*, 108(3–4), pp. 158–169. doi: 10.1016/j.earscirev.2011.06.007.

Dombrowski, O., Franssen, H. H. and Brogi, C. (2021) 'Weather Monitoring'.

Dourte, D. et al. (2013) 'Rainfall Intensity-Duration-Frequency Relationships for Andhra Pradesh, India: Changing Rainfall Patterns and Implications for Runoff and Groundwater Recharge', *Journal of Hydrologic Engineering*, 18(3), pp. 324–330. doi: 10.1061/(asce)he.1943-5584.0000625.

Draper, N. R., & Smith, H. (1998). *Applied regression analysis (Vol. 326)*. John Wiley & Sons.

- Foster, S. et al. (2013) ‘Groundwater-a global focus on the “local resource”’, *Current Opinion in Environmental Sustainability*, 5(6), pp. 685–695. doi: 10.1016/j.cosust.2013.10.010.
- Fountain, A. G. et al. (2012) ‘The disappearing cryosphere: Impacts and ecosystem responses to rapid cryosphere loss’, *BioScience*, 62(4), pp. 405–415. doi: 10.1525/bio.2012.62.4.11.
- Gabrieli, J. and Barbante, C. (2014) ‘The alps in the age of the anthropocene: The impact of human activities on the cryosphere recorded in the Colle Gnifetti glacier’, *Rendiconti Lincei*, 25(1), pp. 71–83. doi: 10.1007/s12210-014-0292-2.
- Gariano, S. L. et al. (2015) ‘Calibration and validation of rainfall thresholds for shallow landslide forecasting in Sicily, southern Italy’, *Geomorphology*, 228, pp. 653–665. doi: 10.1016/j.geomorph.2014.10.019.
- Giardino, M. and Ratto, S. (2005) ‘6 . Analisi del dissesto da frana in Valle d ’ Aosta’, pp. 121–150.
- Girardeau-Montaut, D. (2016). *CloudCompare. France: EDF R&D Telecom ParisTech, 11.*
- Gizzi, M. et al. (2022) ‘Aosta Valley Mountain Springs: A Preliminary Analysis for Understanding Variations in Water Resource Availability under Climate Change’, *Water*, 14(7), p. 1004. doi: 10.3390/w14071004.
- Guenang, G. M. and Mkankam Kanga, F. (2014) ‘Computation of the standardized precipitation index (SPI) and its use to assess drought occurrences in Cameroon over recent decades’, *Journal of Applied Meteorology and Climatology*, 53(10), pp. 2310–2324. doi: 10.1175/JAMC-D-14-0032.1.
- Harris, I. et al. (2020) ‘Version 4 of the CRU TS monthly high-resolution gridded multivariate climate dataset’, *Scientific Data*, 7(1), pp. 1–18. doi: 10.1038/s41597-020-0453-3.
- Hodson, A. J. (2014) ‘Understanding the dynamics of black carbon and associated contaminants in glacial systems’, *Wiley Interdisciplinary Reviews: Water*, 1(2), pp. 141–149. doi: 10.1002/wat2.1016.

Hotaling, S. et al. (2021) 'Biological albedo reduction on ice sheets, glaciers, and snowfields', *Earth-Science Reviews*, 220(January), p. 103728. doi: 10.1016/j.earscirev.2021.103728.

Huang, C. C. and Yuin, S. C. (2010) 'Experimental investigation of rainfall criteria for shallow slope failures', *Geomorphology*, 120(3–4), pp. 326–338. doi: 10.1016/j.geomorph.2010.04.006.

Hutcheson, G. D. (2011). Ordinary least-squares regression. L. Moutinho and GD Hutcheson, *The SAGE dictionary of quantitative management research*, 224-228.

ISTAT. Available online: <https://demo.istat.it/bilmens/index.php?anno=2021&lingua=ita> (accessed on 13 February 2023).

Ivanov, V. et al. (2020) 'Investigation on the role of water for the stability of shallow landslides-insights from experimental tests', *Water (Switzerland)*, 12(4), pp. 1–19. doi: 10.3390/W12041203.

Ivanov, V. et al. (2021) 'Applicability of an interferometric optical fibre sensor for shallow landslide monitoring – Experimental tests', *Engineering Geology*, 288(April), p. 106128. doi: 10.1016/j.enggeo.2021.106128.

Jeelani, G. et al. (2017) 'Distinguishing and estimating recharge to karst springs in snow and glacier dominated mountainous basins of the western Himalaya, India', *Journal of Hydrology*, 550, pp. 239–252. doi: 10.1016/j.jhydrol.2017.05.001.

Jehanzaib, M. et al. (2020) 'Investigating effect of climate change on drought propagation from meteorological to hydrological drought using multi-model ensemble projections', *Stochastic Environmental Research and Risk Assessment*, 34(1), pp. 7–21. doi: 10.1007/s00477-019-01760-5.

Jentsch, A. and Beierkuhnlein, C. (2008) 'Research frontiers in climate change: Effects of extreme meteorological events on ecosystems', *Comptes Rendus - Geoscience*, 340(9–10), pp. 621–628. doi: 10.1016/j.crte.2008.07.002.

Jepsen, S. M. et al. (2016) 'Hydrogeologic influence on changes in snowmelt runoff with climate warming: Numerical experiments on a mid-elevation catchment in the

Sierra Nevada, USA’, *Journal of Hydrology*, 533, pp. 332–342. doi: 10.1016/j.jhydrol.2015.12.010.

Jódar, J. et al. (2020) ‘Snowmelt as a determinant factor in the hydrogeological behaviour of high mountain karst aquifers: The Garcés karst system, Central Pyrenees (Spain)’, *Science of the Total Environment*, 748, p. 141363. doi: 10.1016/j.scitotenv.2020.141363.

Jones, D. B. et al. (2019) ‘Rock glaciers and mountain hydrology: A review’, *Earth-Science Reviews*, 193(October 2018), pp. 66–90. doi: 10.1016/j.earscirev.2019.04.001.

Kappelle, M., Van Vuuren, M. M. I. and Baas, P. (1999) ‘Effects of climate change on biodiversity: A review and identification of key research issues’, *Biodiversity and Conservation*, 8(10), pp. 1383–1397. doi: 10.1023/A:1008934324223.

Karimi, T. et al. (2021) ‘Impact of climate change on greenhouse gas emissions and water balance in a dryland-cropping region with variable precipitation’, *Journal of Environmental Management*, 287. doi: 10.1016/j.jenvman.2021.112301.

Karmegam, U., Chidambaram, S., Prasanna, M. V., Sasidhar, P., Manikandan, S., Johnsonbabu, G., ... & Anandhan, P. (2011). A study on the mixing proportion in groundwater samples by using Piper diagram and Phreeqc model. *Chinese Journal of Geochemistry*, 30, 490-495.

Khamis, K. et al. (2016) ‘Glacier–groundwater stress gradients control alpine river biodiversity’, *Ecohydrology*, 9(7), pp. 1263–1275. doi: 10.1002/eco.1724.

Khan, S., Gabriel, H. F. and Rana, T. (2008) ‘Standard precipitation index to track drought and assess impact of rainfall on watertables in irrigation areas’, *Irrigation and Drainage Systems*, 22(2), pp. 159–177. doi: 10.1007/s10795-008-9049-3.

Kloenne, U. et al. (2022) ‘Only halving emissions by 2030 can minimize risks of crossing cryosphere thresholds’, *Nature Climate Change*, 13(January), pp. 13–15. doi: 10.1038/s41558-022-01566-4.

Knight, J., Harrison, S. and Jones, D. B. (2019) ‘Rock glaciers and the geomorphological evolution of deglaciating mountains’, *Geomorphology*, 324, pp. 14–24. doi: 10.1016/j.geomorph.2018.09.020.

Kresic, N. and Bonacci, O. (2010) 'Spring discharge hydrograph', *Groundwater Hydrology of Springs*, pp. 129–163. doi: 10.1016/B978-1-85617-502-9.00004-9.

Leone, G. et al. (2021) 'A hundred years of Caposele spring discharge measurements: trends and statistics for understanding water resource availability under climate change', *Stochastic Environmental Research and Risk Assessment*, 35(2), pp. 345–370. doi: 10.1007/s00477-020-01908-8.

Levy, A. et al. (2015) 'Long-term variability of proglacial groundwater-fed hydrological systems in an area of glacier retreat, Skeiárásandur, Iceland', *Earth Surface Processes and Landforms*, 40(7), pp. 981–994. doi: 10.1002/esp.3696.

Limet, Centro Meteo Ligure (2023). GRADIENTE TERMICO. <https://www.centrometeoligure.com/meteowiki/gradientetermico/#:~:text=Nella%20ibera%20atmosfera%20la%20temperatura,circa%201%20%C2%B0C%2Fhm>.

Lo Russo, S. et al. (2021) 'SOURCE: a semi-automatic tool for spring-monitoring data analysis and aquifer characterisation', *Environmental Earth Sciences*, 80(21), pp. 1–13. doi: 10.1007/s12665-021-10027-8.

Longoni, L. et al. (2022) 'Laboratory tests with interferometric optical fibre sensors to monitor shallow landslides triggered by rainfalls', *Landslides*, (February). doi: 10.1007/s10346-021-01803-5.

Lu, A. et al. (2009) 'On the relationship between latitude and altitude temperature effects', *Proceedings - 2009 International Conference on Environmental Science and Information Application Technology, ESIAT 2009*, 2, pp. 55–58. doi: 10.1109/ESIAT.2009.335.

Ludbrook, J. (2010) 'Linear regression analysis for comparing two measurers or methods of measurement: But which regression?', *Clinical and Experimental Pharmacology and Physiology*, 37(7), pp. 692–699. doi: 10.1111/j.1440-1681.2010.05376.x.

Machiwal, D. and Jha, M. K. (2006) 'Time series analysis of hydrologic data for water resources planning and management: a review', *Journal of Hydrology and Hydromechanics*, 54(3), pp. 237–257. Available at:

https://www.researchgate.net/publication/47737331_Time_Series_Analysis_of_Hydrologic_Data_for_Water_Resources_Planning_and_Management_A_Review.

Maeda, E. E. et al. (2011) 'Prospective changes in irrigation water requirements caused by agricultural expansion and climate changes in the eastern arc mountains of Kenya', *Journal of Environmental Management*, 92(3), pp. 982–993. doi: 10.1016/j.jenvman.2010.11.005.

Maeno, N., & Ebinuma, T. (1983). Pressure sintering of ice and its implication to the densification of snow at polar glaciers and ice sheets. *The Journal of Physical Chemistry*, 87(21), 4103-4110.

Marinelli, A., Medici, C., Rosi, A., Tofani, V., Bianchini, S., & Casagli, N. (2022). Shallow landslides and rockfalls velocity assessment at regional scale: a methodology based on a morphometric approach. *Geosciences*, 12(4), 177.

Mezaal, M. R. and Pradhan, B. (2018) 'An improved algorithm for identifying shallow and deep-seated landslides in dense tropical forest from airborne laser scanning data', *Catena*, 167(February), pp. 147–159. doi: 10.1016/j.catena.2018.04.038.

Mo, C. et al. (2019) 'Frequency analysis of precipitation extremes under climate change', *International Journal of Climatology*, 39(3), pp. 1373–1387. doi: 10.1002/joc.5887.

Mondani, M., Gizzi, M., & Taddia, G. (2022). Role of Snowpack-Hydrometeorological Sensors for Hydrogeological System Comprehension inside an Alpine Closed-Basin. *Sensors*, 22(19), 7130.

Nienow, P., Sharp, M. and Willis, I. (1998) 'Seasonal changes in the morphology of the subglacial drainage system, Haut Glacier d'Arolla, Switzerland', *Earth Surface Processes and Landforms*, 23(9), pp. 825–843. doi: 10.1002/(SICI)1096-9837(199809)23:9<825::AID-ESP893>3.0.CO;2-2.

Ogasawara, E. et al. (2010) 'Adaptive Normalization: A novel data normalization approach for non-stationary time series', *Proceedings of the International Joint Conference on Neural Networks*. doi: 10.1109/IJCNN.2010.5596746.

Oki, T. and Quijoch, R. E. (2020) 'Economically challenged and water scarce: identification of global populations most vulnerable to water crises', *International*

Journal of Water Resources Development, 36(2–3), pp. 416–428. doi: 10.1080/07900627.2019.1698413.

Padulano, R. et al. (2020) ‘Future rainfall scenarios for the assessment of water availability in Italy’, 2020 IEEE International Workshop on Metrology for Agriculture and Forestry, MetroAgriFor 2020 - Proceedings, pp. 241–246. doi: 10.1109/MetroAgriFor50201.2020.9277599.

Panzeri, L., Mondani, M., Taddia, G., Papini, M., & Longoni, L. (2022). ANALYSIS OF SNOWMELT AS A TRIGGERING FACTOR FOR SHALLOW LANDSLIDE. International Multidisciplinary Scientific GeoConference: SGEM, 22(1.1), 77-83.

Paschetta, M. et al. (2016) ‘Regional catalogue of the spiders (Arachnida, Araneae) of Aosta Valley (NW Italy)’, Zoosystema, 38(1), pp. 49–125. doi: 10.5252/z2016n1a3.

Paterson, W. S. B., Cuffey, K. (2006). The physics of glaciers. 4th Edition. Paperback ISBN: 9781493300761.

Persichillo, M. G. et al. (2017) ‘Shallow landslides susceptibility assessment in different environments’, Geomatics, Natural Hazards and Risk, 8(2), pp. 748–771. doi: 10.1080/19475705.2016.1265011.

Pistone, K., Eisenman, I. and Ramanathan, V. (2014) ‘Observational determination of albedo decrease caused by vanishing Arctic sea ice’, Proceedings of the National Academy of Sciences of the United States of America, 111(9), pp. 3322–3326. doi: 10.1073/pnas.1318201111.

Praveen, V. et al. (2018) ‘Data analysis using box plot and control chart for air quality’, Proceedings - International Conference on Trends in Electronics and Informatics, ICEI 2017, 2018-Janua, pp. 1082–1085. doi: 10.1109/ICOEI.2017.8300877.

Ravbar, N., Engelhardt, I. and Goldscheider, N. (2011) ‘Anomalous behaviour of specific electrical conductivity at a karst spring induced by variable catchment boundaries: The case of the Podstenjšek spring, Slovenia’, Hydrological Processes, 25(13), pp. 2130–2140. doi: 10.1002/hyp.7966.

Regione Autonoma Valle d’Aosta (2022), Catasto ghiacciai - Ghiacciai Areali. <https://mappe.partout.it/pub/GeoNavSCT/?metadato=MTD25N2506>

Ruane, A. C., Goldberg, R. and Chryssanthacopoulos, J. (2015) 'Climate forcing datasets for agricultural modeling: Merged products for gap-filling and historical climate series estimation', *Agricultural and Forest Meteorology*, 200, pp. 233–248. doi: 10.1016/j.agrformet.2014.09.016.

Senatore, G. (2013). *Storia della sostenibilità: dai limiti della crescita alla genesi dello sviluppo. Storia della sostenibilità, 0-0*. Milano : Franco Angeli, - Confini sociologici - ISBN: 9788856864144

Shannon, S. et al. (2019) 'Global glacier volume projections under high-end climate change scenarios', *Cryosphere*, 13(1), pp. 325–350. doi: 10.5194/tc-13-325-2019.

Somers, L. D. and McKenzie, J. M. (2020) 'A review of groundwater in high mountain environments', *Wiley Interdisciplinary Reviews: Water*, 7(6), pp. 1–27. doi: 10.1002/wat2.1475.

Szczucińska, A. M. and Wasielewski, H. (2013) 'Seasonal water temperature variability of springs from porous sediments in Gryżynka Valley, Western Poland', *Quaestiones Geographicae*, 32(3), pp. 111–117. doi: 10.2478/quageo-2013-0019.

Szwed, M. (2019) 'Variability of precipitation in Poland under climate change', *Theoretical and Applied Climatology*, 135(3–4), pp. 1003–1015. doi: 10.1007/s00704-018-2408-6.

T.O.Olatayo and Taiwo, A. I. (2014) 'Statistical Modelling and Prediction of Rainfall Time Series Data', *Global Journal of Computer Science and Technology*, 14(1), pp. 1–10. Available at: <http://computerresearch.org/index.php/computer/article/view/58>.

Taylor, R. (1990). Interpretation of the correlation coefficient: a basic review. *Journal of diagnostic medical sonography*, 6(1), 35-39.

Tokatli, C., Köse, E. and Çiçek, A. (2013) 'Groundwater Quality of Türkmen Mountain', 22(4), pp. 1197–1208.

Tresoldi, G. et al. (2019) 'Long-term hydrogeophysical monitoring of the internal conditions of river levees', *Engineering Geology*, 259(April), p. 105139. doi: 10.1016/j.enggeo.2019.05.016.

Uhlenbrook, S., & Connor, R. (2019). The United Nations world water development report 2019: leaving no one behind. UNESCO World Water Assessment Programme, Paris, UNESCO. ISBN 978-92-3-100309-7.

Varhola, A. et al. (2010) 'A new low-cost, stand-alone sensor system for snow monitoring', *Journal of Atmospheric and Oceanic Technology*, 27(12), pp. 1973–1978. doi: 10.1175/2010JTECHA1508.1.

van der Veen, C. J. (1999) 'Crevasses on glaciers', *Polar Geography*, 23(3), pp. 213–245. doi: 10.1080/10889379909377677.

Van Everdingen, R. O. (Ed.). (1998). Multi-language glossary of permafrost and related ground-ice terms in Chinese, English, French, German, Icelandic, Italian, Norwegian, polish, Romanian, Russian, Spanish, and Swedish. International Permafrost Association, Terminology Working Group.

Viviroli, D. et al. (2011) 'Climate change and mountain water resources: Overview and recommendations for research, management and policy', *Hydrology and Earth System Sciences*, 15(2), pp. 471–504. doi: 10.5194/hess-15-471-2011.

Wang, Y. et al. (2017) 'Flood/drought event identification using an effective indicator based on the correlations between multiple time scales of the Standardized Precipitation Index and river discharge', *Theoretical and Applied Climatology*, 128(1–2), pp. 159–168. doi: 10.1007/s00704-015-1699-0.

Weiskopf, S. R. et al. (2020) 'Climate change effects on biodiversity, ecosystems, ecosystem services, and natural resource management in the United States', *Science of the Total Environment*, 733. doi: 10.1016/j.scitotenv.2020.137782.

Welch, A. H., Westjohn, D. B., Helsel, D. R., & Wanty, R. B. (2000). Arsenic in ground water of the United States: occurrence and geochemistry. *Groundwater*, 38(4), 589-604.

White, G. F. (1993) 'World_Watershed_Re.Pdf'.

Williams, M. R. and King, K. W. (2020) 'Changing Rainfall Patterns Over the Western Lake Erie Basin (1975–2017): Effects on Tributary Discharge and Phosphorus Load', *Water Resources Research*, 56(3). doi: 10.1029/2019WR025985.

Wu, L. Z. et al. (2015) 'Analysis of physical testing of rainfall-induced soil slope failures', *Environmental Earth Sciences*, 73(12), pp. 8519–8531. doi: 10.1007/s12665-014-4009-8.

Wu, W. Y. et al. (2020) 'Divergent effects of climate change on future groundwater availability in key mid-latitude aquifers', *Nature Communications*, 11(1), pp. 1–9. doi: 10.1038/s41467-020-17581-y.

Xie, Y. et al. (2022) 'Water cost for water purification: Renewability assessment of a typical wastewater treatment plant in China', *Journal of Cleaner Production*, 349(November 2021), p. 131474. doi: 10.1016/j.jclepro.2022.131474.